



# Reactivity of the Solvated Electron, the Hydroxyl Radical and its Precursor in Deuterated Water Studied by Picosecond Pulse Radiolysis

Furong Wang

## ► To cite this version:

Furong Wang. Reactivity of the Solvated Electron, the Hydroxyl Radical and its Precursor in Deuterated Water Studied by Picosecond Pulse Radiolysis. Theoretical and/or physical chemistry. Université Paris Saclay (COMUE), 2018. English. NNT : 2018SACLS399 . tel-02057515

**HAL Id: tel-02057515**

**<https://tel.archives-ouvertes.fr/tel-02057515>**

Submitted on 5 Mar 2019

**HAL** is a multi-disciplinary open access archive for the deposit and dissemination of scientific research documents, whether they are published or not. The documents may come from teaching and research institutions in France or abroad, or from public or private research centers.

L'archive ouverte pluridisciplinaire **HAL**, est destinée au dépôt et à la diffusion de documents scientifiques de niveau recherche, publiés ou non, émanant des établissements d'enseignement et de recherche français ou étrangers, des laboratoires publics ou privés.

# Reactivity of the Solvated Electron, the Hydroxyl Radical and its Precursor in Deuterated Water Studied by Picosecond Pulse Radiolysis

Thèse de doctorat de l'Université Paris-Saclay  
préparée à l'Université Paris-Sud

École doctorale n°571 : sciences chimiques : molécules, matériaux  
instrumentation et biosystèmes (2MIB)  
Spécialité de doctorat : Chimie

Thèse présentée et soutenue, le 22 Octobre, 2018, par

**Mme Furong WANG**

Composition du Jury :

Mme Isabelle Lampre	
Professeur, Université Paris-Sud (– LCP)	Présidente
M. Jean-Marc Jung	
Professeur, Université de Strasbourg (– IPHC)	Rapporteur
M. Philippe Moisy	
Directeur de recherche, CEA Marcoule	Rapporteur
Mme Sophie Le Caer	
Directrice de recherche, CEA (– LIONS)	Examineur
M. Khashayar Ghandi	
Professeur, University of Guelph	Examineur
M. Mehran Mostafavi	
Professeur, Université Paris-Sud (– LCP)	Directeur de thèse

## Acknowledgements

Firstly, I would like to express my sincere gratitude to my advisor Prof. Mehran Mostafavi for the continuous support of my Ph.D study and related research, for his patience, motivation, and immense knowledge. His guidance helped me in all the time of research and writing of this thesis. I could not have imagined having a better advisor and mentor for my Ph.D study.

Besides my advisor, I would like to thank the rest of my thesis committee: Prof. Jean-Marc Jung, Dr. Philippe Moisy, Dr. Sophie Le Caer, Prof. Isabelle Lampre and Prof. Khashayar Ghandi, for their insightful comments and encouragement, but also for the hard question which incited me to widen my research from various perspectives.

I would like to thank Dr. Pascal Pernot, Dr. Pierre Archirel and Dr. Aurélien De Lande for their strong support, collaboration and insightful encouragement for my Ph.D research. Their excellent computation makes important sense to my thesis.

My sincere thanks also goes to Prof. Jacqueline Belloni, Dr. Jean-Louis Marignier and Hydn Remita. Their personalities, curiosity to the science, the ways of thinking and performing research encouraged me to be a person like them.

I would like to thank the engineers in our team, Dr. Uli Schmidhammer, Dr. Sergey Denisov, Jean-Philippe Larbre, Audrey Gayral, Pierre Jeunesse, Alexandre Demarque and Nicolas Decovemacher. Without them, I can't perform experiments in ELYSE.

I take this opportunity to express gratitude to all of administration group in the lab for helping me focusing the research, they are Séverine Bourguignon, Eve Ranvier, Anne Morel and Delphine Lelievre.

I thank Mireille Benoit for careful arrangement of all the chemical compounds during my Ph.D.

My sincere thanks also goes to my dear friends, Anna Balcerzyk, Jun Ma, Abdel Karim El Omar, Zhenpeng Cui, Xiaojing Wu, Xiaojiao Yuan, Viacheslav Shcherbakov, Raluca Musat, Teseer Bahry, Sarah Al-gharib..... I couldn't put all their name on the list. We have good time through my four year's life. I really enjoy the life here and never forget the memory in LCP.

Last but not the least, I would like to thank my family: my parents and my sister. My study is always backed by their support.

# Reactivity of the Solvated electron, the Hydroxyl radical and its Precursor in Deuterated Water Studied by Picosecond Pulse Radiolysis

<b>Chapter I: Introduction .....</b>	<b>3</b>
<b>1.1 General introduction.....</b>	<b>3</b>
<b>1.2 Quantification of radiation.....</b>	<b>4</b>
1.2.1 Definition of linear energy transfer (LET).....	5
1.2.2 Definition of radiolytic yield .....	7
<b>1.3 Radiolysis in water .....</b>	<b>8</b>
1.3.1 Physical stage ( $<10^{-15}$ s) .....	9
1.3.2 Physicochemical stage ( $\sim 10^{-15} \sim 10^{-12}$ s).....	9
1.3.3 Non-homogenous chemical stage ( $\sim 10^{-12} - 10^{-6}$ s).....	11
<b>1.4 Concluding remark .....</b>	<b>11</b>
<b>References .....</b>	<b>13</b>
<b>Chapter II: Experimental methodology.....</b>	<b>18</b>
<b>2.1 State of art.....</b>	<b>18</b>
2.1.1 High LET .....	18
2.1.2 Low LET .....	20
2.1.3 Detection technique for ultrafast radiolysis .....	25
<b>2.2 ELYSE — A picosecond pump-probe radiolysis platform.....</b>	<b>27</b>
2.2.1 EA-1 — Picosecond pulse-probe setup.....	35
2.2.2 EA-3 — Streak camera .....	39
2.2.3 $\gamma$ -source .....	46
<b>2.3 SK-Ana — MCR-ALS analysis method.....</b>	<b>47</b>



<b>2.4 Chemicals .....</b>	<b>51</b>
<b>2.5 Concluding remark .....</b>	<b>52</b>
<b>References .....</b>	<b>53</b>
 <b><i>Chapter III: Time Dependent Yield of Solvated Electron and OD<sup>•</sup> Radical in Deuterated Water at Low LET Studied by Picosecond Pulse Radiolysis.....</i></b>	
<b>3.1 State of the art and objective .....</b>	<b>59</b>
3.1.1 Introduction .....	59
3.1.2 Objective .....	64
<b>3.3 The solvated electron in D<sub>2</sub>O.....</b>	<b>65</b>
3.3.1 Isosbestic method.....	67
3.3.2 Absorption spectrum of $e_{D_2O}^-$ .....	71
3.3.3 Determination of the time-dependent yield of $e_{D_2O}^-$ .....	77
<b>3.4 Time-dependent yield of OD<sup>•</sup> radical .....</b>	<b>81</b>
3.4.1 Transient absorption induced in FSOFC.....	82
3.4.2 Determination of the time-dependent yield of OD <sup>•</sup> radical .....	90
<b>3.5 Conclusions .....</b>	<b>92</b>
<b>Reference.....</b>	<b>96</b>
 <b>Appendix: Molar absorption coefficient of <math>e_s^-</math> in D<sub>2</sub>O (250 to 1500 nm) obtained in the present work.....</b>	
<b>Chapter IV: Ultra-fast Charge Migration Competes with Proton Transfer in the Early Chemistry of H<sub>2</sub>O<sup>•+</sup> .....</b>	<b>108</b>
<b>4.1 State of the art .....</b>	<b>108</b>

4.1.1 General introduction .....	108
4.1.2 Oxidation reactions by radicals.....	113
4.1.3 Reactivity of $\text{H}_2\text{O}^{*+}$ in halide solution.....	117
4.1.4 Reactivity of $\text{H}_2\text{O}^{*+}$ in concentrated acidic solution .....	121
<b>4.2 Results — Reactivity of radical cation of water in <math>\text{D}_2\text{SO}_4/\text{D}_2\text{O}</math> system</b>	<b>136</b>
4.2.1 Transient absorption spectra .....	137
4.2.2 Analysis of the kinetics .....	141
4.2.2 Yield of scavenging $\text{D}_2\text{O}^{*+}$ in $\text{D}_2\text{SO}_4/\text{D}_2\text{O}$ solution .....	144
<b>4.3 Results — Isotopic effect on the chemistry of <math>\text{H}_2\text{O}^{*+}</math></b> .....	<b>147</b>
4.3.1 Experiment on isotopic effect .....	147
4.3.2 Analysis and discussion .....	150
<b>4.4 Conclusions .....</b>	<b>153</b>
<b>References .....</b>	<b>155</b>
<b><i>Chapter V: Conclusions and perspectives</i> .....</b>	<b><i>163</i></b>
<b>5.1 Conclusions .....</b>	<b>163</b>
<b>5.2 Perspectives.....</b>	<b>166</b>
<b>References .....</b>	<b>168</b>
<b><i>Publications During Thesis</i>.....</b>	<b><i>169</i></b>
<b><i>Résumé</i> .....</b>	<b><i>171</i></b>

# Chapter I: Introduction

## **Table of content**

### 1.1 General introduction

### 1.2 Quantification of radiation

#### 1.2.1 Definition of linear energy transfer

#### 1.2.2 Definition of radiolytic yield

### 1.3 Radiolysis in water

#### 1.3.1 Physical stage ( $<10^{-15}$ s)

#### 1.3.2 Physicochemical stage ( $\sim 10^{-15}$ - $10^{-12}$ s)

#### 1.3.2 Non-homogenous chemical stage ( $\sim 10^{-12}$ - $10^{-6}$ s)

### 1.4 Concluding remark

### References

# Chapter I: Introduction

## 1.1 General introduction

Radiation chemistry is a branch of chemistry that studies chemical transformations in materials exposed to high-energy radiations. It uses radiation as the initiator of chemical reactions, as a source of energy that disrupts the sensitive energy balance in stable systems. In that way it is a younger sister of photochemistry, which does the same, but uses another type of electromagnetic energy—light — as the initiator. Radiation chemistry does not deal with radioactive elements (as radiochemistry does), except to use them as a source of radiation, always physically separated from the irradiated system.

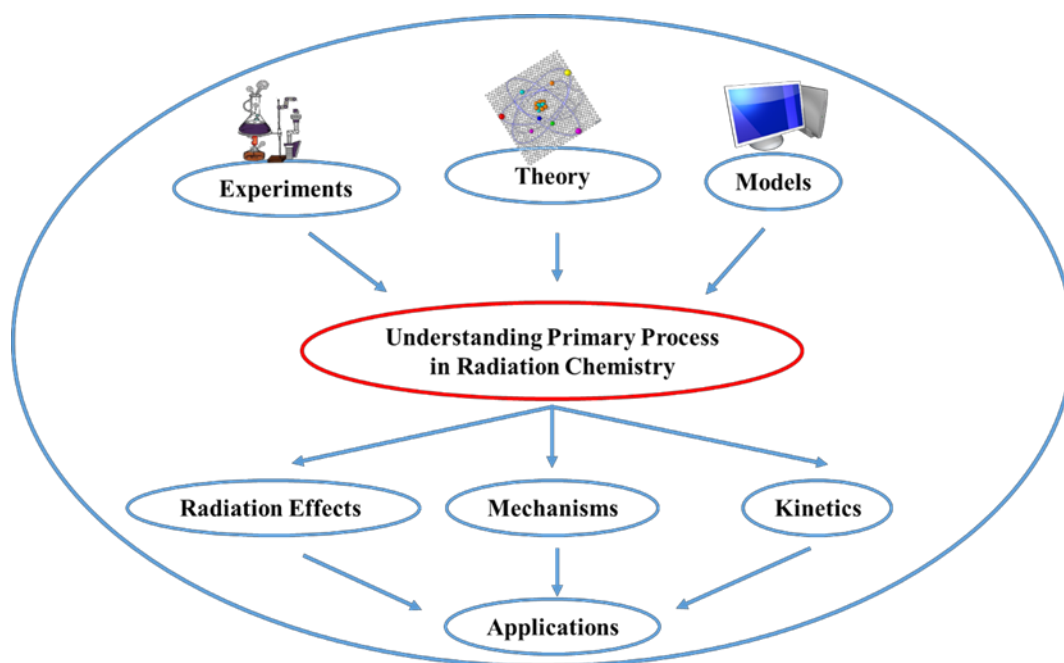


**Figure 1.1** The key role of fundamental studies in radiation chemistry

Understanding radiation-induced processes is of vital significance in such diverse fields as waste remediation in environmental cleanup,<sup>1–3</sup> radiation processing of polymers<sup>4,5</sup> and food<sup>6–8</sup>, medical diagnosis and therapy,<sup>9,10</sup> catalysis of chemical reactions,<sup>11–14</sup> environmentally benign synthesis,<sup>1,15</sup> and nuclear energy production.<sup>16–18</sup> Radiation chemistry provides for these fields fundamental quantitative data, such as reaction rate coefficients, diffusion coefficients, radiation chemical yields, etc., as well as providing useful quantitative information of technological and

medical importance, radiation chemistry is also a valuable tool for solving fundamental problems in chemistry and in material sciences. Exploiting the many facets of radiation chemistry requires a thorough and comprehensive understanding of the underlying chemical and physical processes. An understanding of the structure and dynamics of “tracks” produced by ionizing radiation is a central issue in the field. There is a continuing need to study the ultrafast processes that link the chemistry and physics of radiation-induced phenomena. This is especially true for practically important, but less well understood, nonstandard environments such as interfacial systems, supercritical media, and heterogeneous systems. These various goals necessitate the development and application of complementary programs of experiment and theory, and will involve the use of nonconventional radiation sources and the study of novel homogeneous and heterogeneous chemical systems. There is also a need to upgrade other types of instrumentation used in radiation chemistry in the national laboratories, including high field electron paramagnetic resonance, and modern analytical tools. The development and enhancement of these various tools will allow for a much wider use of the national radiation chemistry facilities.

Water is a major constituent of all living matter, representing 70-85% of the weight of cells. For this reason, water plays a major role in radiotherapy,<sup>19</sup> radiosterilization,<sup>20</sup> sewage treatment<sup>21</sup> and food irradiation<sup>22</sup>, *etc.* because its radiolysis produces reactive species which are responsible for indirect and/or direct effects. Furthermore, its absorption properties being very similar to those of the human body, water is also widely used for clinical dosimetry. For these reasons, radiolysis of water and aqueous solution has been extensively studied for more than a century. In fact, very shortly after the discovery of X-rays by Wilhelm Conrad Roentgen in 1895, the natural radioactivity of uranium compounds by Henri Becquerel in 1896, and the radioactive element radium by Pierre Curie, Marie Curie and Gustave Bémont in 1898, dissolved radium salt has been shown to decompose aqueous solutions by liberating hydrogen gas continuously, due principally to the release of  $\alpha$ -particles from the decomposition of radium.<sup>23</sup>  $\text{H}_2\text{O}_2$  was also found in the irradiated solution.<sup>24-26</sup> The mechanism accounting for the radiolysis of water has been presented after a century's survey. Nevertheless, it is unclear in the earliest term of the radiolysis of water because of the limitation of the technology.

## 1.2 Quantification of radiation

Energy emitted from a source is generally referred to as radiation. Ionizing radiation is the type of radiation that the emission occurs with enough energy so that during an interaction with an atom, it can remove tightly bound electrons from the orbit of an atom, causing the atom to become charged or ionized. Quantified parameters are essential to understand the radiation process that occur in the system.

### 1.2.1 Definition of linear energy transfer (LET)

Radiation effects depend on the type of irradiation and its mechanisms of deposition of energy into the irradiated medium. From the quantitative point of view, the impact of radiation with matter can be characterized as the rate of energy loss per unit length of track of the particle. The rate of energy loss per unit length of track of the particle is known as the stopping power or linear energy transfer (LET). LET could be expressed as:

$$LET = -\left(\frac{dE}{dx}\right)_{x=r} \quad \text{EQ. 1-1}$$

The units used for LET can be keV mm<sup>-1</sup>, eV m<sup>-1</sup> or eV Å<sup>-1</sup>.

The rate of energy loss of an energetic particle passing through a liquid is non-uniform; it increases as the kinetic energy of the particle decreases. When the ionizing particle is a high energy electron, the ionization events occur in small clusters called spurs that are widely separated along the track and the radiation is classed as low LET (**Figure 1.2**). For energetic nuclear ions, e.g. H<sup>+</sup>, He<sup>2+</sup>, etc., the rate of energy loss is much higher so that the spurs are much closer together and can overlap to form cylindrical columns of ionized molecules in the liquid. In this case the radiation is classed as high LET. Actually, low LET radiation has a high LET component due to low-energy secondary electrons, and high LET radiation has a low LET component due to high-energy secondary electrons, so it is common practice to classify types of radiation by their average LET over the length of the particle track.

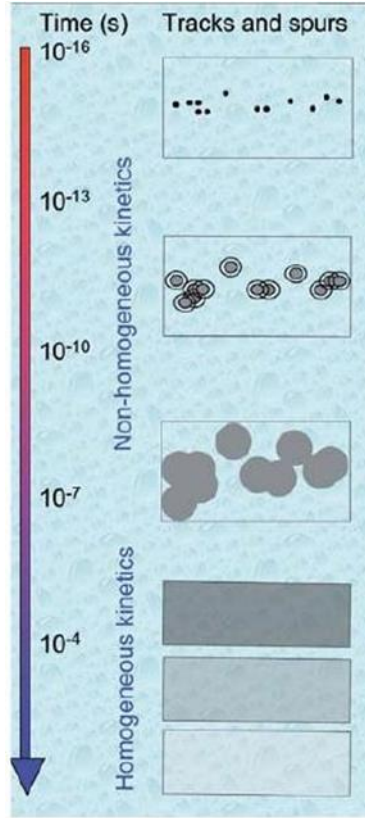


**Figure 1.2** Initial non-homogeneous spatial distribution of ionization events in spurs along the track, and evolution with time by diffusion and reaction up to homogeneous distribution at  $\approx 10^{-7}$  s.<sup>27</sup>

In most cases, the LET is equal to the “stopping power”. The Bethe theory of stopping power describes the mean energy loss by a charged particle due to the electrostatic interactions between the particle and the electrons of atoms in the medium.<sup>28</sup> For non-relativistic ions, the Bethe formula can be written as:

$$-\frac{dE}{dx} = \left( \frac{1}{4\pi\epsilon_0} \right)^2 \frac{4\pi Z^2 e^4}{m_0 V^2} N \ln \left( \frac{2m_0 V^2}{I} \right) \quad \text{EQ. 1-2}$$

In the equation,

- $Z$  is the charge of the incident ion.
- $V$  is the velocity of the incident ion.
- $m_0$  is the mass of electron.
- $N$  is target electron density.
- $I$  is the average of ionization potentials of the target.



Several important aspects are illustrated in this formula. Since  $\frac{dE}{dx} \propto \frac{Z^2}{V^2}$ , the LET of two ions of the same charge is higher for the ion with the lowest energy. This can be understood by noting that a slower ion has more time to interact with electrons of the medium than a faster ion; thus, the LET of the ion with the lowest energy is higher.

**Table 1.1** LET value for radiation.<sup>29</sup>

<b>Radiation</b>	<b>LET (keV/μm)</b>	<b>Radiation</b>	<b>LET ( keV/μm)</b>
1 MeV electrons	0.3	<sup>1</sup> H <sup>+</sup> 300eV/amu	0.3
<sup>60</sup> Co γ-rays	0.3	<sup>4</sup> He <sup>2+</sup> 6 Mev/amu	26
<sup>137</sup> Cs γ-rays	0.9	<sup>56</sup> Fe <sup>26+</sup> 1 GeV/amu	150
200 kV X-rays	1.7		

### 1.2.2 Definition of radiolytic yield

Radiolytic yields presents the results of quantitative research on the chemical effects of ionizing radiation. The yields are expressed in terms of G: a number of molecules, of ions, of radicals, and of bonds etc., either formed or destroyed by 100 eV of absorbed energy at certain time. The formula of calculation of the G value is defined as:

$$G(\text{molecule} / 100 \text{ eV}) = \frac{\text{Number of species formed or disappeared}}{100 \text{ eV absorbed}} \quad \text{EQ. 1-3}$$

Today, the most common unit of G value is mol J<sup>-1</sup>. It can be converted as:

$$1 \text{ molecules} / 100 \text{ eV} = 1.036 \times 10^{-7} \text{ mol J}^{-1} \quad \text{EQ.1-4}$$

Generally, G value could be determined by:

$$G(t) = \frac{C(t)}{\text{Dose} \times \rho} \quad \text{EQ.1-5}$$

– C(t) is the concentration of the species at a given time t (in mol L<sup>-1</sup>).

– *Dose* is the absorbed energy per unit of mass by the system (in  $\text{J kg}^{-1}$  or Gy).

–  $\rho$  is the density of the sample ( $\text{g mL}^{-1}$ ).

Knowing the G value is particularly important for both the sample and the dosimetry. Usually, the G value of the given species itself is not measured directly. It is mostly based on a yield of primary radicals that has been estimated from measured yield at infinite dilution of all scavengers. These yields represent the number of the primary radicals that diffuse out of the tracks formed by the ionizing radiation and their secondary electrons. Immediately after the arrival of the high energy radiation, the tracks contain a high density of radicals and other fragments, and many of the radicals combine with each other. Thus only a fraction of the original primary radicals escapes into the bulk solution and is measured.

### 1.3 Radiolysis in water

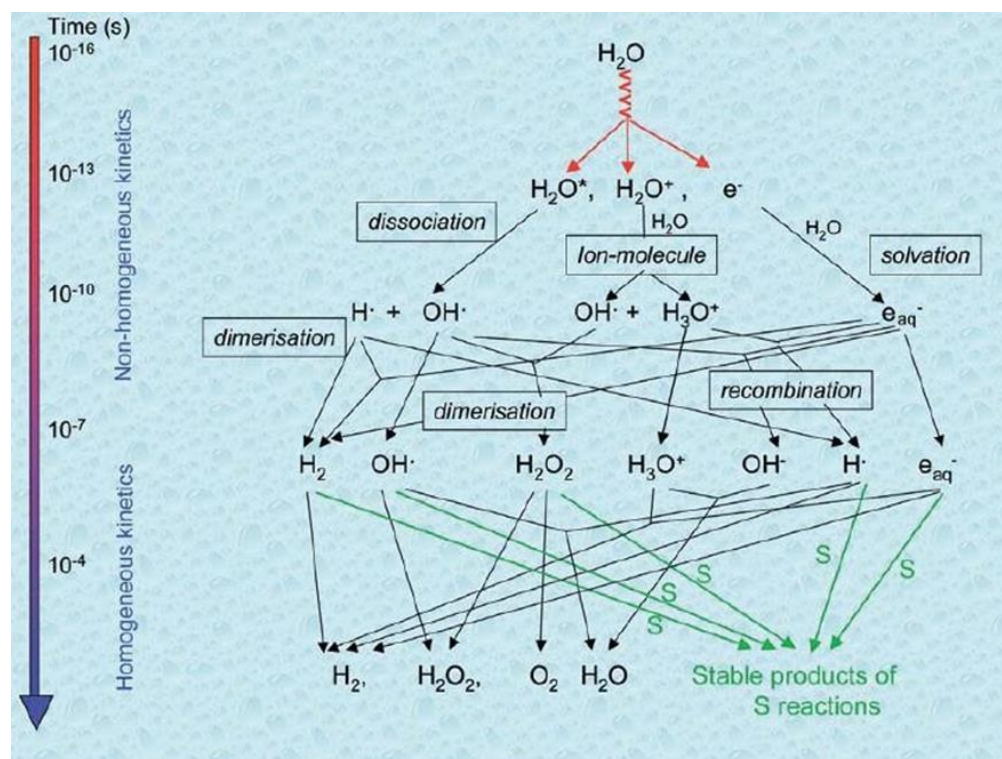


**Figure 1.3** Scheme of reactions of transient species produced by irradiation in water without or with a diluted solute S acting as a radical scavenger.<sup>9</sup>

The radiolysis of water is usually divided in three more or less overlapping stages: physical

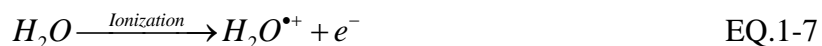
(<10<sup>-15</sup> s) (**Figure 1.3**), physicochemical stage (~10<sup>-15</sup>-10<sup>-12</sup> s) and non-homogeneous chemical stage (~10<sup>-12</sup>-10<sup>-6</sup> s). This time division is controversial, it gives a convenient way to describe the mechanisms involved in water radiolysis.

### 1.3.1 Physical stage (<10<sup>-15</sup> s)

Direct ionization of water produces a radical ion and a free subexcitation electron (E < 7.4 eV). Energy transfer can produce a water molecule in an excited state.



Direct ionization of water produces a radical ion and a free subexcitation electron (E < 7.4 eV).



The time scale for the creation of these species is on the order of 10<sup>-16</sup> seconds.

### 1.3.2 Physicochemical stage (~10<sup>-15</sup>~10<sup>-12</sup> s)

The ionized and excited molecules created during the physical stage are highly unstable. During this stage, lasting ~10<sup>-12</sup> s, the ionized and excited water molecules dissipate their energy by energy transfer to neighboring molecules and bond rupture. The sequence of events of the physicochemical stage is, in fact, not well characterized experimentally. However, some important physicochemical stage events worth mentioning: proton transfer to a neighboring molecule, dissociation of excited water molecule and electron thermalization and solvation.

The proton transfer to a neighboring water molecule is very important, because it leads to the production of an OH<sup>•</sup> radical:



For an excited water molecule, there are several channels for the dissociation



The excited water molecule can dissipate excess energy by bond breakage to produce hydroxyl and hydrogen radicals. It takes ~5eV to break the O-H bond.



Where  $O(^1D)$  and  $O(^3p)$  are the singlet and triplet state of the atomic oxygen, respectively.



The excited water molecule can also return to its fundamental state without dissociation by heat loss.

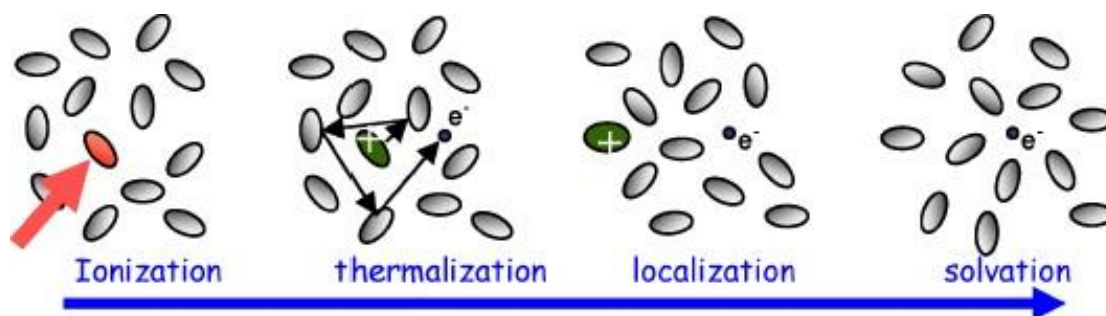
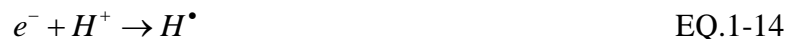


**Figure 1.4** Cartoon showing the formation of the solvated electron upon solvent ionization.<sup>9</sup>

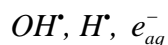
Most secondary electrons have low energy,<sup>30</sup> but some of them may have energy in the keV or even in the MeV range. These electrons lose their energy into medium by doing further ionization, excitations until they eventually reach thermal equilibrium with the liquid. The electron, which is negatively charged, interacts with the dipoles of the surrounding water molecules and becomes trapped in a state called “trapped electron”. Finally, this electron becomes a “hydrated electron”, which behaves like chemical species (**Figure 1.4**). This rapid sequence of events can be written as follows:



Besides, the electron could react with  $H^+$  to form a H atom in acidic condition:

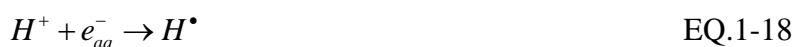


The concentrations of the radicals depend on the energy deposited in water. Thus, the three initial species  $H_2O^*$ ,  $H_2O^{*+}$ , and  $e^-$ , react further to produce chemically reactive species:



### 1.3.3 Non-homogenous chemical stage ( $\sim 10^{-12}$ - $10^{-6}$ s)

Three of the new species created are radicals:  $\text{OH}^\bullet$ ,  $\text{H}^\bullet$ ,  $e_{aq}^-$ . These species now begin to migrate randomly about their initial positions. As this diffusion proceeds, individual pairs may come close enough together to react with each other. A variety of reactions are possible in the track of the charged particle.



Most of these reactions remove chemically reactive species from the system. With time (by  $\sim 10^{-6}$  s) all of the reactive species have diffused sufficiently far that further reactions are unlikely. The chemical development of the track is over by  $10^{-6}$  s.

At the end of the physicochemical stage, the species  $\text{H}^\bullet$ ,  $\text{OH}^\bullet$ ,  $\text{H}_2$ ,  $\text{H}_2\text{O}_2$  are created in very high concentration in the spurs. Other species such as  $\text{O}(^3\text{P})$  may also be present, in small quantity. They diffuse in the medium and eventually encounter chemical species created in other spurs, which gives them the opportunity to react. In general, the radical species (such as  $\text{H}^\bullet$ ,  $\text{OH}^\bullet$  and  $e_{aq}^-$ ) react in  $\sim 1$   $\mu\text{s}$  to form the molecular species  $\text{H}_2$  and  $\text{H}_2\text{O}_2$ .

## 1.4 Concluding remark

Deuterated water ( $\text{D}_2\text{O}$ ), generally known as heavy water, is a form of water that contains a larger than normal amount of the hydrogen isotope deuterium ( $^2\text{H}$  or  $\text{D}$ ).  $\text{D}_2\text{O}$  is one of the distinct features of pressurized heavy water reactor (PHWR), where it is used as coolant and moderator

because it exhibits a thousand times enhanced neutron-moderating ability compared to  $\text{H}_2\text{O}$ . In PHWR, the nuclear core is cooled by liquid heavy water that undergoes radiolytic decomposition induced by an intense ionizing radiation field. The incident energy comprises low LET X-rays, fast neutrons whose energy is transferred to protons and oxygen nuclei resulting in the emission of charged particle recoils of high LET, and also much higher LET radiation (recoils of  $^7\text{Li}$  ions and  $\alpha$ -particles). The aqueous radiolysis products must be assessed because they can induce unwanted deleterious corrosion, hydriding, and cracking of sensitive materials both in the core and in the various piping components of the reactors.<sup>31–33</sup> The basic interest of nuclear power engineers is to know the real concentrations of the oxidizing products and to select conditions at which their formation could be suppressed. Consequently, knowledge of the radiolytic yield of the product in  $\text{D}_2\text{O}$  formed by ionizing radiation is essential. Additionally, it is captivating to explore the isotopic effect of H-D on the radiolytic behavior of the species produced in the water after irradiation.

In this thesis, the subject of interest is on the time dependent radiolytic yield of the solvated electron and the hydroxyl radical (Chapter III) and the reactivity of the precursor of hydroxyl radical—the water cation radical (Chapter IV) in deuterated water on picosecond range.

## References

- (1) Getoff, N. The Role of Peroxyl Radicals and Related Species in the Radiation-Induced Degradation of Water Pollutants. In *Environmental Applications of Ionizing Radiation*; Cooper, W. J., Curry, R. D., O'Shea, K. E., Eds.; Wiley: New York, 1998; pp 231–246.
- (2) Pikaev A.K. Electron Beam Purification of Water and Wastewater. In *Environmental Application of Ionizing Radiation*; Cooper, W. J., Curry, R. D., O'Shea, K. E., Eds.; Wiley: New York, 1998; pp 495–506.
- (3) Pera-Titus, M.; García-Molina, V.; Baños, M. A.; Giménez, J.; Esplugas, S. Degradation of Chlorophenols by Means of Advanced Oxidation Processes: A General Review. *Appl. Catal. B Environ.* **2004**, *47*, 219–256.
- (4) Chapiro, A. *Radiation Chemistry of Polymeric Systems*; Wiley: New York, 1962.
- (5) Ivanov, V. S. *Radiation Chemistry of Polymers*”; VSP Publisher: Utrecht, 1992.
- (6) Vasseur, J.-P. *Ionisation Des Produits Alimentaires*; Tec & Doc - Lavoisier - APRIA - Teknéa: Paris, 1991.
- (7) A. E. Ehlermann, D. *Four Decades in Food Irradiation*; 2005; Vol. 73.
- (8) Raffi, J. The State of Food Irradiation and of Detection of Irradiated Foodstuffs. *Res. Adv. Food Sci.* **2002**, *3*, 11–19.
- (9) *Radiation in Medicine: A Need for Regulatory Reform*; Gottfried, K.-L. D., Penn, G., Eds.; The National Academies Press: Washington, DC, 1996.
- (10) Rose, J. H.; Norman, A.; Ingram, M.; Aoki, C.; Solberg, T.; Mesa, A. First Radiotherapy of Human Metastatic Brain Tumors Delivered by a Computerized Tomography Scanner (CTRx). *Int. J. Radiat. Oncol. • Biol. • Phys.* **1999**, *45*, 1127–1132.
- (11) Henglein, A. Small-Particle Research: Physicochemical Properties of Extremely Small Colloidal Metal and Semiconductor Particles. *Chem. Rev.* **1989**, *89*, 1861–1873.
- (12) Henglein, A. Colloidal Silver Nanoparticles: Photochemical Preparation and Interaction with O<sub>2</sub>, CCl<sub>4</sub>, and Some Metal Ions. *Chem. Mater.* **1998**, *10*, 444–450.
- (13) Belloni, J.; Mostafavi, M.; Remita, H.; Marignier, J.-L.; Marie-Odile Delcourt. Radiation-

- Induced Synthesis of Mono- and Multi-Metallic Clusters and Nanocolloids. *New J. Chem.* **1998**, 22, 1239–1255.
- (14) Belloni, J. Nucleation, Growth and Properties of Nanoclusters Studied by Radiation Chemistry: Application to Catalysis. *Catal. Today* **2006**, 113, 141–156.
- (15) Cooper, W. J. .; Curry, R. D.; O'Shea, K. *Environmental Applications of Ionizing Radiation*; John Wiley: New York, 1998.
- (16) Elliot, A. J. *Rate Constants and G-Values for the Simulation of the Radiolysis of Light Water over the Range 0-300 °C*; AECL--11073, COG--94-167: Chalk river, Ontario, Canada, 1994.
- (17) Miller, A. I.; van Alstyne, H. M. Heavy Water: A Distinctive and Essential Component of CANDU. *At. Energy Canada Limited, AECL* **1994**, No. 10962, 1–11.
- (18) Elliot, A.; Ouellette, D. C.; Stuart, C. R. The Temperature Dependence of the Rate Constants and Yields for the Simulation of the Radiolysis of Heavy Water. **1996**, No. December.
- (19) Schmid, T. E.; Dollinger, G.; Hable, V.; Greubel, C.; Zlobinskaya, O.; Michalski, D.; Molls, M.; Röper, B. Relative Biological Effectiveness of Pulsed and Continuous 20MeV Protons for Micronucleus Induction in 3D Human Reconstructed Skin Tissue. *Radiother. Oncol.* **2010**, 95, 66–72.
- (20) Maquille, A.; Jiwan, J.-L. H.; Tilquin, B. Radiosterilization of Drugs in Aqueous Solutions May Be Achieved by the Use of Radioprotective Excipients. *Int. J. Pharm.* **2008**, 349, 74–82.
- (21) Guo, Z.; Tang, D.; Liu, X.; Zheng, Z. Gamma Irradiation-Induced Cd<sup>2+</sup> and Pb<sup>2+</sup> Removal from Different Kinds of Water. *Radiat. Phys. Chem.* **2008**, 77, 1021–1026.
- (22) Katayama, T.; Nakauma, M.; Todoriki, S.; Phillips, G. O.; Tada, M. Radiation-Induced Polymerization of Gum Arabic (Acacia Senegal) in Aqueous Solution. *Food Hydrocoll.* **2006**, 20, 983–989.
- (23) Ramsay, W.; Soddy, F. Experiments in Radioactivity, and the Production of Helium from Radium. *Proc. R. Soc. London* **1903**, 72, 204–207.
- (24) Jonah, C. D. A Short History of the Radiation Chemistry of Water. *Radiat. Res.* **1995**, 144,



- 141–147.
- (25) Ferradini, C.; Jay-Gerin, J.-P. La Radiolyse de l'eau et Des Solutions Aqueuses : Historique et Actualité. *Can. J. Chem.* **1999**, 77, 1542–1575.
- (26) Zimbrick, J. D. Radiation Chemistry and the Radiation Research Society: A History from the Beginning. *Radiat. Res.* **2002**, 158, 127–140.
- (27) Spothem-maurizot, M.; Mostafavi, M.; DOUKI, T.; Belloni, J. *Radiation Chemistry- From Basics to Applications in Material and Life Sciences*; Spothem-maurizot, M., Mostafavi, M., DOUKI, T., Belloni, J., Eds.; EDP SCIENCES: Les Ulis Cedex A, France, 2008.
- (28) Bethe, H. Zur Theorie Des Durchgangs Schneller Korpuskularstrahlen Durch Materie. *Ann. Phys.* **2006**, 397, 325–400.
- (29) Watt, D. *Quantities For Generalized Dosimetry Of Ionizing Radiations in Liquid Water*; CRC Press: London, 1996.
- (30) Pimblott, S. M.; LaVerne, J. A. Production of Low-Energy Electrons by Ionizing Radiation. *Radiat. Phys. Chem.* **2007**, 76, 1244–1247.
- (31) McCracken, D. R.; Tsang, K. T.; Laughton, P. J. *Aspects of the Physics and Chemistry of Water Radiolysis by Fast Neutrons and Fast Electrons in Nuclear Reactions*; Canada, 1999.
- (32) Lin, C. C. *Radiochemistry in Nuclear Power Reactors*; The National Academies Press: Washington, DC, 1996.
- (33) Katsumura, Y. Applications of Radiation Chemistry to Nuclear Technology, Y. Katsumura Charged Particle and Photon Interactions with Matter. In *Charged Particle and Photon Interactions with Matter: Chemical, Physicochemical, and Biological Consequences with Applications*; Mozumder, A., Hatano, Y., Eds.; CRC Press: New York, 2003.

## Chapter II: Experimental Methodology

## **Table of Content**

### 2.1 State of art

#### 2.1.1 High LET

#### 2.1.2 Low LET

#### 2.1.3 Detection technique for ultrafast radiolysis

### 2.2 ELYSE — A picosecond pump-probe radiolysis platform

#### 2.2.1 EA-1 — Picosecond pulse-probe setup

#### 2.2.2 EA-3 — Streak camera

#### 2.2.3 $\gamma$ -source

### 2.3 SK-Ana — MCR-ALS analysis method

### 2.4 Chemicals

### References

## **Chapter II: Experimental methodology**

### **2.1 State of art**

Radiation chemistry has been strongly influenced by the techniques to make measurements. The radiation chemists have developed and utilized powerful facilities to study both time resolved and steady-state chemical phenomena resulting from the interaction of ionizing radiation with matters. Nowadays the instruments in the field of radiation chemistry are able to explore the chemical process in various time scale, temperature, pressure and phase stage. It is notable that the special pattern of the reactive species produces by the radiolytic energy deposited within the sample depends on the type of incident radiation and its energy. When the energy deposited in the sample is by phonic radiation (X – and gamma ray), it is well separated interactions within the sample. In the case of highly charged nucleons, it would produce much denser deposition patterns with higher probability of overlapping region of ionized species. The effect is quantified as liner energy transfer (shorted as LET). Photons and electrons are considered to be low LET radiation whereas protons and heavy nucleons (heavy ions, alpha particles and neutrons) are high LET. The technical methods in radiation chemistry can be quickly summarized as:

#### **2.1.1 High LET**

##### **i. Heavy ion**

Heavy ion beams occupy an important role in radiolysis experiments as a result that heavy ions have higher LET values, which deposits energy to material at a high density per thickness. Generally, heavy ion radiolysis experiments are performed at large, multipurpose accelerator facilities with cyclotrons or tandem Van de Graaff accelerators. The yield of radiolytic products as a function of LET and the effects on the concentration of scavengers on these yield have provided critical favor for the understanding of the radiolytic process. For an example, when applied to modification of polymers, ion beam caused less deterioration compared with electron beam.<sup>1</sup> By far, ion beams have been used to fragment polymers to form membranes, and conversely, to polymerize precursor substrates to form forests of polymer rods on surfaces.<sup>2</sup> Additionally, the localized damage due to heavy ion radiation plays unreplaceable role in radiation biology and radiation medicine. Proton therapy is a precise way to deliver large radiation doses to kill tumors.

Besides, hydroperoxyl radical  $\text{HO}_2^\bullet$ , only produced by the heavy ion radiolysis in water not by low LET radiolysis in the absence of molecular oxygen. It is a significant method to give rise to oxidative damage to hypoxic tumors.

ii. Alpha particles and neutrons

Alpha particles are the largest particles emitted from the nucleus of an atom. Alpha particles will quickly interact with an atom and lose their energy soon after they are emitting because of their relatively low velocity and large charge. Alpha particles travel only a few centimeters in the air. A piece of paper, normal work clothes, or the dead layer of skin on a human body can stop an alpha particle. Because of their high energy, alpha particles can deposit a significant internal dose if inhaled or ingested. The early radiation chemistry studies were predominately performed with  $\alpha$ -particles because they were available and the chemical effects were large enough that they could be observed using the techniques of the time. Nowadays, there are many ways in which science successfully uses alpha radiation in a beneficial way. In cancer treatment, alpha radiation is used to treat various forms of cancer what is called unsealed source radiotherapy. This process involves inserting tiny amounts of radium-226 into cancerous masses. The alpha particles destroy cancer cells but lack the penetrating ability to damage the surrounding healthy cells. Moreover, alpha radiation is also applied as static eliminator, spacecraft power and so on.<sup>3</sup>

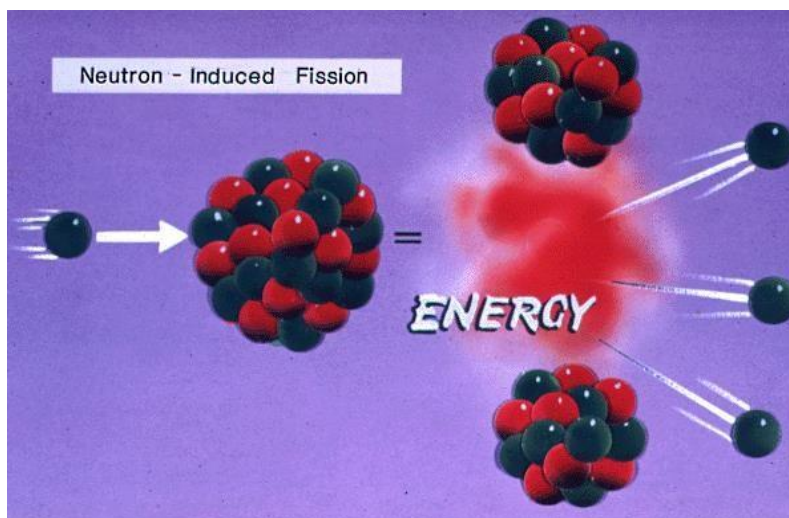


**Figure 2.1** Neutron induced fission.

In the past, neutron radiation normally was found only in the immediate vicinity of a nuclear reactor or nuclear weapons burst. Today there are more and more industrial use of neutron-emitting

radionuclides. Neutron-emitting radionuclides are being applied in some specialized radiographic procedures, in well logging and soil moisture analysis. If accelerator energy is above 8 MeV, neutrons may be an important component of the radiation generated.

Neutron radiation is extremely difficult to detect. Because neutron radiation is extremely penetrating, protecting workers is equally difficult. Effective shielding for neutron radiation usually involves a material that has a high hydrogen atom concentration. Such shielding might employ several feet of soil, paraffin (materials saturated with hydrogen atoms), or concrete.

### 2.1.2 Low LET

#### i. Gamma and X- rays

Gamma radiation is by far the most penetrating of the three common types of radiation (alpha, beta, gamma). Gamma rays have no mass or charge and are considered to be pure energy. They can travel great distances and have the ability to pass through the human body and interact with living cells. Lead, concrete, and other dense materials are used to attenuate (not to stop) gamma rays. Radioactive gamma sources based on  $^{60}\text{Co}$  or  $^{137}\text{Cs}$  isotopes are two basic types of source-based irradiators for chemical research. They are commonly used in continuous radiation mode for radiolysis product studies and competition kinetics measurements.

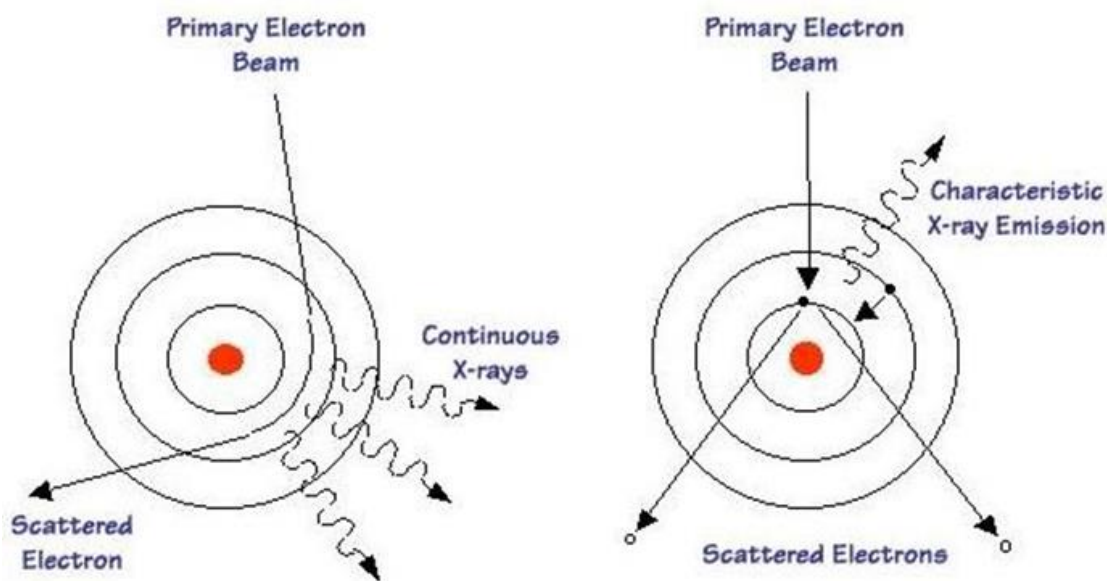


**Figure 2.2** The mechanic diagram of generation of X-rays.

X-rays differ from gamma radiation only in their origin and the fact that they tend to be less energetic. Whereas gamma radiation originates in the nucleus of an atom, x-rays are generated by the shell transition of orbital electrons (**Figure 2.2**). They are also formed from the deceleration of electrons interacting with matter (known as bremsstrahlung). Nowadays particles accelerators can be used as continuous or pulse X-ray source by stopping the particle beam (typically electrons) in a high atomic number material (gold or tungsten).

ii. Charged particles by accelerators

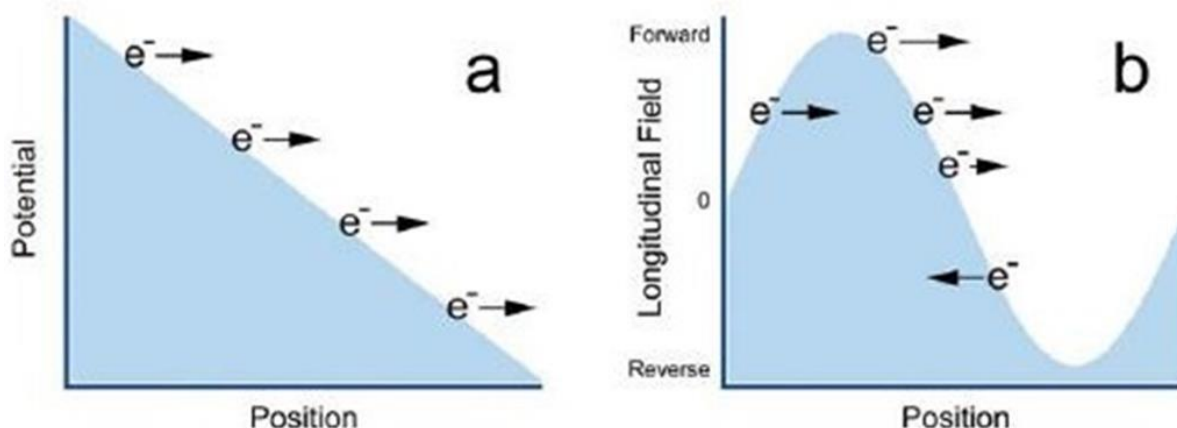


**Figure 2.3** Schematic depictions of electrostatic (a) and oscillating electromagnetic (b) field for charged particle acceleration.<sup>4</sup>

In radiation chemistry there are many methods of accelerating particles beam for pulse radiolysis. Generally, acceleration could be sorted by the type of the force applied by electric field. The field may be direct current as produced by electrostatic potential or oscillating in time and space as produced by radio frequency, microwave or optical laser radiation (**Figure 2.3**)

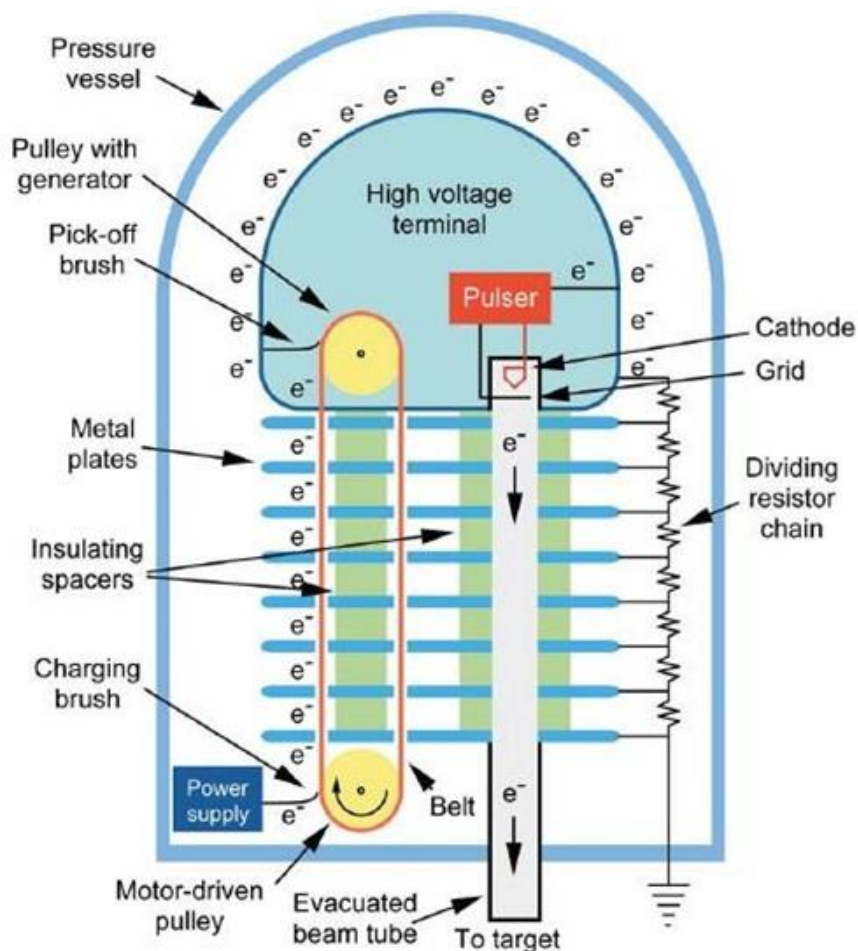


**Figure 2.4** Schematic of a Van de Graaff Accelerator. Made by *J. Wishart*.<sup>4</sup>

The examples of accelerator based on electrostatic potential are Van de Graaff generator and capacitor-driven direct current impulse generator. A schematic is shown in **Figure 2.4**. The Van de Graaff develops and maintain a continuous electrostatic field by transferring electron on a belt. The belt is made of non-conducting material and passes electron between two terminals at ground and high potential. The typical operating potential of Van de Graaff accelerator is 2–5 MV. It becomes more progressively difficult to stand electrostatic potentials higher than 5 MV to sustain without extraordinary measures. Furthermore, the beam energies of 2–5 MeV are adequate for many pulse radiolysis applications.



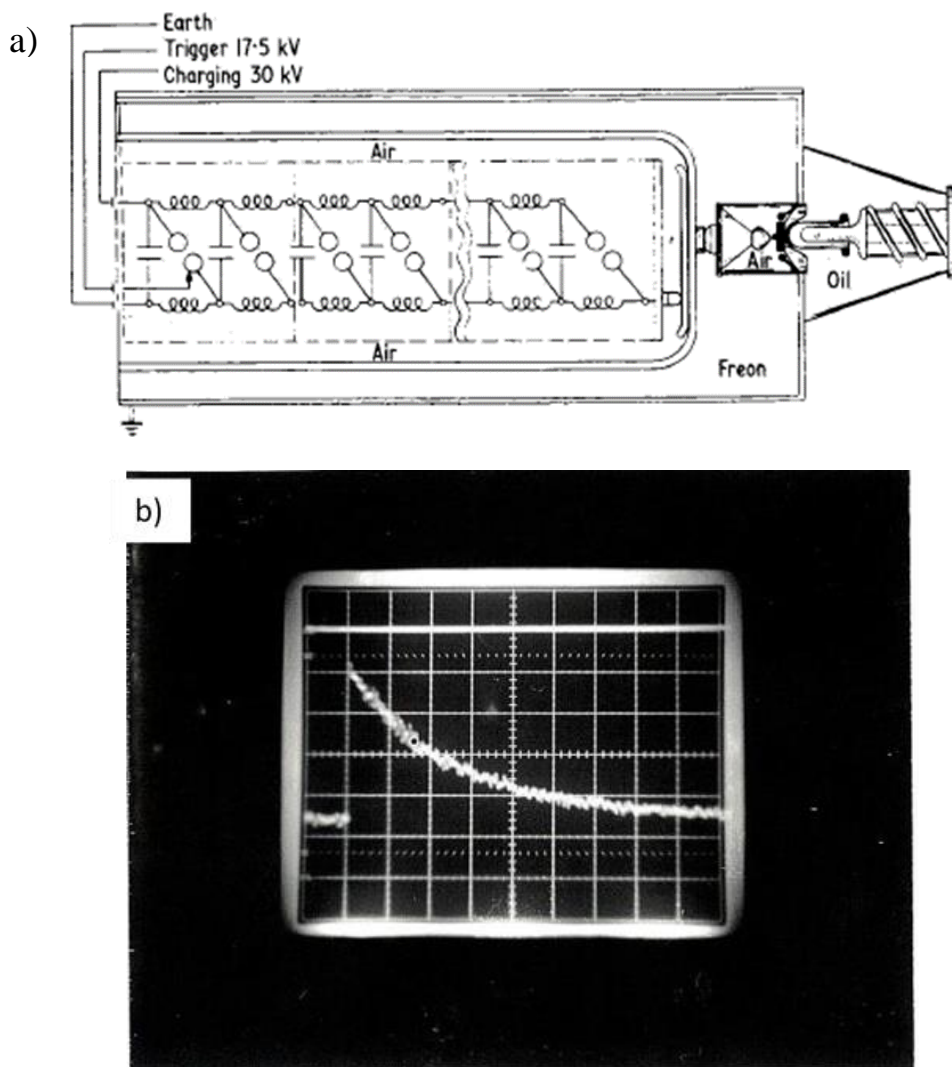


**Figure 2.5** a) Schematic diagram of high voltage generation in Febetron Model 706.<sup>5</sup> b) Transient absorbance recorded at 500 nm with resolution of 50 ns by Febetron 706. Performed by J-L. Marignier in 1985.

The second series of electrostatic accelerators are based on direct-current impulse generators. The best-known examples of these are Febetron produced by the Field Emission technology (**Figure 2.5** a)<sup>5</sup> These machines are based on a Marx-surge impulse generator, which is used to pulse charge through a series spark gap to switch central electrode of a short coaxial section. Then very large electron currents ( $\sim 7000$  A) are passed in pulses and delivered to the field emission electron tube. It could last several to tens of nanoseconds and deliver radiolytic doses up to 20 kGy. The large doses are well suited for the study of radical-radical reactions and gas phase pulse

radiolysis. The electrical noise generated by the spark gaps and the discharge of the Febetron is a major problem for detection systems, requiring much signal averaging and background correction.

Accelerators that use electromagnetic radiation to produce the accelerating field could generate particles with much higher energies than that produced by electrostatic accelerators. Higher beam energies provide more penetrating power for elaborate experimental setups such as pressure vessels and cryostats, and the ability to better focus more charge into a smaller target to produce a higher radiolytic dose. However, the beam energies above 40 MeV for electrons are less desirable for pulse radiolysis as a practical consideration. The reason is that when the beam energy increase, the fraction of the beam energy that converted into bremsstrahlung instead of being deposited in the sample in radiolytic events will increase along with increasing the beam energy.

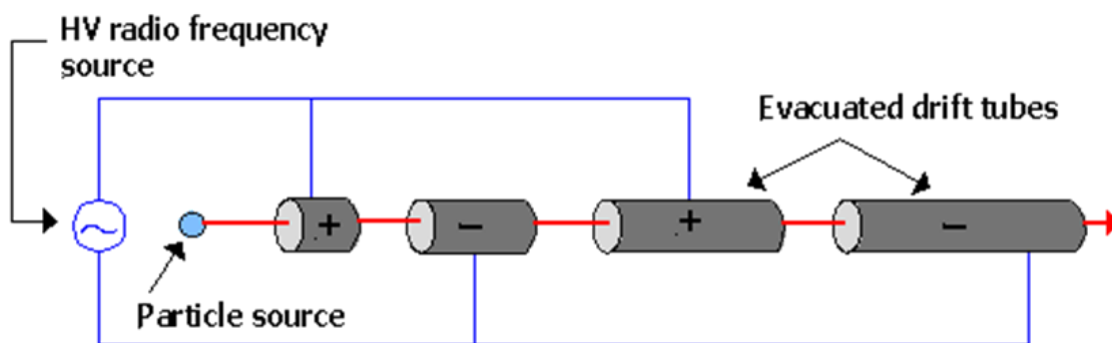


**Figure 2.6** Diagram of LINAC.

The most common type of oscillating-field accelerator for pulse radiolysis is Linear accelerator (LINAC). **Figure 2.6** shows a diagram of LINAC. There is a series of resonant cavities for radio-frequency in the accelerating sections. The frequency could range from 100 MHz to 10 GHz, and 1-3 GHz is the most common one. Keeping in phase with the radio frequency supply, the charged particles are accelerated in the gaps between the electrodes. In other words, initially, the tube in front of the particles has an opposite charge to that of the particles, and hence attracts the particles. Once in the tube, the polarity of the tube changes. The particles are repelled from the tube and attracted to the next tube, and so on. Since the frequency of the electric field is constant and the particles' speed increases, the tubes get progressively longer to ensure that the particles spend the same amount of time in each tube and therefore keep in phase with the electric field. In older type of LINAC the cylindrical electrodes were called drift tubes which are aligned coaxially with the chamber. No drift tubes are used in the modern high-energy. The radio frequency is boosted at

regular intervals along the chamber by means of klystrons (electron tubes used for the amplification or generation of high frequency waves). Only a small magnetic field, supplied by magnetic lenses between the radio frequency cavities is required to focus the particles and keep them in a straight line. Typical rates of energy gain in a LINAC are 7 MeV per metre for electrons.

### 2.1.3 Detection technique for ultrafast radiolysis

To start the chemical processes under investigation, irradiation produces chemically highly reactive species at intervals generally much shorter than the observation period. The detection apparatus consists of appropriate devices depending on the physical properties being studied. For the long alive species produced by  $\gamma$ -source, an analyzing light source and a photodetector for optical detection is applicable. A voltage generator and an electrical detection circuit for conductometric studies is essential meanwhile a device for recording the kinetic voltage vs. time curves is also necessary. A computer may be used to store the transient curves for later analysis or may even be used to control the entire experiment for picosecond pulse radiolysis.

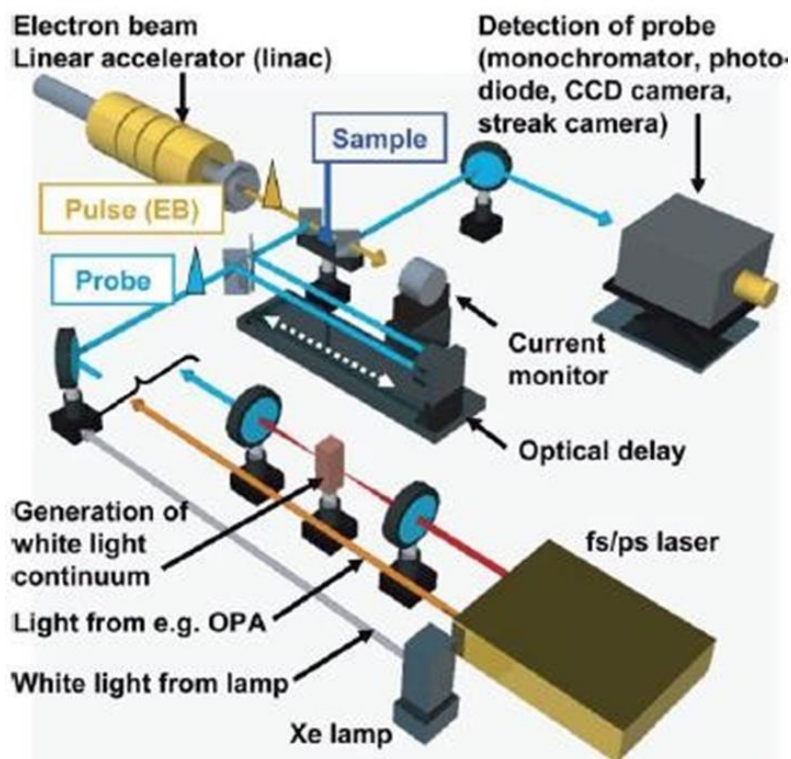


**Figure 2.7** Schematic of a general detection system for picosecond pulse radiolysis. By A. Saeki.<sup>4</sup>

With the development of technology, more and more elaborated detection methods have been applied to investigating the radiation process. In pulse-probe transient absorption spectroscopy, a short pulse of light is used to measure the absorbance of a sample as a function of time delay between the electron pulse and the probe beam. Time resolution using this method is typically on the order of the electron pulse width. Originally, Cerenkov light generated from the electron beam itself was used as a variable-delay probe beam.<sup>6,7</sup> Later, a free-running Ti-Sapphire oscillator was used with a time-amplitude converter to measure spur decay of the solvated electron. With the advent of laser photocathode electron gun systems that provide picosecond-synchronized laser pulses, high-resolution pulse-probe kinetics measurements have nearly become routine. Timing improvements<sup>8</sup> and streak-camera jitter detection have made such measurements possible on thermionic, pre-bunched picosecond linacs as well. For transient spectroscopy, two methods of probe pulse generation are used to measure kinetics at wavelengths other than the fundamental of the gun-driving laser system ( $\sim 800$  nm). At some facilities, a white light continuum is generated by focusing intense laser pulses into a substrate such as a sapphire plate, fused silica or  $D_2O$ ,<sup>9-11</sup> while at others a specified probe wavelength is produced by an optical parametric amplifier pumped by the gun-driving laser system.<sup>8,12</sup> Broadband detection of the white-light probe is accomplished with a spectrograph/CCD or diode array combination,<sup>10</sup> while single-wavelength detection is done with a pair of diodes.<sup>10-13</sup> Broadband detection works within the sensitivity range of silicon detectors (up to 950 nm), while NIR-sensitive photodiodes (Ge and InGaAs) extend the range of single-wavelength detection up to 1700 nm. Pulse-probe transient spectroscopy has been used to follow the formation of  $Xe_2^*$  excimers in the radiolysis of supercritical xenon,<sup>14</sup> measure dissociation rates of aryl halide radical anions, to re-evaluate the yield of hydrated electron at picosecond times,<sup>15</sup> and to observe the solvation of excess electrons in ionic liquids.



**Figure 2.8** A picture of an overview in ELYSE

In my thesis, most studies were performed in picosecond pump-probe radiolysis platform — ELYSE (**Figure 2.8**). Part of experiments were performed by  $\gamma$ -source. Moreover, global data analysis was involved in data treatments.

## 2.2 ELYSE — A picosecond pump-probe radiolysis platform

ELYSE is named after Lysis (Greek for degradation) by Electrons. This Fast Kinetics Centre at Orsay is based around a femtosecond laser facility used for triggering the photo-cathode and a picosecond electron accelerator used for pulse radiolysis experiments. The combination of laser and electron beams will allow the physical chemistry community to perform pump — probe experiments with high time resolution. The electron pulse is extracted from a  $\text{Cs}_2\text{Te}$  photocathode by a femtosecond laser pulse. The synchronization of laser and electron beams allows the physical chemistry community to perform pump-probe experiments with high time- resolution. Irradiation of chemical samples will be possible with both electron beams (pulse radiolysis) or laser beams (also used independently for ultra-fast photochemistry).



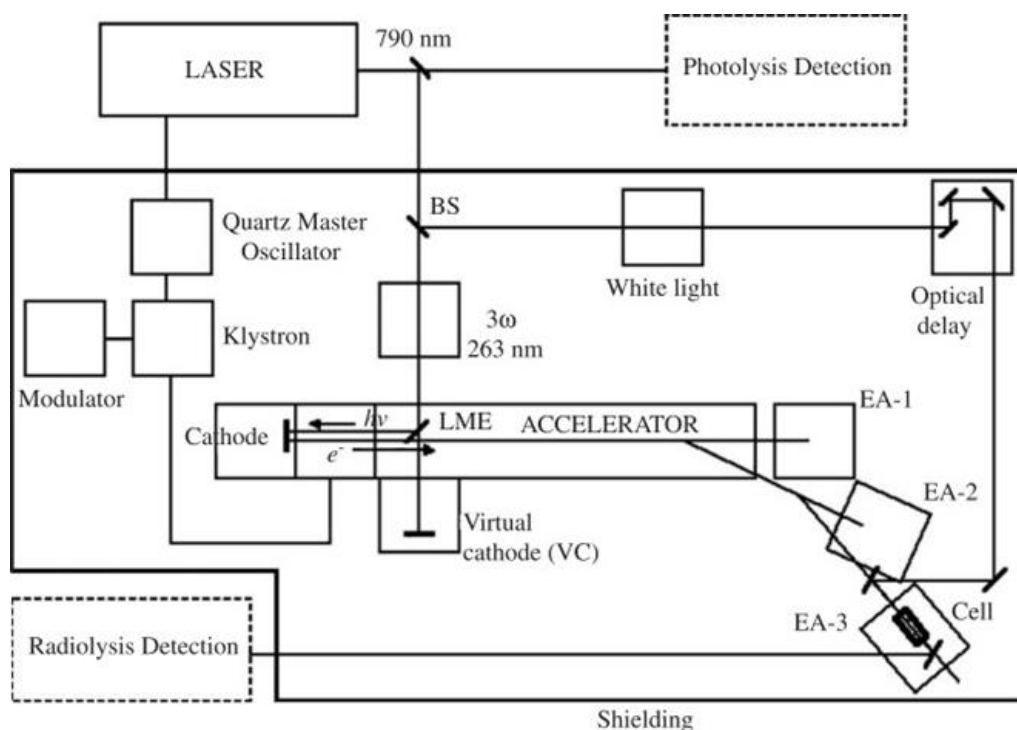


**Figure 2.9** Principle of the laser-driven RF electron accelerator. BS – laser beam splitter. LME – laser entrance mirror. VC – virtual cathode. EA-1, EA-2, EA-3 – experimental areas.<sup>13</sup>

The photocathode is triggered by a 263 nm laser pulse obtained from a 780 nm, frequency-tripled, amplified Ti-sapphire laser (120 fs, 2 mJ, 10-50 Hz). Using an 80 MHz quartz oscillator controlling both the pump laser beam and the klystron RF of the laser-triggered electron beam provides a precise synchronization of both laser and electron beams. Therefore, a small fraction of the 780 nm laser beam (10%) can be deviated by a beam splitter (BS) to be used as a synchronized probe pulse, of this wavelength or after generating a pulsed white light continuum through a sapphire plate, to detect the kinetics of the transients. The ELYSE facility is shown schematically in **Figure 2.9** along with the areas used for ultrafast pulse radiolysis, the whole being surrounded by radiation shielding. Three experimental areas are available for irradiation<sup>16</sup> EA-1 at the exit of the direct electron beam, EA-2 and EA-3 at the exit of the deviated lines.

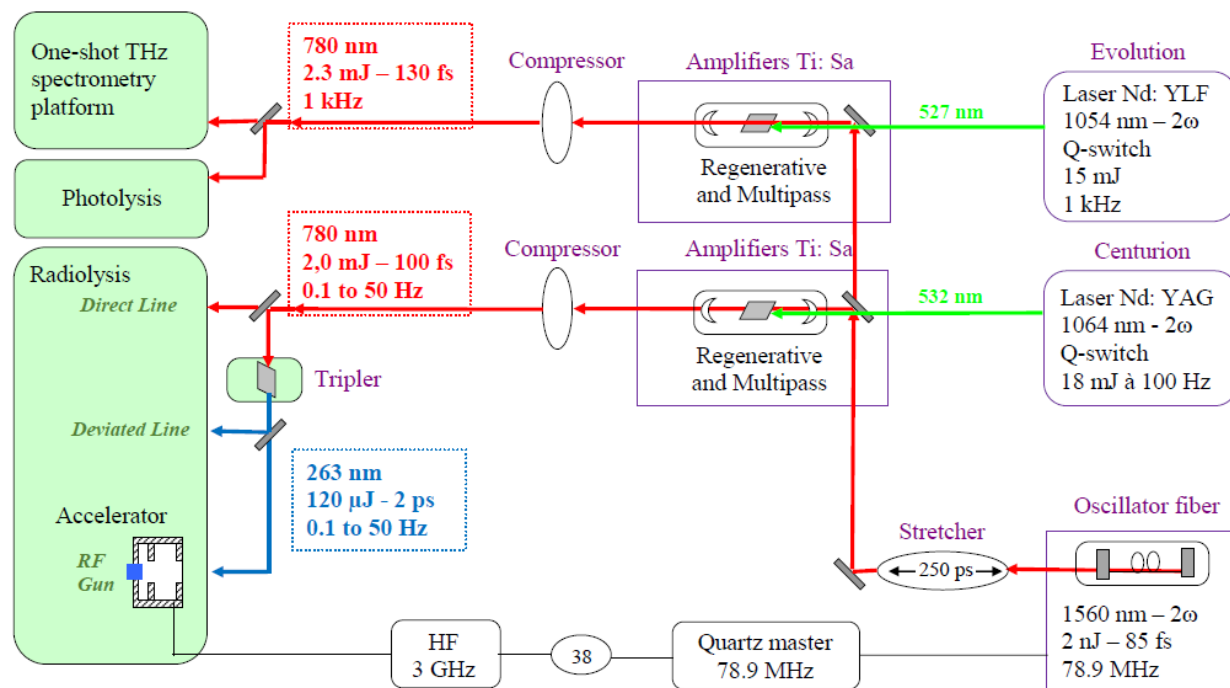


**Figure 2.10** A schematic of femtosecond laser chain in ELYSE.

The disposition of the existing building which was renovated to house ELYSE, was such that the ideal place to install the laser was on the ground floor, vertically above the shielded target room in the basement where the electron gun was installed. The femtosecond laser chain is based on a commercial system (**Figure 2.10**). The cavity length of a Ti: Sapphire oscillator is adjusted to be synchronized with the 78.9 MHz frequency of the quartz master-oscillator which also controls the accelerator timing. Ultra-short pulses of 85 fs are delivered at 780 nm. The energy of the pulses at this stage is only about 2 nJ. They are therefore amplified by a regenerative amplifier using the chirped pulse amplification (CPA) technique (**Figure 2.11**). At the output, the (780 nm, 100 fs) pulses have an energy of 2 mJ. The laser source is unique in as far as, just before the laser pulse compression, a fraction of 0.1–50 pulses from the 1000 per second (1 kHz) are separated by a Pockels cell and Glan–Taylor polarizer system defining the repetition rate. Both pulses, which are produced in parallel at 780 nm, (and 2 mJ) are compressed differently. Those used to excite the accelerator photo-cathode (0.1–50 Hz) were of 2 ps and more recently of 100 fs, whereas the others used independently for femtochemistry studies are ultra-short, 100 fs at 780 nm.

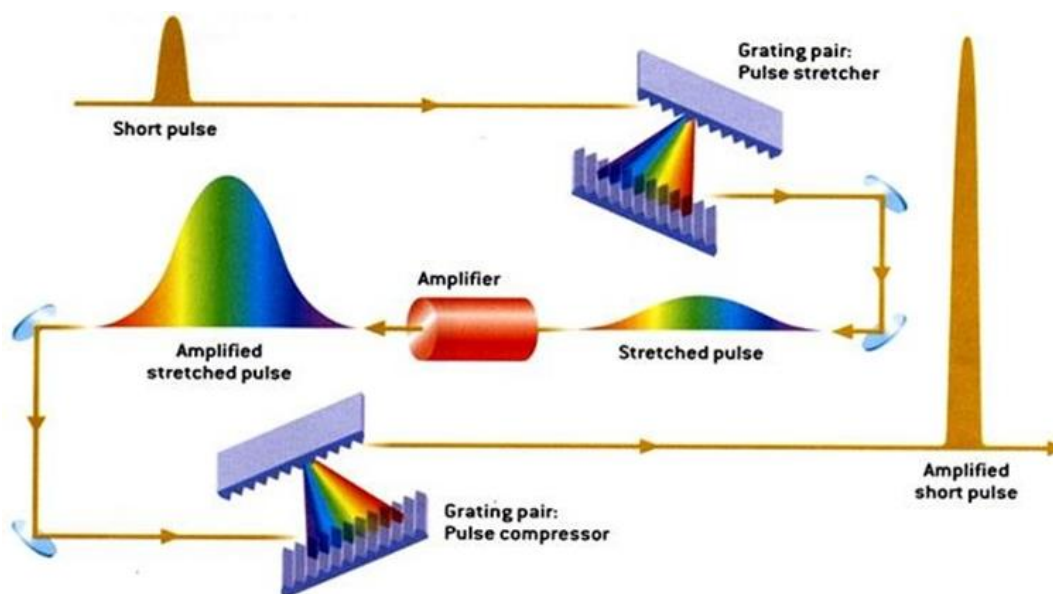


**Figure 2.11** The principle of chirped pulse amplification for femtosecond laser.

The laser beam at 1–50 Hz is transferred through a hole in the concrete/lead shielding between the laser and the accelerator rooms down to the photocathode after being frequency tripled to 263 nm. The energy per pulse at 263 nm is up to 120  $\mu\text{J}$ . In order to obtain normal incidence of the laser beam onto the photocathode, and thus to produce photoelectrons with a time structure as close as possible to that of the laser, the beam, which is injected into the vacuum gun chamber through a transparent window, is reflected for almost normal incidence onto the cathode by a laser entrance mirror (LME) (**Figure 2.9**). The mirror is in fact slightly shifted relative to the electron beam axis so as to prevent irradiation. The laser pulse energy delivered to the photocathode is measured, by using a switchable laser exit mirror to deflect it onto a virtual cathode (VC) located on a side line perpendicular to the main gun axis and equipped in situ with a Joulemeter.

The intensity and position of the electron beam is observed upstream of each experimental area by a wall current monitor and a moveable Faraday cup. Ceramic screens are used to indicate the transverse beam profile. The bunch length is measured from the pulse length of Cerenkov light which is emitted by sapphire screens and transferred through a series of mirrors to the detection room.



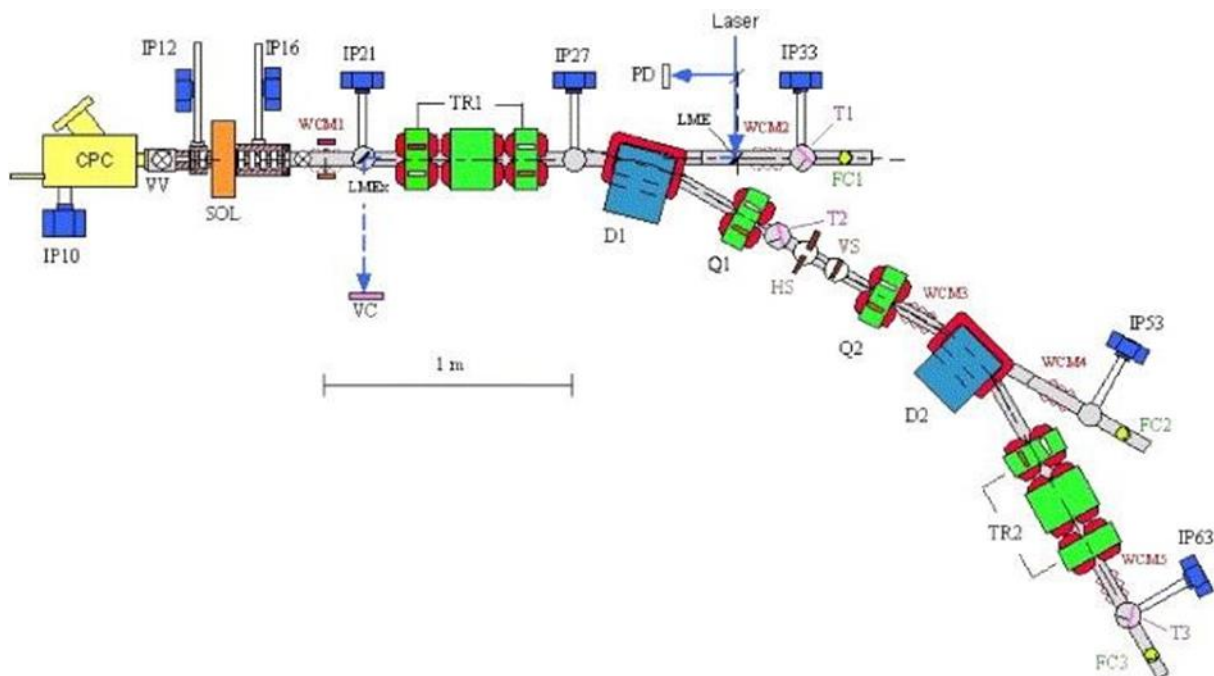


**Figure 2.12** A general schematic of the ELYSE accelerator. IP: ion vacuum pump; CPC: cathode preparation chamber; VV: vacuum valve; SOL: solenoid; D: dipole; TR1 and 2: triplets; Q: quadrupole; WCM: wall current monitor; FC: Faraday cup; PIQ: Ion pump; T: translator for Cherenkov light emitter and visualization screen; LME: laser entrance mirror; LMEx: laser exit mirror; VC: virtual cathode; HS: horizontal slit; VS: vertical slit. Vacuum.

The need to extract high charges with  $\mu\text{J}$  laser pulses requires the use of  $\text{Cs}_2\text{Te}$  photocathodes, which are presently considered to be the best choice for high quantum efficiency<sup>17,18</sup> and acceptable lifetime. Since the  $\text{Cs}_2\text{Te}$  coating is sensitive to oxidation by air,<sup>19,20</sup> it should be prepared in situ under extremely low-pressure conditions. A vacuum chamber based on the chamber used at CERN/CTF<sup>17</sup> and dedicated to  $\text{Cs}_2\text{Te}$  preparation was built for this purpose,<sup>16</sup> representing the first such installation in a pulse radiolysis facility. The photocathode preparation chamber is connected to the accelerator cavity by a vacuum valve that allows the chamber to be isolated from the gun.

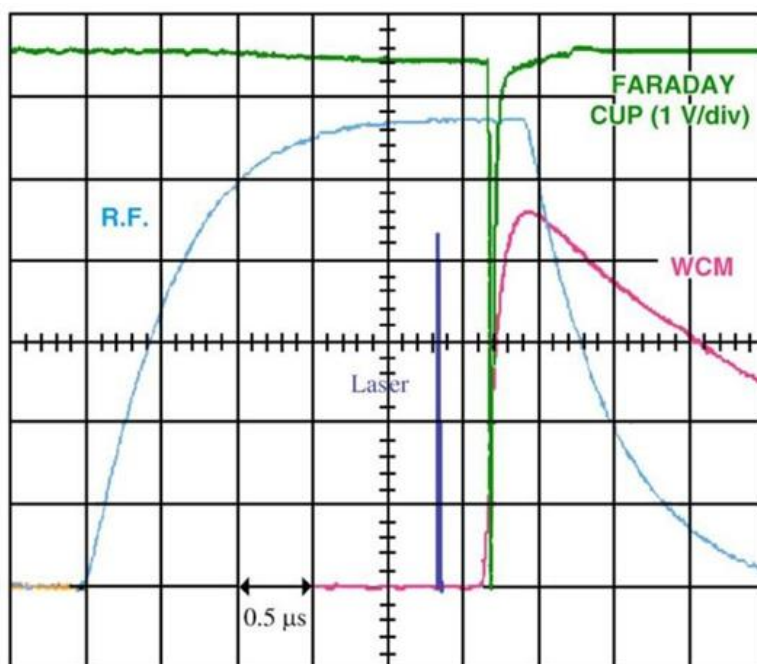


**Figure 2.13** Oscillograms showing (left to right): the RF filling of the gun, the laser pulse as measured by the fast photodiode and the electron pulse as measured by a wall current monitor (WCM) and a Faraday cup.

The diameter of the laser spot on the cathode is about 5mm. The charge extracted from the  $\text{Cs}_2\text{Te}$  photo-cathode is 1–5nC (**Figure 2.13**). Therefore, the charge due to the dark current becomes a negligible part of the total charge.<sup>16</sup> When the cathode is freshly prepared, the current is somewhat larger. The photocurrent decreases slowly as a function of photo-cathode ageing. The current emitted by the photo-cathode over 2 yr of running is remarkably stable. In the absence of any vacuum leak in the chamber (**Figure 2.14**), the  $\text{Cs}_2\text{Te}$  deposit is particularly robust and does not need to be prepared very frequent.

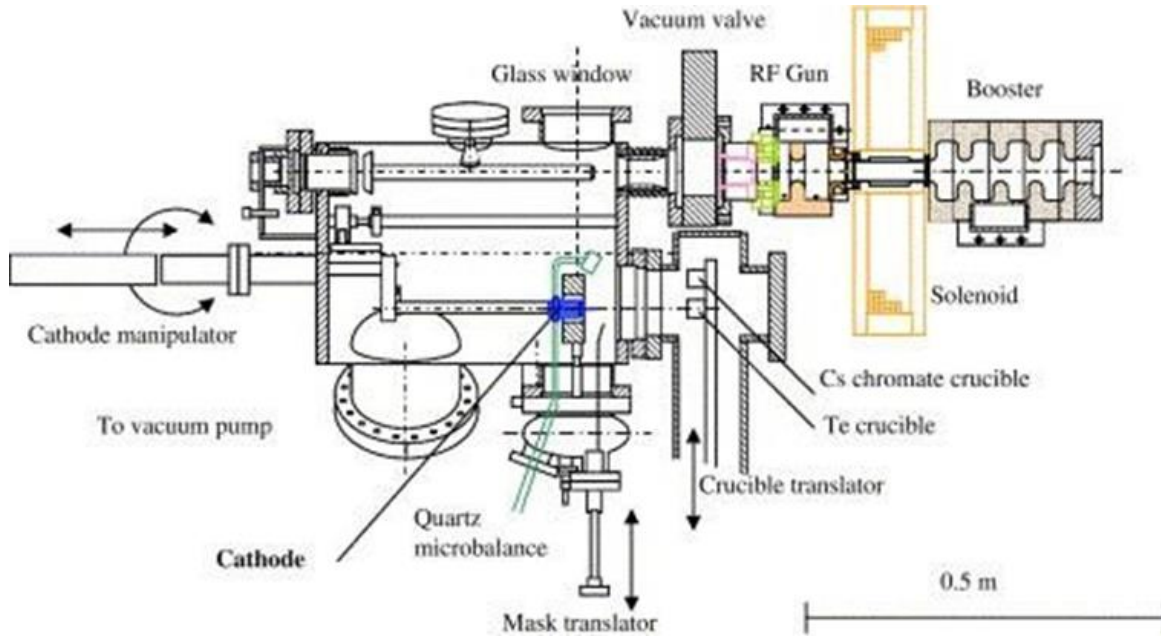


**Figure 2.14** Horizontal section through the vacuum chamber for the  $\text{Cs}_2\text{Te}$  photo-cathode preparation.<sup>16</sup>

At a fixed laser pulse energy (about 15 mJ), the charge extracted from the photocathode increases with the size of the laser beam spot on the cathode due to lower charge recombination. Charges as high as 7.5 nC have been measured at the beam exit EA-1 for a spot diameter of 15 mm. However, the pulse width also increases up to about 15 ps. The charge depends linearly on the laser pulse energy up to 4 mJ, with a slope of  $\eta = 0.25\%$  electron per 263 nm photon absorbed. Between 4 and 18  $\mu\text{J}$ , the current still increases but the quantum efficiency decreases.<sup>16</sup> After turning on microwave power to the machine, about 2 h are required for reaching a stable electron beam and reproducible pulses in width and intensity (or less than 45 min after short stops for manipulations in the machine room).

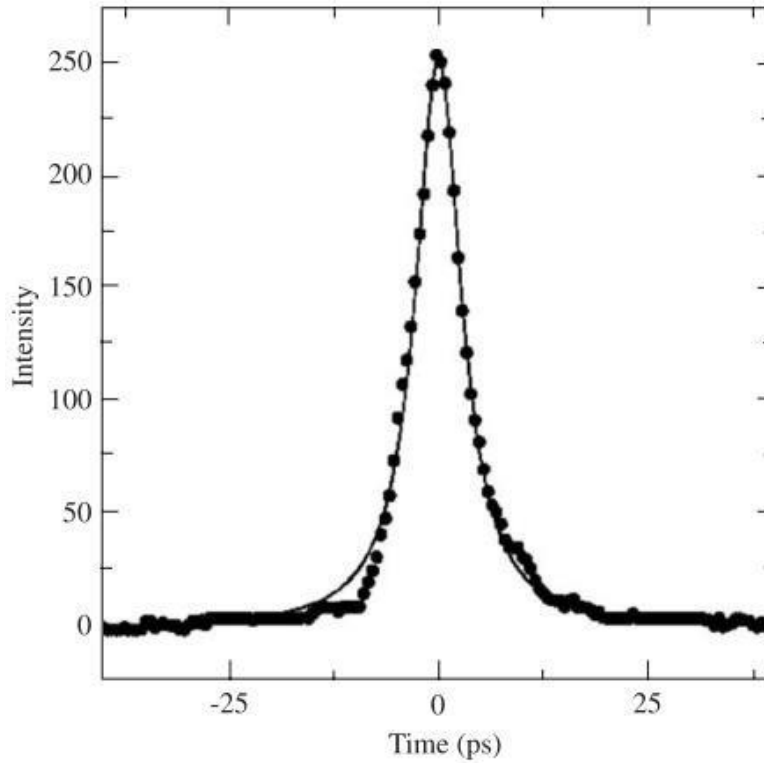


**Figure 2.15** Time-resolved photocurrent signals with the Cs<sub>2</sub>Te photocathode. Pulse duration of the Cerenkov light measured by the streak camera at 500nm. Deviated beam location EA-3, 9 MeV.

The duration of the pulse is measured using the Cerenkov light pulse emitted by sapphire screens moved across the electron beam. The screen can be located inside the vacuum tube or outside the electron beam exit window. The light beam is transferred by the mirrors of an optical line and through a hole in the concrete/lead wall to the entrance window of the fast streak camera Hamamatsu located in the detection room. **Figure 2.15** shows a streak camera profile at 500 nm obtained from Cerenkov radiation of the electron pulses obtained on the deviated line EA-3. As an example, the pulse width (FWHM) for 9MeV electrons is 6.3 ps.

To conclude, the ELYSE accelerator has produced, at a repetition frequency of 25 Hz, a few nC, 6 ps pulses of 9MeV electrons for the direct line EA-1 and pulses of a few nC, 3.6 ps pulses, 9MeV, for the deviated line EA-3, using a Cs<sub>2</sub>Te photo-cathode prepared *in situ* in a vacuum chamber. The response of the cathode is particularly stable when ageing. The ratio of dark current to photocurrent is less than 2% at 5 and 9MeV for the direct line EA-1 and the deviated line EA-3, respectively.

### 2.2.1 EA-1 — Picosecond pulse-probe setup

In the experiments, the electron pulse constitutes the pump of the pulse-probe methods. It generates the transient species in the solution by radiolysis of the sample. As shown in **Figure 2.9**, a 10% part of the 780 nm pulsed laser beam is reflected by a beam splitter, before frequency tripling (THG), to be used for probing the time-resolved absorbance in the cell. **Figure 2.16** presents a scheme of the set-up.

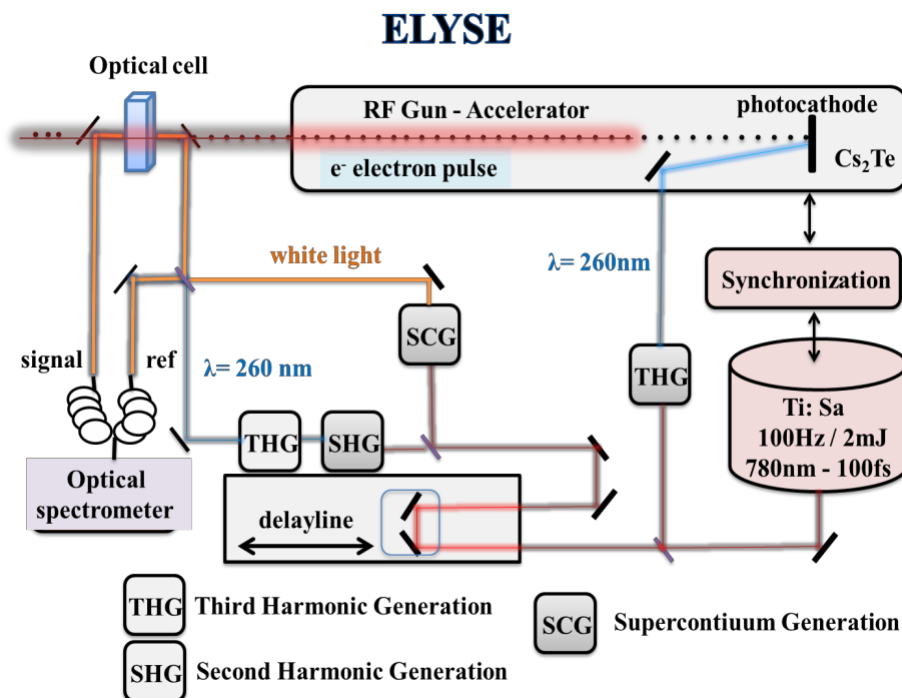


**Figure 2.16** Schematic representation of picosecond pulse-probe pathway in ELYSE.

The delay between the electron pulse and the probe laser pulse, which are synchronized, is adjusted using a variable optical length with a delay line (1 meter for the total length) controlled by a stepper motor (Owis). The maximum delay is 11 ns. The probe laser pulse at 780 nm is then divided by a beam splitter into two parts, 50% being used as the reference signal needed to take into account the shot-to-shot laser fluctuations of the probe light and the other 50% being used as the absorbed signal after passing through the sample almost collinearly with the electron beam. For that purpose, a thin mirror (200  $\mu\text{m}$ ) is interposed in the narrow space between the electron exit window and the cell. A mechanical chopper (Thorlabs MC1000) is located on the 260 nm beam exciting the photocathode in order to alternatively measure the intensity of the probe beam with and without

excitation by the electron pulse,  $I$ , and  $I_0$ , respectively. In order to avoid RF noise, both probe signals are collected and transferred by long Si/Si low OH optical fibers (400  $\mu\text{m}$  core diameter, Ocean Optics) to be recorded by the reference photodiode and the signal detectors (Thorlabs, PDA55, Si 400 – 1100nm), respectively, both located in the shielded detection room.

For the measurement in the near infrared down to the visible a custom made ultrafast broadband spectrometer was used at EA-1 (**Figure 2.9**).<sup>21</sup> An adapted version with a custom-made prism spectrometer and an InGaAs array with extended spectral sensitivity was used to cover the near infrared from 700 – 1500 nm.<sup>22</sup> A particular configuration was applied in order to measure the transient absorbance changes simultaneously in the middle UV around 260 nm and in the near UV to visible. After passing the optical delay line, two probe beams were generated in a rectangular arrangement before they were unified by a 50% beam splitter. In one arm of the rectangle, a supercontinuum was generated by focusing  $\sim 1 \mu\text{J}$  of the laser source into a 6 mm thick  $\text{CaF}_2$  disk. It was used as the optical probe covering a wavelength range from the visible down to the ultraviolet. In the other arm a second probe beam at 260 nm was generated by third harmonic generation. The optical path length of these two probe beams and their beam divergence were kept similar in the rectangle. Both probe beams were coupled to each other in a collinear manner with the 50% beam splitter that was also used to split off collinear reference beams from both probe sources before the fused silica optical flow cell (FSOFC). These dual probe and reference beams were both coupled into an optical fiber, transmitted to a spectrometer, and dispersed onto a CCD. The combination of the broadband probe and the multichannel detector allowed the entire transient spectra to be recorded, independently of the shot-to-shot fluctuations and possible long-term drifts of the electron source. All measurements were made in a custom made FSOFC with a 5 mm optical path collinear to the electron pulse propagation and 200  $\mu\text{m}$  thick optical windows. The electron pulses were of  $\sim 4 \text{ nC}$ , with an electron energy of 6-8 MeV, delivered at repetition frequency of 10 Hz.



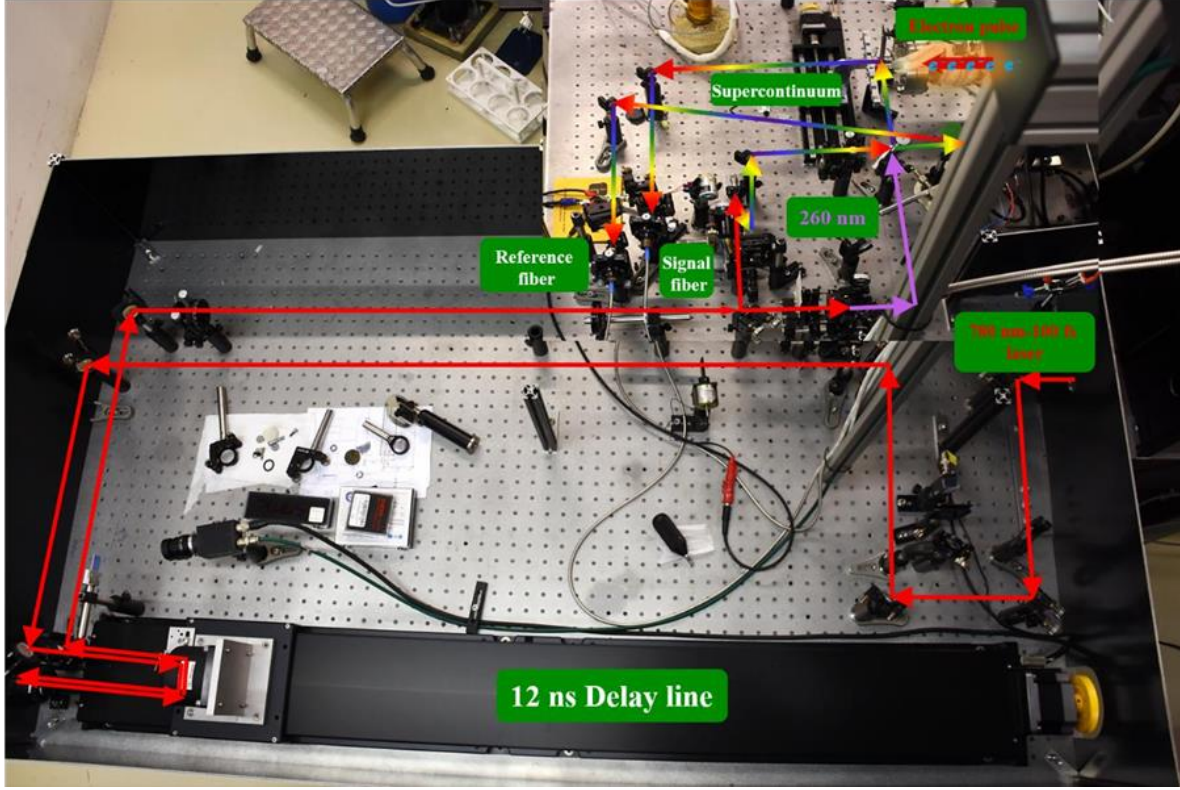


**Figure 2.17** The optical path of pulse-probe detection in the direct line of ELYSE. The red line indicates the fundamental laser light of 780 nm used to generate the probe light and the pump electron beam. The rainbow color line indicates the supercontinuum light from 350 to 780 nm meanwhile the purple line represents the 260 nm probe light.

With time-resolved pulse-probe setup, three types of data acquisitions are recorded point by point during the measurements, the optical density could be determined as follow:

$$A_{obs} = \log_{10} \left[ \frac{\frac{I_{ref}^0 - I_{base}}{I_{sig}^0 - I_{base}}}{\frac{I_{ref} - I_{base}}{I_{sig} - I_{base} - I_{cer}}} \right] \quad \text{EQ. 2-1}$$

- $I_{ref}^0$  and  $I_{sig}^0$  are the reference and signal in the absence of electron beam.
- $I_{ref}$  and  $I_{sig}$  are the reference and signal in the presence of electron beam.
- $I_{base}$  is measured in the condition that both of probe and electron pulse are absent. It is the signal produced probably by the environment background.

The detected Cerenkov light ( $I_{cer}$ ) is subtracted from the acquired data as the change of absorbance recorded before the time zero.

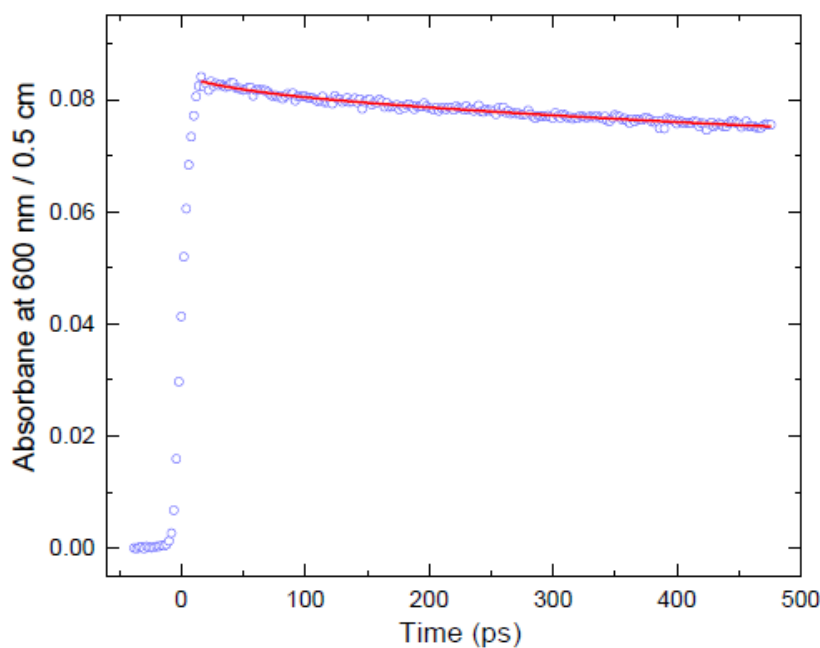


**Figure 2.18** Time dependent absorbance in water at 600 nm.

To determine the dose deposited in the sample, the time dependent absorbance of the solvated electron in static cell is measured for each experiment. For example, in **Figure 2.18** the time-dependent decay of the solvated electron is recorded at 600 nm, according the formula

$$Dose(Gy) = \frac{A_{t=7\text{ ps}}}{\epsilon_{\lambda=600\text{ nm}} \times G_{t=7\text{ ps}} \times l \times \rho} \quad \text{EQ. 2-2}$$

- $A_{t=7\text{ ps}}$  is the absorbance of the solvated electron measured at 7 ps.
- $\epsilon_{\lambda=600\text{ nm}}$  is the extinction coefficient value of the solvated electron at 600 nm, i.e.  $13482\text{ M}^{-1}\text{ cm}^{-1}$ .
- $G_{t=7\text{ ps}}$  is the radiolytic yield of the solvated electron at 7 ps, i.e.  $4.4 \times 10^{-7}\text{ mol J}^{-1}$ .<sup>15</sup>
- $l$  is the length of the optical path in the fused silica optical cell, i.e. 0.5 cm.
- $\rho$  is the density of water, i.e.  $1\text{ g mL}^{-1}$ .

Thus,



$$Dose(Gy) = \frac{0.083}{13482 \times 4.4 \times 10^{-7} \times 0.5 \times 1} = 28 \text{ Gy}$$

### 2.2.2 EA-3 — Streak camera

Another approach for picosecond optical absorption detection is to use a light source with an intensity stable for a time period much longer and an optical detector with a response time much shorter than the absorbance variation to be studied. For this purpose, an original setup was developed at ELYSE based on a high-repetition Xe flash lamp<sup>23</sup> coupled with a high dynamic range streak camera used in absorbance mode, both being synchronized with the electron pulses.

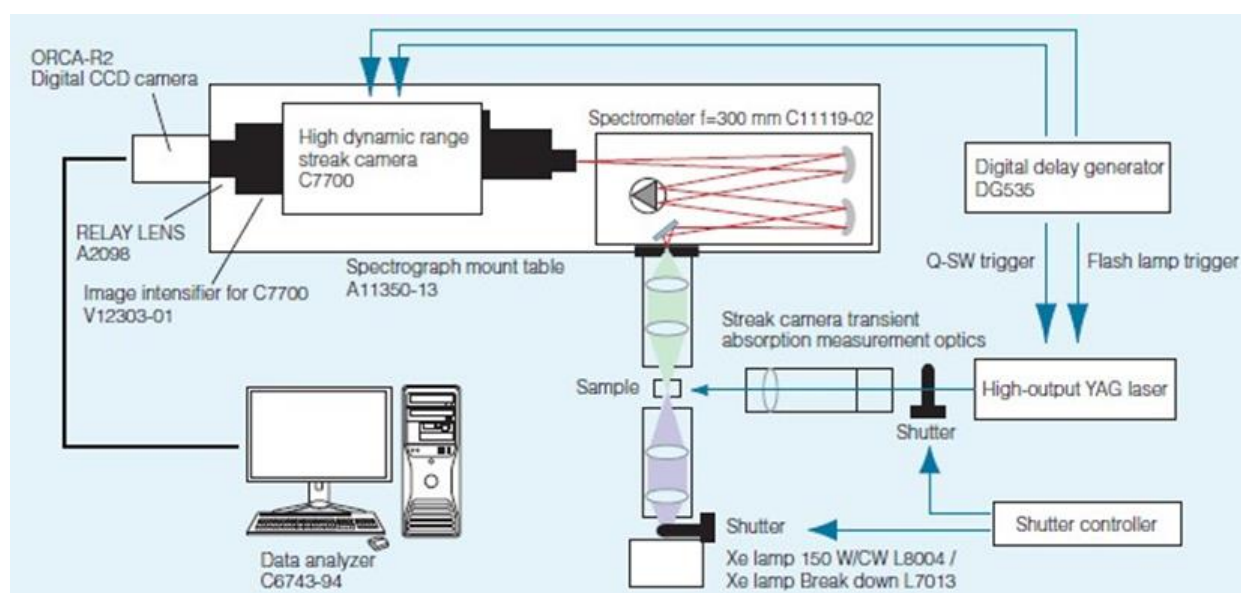


**Figure 2.19** The diagram of the system configuration of a streak camera.

The time-resolved UV-Vis absorbance detection system consists of a Hamamatsu C7700-01(**Figure 2.19**) high dynamic range streak camera connected to a Chromex 250 IS flat field spectrograph.<sup>24</sup> The role of the spectrograph is to spectrally disperse the white-light probe pulse across the entrance slit of the streak camera. Schematically, in order to time-resolve the signals, light is converted via a semiconductor photocathode into a corresponding extended photoelectron beam that is rapidly swept in the streak tube in the direction transverse to the entrance slit (**Figure 2.20**). The photoelectrons are then amplified by a microchannel plate before exciting a phosphor screen which is recorded by a CCD camera in the form of a 2D image digitalized into  $1024 \times 1344$  points along the time and wavelength axes, respectively. This system is suitable for high-intensity

pulsed light with a dynamic range up to 104:1. The absorbance data result from a series of four measurements: the background of the streak camera, the analyzing light only, the analyzing light with the electron beam and the Cerenkov light. Data are collected as the average of at least 20 pulses, but are generally acquired by averaging 400 pulses. Because of the rather long transfer distance from the light source to the streak camera, a time of flight difference between the blue and the red parts of the spectrum can be observed on records at the 500 ps time scale.

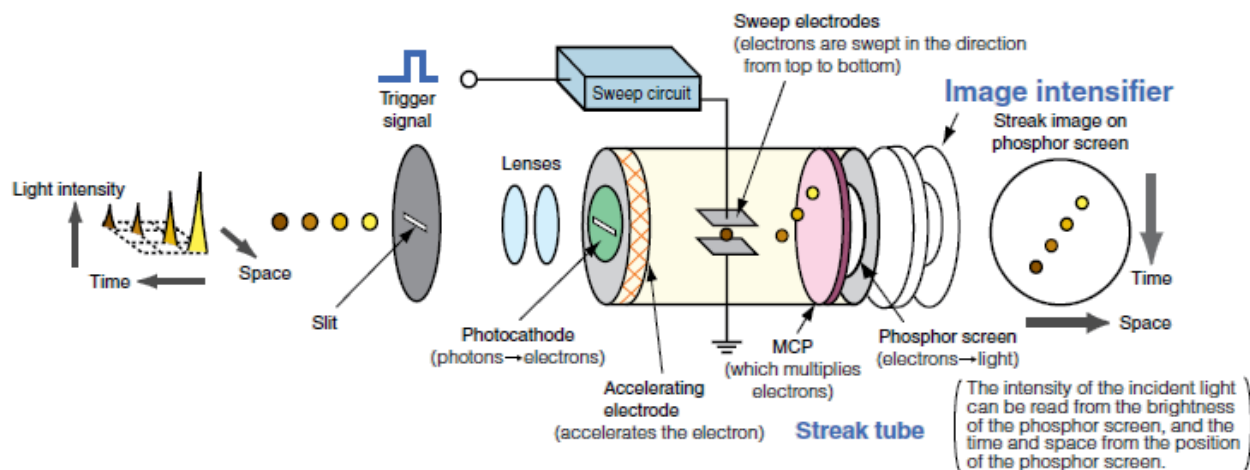


**Figure 2.20** Operating principle of streak tube.

This is easily seen on streak images of the Cerenkov light (measurements for subtraction of the Cerenkov light from the absorbance signal or for the estimation of the duration of the electron pulse). At least for the highest time resolution, the time origin is therefore taken from the ultra-short Cerenkov emission signal at the corresponding wavelength. From a single shot of the accelerator, the transient spectrum at any time (sweep time/full screen 500 ps to 1  $\mu$ s) and the time evolution of the short-lived species at each wavelength (from 250 to 850 nm in 360 nm sections) can be simultaneously obtained. However, when the 360 nm spectral range is recorded at 500 ps full sweep, a fogging effect appears due to the high light intensity required to get an image. This is why the highest resolution is only obtained by recording a restricted wavelength domain ( $\pm 5$  nm) so that the fogging effect is negligible. Work is in progress to evaluate this effect using known reference systems, and thus to obtain the highest time resolution over the entire spectral range.

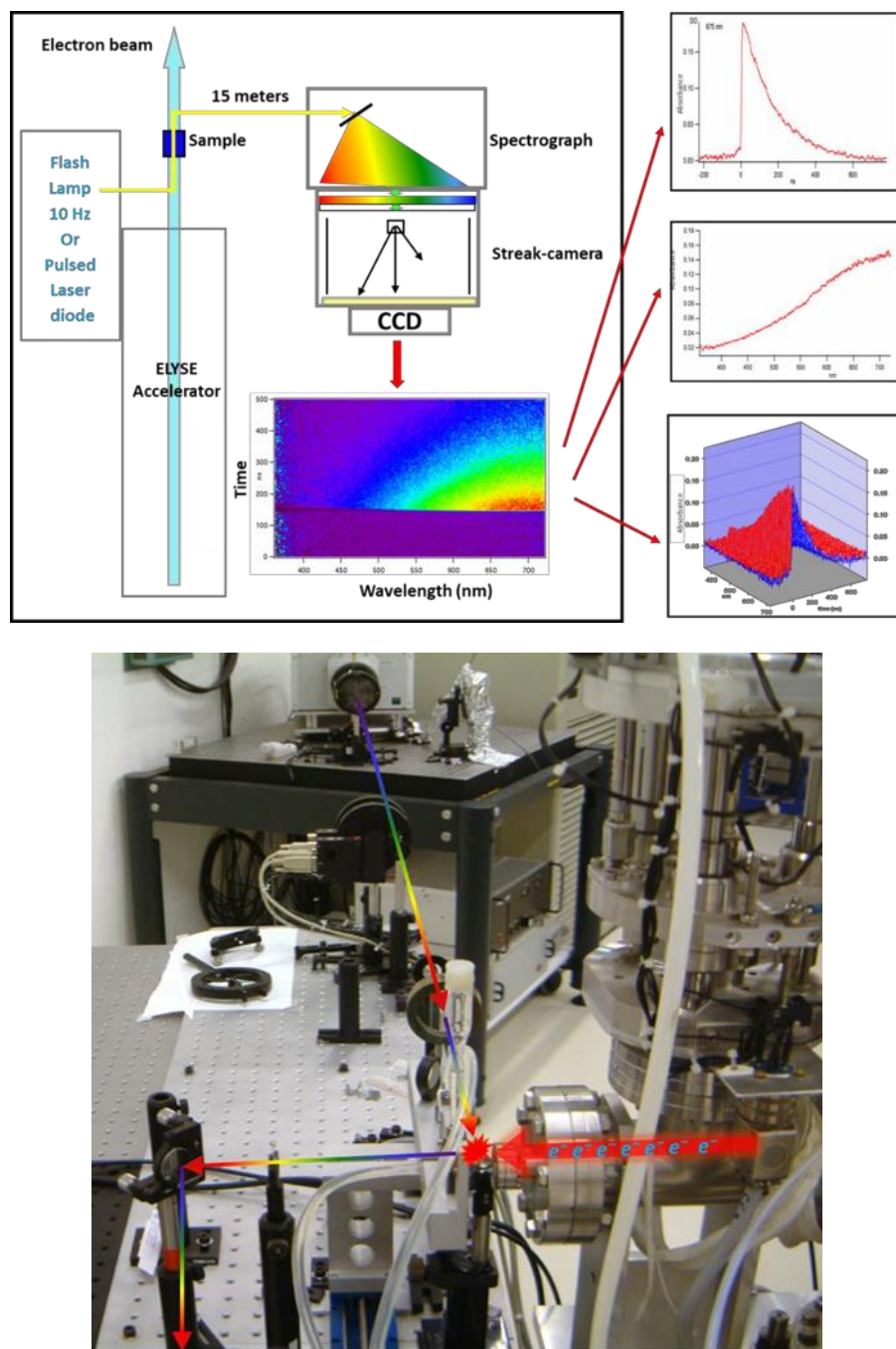


**Figure 2.21** Up: the mechanic scheme of streak camera in ELYSE. On the left are different signals extracted from a 2D experimental image. Bottom: The optical path of the optical detection by streak camera.

The light source consists of a home-made pulse generator driving a commercial Xenon lamp having a high and constant maximum intensity for a period of about 500 ns, with a rise time of 2  $\mu$ s and a repetition rate up to 25 Hz.<sup>23</sup> The cross section of the analyzing light beam is smaller (0.2

cm) than that of the electron beam and both are collinear. Alignment of the electron beam relative to the probe light beam is optimized by adjusting the magnets to maximize the reference absorbance signal (generally of the hydrated electron) recorded by a control photomultiplier equipped with filters selecting the wavelength range. The photomultiplier is located in the detection room at the arrival of the probe beam and systematically used to control the optimization of the absorbance before reflecting the beam to the spectrograph-streak camera set-up (**Figure 2.21**). The major advantage of using such a device is to obtain in a single pulse the information both on kinetics and on the transient absorption spectrum. The method is particularly well adapted to the spectral identification of the transients and to an overview of the chemical mechanism. This set-up can be used to observe transients from the end of the pulse up to rather long time, in the range of 500 ns, or with an adequate light source, up to 1 ms full scale for longer-lived species.

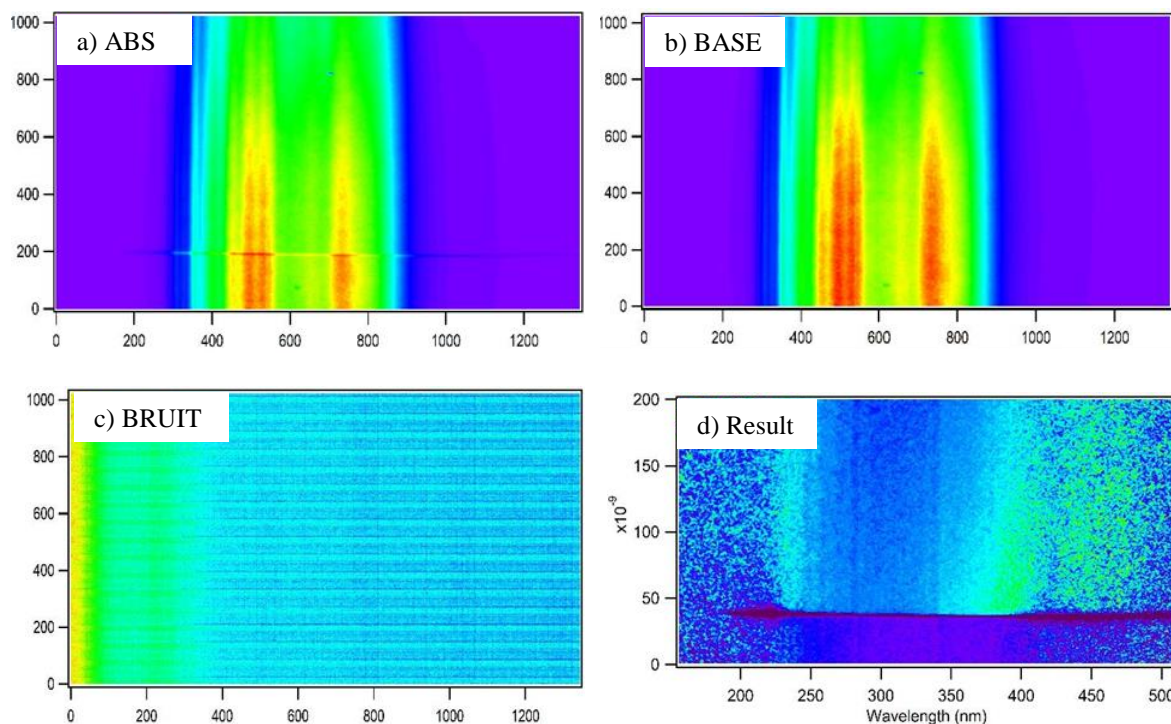


**Figure 2.22** a) Image recorded by streak camera with analysis light and electron beam, b) Image recorded by streak camera with analysis solely, c) The background noise recorded by streak camera and d) the analyzed result.

The results collected by the Streak-camera are in the form of 2D images with resolution of 1023x1344 pixels (resolution of the CCD camera) (**Figure 2.21** Up). The final image constituting the optical density is obtained from a series of four measurements made on the cell containing the



sample to be studied: firstly, the background noise of the camera is recorded in the absence of any light signal (BRUIT) (**Figure 2.22 c**), then the analysis light is recorded alone (BASE) (**Figure 2.22 b**). The third measurement is made on presence of the electron beam sent into the cell and the analysis lamp. Thus, the light of analysis is absorbed not only by the formed species, but also by the Cerenkov light itself (ABS) (**Figure 2.22 a**). In order to eliminate it, the Cerenkov light is recorded alone by sending the electron beam into the sample without any analysis light (CER). Thus, the Optical Density can be calculated from the following Beer-Lambert law:

$$OD = \log \left( \frac{BASE - BRUIT}{ABS - CER} \right) \quad \text{EQ.2-3}$$

The time-resolved absorbance of the species in 2D image is determined (**Figure 2.22 d**). Generally, the data collected is acquired by averaging 400 pulses (or images) to improve the signal to noise ratio. Images are first received and averaged by Hammamtsu software in the streak-camera. In order to work simultaneously, the computer that drives the streak camera does not store the data but sends it directly to a second computer that has 3 fast SCSI hard disks. Thus it is possible to average the 400 images of an acquisition on a hard disk instead of acquiring another series of images on another hard disk.

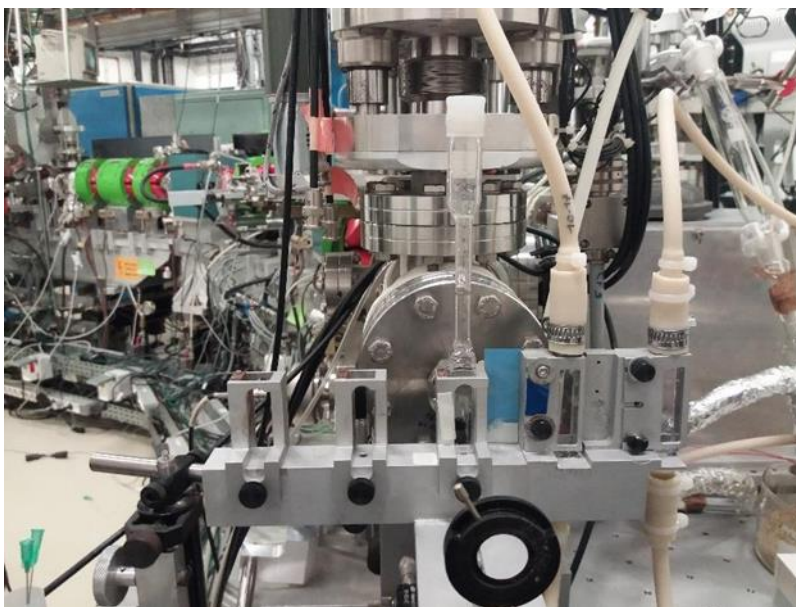


**Figure 2.22** The cycling system in the optical detection by streak camera.

The suprasil quartz optical cell (Ets. Thuet) is connected by tubes with a reservoir where the solution to be studied is stored and deaerated by flushing with an inert gas. A peristaltic pump ensures the circulation of the solution. The optical path is 0.2–1 cm. In order to optimize the time resolution of the detection line, the analyzing light beam is orientated almost collinearly with the electron beam and in the same direction. For this purpose, a very thin mirror (0.2 mm thick aluminum coated silica, to minimize scattering of the electrons) is located in the narrow space between the electron beam exit window and the optical cell (**Figure 2.21**). After crossing the sample, the light beam is then reflected by a mirror, either to the series of mirrors and lenses of the optical line to the streak camera, or through optical fibers to the photodiodes (**Figure 2.21**). The streak camera and photodiodes are located in the detection rooms about 15m from the samples. Since most of the electromagnetic noise picked up by the signal cables is produced by the charges of the electron beam itself, the ensemble of the cell and nearby mirrors is thoroughly connected to the ground. The flowing system is shown in **Figure 2.22**.

In order to determine the dose deposited in the water, the time dependent absorbance of the solvated electron at 660 nm is measured corresponding to 3 ns at the beginning of each experiment (**Figure 2.23 a**). **Figure 2.23 b** shows the decay of the solvated electron recorded at 660 nm on an average image averaging from 400 acquisitions.

For example, the decay of the solvated electron presented below (**Figure 2.23 b**), the value of the optical density at 3 ns:  $A_{t=3\text{ ns}} = 0.34$ , the dose deposited in the water could be given by:

$$Dose(Gy) = \frac{A_{t=3ns}}{\varepsilon_{\lambda=660nm} \times G_{t=3ns} \times l \times \rho} \quad \text{EQ. 2-4}$$

- $G_{t=3\text{ ns}}$  is the radiolytic yield of solvated electron at 3 ns, i.e.,  $3.4 \times 10^{-7} \text{ mol J}^{-1}$ .
- $\varepsilon_{\lambda=660nm}$  is the molar extinction coefficient value of solvated electron at 660 nm, i.e., 18 000  $\text{M}^{-1} \text{ cm}^{-1}$ .
- $L$  is the length of the optical path in the optical cell, i.e., 1 cm.
- $\rho$  is the density of water, i.e., 1  $\text{g mL}^{-1}$ .

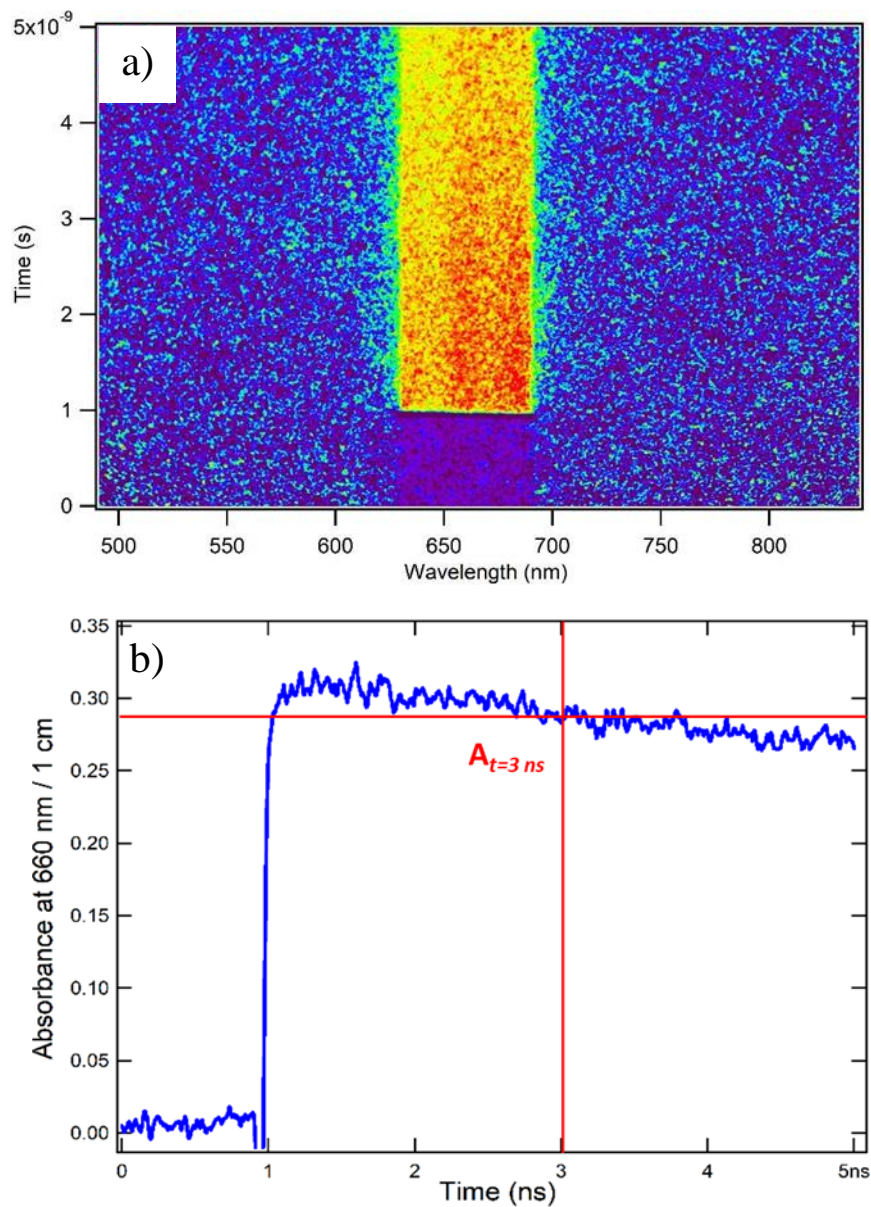


**Figure 2.23** The decay of solvated electron in H<sub>2</sub>O recorded by streak camera. a) Image in 2D form, and b) Kinetics at 660 nm.

So, the dose could be determined as:

$$Dose(Gy) = \frac{0.29}{18000 \times 3.4 \times 10^{-7} \times 1 \times 1} = 47 \text{ Gy}$$

It should be noted that according to the purpose of the experiment, the dose can be reduced either by placing neutral densities in front of the laser in order to lower its intensity and thus generate fewer electrons; or by changing the position of a lens on the laser path to focus the beam more or less at the photocathode. All these manipulations are done without access to the accelerator room during the experiments from the control room.

### 2.2.3 $\gamma$ -source

Cobalt-60 ( $^{60}\text{Co}$ ) is the most common gamma radiation source. It is synthetic radioactive isotope of cobalt with a half-life of 5.2714 years,<sup>25</sup> produced artificially in nuclear reactors.  $^{60}\text{Co}$  decays by beta ray to stable isotope nickel-60 ( $^{60}\text{Ni}$ ). The activated nickel nucleus emits two gamma rays with energies of 1.17 and 1.33 MeV, hence the overall nuclear equation of the reaction is:



$^{60}\text{Co}$  source installed in Laboratoire de Chimie Physique, Université Paris-Sud is a panoramic irradiation source of 7,000 Ci (Curie). The container is shaped as a cylinder and the  $^{60}\text{Co}$  source is placed in a lead jar (**Figure 2.24**). The system could be controlled by an operator far distance. The source is located in a chamber with thick concrete wall, where the door is made of lead. A zigzag passage is designed among those walls on the purpose of protection. The sample would be fixed on the plate when irradiated by  $^{60}\text{Co}$  source. The dose rate depends on the distance to the source and determined by Fricke's dosimetry.<sup>26</sup> For the dose deposited in the sample, it can be estimated as in water as following:

$$\text{Dose (Gy)} = \text{Dose rate (Gy / min or Gy / h)} \times \text{Time (min or h)} \quad \text{EQ. 2-7}$$



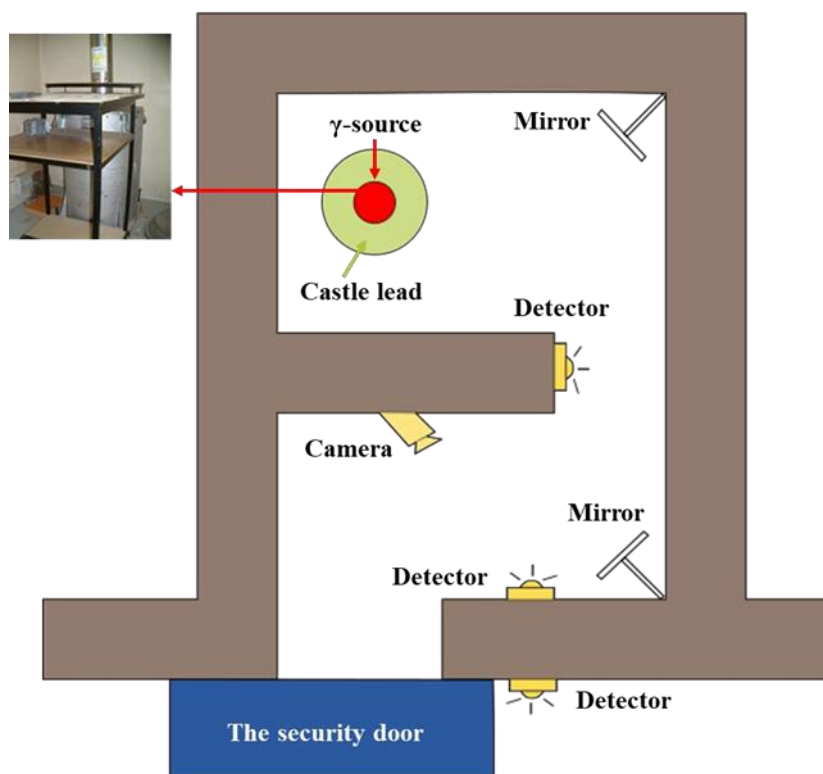


**Figure 2.24** Schematic representation of  $^{60}\text{Co}$  source (Laboratoire de Chimie Physique, Université Paris-Sud).

## 2.3 SK-Ana — MCR-ALS analysis method

In transient absorbance spectroscopy, measurements are usually performed for all the wavelengths for a given pump-probe time delay. Consequently, time-resolved absorption spectroscopy data values consist of a series of such time-gated spectra. The spectra are usually arranged in a two-way structure (a table or a matrix), where each row corresponds to a full spectrum recorded at a certain time delay and each column to the variation of the absorbance at a particular wavelength as a function of the time delay. In an ideal situation, the underlying model of the spectroscopic measurements in  $D$  would be written as a sum of the contributions of the spectra of  $k$  different components (**Figure 2.25**), related to the different absorbing species (intermediate and product states), weighted by their respective time-dependent concentration, as expressed by the bilinear model as follow:

$$D = C \times S^T \quad \text{EQ. 2-}$$

where the columns of matrix  $C$ , sized  $m \times k$ , are the time-dependent profiles of the  $k$  components at the  $m$  time delay values and the rows of matrix  $S^T$ , sized  $k \times n$ , are the related  $k$  difference transient spectra measured at  $n$  spectroscopic variables. The elements of  $D$  are denoted  $d_{ij}$ , where the time delays  $t_i$  design the rows and the wavelengths  $j$  design the columns. It should be noted that the situation described above corresponds to noise-free data. The term “component” should also be clarified since it can sometimes be quite misleading. It would refer, in an ideal case, to pure physical or chemical factors, i.e., photochemical species involved in the transient multi-species system studied.

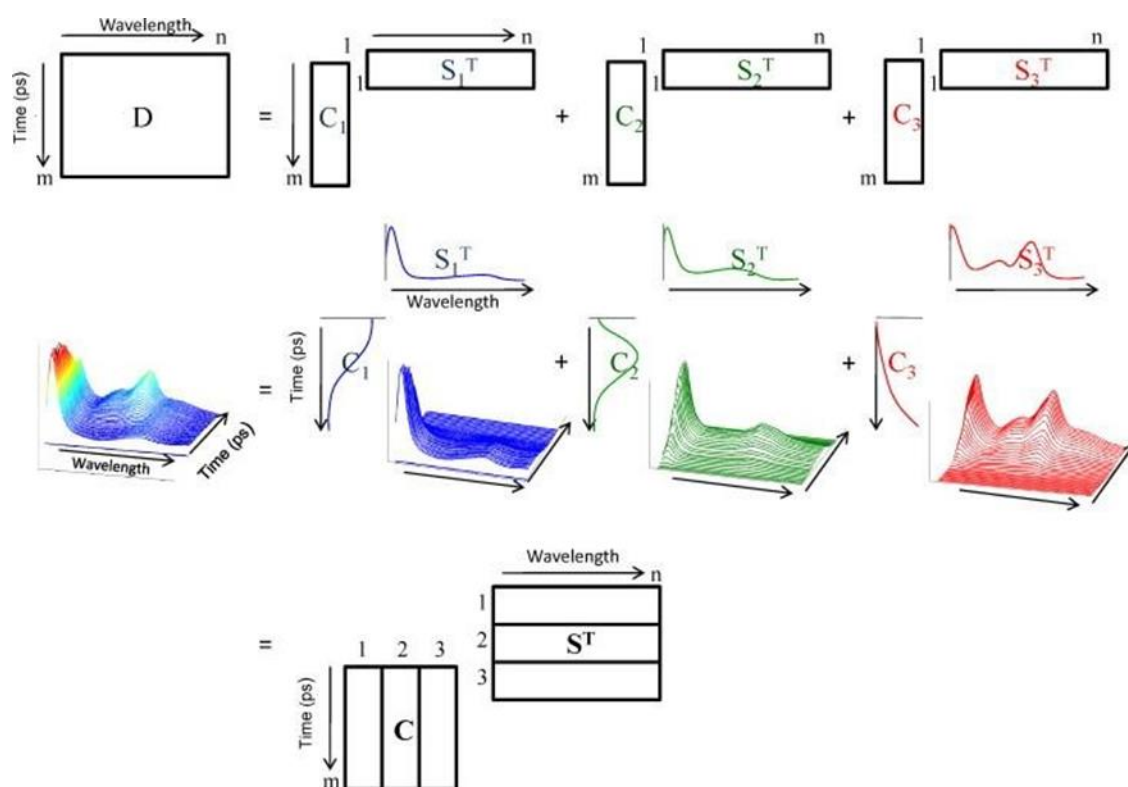


**Figure 2.25** Bilinear model related to a three-component process monitored by time-resolved spectroscopy.<sup>27</sup>

When multiple and complementary experiments are performed, it is possible and highly positive to organize and analyze these data sets under the form of a single multiset data structure (second-order global analysis).<sup>28,29</sup> Indeed, the bilinear model in EQ. 2-8 can be extended to describe the structure of the measurements of the different experiments forming a multiset. The only structural requirement when performing multiset analysis is that the information on one of the

modes of the data sets, e.g., the spectral information for a column-wise data set, be the same for all the multiset structure (**Figure. 2.26**). In practice, multiset analysis may help to determine the correct rank of the data matrix<sup>30</sup> and, thus, the components of the model for data description. Müller *et al.*<sup>31</sup> have also demonstrated that global analysis of multisets reduces the variance of the parameters in model-based analysis. In other words, the combination of several experiments (different time scale, different probe wavelength or different molecular environment, for example) involving the same molecule or complementary species will always help in a better description of the system.

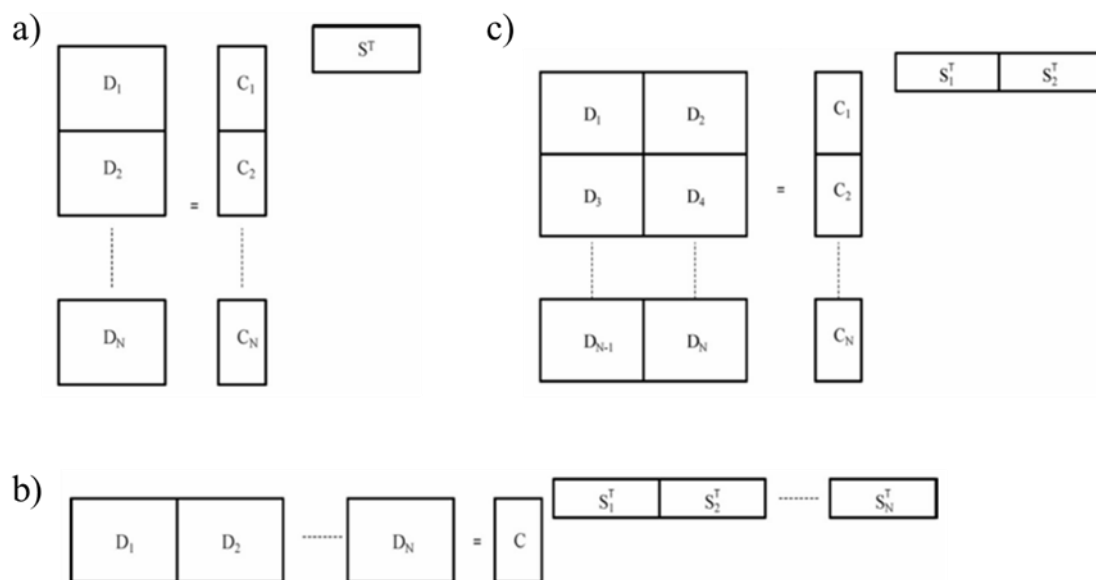


**Figure 2.26** Examples of multiset structures: (a) column-wise appended data sets sharing the pure spectra for all data sets; (b) row-wise appended data sets sharing the same time-dependent profiles for all components, (c) column-wise and row-wise appended data sets, with subsets of experiments sharing time-dependent profiles or pure spectra.<sup>27</sup>

In my thesis, the data treatment was involved with a multivariate curve resolution alternating least squares (MCR- ALS) approach — SpectroKinetics Analysis (SK-Ana).<sup>32</sup> As in this type of system, the spectra of the absorbing species strongly overlap that causes the difficulty to unmix and sort out individual spectra, a global data analysis approach was used. Global matrices were built by delay-wise binding matrices with the data matrices for different time resolutions and concentrations. In this configuration, the components spectra are common to all the experiments in the global dataset, while each experiment has its own set of kinetic traces. The number of absorbing

species in a matrix was assessed by Singular Value Decomposition (SVD) of the matrix, and a MCR-ALS analysis with the corresponding number of species was performed. Positivity constraints were imposed for both spectra and kinetics, and the shape of some spectra can be imposed. Based on quantum mechanical information, unimodality constraints can also be imposed to the spectra. All the calculations have been made with codes developed in-house in the R environment.<sup>33</sup> Our MCR-ALS code was adapted from the ALS package by K.M. Mullen.<sup>34</sup>

## 2.4 Chemicals

All the chemicals were purchased from Sigma Aldrich. Water for dilution or dosimetry was purified until the value of conductivity reaches 18 MΩ.cm by passage through a Millipore purification system. **Table 2.1** gathers the properties of the chemical products used in the thesis.

**Table 2.1** The chemical products used in the thesis

Product	Chemical formula	State	Role	Molecular mass (g mol <sup>-1</sup> )	Density (g mL <sup>-1</sup> )	Purity (%)
Deuterium oxide	D <sub>2</sub> O	Liquid	Solvent	20.03	1.107	99.9
Sulfuric acid-d <sub>2</sub>	D <sub>2</sub> SO <sub>4</sub>	Liquid	Solute	100.09	1.88	99.5
Sulfuric acid	H <sub>2</sub> SO <sub>4</sub>	Liquid	Solute	98.08	1.84	99.99
Methyl viologen dichloride hydrate	C <sub>12</sub> H <sub>14</sub> Cl <sub>2</sub> N <sub>2</sub> ·xH <sub>2</sub> O	Solid	Solute	257.16	—	98
tert- Butanol	(CH <sub>3</sub> ) <sub>3</sub> CO H	Liquid	Solute	74.12	0.775	≥ 99.5

## 2.5 Concluding remark

The primary events as a result of the interaction of ionizing radiation with matter mostly occur in ultra-short time. Thanks to the development of technology, pulsed radiolysis gives us access to study the radiation chemistry within ultra-short time scale in terms of the behavior of different solvents vis-à-vis their interactions with ionizing radiation, the physical and chemical characteristics of the formed radical and molecular species, the formation mechanisms of radical and molecular species, *etc.* The picosecond pump-probe radiolysis facility ELYSE is a powerful tool to study the ultra-fast chemical reaction induced by ionizing radiation. In the course of my thesis, the work was mainly performed in ELYSE. The setup—picosecond pulse-probe and streak camera, were employed to collect the time resolved absorption matrix data. The UV-Vis absorption spectra of methyl viologen cation radical in water and deuterated water was obtained by irradiation with  $\gamma$ -source. MCR-ALS analysis method SK-Ana was involved in data treatment.

## References

- (1) Sasuga, T.; Kudoh, H.; Seguchi, T. High Energy Ion Irradiation Effects on Polymer Materials – Changes in Mechanical Properties of PE, PSF and PES. **1999**, *40*, 5095–5102.
- (2) Saito, K.; Sugo, T. High-Performance Polymeric Materials for Separation and Reaction, Prepared by Radiation-Induced Graft Polymerization. In *Radiation Chemistry*; Jonah, C. D., Rao, B. S. M., Eds.; Studies in Physical and Theoretical Chemistry; Elsevier, 2001; Vol. 87, pp 671–704.
- (3) *Power Sources for Remote Arctic Applications, OTA-BP-ETI 129*; U.S. Congress, Office of Technology Assessment: Washington, DC, 1994.
- (4) Spothem-maurizot, M.; Mostafavi, M.; DOUKI, T.; Belloni, J. *Radiation Chemistry- From Basics to Applications in Material and Life Sciences*; Spothem-maurizot, M., Mostafavi, M., DOUKI, T., Belloni, J., Eds.; EDP SCIENCES: Les Ulis Cedex A, France, 2008.
- (5) Quint, R. M.; Getoff, N. Dose Reduction and Dose Measurement for Pulse Radiolysis Equipment, Type FEBETRON 708. *Nucl. Instruments Methods Phys. Res. Sect. A Accel. Spectrometers, Detect. Assoc. Equip.* **2002**, *481*, 81–85.
- (6) Bronskill, M. J.; Taylor, W. B.; Wolff, R. K.; Hunt, J. W. Design and Performance of a Pulse Radiolysis System Capable of Picosecond Time Resolution. *Cit. Rev. Sci. Instruments Sci. Instrum* **1970**, *41*.
- (7) Jonah, C. D. A Wide-time Range Pulse Radiolysis System of Picosecond Time Resolution. *Rev. Sci. Instrum.* **1975**, *46*, 62–66.
- (8) Saeki, A.; Kozawa, T.; Kashiwagi, S.; Okamoto, K.; Isoyama, G.; Yoshida, Y.; Tagawa, S. Synchronization of Femtosecond UV-IR Laser with Electron Beam for Pulse Radiolysis Studies. *Nucl. Instruments Methods Phys. Res. Sect. A Accel. Spectrometers, Detect. Assoc. Equip.* **2005**, *546*, 627–633.
- (9) Muroya, Y.; Lin, M.; Iijima, H.; Ueda, T.; Katsumura, Y. Current Status of the Ultra-Fast Pulse Radiolysis System at NERL, the University of Tokyo. *Res. Chem. Intermed.* **2005**, *31*, 261–272.
- (10) Saeki, A.; Kozawa, T.; Tagawa, S. Picosecond Pulse Radiolysis Using Femtosecond White

- Light with A High S/N Spectrum Acquisition System in One Beam Shot. *Nucl. Instruments Methods Phys. Res. Sect. A Accel. Spectrometers, Detect. Assoc. Equip.* **2006**, 556, 391–396.
- (11) Nagai, H.; Kawaguchi, M.; Sakaue, K.; Komiya, K.; Nomoto, T.; Kamiya, Y.; Hama, Y.; Washio, M.; Ushida, K.; Kashiwagi, S.; et al. Improvements in Time Resolution and Signal-to-Noise Ratio in a Compact Pico-Second Pulse Radiolysis System. *Nucl. Instruments Methods Phys. Res. Sect. B Beam Interact. with Mater. Atoms* **2007**, 265, 82–86.
  - (12) Wishart, J. F.; Cook, A. R.; Miller, J. R. The LEAF Picosecond Pulse Radiolysis Facility at Brookhaven National Laboratory. *Rev. Sci. Instrum.* **2004**, 75, 4359–4366.
  - (13) Marignier, J.-L.; de Waele, V.; Monard, H.; Gobert, F.; Larbre, J.-P.; Demarque, A.; Mostafavi, M.; Belloni, J. Time-Resolved Spectroscopy at the Picosecond Laser-Triggered Electron Accelerator ELYSE. *Radiat. Phys. Chem.* **2006**, 75, 1024–1033.
  - (14) Holroyd, R.; Wishart, J.; Nishikawa, M.; Itoh, K. Reactions of Charged Species in Supercritical Xenon as Studied by Pulse Radiolysis†. **2003**.
  - (15) Muroya, Y.; Lin, M.; Wu, G.; Iijima, H.; Yoshii, K.; Ueda, T.; Kudo, H.; Katsumura, Y. A Re-Evaluation of the Initial Yield of the Hydrated Electron in the Picosecond Time Range. *Radiat. Phys. Chem.* **2005**, 72, 169–172.
  - (16) Belloni, J.; Monard, H.; Gobert, F.; Larbre, J.-P. P.; Demarque, A.; De Waele, V.; Lampre, I.; Marignier, J.-L. L.; Mostafavi, M.; Bourdon, J. C. C.; et al. ELYSE—A Picosecond Electron Accelerator for Pulse Radiolysis Research. *Nucl. Instruments Methods Phys. Res. Sect. A Accel. Spectrometers, Detect. Assoc. Equip.* **2005**, 539, 527–539.
  - (17) Chevallay, E.; Durand, J.; Hutchins, S.; Suberlucq, G.; Wurgel, M. Photocathodes Tested in the Dc Gun of the CERN Photoemission Laboratory. *Nucl. Instruments Methods Phys. Res. Sect. A Accel. Spectrometers, Detect. Assoc. Equip.* **1994**, 340, 146–156.
  - (18) Eyberger, C. E.; Pardo, R. C.; White, M. M.; Jaje, K. M. Linear Accelerator. Proceedings, 19th International Conference, Linac'98, Chicago, USA, August 23-28, 1998; Eyberger, C. E., Pardo, R. C., White, M. M., Jaje, K. M., Eds.; 1998.
  - (19) di Bona, A.; Sabary, F.; Valeri, S.; Michelato, P.; Sertore, D.; Suberlucq, G. Auger and X-ray Photoemission Spectroscopy Study on Cs<sub>2</sub>Te Photocathodes. *J. Appl. Phys.* **1996**, 80, 3024–3030.



- (20) Srinivasan-Rao, T.; Fischer, J.; Tsang, T. Photoemission Studies on Metals Using Picosecond Ultraviolet Laser Pulses. *J. Appl. Phys.* **1991**, *69*, 3291–3296.
- (21) Schmidhammer, U.; El Omar, A. K.; Balcerzyk, A.; Mostafavi, M. Transient Absorption Induced by A Picosecond Electron Pulse in the Pused Silica Windows of An Optical Cell. *Radiat. Phys. Chem.* **2012**, *81*, 1715–1719.
- (22) Schmidhammer, U.; Jeunesse, P.; Stresing, G.; Mostafavi, M. A Broadband Ultrafast Transient Absorption Spectrometer Covering the Range from Near-Infrared (NIR) down to Green. *Appl. Spectrosc.* **2014**, *68*, 1137–1147.
- (23) Marignier, J.-L.; Herren, R.; Bazouin, J. R. Générateur de Flashs Lumineux, Spectromètre d'absorption Utilisant Un Tel Générateur et Procédé de Génération de Flashs Lumineux., 2008.
- (24) De Waele, V.; Schmidhammer, U.; Marquès, J.-R.; Monard, H.; Larbre, J.-P.; Bourgeois, N.; Mostafavi, M. Non-Invasive Single Bunch Monitoring for Ps Pulse Radiolysis. *Radiat. Phys. Chem.* **2009**, *78*, 1099–1101.
- (25) *Practical Radiotherapy: Physics and Equipment*; Cherry, P., Duxbury Angela, Eds.; Oxford university press: New york, NY, 2000; Vol. 214.
- (26) Jayson, G. G.; Parsons, B. J.; Swallow, A. J. The Mechanism of the Fricke Dosimeter. *Int. J. Radiat. Phys. Chem.* **1975**, *7*, 363–370.
- (27) Ruckebusch, C.; Sliwa, M.; Pernot, P.; de Juan, A.; Tauler, R. Comprehensive Data Analysis of Femtosecond Transient Absorption Spectra: A Review. *J. Photochem. Photobiol. C Photochem. Rev.* **2012**, *13*, 1–27.
- (28) Gampp, H.; Maeder, M.; Meyer, C. J.; Zuberbühler, A. D. Calculation of Equilibrium Constants from Multiwavelength Spectroscopic Data—IV: Model-Free Least-Squares Refinement by Use of Evolving Factor Analysis. *Talanta* **1986**, *33*, 943–951.
- (29) Bugnon, P.; Chottard, J.-C.; Jestin, J.-L.; Jung, B.; Laurenczy, G.; Maeder, M.; Merbach, A. E.; Zuberbühler, A. D. Second-Order Globalisation for the Determination of Activation Parameters in Kinetics. *Anal. Chim. Acta* **1994**, *298*, 193–201.
- (30) Amrhein, M.; Srinivasan, B.; Bonvin, D.; Schumacher, M. M. On the Rank Deficiency and

- Rank Augmentation of the Spectral Measurement Matrix. *Chemom. Intell. Lab. Syst.* **1996**, 33, 17–33.
- (31) Müller, K.-H.; Plessner, T. Variance Reduction by Simultaneous Multi-Exponential Analysis of Data Sets from Different Experiments. *Eur. Biophys. J.* **1991**, 19, 231–240.
- (32) Pernot, P. SK-Ana: Spectro-Kinetic Analysis ([Http://Doi.Org/10.5281/zenodo.1120307](http://doi.org/10.5281/zenodo.1120307)). Laboratoire de Chimie Physique: Orsay 2017.
- (33) R Development Core Team (2011). R: A Language and Environment for Statistical Computing. R Foundation for Statistical Computing: Vienna, Austria 2011.
- (34) Mullen, K. M. ALS: Multivariate Curve Resolution Alternating Least Squares (MCR-ALS). R Package Version 0.0.5. [Http://CRAN.R-Project.Org/Package=ALS](http://CRAN.R-project.org/package=ALS) in the R Language [R Core Team (2012). R: A Language and Environment for Statistical Computing. R Foundation for Statis. 2012.

# Chapter III: Time Dependent Yield of the Solvated Electron and the OD<sup>•</sup> Radical in Deuterated Water at Low LET Studied by Picosecond Pulse Radiolysis

## **Table of contents**

### 3.1 State of the art and objective

#### 3.1.1 Introduction

#### 3.1.2 Objective

### 3.3 Hydrated electron in D<sub>2</sub>O

#### 3.3.1 Isosbestic method

#### 3.2.2 Absorption spectrum of $e_{D_2O}^-$

#### 3.2.3 Time dependent yield of $e_{D_2O}^-$

### 3.4 OD<sup>•</sup> radical in D<sub>2</sub>O

#### 3.4.1 Transient absorption induced in FSOFC

#### 3.4.2 Time dependent yield of OD<sup>•</sup>

### 3.5 Conclusions

### Reference

Appendix: Molar absorption extinction coefficient of  $e_s^-$  in D<sub>2</sub>O (250 to 1500 nm)  
obtained in the present work

## **Chapter III: Time Dependent Yield of Solvated Electron and OD<sup>•</sup> Radical in Deuterated Water at Low LET Studied by Picosecond Pulse Radiolysis**

### **3.1 State of the art and objective**

#### **3.1.1 Introduction**

Water is the subject of radiation reaction of many experimental and theoretical investigation for more than 70 years. The ionizing radiation reaction impact on neat water has great importance in biology, medicine and nuclear energy industries. It is well known that the radicals  $e_s^-$ , OH<sup>•</sup>, H<sup>•</sup>, and the molecules H<sub>2</sub>, and H<sub>2</sub>O<sub>2</sub> are produced during the decomposition of water under ionizing radiation with linear energy transfer (LET, such as electron beam or  $\gamma$  ray). For the determination of the time dependent radical yield in non-homogenous step (shorter than 100 ns in water) of the radiolytic process, the parameters involved in the simulation code of water radiolysis were adjusted by fitting the data obtained by scavenging method during the 70's and 80's, except a few works performed with picosecond pulse radiolysis time resolution.<sup>1</sup>. Important progress made during the last decade in the pulse radiolysis techniques allowed obtaining an acceptable model for the water radiolysis with an accurate determination of the initial yield of the hydrated electron and the hydroxyl radical in H<sub>2</sub>O. Their time dependent yield are now well known from the picosecond range, and the simulations can at least fit well the new experimental data in the case of the hydrated electron.<sup>2-7</sup>

**Table 3.1.** Comparison of the physical properties of H<sub>2</sub>O and D<sub>2</sub>O

	Molecular weight (g/mol)	Density (g mL <sup>-1</sup> )	Viscosity (mPa) at room temperature	Dielectric constant at 25°C
H <sub>2</sub> O	18.02	1.000	1.00	78.54
D <sub>2</sub> O	20.03	1.107	1.25	78.3

Heavy water (D<sub>2</sub>O) was discovered by Dr. H. C. Urey in 1932 and attracted enormous interest in industry, biology and medicine. D<sub>2</sub>O exhibits different physical properties compared to normal water (H<sub>2</sub>O). As shown in **Table 3.1**, there are higher molecular weight, density and viscosity in D<sub>2</sub>O than that in H<sub>2</sub>O. The deviations are expected to result in different behavior of the radicals  $e_s^-$ , OD<sup>•</sup>, D<sup>•</sup>, and the molecules D<sub>2</sub>, and D<sub>2</sub>O<sub>2</sub> in irradiated D<sub>2</sub>O. However, there is important controversy for the time dependent yield of these radicals in deuterated water D<sub>2</sub>O.

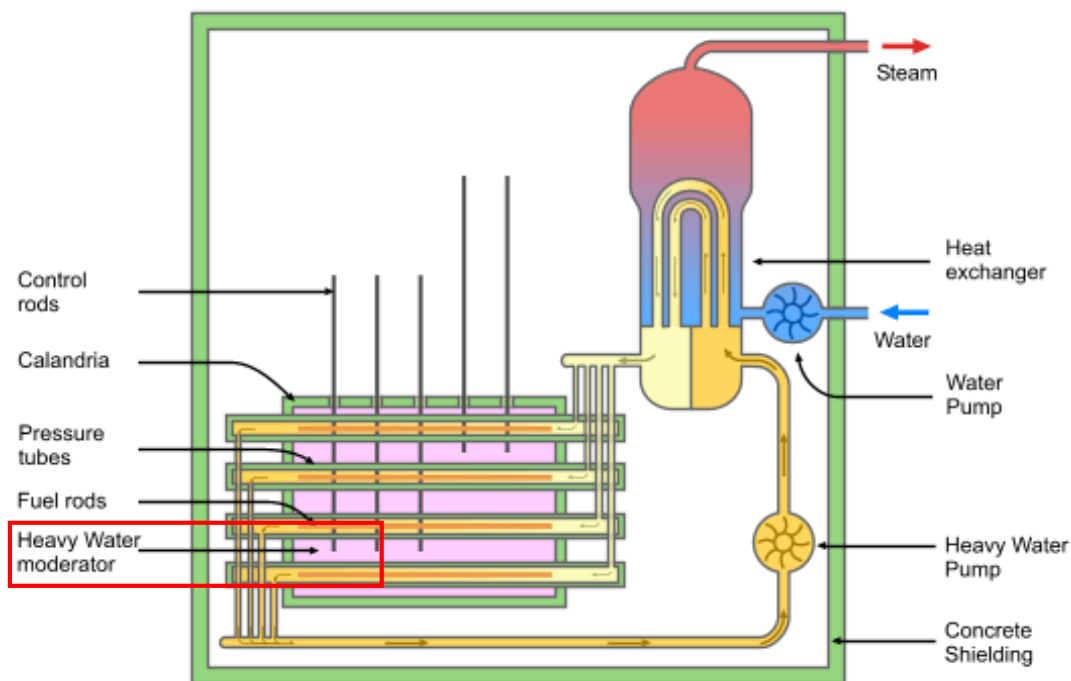


**Figure 3.1** A schematic of CANDU nuclear reactor.

Furthermore, heavy water is one of the distinctive features of CANDU nuclear reactors as a moderator and coolant (**Figure 3.1**) because of its low probability of absorption of neutrons, which is able to slow down neutrons effectively. There are 29 CANDU nuclear power plants present in the world, and there are more heavy water nuclear reactors which designed based on CANDU. A clear understanding of the radiolysis of heavy water will be helpful to attain good chemistry control and consequently reduce corrosion and hydriding of the system components.<sup>8</sup>

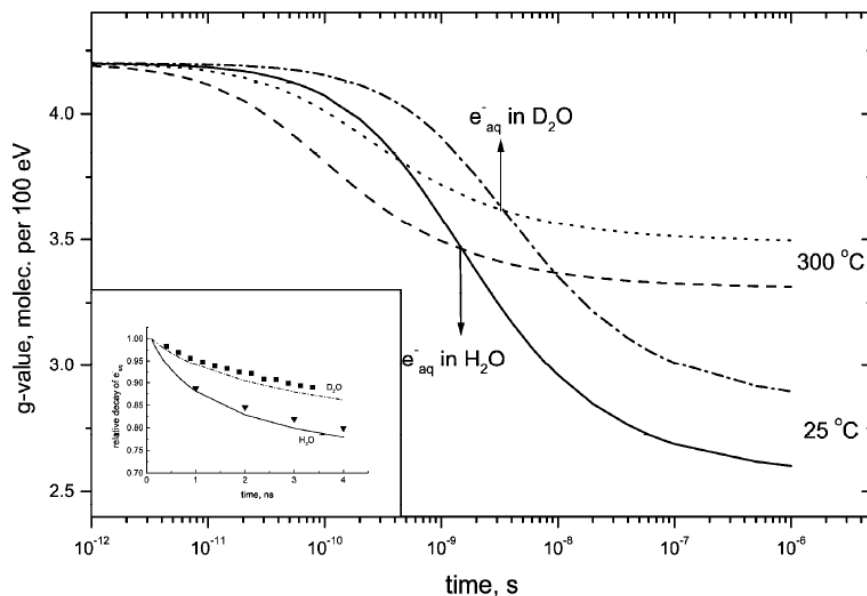


**Figure 3.2** Simulation of the time dependent decay of solvated electron in  $H_2O$  and  $D_2O$  under low LET radiolysis at 25 °C and 300 °C, respectively.<sup>9</sup> The inset was experimental results from C. D. Jonah *et al.*<sup>2, 10</sup>

Up to now, there is no picosecond pulse radiolysis measurement in neat  $D_2O$  showing simultaneously the radiolytic yield of  $OD^\bullet$  and  $e_{D_2O}^-$  in the spurs. Experimental results reported that the primary yield ( $\sim 200$  ns) of radicals is not the same in  $H_2O$  or  $D_2O$  solutions. The first pulse radiolysis measurement was performed by microsecond X-ray pulse radiolysis giving the primary yield ( $3 \times 10^{-7} \text{ mol J}^{-1}$ ) and the extinction coefficient ( $20200 \text{ L mol}^{-1} \text{ cm}^{-1}$  at 700 nm) of the hydrated electron in  $D_2O$ .<sup>11</sup> In 1975, G. R. Freeman first reported the primary yield (homogenous step) of the hydrated electron to be  $2.7 \pm 0.1$  in  $H_2O$  and  $3.1 \pm 0.1$  in  $D_2O$  using  $SF_6$  as scavenger at 23 °C, and obtained similar results with  $N_2O$  scavenging of hydrated electron.<sup>12</sup> Later, transient conductivity experiments were used to measure the primary yield of the solvated electron exhibiting also a higher value in  $D_2O$  ( $3.36 \times 10^{-7} \text{ mol J}^{-1}$ ) than in  $H_2O$  ( $2.83 \times 10^{-7} \text{ mol J}^{-1}$ ).<sup>13</sup> Chase and Hunt observed the spectrum of  $e_{D_2O}^-$  slightly shifted towards the blue as compared with that in  $H_2O$ , and deduced the primary yield and extinction coefficient of  $e_{D_2O}^-$  based on previous work with salicylate anion as scavenger.<sup>14</sup> It was reported that  $G\epsilon_{\text{max}}$  of  $e_{D_2O}^-$  is higher than in  $H_2O$ . Later Freeman *et al.* also confirmed this point.<sup>15</sup> By measuring with a 30 ps time resolution, the decay of solvated electron in  $D_2O$  and the mixture of  $D_2O$  and water, it was concluded that the slower decay of the solvated electron in neat  $D_2O$  was due to a larger distance that electron travels

before its solvation.<sup>16</sup> That means the geminate recombination is less effective in  $D_2O$ .

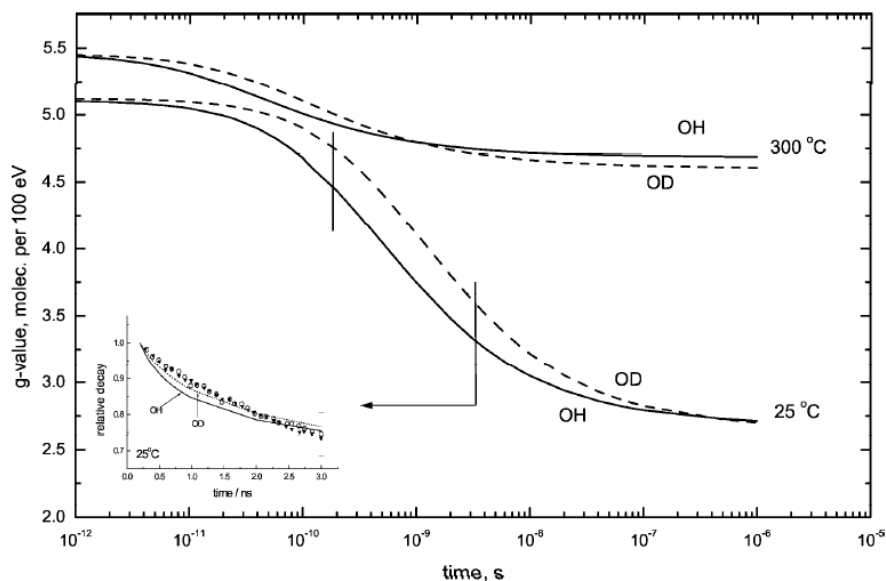


**Figure 3.3** Simulation of the time dependent decay of hydroxyl radical in  $H_2O$  and  $D_2O$  under low LET radiolysis at 25 °C and 300 °C by G.V. Buxton *et al.*, respectively.<sup>9</sup> The inset is the experimental results from C. D. Jonah *et al.*<sup>10</sup>

In 2001, diffusion-kinetic calculations were analyzed to understand the isotopic effect in the radiolysis of water (**Figure 3.2**).<sup>17</sup> The study showed that the initial yield (at ps range) of  $e_s^-$  in  $H_2O$  and  $D_2O$  is equal, but the spur decay of  $e_s^-$  is slower in  $D_2O$ , resulting in a higher yield of  $e_{D_2O}^-$  at  $10^{-7}$ - $10^{-6}$  s with low LET (linear energy transfer) radiolysis. The recent picosecond pulse radiolysis measurements of hydrated electron also found a similar initial yield of  $e_s^-$  in  $H_2O$  and  $D_2O$  in 2012.<sup>5</sup> To have a better understanding of the evolution of  $e_{D_2O}^-$ , the related knowledge has been remarked in **Table 3.2**. It's obvious that there are controversial results on the time dependent yield and the absorption peak of  $e_{D_2O}^-$  both in the spur reaction and in the homogenous stage.



**Table 3.2** The radiolytic yield value of  $e_{D_2O}^-$  at various stage and  $\epsilon_{e_{D_2O}^-}$  reported in literatures at room temperature.

$G(e_{D_2O}^-)$ ( $10^{-7}$ mol J <sup>-1</sup> )	$\epsilon_{e_{D_2O}^-}$ (M <sup>-1</sup> cm <sup>-1</sup> )	Description	Dose (Gy)	Time of measurement	Reference
2.9	20200 at 700 nm	X-ray	0.05	Homogenous stage	Fielden <sup>11</sup>
3.06 ± 0.05	--	SF <sub>6</sub> scavenger method	--	Homogenous stage	Chase <sup>18</sup>
3.1	--	SF <sub>6</sub> scavenger method	--	Homogenous stage	Schmidt <sup>12</sup>
4.5	19100 at 705 nm	Picosecond pulse radiolysis	30 ~ 50	30 ps	Nielsen <sup>19</sup>
--	--	Radiolysis and calculations	--		Jonah* <sup>15</sup>
3.24	--	Radiolysis and calculations	--	Homogenous stage	Singh <sup>13</sup>
4.25	--	Calculations	--	1 ps	Chernovitz <sup>9</sup>
4.4	--	Picosecond pulse radiolysis	--	60 ps	Muroya <sup>5</sup>

\*  $G\epsilon_{max}$  in D<sub>2</sub>O was reported 25% higher than that in H<sub>2</sub>O.

However, due to its low absorbance, there is not so much knowledge on the kinetics of OD<sup>•</sup> at picosecond range. The first absorption spectra of OD<sup>•</sup> from 190 to 260 nm was given by Nielsen et al. in 1976.<sup>20</sup> G.V. Buxton *et al.* performed similar measurements from 220 to 320 nm.<sup>21</sup> The two

absorption spectra were consistent. Buxton's simulations with low LET, predicted that the initial yield of OD<sup>•</sup> and OH<sup>•</sup> are similar (**Figure 3.4**).<sup>17</sup>

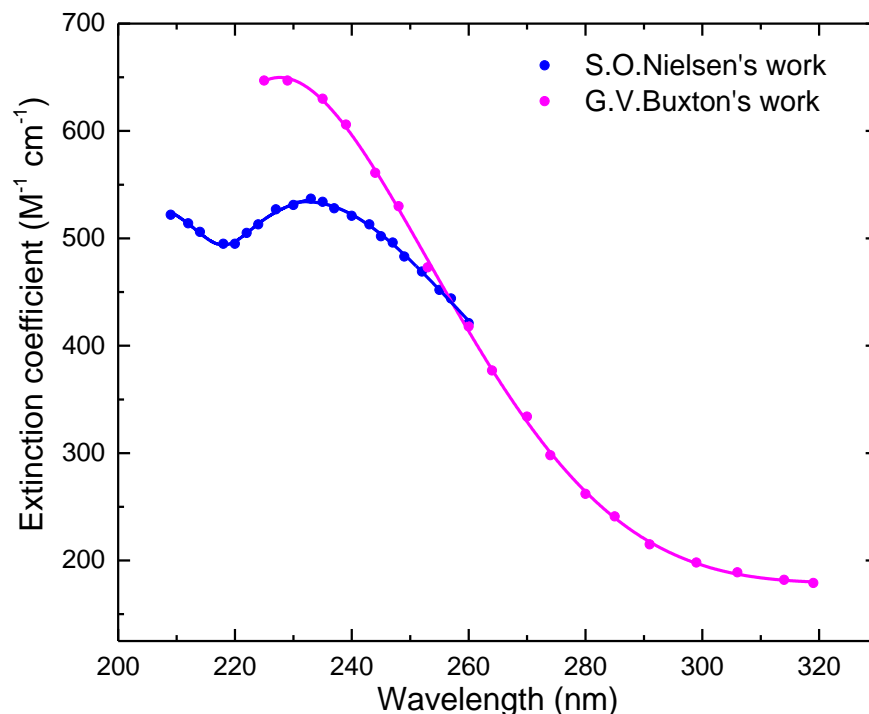


**Figure 3.4** Absorption spectra of OD<sup>•</sup> by S. O. Nielsen (in blue)<sup>20</sup> and G. V. Buxton (in pink).<sup>21</sup> The solid lines are the guide to eyes.

### 3.1.2 Objective

To have a better understanding of the earliest mechanisms induced by ionizing radiation in D<sub>2</sub>O, it is important to determine the time dependent yield of  $e_{D_2O}^-$  and OD<sup>•</sup> simultaneously. In the present work, we measured the absorption spectrum of the hydrated electron in D<sub>2</sub>O from 250 to 1500 nm for the first time (**Figure 3.5**). The time dependent yield of  $e_{D_2O}^-$  and OD<sup>•</sup> were determined and compared with those in H<sub>2</sub>O. For the study of OD<sup>•</sup>, with its low molar absorbance coefficient, the pulse radiolysis detection configuration was adapted to measure precisely *in situ* the dose per pulse via the solvated electron in the visible and the absorbance of OD<sup>•</sup> radical in the UV at 260 nm in the same volume irradiated by electron beam.

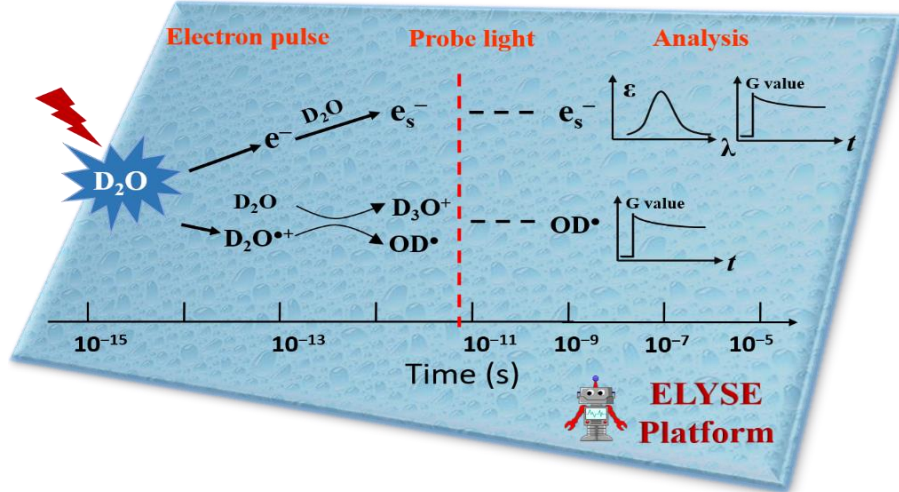


Figure 3.5 Scheme of objective in this work

### 3.3 The solvated electron in D<sub>2</sub>O

As known the transient absorbance of  $e_{D_2O}^-$  equation can be expressed as:

$$A_{e_{D_2O}^-}(\lambda, t) = \epsilon_{e_{D_2O}^-}(\lambda) \times D \times G_{e_{D_2O}^-}(t) \times l \times \rho \quad \text{EQ. 3-1}$$

In the formula,  $l$  is the optic path length and  $\rho$  represents the density of D<sub>2</sub>O. To determine the dose deposited in neat D<sub>2</sub>O, it can be estimated as:

$$\frac{D(H_2O)}{D(D_2O)} = \frac{1}{\rho} \times \frac{M(D_2O)}{M(H_2O)} \times \frac{N_{e^-}(H_2O)}{N_{e^-}(D_2O)} \quad \text{EQ. 3-2}$$

In this equation,  $M$  the molar mass, and  $N_{e^-}$  the total number of electron per molecule. Then,

$$\frac{D(H_2O)}{D(D_2O)} = \frac{1}{1.107} \times \frac{20}{18} \times \frac{10}{10} \approx 1.0$$

Therefore, the dose deposited in D<sub>2</sub>O is same with that in H<sub>2</sub>O. Obviously, to determine the time dependent yield of  $e_{D_2O}^-$  by measuring the time dependent absorbance, it is essential to confirm the molar absorption coefficient of  $e_{D_2O}^-$  first of all. Considering the evolution of the molar absorption coefficient of  $e_{D_2O}^-$ , there were scarce information and all the measurements were

performed by indirect methods.<sup>8,11,22</sup> In this work, a stoichiometric reaction between  $e_{D_2O}^-$  and an oxidizing species giving a product with a very well-known absorption spectrum which overlaps the spectrum of  $e_{D_2O}^-$  will be used. Thus, one or several wavelengths corresponding to the intersection between the spectra of  $e_{D_2O}^-$  and the oxidizing species used are in accordance with the wavelength where the molar absorption coefficients of both species are identical. If there exists only one reaction of  $e_{D_2O}^-$  with the acceptor, then these wavelengths where an optical density remains constant are going to be observed during the reaction. And these wavelengths are the isosbestic points of  $e_{D_2O}^-$  and the product.

It is important to identify precisely an isosbestic point and confirm that the reaction of  $e_{D_2O}^-$  with the acceptor is stoichiometric by using the invariance of the absorbance.<sup>23</sup> The accurate determination of an isosbestic point requires that the time evolution of the full absorption spectra can be observed, in order to be able to examine the various wavelengths and find out the wavelengths which keep stable with time. In this method, the solute which scavenges  $e_{D_2O}^-$ , must fulfill five criteria: (1) it must be an efficient scavenger, (2) the molar absorption coefficient of the reduced species has to be very carefully determined, (3) the spectrum of the reduced species must overlap with that of the  $e_{D_2O}^-$ , (4) the species must be stable at least during the reaction, and (5) its reaction with  $e_{D_2O}^-$  must be stoichiometric and it should not be involved in other reactions during the considered time range. This isosbestic method, particularly in the case of pulse radiolysis experiments, does not require knowledge of the radiolytic yields, the dose deposited in the medium and the concentration of the species involved. In this work, methyl viologen dication (marked as MV<sup>2+</sup>) used as the efficient scavenger of the solvated electron, which has well established molar absorption coefficient and spectrum overlapping with solvated electron in various solvents, is employed in the measurements to determine the extinction coefficient value on the isosbestic point with  $e_{D_2O}^-$ .

Furthermore, the shape of the absorption spectrum of  $e_{D_2O}^-$  can be measured from UV to near infrared (NIR) by streak camera and picosecond pump-probe. Hence, the molar absorption spectra of  $e_{D_2O}^-$  can be established with calibrating with the confirmed molar extinction coefficient values

of  $e_{D_2O}^-$  by isosbestic method.

### 3.3.1 Isosbestic method

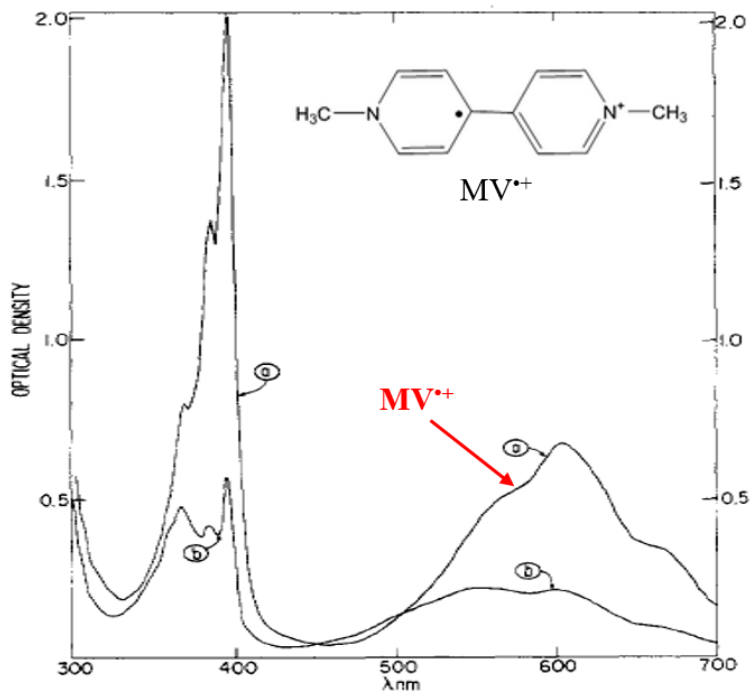
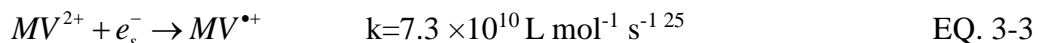


**Figure 3.6** Spectra of  $MV^{\bullet+}$  radical following  $\gamma$  radiation of  $10^{-4}$  M  $MV^{2+}$ , 1% 2-propanol, and 1 % acetone at pH 7.

Methyl viologen dication ( $MV^{2+}$ ) can scavenge the solvated electron.<sup>24</sup> The product of the reaction is the radical of the methyl viologen cation (marked as  $MV^{\bullet+}$ ), which has a long life time and strong absorption both in UV and visible region.



The absorbed spectra of  $MV^{\bullet+}$  in  $H_2O$  has already been presented by J. L cotter and M. S. Matheson (**Figure 3.6**), respectively. In 1982, the work done by K. Honda *et al*<sup>26</sup> provided the molar extinction coefficient values of  $MV^{\bullet+}$  at three peak wavelengths (257, 396 and 606 nm). To estimate the experimental results carefully, we repeated exactly the same experiment of  $MV^{2+}$  in  $H_2O$  and  $D_2O$  as M. S. Metheson's work to confirm the spectrum of  $MV^{\bullet+}$  in aqueous system. As shown in **Figure 3.7**, the absorption band of  $MV^{\bullet+}$  is not affected by the isotopic change. However, the third maximum of the absorption band in this work is at 603 nm different from Honda's work. We used

the spectrum obtained in this work and the extinction coefficient value presented by K. Honda to process the isosbestic method.

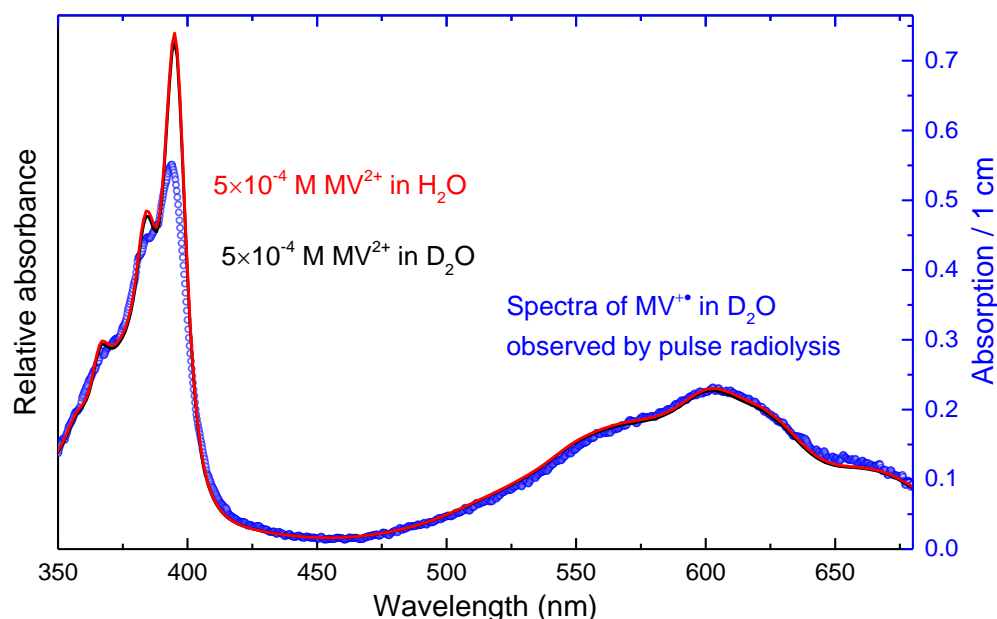
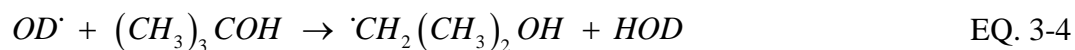


**Figure 3.7 Left axis:** UV-Visible absorption spectra of MV<sup>2+</sup> in two solutions (containing  $5 \times 10^{-4}$  M MV<sup>2+</sup>, 0.2 M isopropanol and 2% acetone in H<sub>2</sub>O and D<sub>2</sub>O, respectively) after irradiation with  $\gamma$  source. Isopropanol was used to scavenge hydroxyl radical and Acetone was used to slow down the reduction of MV<sup>2+</sup>. The dose is 600 Gy. **Right axis:** The spectra of MV<sup>2+</sup> detected by streak camera for a D<sub>2</sub>O sample containing  $5.5 \times 10^{-4}$  mol L<sup>-1</sup> methyl viologena and 0.5 M tert-butanol (to scavenge OD<sup>•</sup>). The dose was 54 Gy per pulse. It is clear that the spectra of MV<sup>2+</sup> in D<sub>2</sub>O observed by streak camera at ELYSE from 400 to 650 nm fits well with that obtained by  $\gamma$  source. The intensity of the absorption band from 350 to 400 nm measured by Streak Camera is lower than that measured by  $\gamma$  source because the resolution of streak camera is not enough high to detect the narrow peak of MV<sup>2+</sup> around 394 nm.

Similarly to the approach previously used for the hydrated electron in water by J-L. Marignier *et al.*,<sup>27</sup> in deuterated solutions containing methyl viologen and tert-butyl alcohol, the kinetics were measured at different wavelengths. To avoid any other competitive reactions, 0.5 mol L<sup>-1</sup> tert-butyl alcohol was added to the solution to scavenge OD<sup>•</sup> radicals:



Assuming that the rate of this reaction in D<sub>2</sub>O is similar to that in H<sub>2</sub>O i.e.  $6 \times 10^8 \text{ L mol}^{-1} \text{ s}^{-1}$  <sup>28</sup> in our conditions, the halftime of the OD<sup>•</sup> scavenging is around 3 ns. In these conditions, the decay of the hydrated electron is only due to the reaction with methyl viologen.

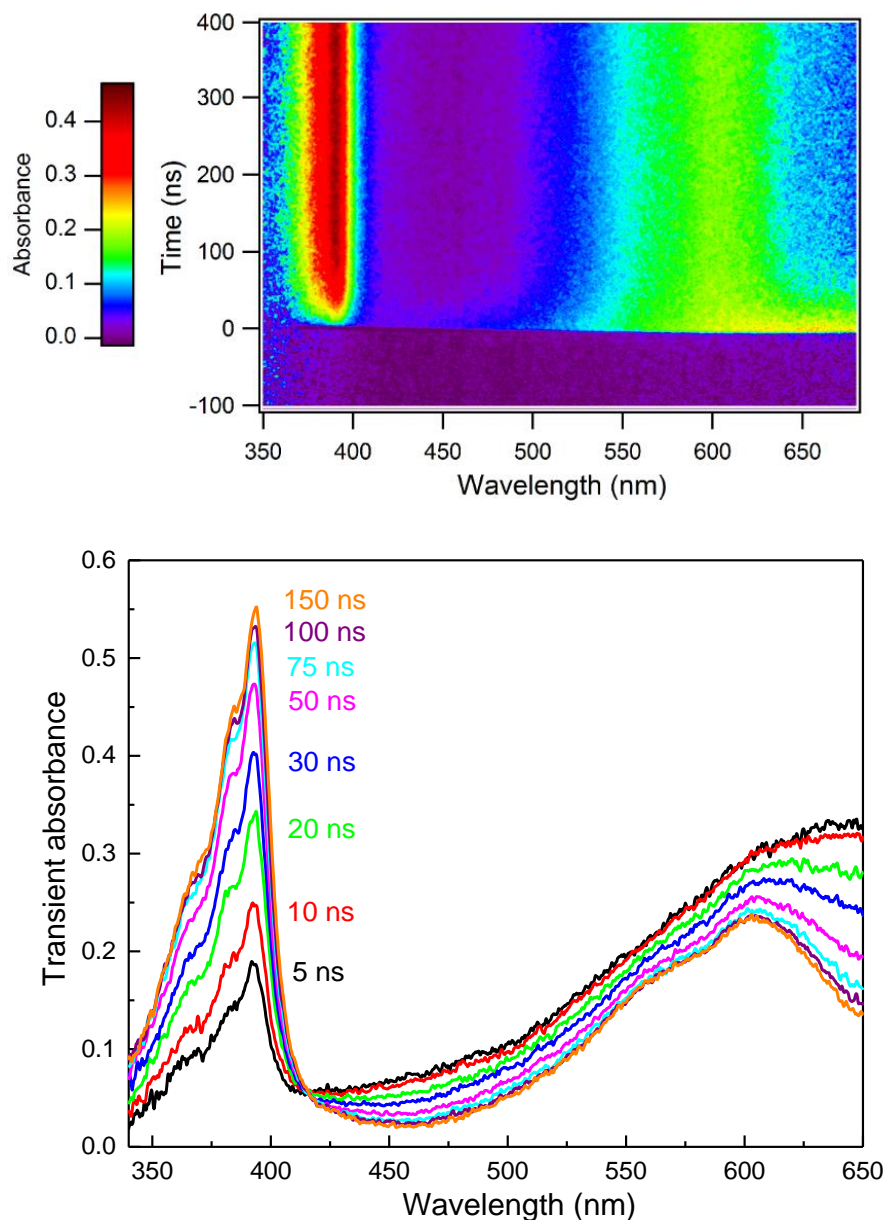


**Figure 3.8** Up: Image obtained by streak camera after electron pulse (dose is 71 Gy per pulse). Bottom: Transient spectra in  $5.5 \times 10^{-4} \text{ mole L}^{-1}$  methyl viologen / D<sub>2</sub>O (Containing 0.5 M tert-butanol to scavenge OH<sup>•</sup>).

In fact, the hydrated electron might exclusively react with MV<sup>2+</sup> that is in large excess ( $5.5 \times 10^{-4} \text{ mol L}^{-1}$ ) while the concentration of the hydrated electron is only few  $10^{-5} \text{ mol L}^{-1}$  compared to the

concentration of the hydrated electron of a few  $10^{-5}$  mol L $^{-1}$  only. The reduction of  $MV^{2+}$  by hydrogen atom (with a concentration per pulse 4.5 times lower than that of the hydrated electron, the rate constant of this reaction is  $6.0 \times 10^8$  L mol $^{-1}$  s $^{-1}$  in H $_2$ O) as well as by the radical of tert-butyl alcohol (with almost the same concentration per pulse than hydrated electron) can occur but only at longer time (The rate constant of  $MV^{2+}$  and tert-butyl alcohol in H $_2$ O is  $1 \times 10^7$  L mol $^{-1}$  s $^{-1}$ ).<sup>29</sup>

However, these reduction reactions are negligible during the reduction of  $MV^{2+}$  by the hydrated electron. Therefore, as recently reported by Marignier *et al.*<sup>27</sup> the radical of the methyl viologen with well-known absorption spectra is used to calibrate the extinction coefficient of the hydrated electron in D $_2$ O. The time dependence of the absorption spectra is presented in **Figure 3.8**. The global data analysis of the matrix of data up to 200 ns and 500 ns shows that only two species are involved in the transient absorption, the hydrated electron and the radical of methyl viologen (**Figure 3.9**).

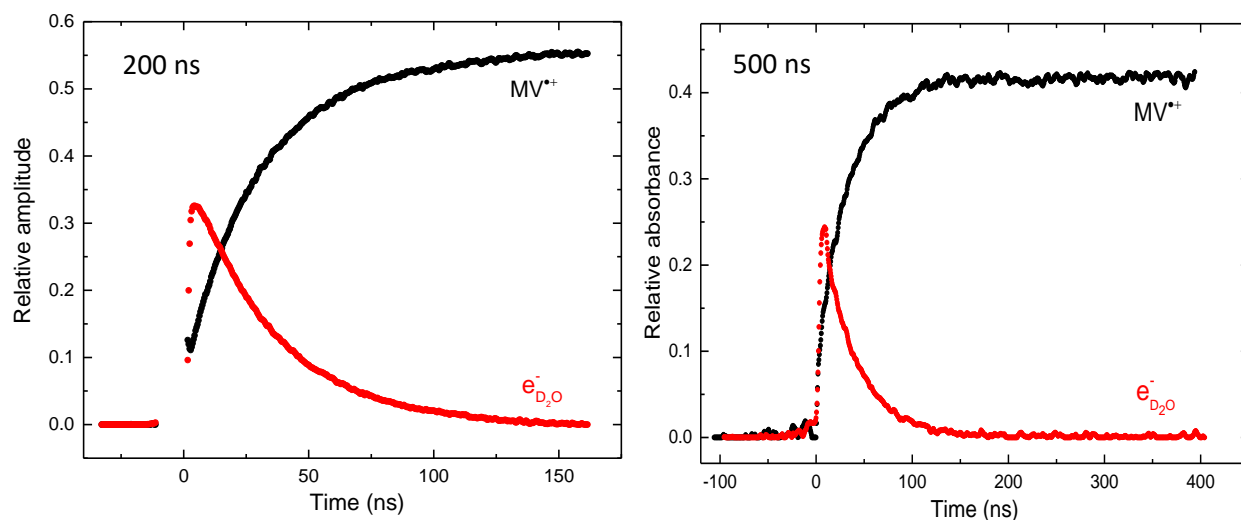


**Figure 3.9** The kinetics of the species involved in the transient absorption analyzed by MCR-ALS with the matrix of the time-resolved measurements. The left is the matrix measured within 200 ns and the right within 500 ns.

As an example, three kinetics are reported within 150 ns in **Figure 3.10**. During the first 100 ns the signal is stable at 415 nm while decreasing at 420 nm and increasing at 408 nm, respectively. The increase of the absorbance at 410 nm and the decrease at 420 nm show that the absorption coefficient of  $e_{D_2O}^-$  at 410 nm is lower and at 420 nm is higher than that of  $MV^{2+}$ . It is clear that



415 nm constitutes an isosbestic wavelength, consequently the molar absorption coefficient of the hydrated electron in deuterated water is the same than that of the  $MV^{++}$  at 415 nm. The molar absorption coefficient spectrum of  $MV^{++}$  with a maximum of  $13700 \pm 300 \text{ L mol}^{-1} \text{ cm}^{-1}$  at 606 nm in  $H_2O$ , has been investigated by Watanabe and Honda.<sup>26</sup> According to their work, we calibrated the measured spectra recorded after 100 ns, and we evaluated that the molar absorption coefficient of hydrated electron in deuterated water at 415 nm is  $3000 \pm 200 \text{ L mol}^{-1} \text{ cm}^{-1}$ .

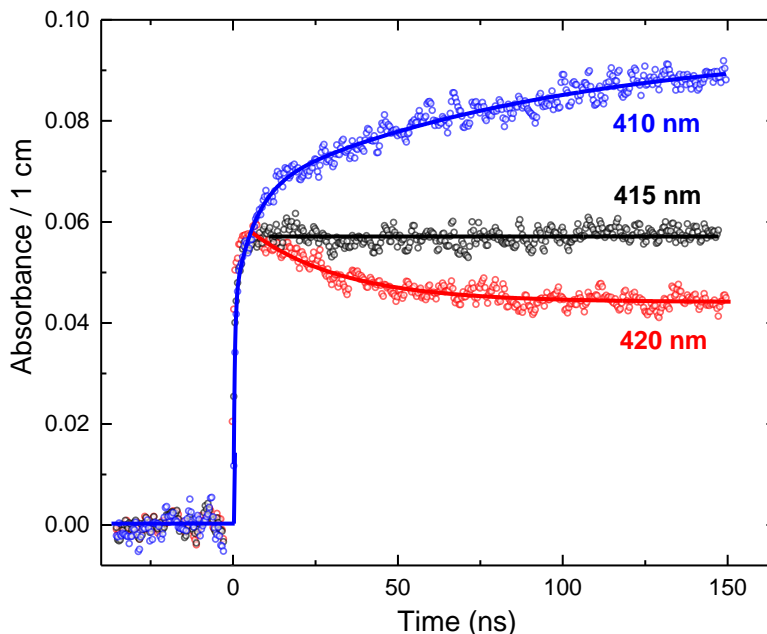


**Figure 3.10** Kinetics at 408, 413 and 420 nm in  $5.5 \times 10^{-4} \text{ mol L}^{-1}$  methyl viologen /  $D_2O$  (Containing 0.5 M tert-butanol to scavenge  $OH^\bullet$ ) (Dose=71 Gy).

### 3.3..2 Absorption spectrum of $e_{D_2O}^-$

To complete the absorption spectra of  $e_{D_2O}^-$ , the experiments were performed in three parts: UV, Visible and NIR. In the UV region ( $\lambda < 400 \text{ nm}$ ), not only  $e_{D_2O}^-$ , but also  $OD^\bullet$ ,  $D^\bullet$  are absorbing, and the absorbance of these species are commensurable compared with  $e_{D_2O}^-$ . So we need to evaluate the effect of  $OD^\bullet$  and  $D^\bullet$  to obtain the absorbed spectrum of  $e_{D_2O}^-$ . In visible and NIR,  $e_{D_2O}^-$  is the only species which has strong absorption in  $D_2O$ , hence the absorbed spectra can be achieved by picosecond pump-probe.

## I. UV region

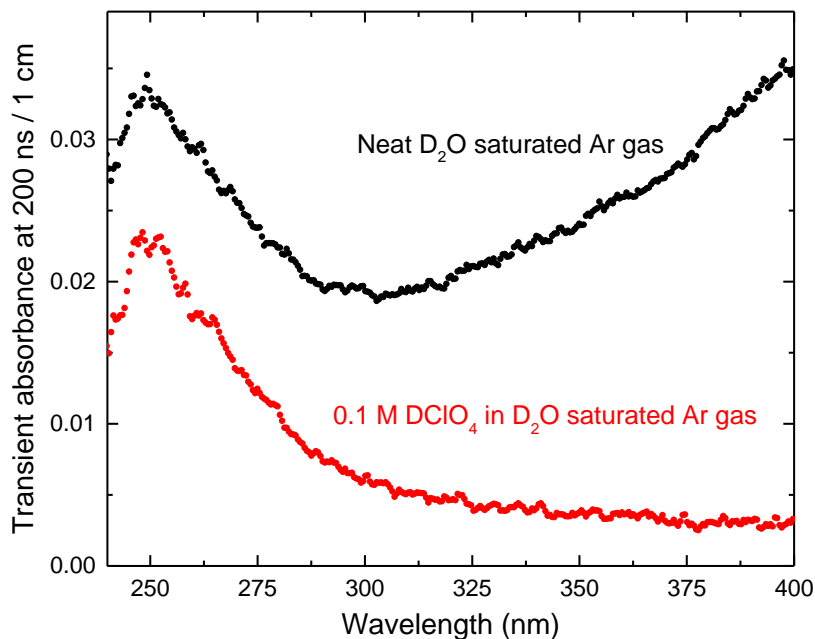
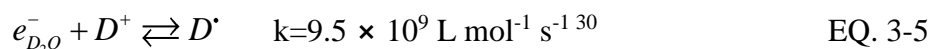


**Figure 3.11** Transient spectra in neat D<sub>2</sub>O and 0.1 M DClO<sub>4</sub> in D<sub>2</sub>O (both saturated with Ar gas) at 200 ns. The dosimetry is 48 Gy per pulse.

To obtain the absorption band of the hydrated electron between 250 to 400 nm, the contribution of OD<sup>•</sup> absorbing between 200 and 350 nm should be removed. In the same condition of dose, two solutions, neat D<sub>2</sub>O (saturated with Ar gas) and 0.1 mol L<sup>-1</sup> DClO<sub>4</sub> in D<sub>2</sub>O (saturated with Ar gas) were used to obtain the spectra shape of  $e_{D_2O}^-$ .

In the solution containing 0.1 mol L<sup>-1</sup> DClO<sub>4</sub> in D<sub>2</sub>O,  $e_{D_2O}^-$  reacts with D<sup>+</sup>, forming D<sup>•</sup> radical which absorbs in the region of  $\lambda < 250$  nm,<sup>20</sup> the reaction can be written as :



In this condition, the half time of the reaction above is less than 1 ns. All  $e_{D_2O}^-$  have been converted into D<sup>•</sup> in the observed time scale. Then only OD<sup>•</sup> is absorbing in the region detected by streak camera. In neat D<sub>2</sub>O, the transient absorbance contains the contribution of both  $e_{D_2O}^-$  and OD<sup>•</sup>. We assumed that OD<sup>•</sup> has the same decay in the two systems (**Figure 3.11**). In this case, at a given

wavelength and time in neutral and acidic solution, by measuring the transient absorption with streak camera we obtain:

$$A_{neutral}(\lambda, t) = D \times l \times \left[ \varepsilon_{e_{D_2O}^-} G_{e_{D_2O}^-}(t) + \varepsilon_{OD\cdot} G_{OD\cdot}(t) \right] \times \rho \quad \text{EQ. 3-6}$$

$$A_{acid}(\lambda, t) = D \times l \times \varepsilon_{OD\cdot} \times G_{OD\cdot}(t) \times \rho \quad \text{EQ. 3-7}$$

From the difference of these two absorbance the extinction coefficient shape of the  $e_{D_2O}^-$  can be deduced as shown in **Figure 3.12**.

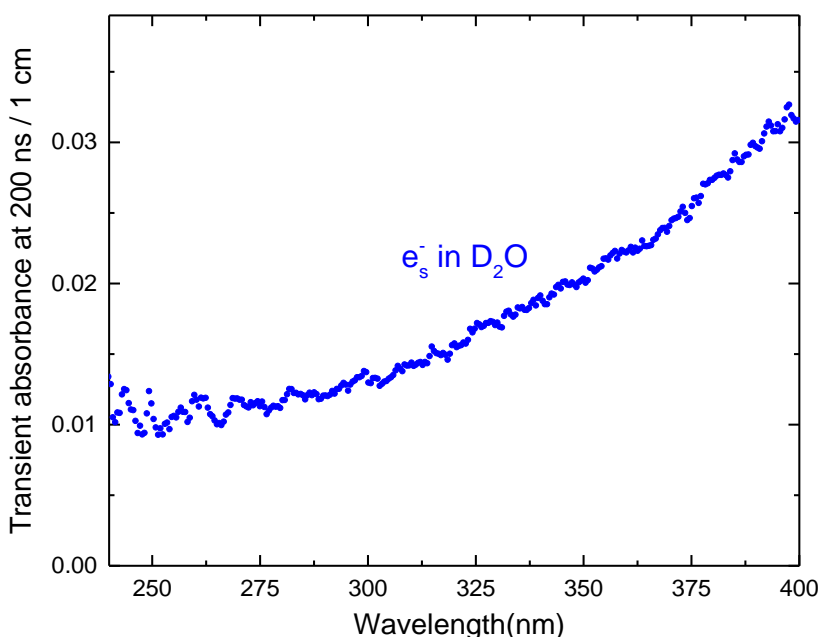


**Figure 3.12** Transient spectra of  $e_s^-$  in  $D_2O$  at 200 ns after subtracting the contribution of  $OD\cdot$  radical.

## II. Visible and NIR region

For the wavelength range from 400 nm to 1500 nm, as only  $e_{D_2O}^-$  is absorbing, the direct measurements by streak camera and pulse-probe detections gave the shape of the absorption band (**Figure 3.13**). With all the measurements above, it is possible to normalize the spectrum with the  $\varepsilon_{e_{D_2O}^-}$  value at 413 nm determined by the isosbestic point. Finally, the calibration of the extinction coefficient spectrum of  $e_{D_2O}^-$  in  $D_2O$  from 250 to 1500 nm is obtained as shown in **Figure 3.14**.

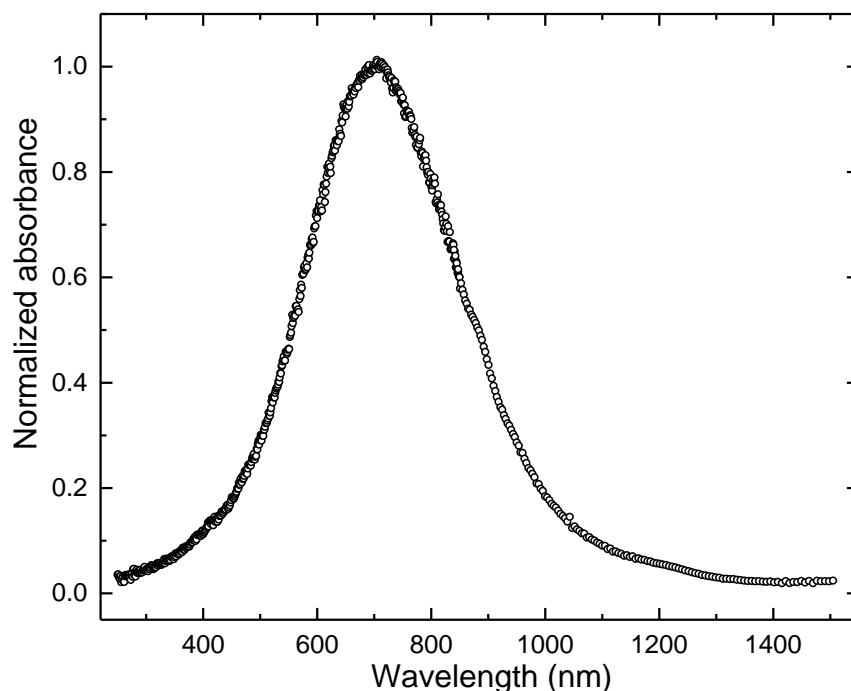


**Figure 3.13** Absorption spectra of  $e_s^-$  in neat  $D_2O$ . The solid line is a guide to the eyes.

The maximum of the absorption band of the hydrated electron is found at 705 nm with the extinction coefficient of  $22900 \pm 400 \text{ L mol}^{-1} \text{ cm}^{-1}$ . The Appendix Table at the end of this chapter reports the numerical value for the absorption band of  $e_{D_2O}^-$  from this work. Note that contrary to the present case, in the case of hydrated electron in  $H_2O$  by using  $MV^{2+}$  as scavenger three isosbestic points were found. The reason is that the value of the extinction coefficient of the solvated electron in  $D_2O$  is higher than that of the hydrated electron in water, which was recently determined to be  $19700 \pm 400 \text{ L mol}^{-1} \text{ cm}^{-1}$  at 713 nm.<sup>27</sup>

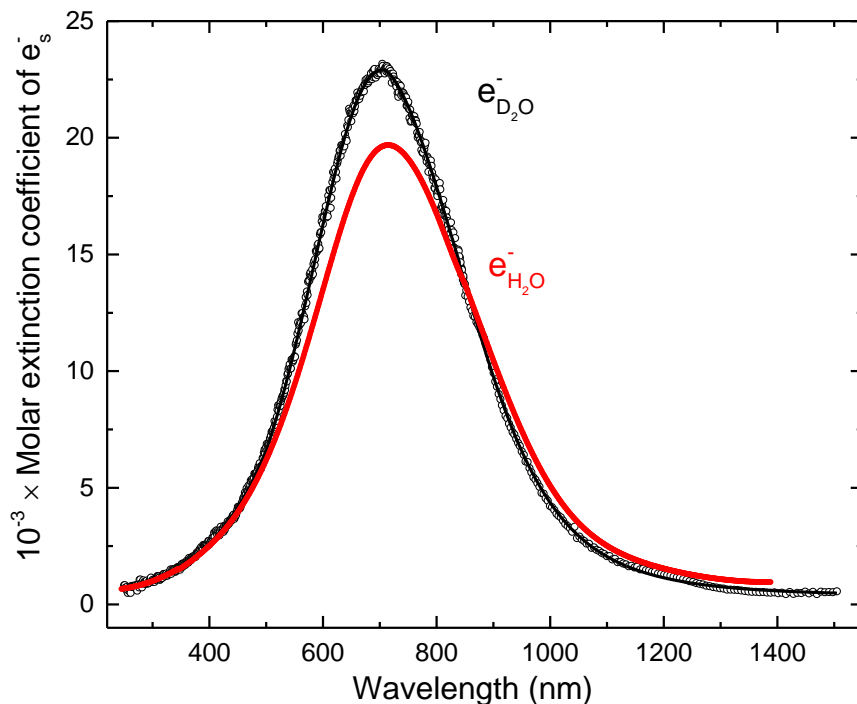


**Figure 3.14** Molar absorption coefficient spectra of solvated electron in  $H_2O$  and  $D_2O$ , respectively. For  $e_{H_2O}^-$ , the extinction coefficient value from 250 to 850 nm is from Ref <sup>27</sup>, the rest was done by this work. For  $e_{D_2O}^-$ , the black solid line is guide to eye, and the numeric value is in appendix at end of this chapter.

**Table 3.3** presented the extinction coefficient values on selected wavelengths from UV to near infrared region between  $e_{D_2O}^-$  and  $e_{H_2O}^-$ . It can be concluded that the intensity of the absorption of  $e_{D_2O}^-$  is larger than that of  $e_{H_2O}^-$  at the maximum of the absorption, then falls lower when increasing wavelength. Moreover, the absorbed band of  $e_{D_2O}^-$  shifts to blue when compared with  $e_{H_2O}^-$ .

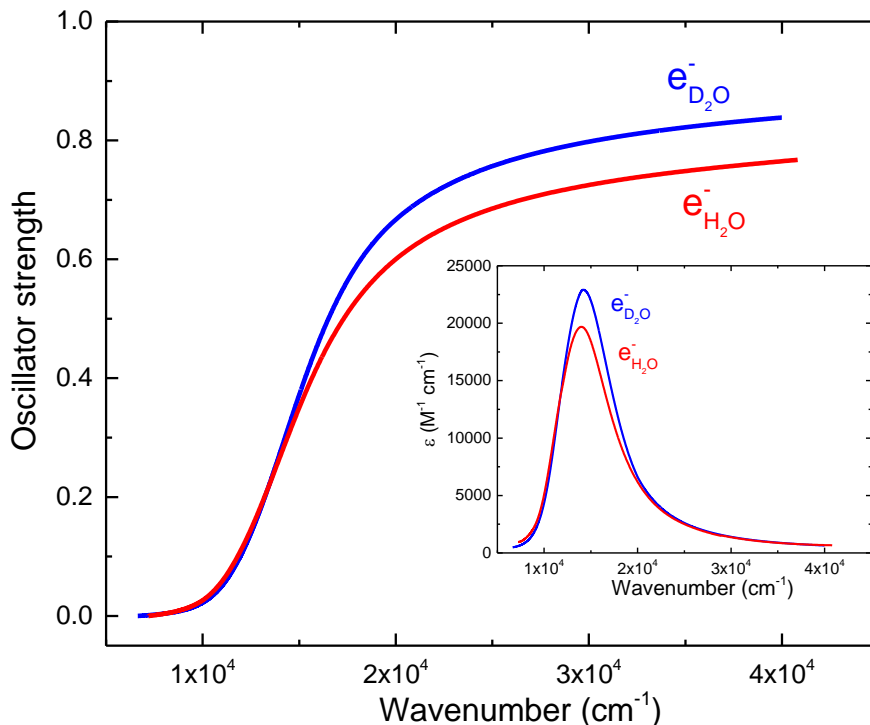


**Figure 3.15** The **oscillator** strength of the solvated electron in H<sub>2</sub>O and D<sub>2</sub>O as the function of the wavenumber. The inset is the molar absorption coefficient of the solvated electron in H<sub>2</sub>O and D<sub>2</sub>O on wavenumber.

Oscillator strength is a dimensionless quantity that expresses the probability of absorption or emission of electromagnetic radiation in transitions between energy levels of an atom or molecule. It is of transition that could be expressed as:

$$f = 4.319 \times 10^{-9} \times \int_{band} \varepsilon(\nu) d\nu \quad \text{EQ. 3-8}$$

Where  $\varepsilon(\nu)$  is the molar extinction coefficient in  $\text{M}^{-1} \text{cm}^{-1}$ , and  $\nu$  is the wave number in  $\text{cm}^{-1}$ . With EQ. 3-8, we found that the oscillator strength is larger in D<sub>2</sub>O than in H<sub>2</sub>O. The oscillator strength of the absorption band of the hydrated electron at room temperature in H<sub>2</sub>O was reported to be 0.75<sup>15</sup> and later 0.85<sup>31</sup>. The value of the oscillator strength in D<sub>2</sub>O estimated by Jou *et al.*<sup>15</sup> is almost the same as in H<sub>2</sub>O. The experimental data reported in **Figure 3.15** give the value of 0.76 (according to the recent extinction coefficient value in H<sub>2</sub>O)<sup>27</sup> and 0.83 for D<sub>2</sub>O (from the present work). It is important to note that the values obtained here took into account the UV component of the absorption band only up to  $4 \times 10^4 \text{ cm}^{-1}$  (250 nm). Therefore, the oscillator strength can be slightly larger than our value.

**Table 3.3** Comparison of the molar extinction coefficient of solvated electron in H<sub>2</sub>O and D<sub>2</sub>O at various wavelength, respectively.

$\lambda$ (nm) \ Species	$\varepsilon(e_{H_2O}^-)$ (M <sup>-1</sup> cm <sup>-1</sup> ) <sup>27</sup>	$\varepsilon(e_{D_2O}^-)$ (M <sup>-1</sup> cm <sup>-1</sup> )
260	723	707
400	2510	2611
500	6183	6653
600	13482	16270
705 (maximum)	19634	22900
713 (maximum)	19687	22851
800	16749	17894
900	10460	9845
1000	5085	4558
1100	2512	2053
1200	1538	1145
1300	1082	758

### 3.3.3 Determination of the time-dependent yield of $e_{D_2O}^-$

The kinetics measured at 600 nm in neat H<sub>2</sub>O and neat D<sub>2</sub>O are reported in **Figure 3.16**. The measured absorbance of solvated electron at 600 nm in D<sub>2</sub>O is  $1.20 \pm 0.01$  times larger than that in H<sub>2</sub>O. The difference can be either due to the extinction coefficient or due to the radiolytic yield. The kinetics within the first 500 ps superimposed by normalization show that there is no important isotopic effect on the decay of solvated electron within 500 ps (**Figure 3.16 inset**). The decay is almost same within the first 500 ps.

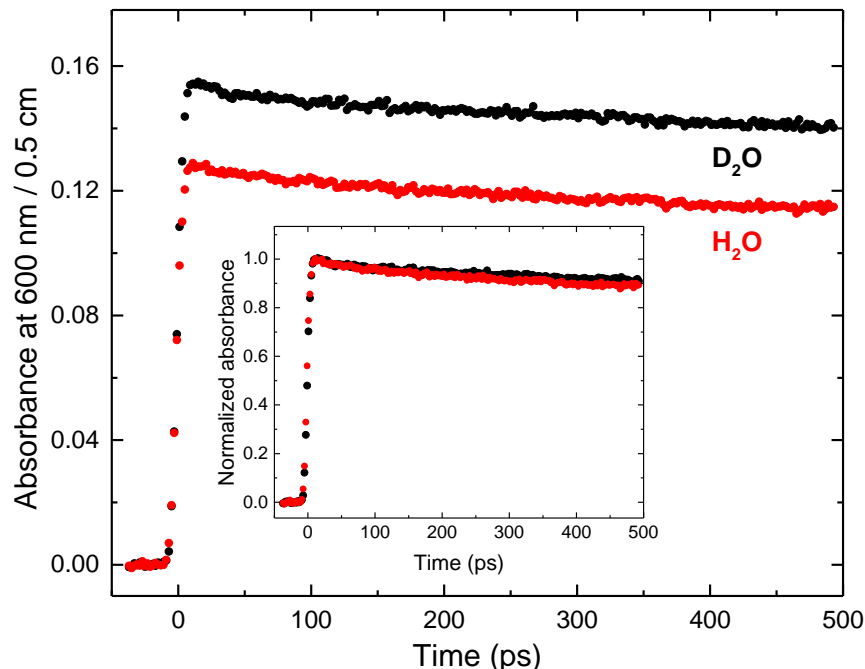


**Figure 3.16** Kinetics of  $e_s^-$  at 600 nm in neat water and neat deuterated water (Dose per pulse is 42.5 Gy). Inset: the normalized kinetics in  $H_2O$  and  $D_2O$ .

With the ratio of determined  $\mathcal{E}$  value of  $e_s^-$  in  $H_2O$ <sup>27</sup> and  $D_2O$  in this work (according to **Figure 3.14**,  $\mathcal{E}_{\lambda=600nm}^{e_{D_2O}^-} / \mathcal{E}_{\lambda=600nm}^{e_{H_2O}^-} \approx 1.20$ ), it is found that the initial yield of  $e_{D_2O}^-$  within the experimental error, is the same as in  $H_2O$ . Using the established G value of  $e_s^-$  in  $H_2O$   $G_{10ps} = (4.5 \pm 0.1) \times 10^{-7}$  mol J<sup>-1</sup>,<sup>32</sup> the yield of  $e_{D_2O}^-$  at 10 ps is found to be  $(4.5 \pm 0.1) \times 10^{-7}$  mol J<sup>-1</sup>. In contrast, the yield of  $e_{D_2O}^-$  is decreasing slower on the nanosecond scale than that of hydrated electron in  $H_2O$  (**Figure 3.17**) due to the higher viscosity of  $D_2O$ . To conclude about the time dependent radiolytic yield of  $e_{D_2O}^-$ , it is essential to check the effect of the dose per pulse on the kinetics of  $e_{D_2O}^-$ .



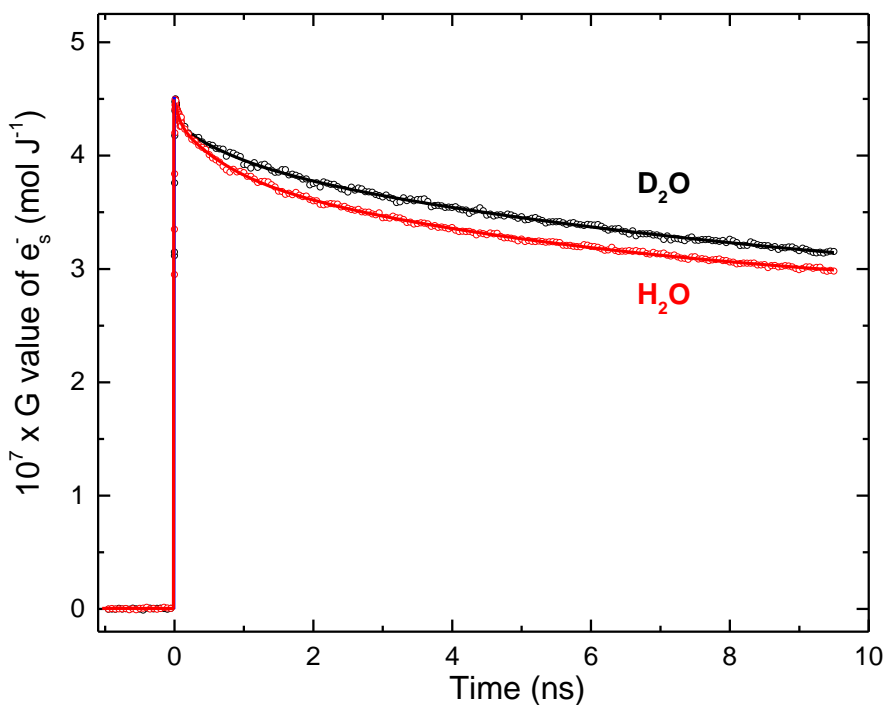


**Figure 3.17** Time dependent yield of the solvated electron in neat  $D_2O$  and neat  $H_2O$ .

It is worth noting that the dose per pulse can have an effect on the time dependent yield of solvated electron. In 1975, J E. Fanning gave the most cited results about the accelerated decline of the solvated electron from 40 ns to 1  $\mu s$ .<sup>33</sup> The decay of the hydrated electron which accelerates beyond a few tens of nanoseconds has been interpreted by Trumbore *et al.* as an effect of the dose per pulse described essentially in terms of density, diffusion and cluster overlap.<sup>34,35</sup> These authors developed a model based on the classical kinetic diffusion model applied to radiation chemistry in which they modified the probability function of the hydrated electron distribution and added terms describing the cluster overlap. The simulations of the decay of the solvated electron concentration were performed for doses of 0.5, 1.0, 3.1, 7.8, 24 and 79 Gy. Recently F.Torche<sup>36</sup> performed the same experiments with a dose rate of 26.3 Gy in ELYSE and the result was superimposed in the **Figure 3.18**. It is found that in relation to the calculated curve by Trumbore<sup>34,35</sup> and with respect to the experimental points given by Fanning, the curve measured by Torche showed a faster decay of the solvated electron. The difference is due to the higher dose rate in ELYSE.

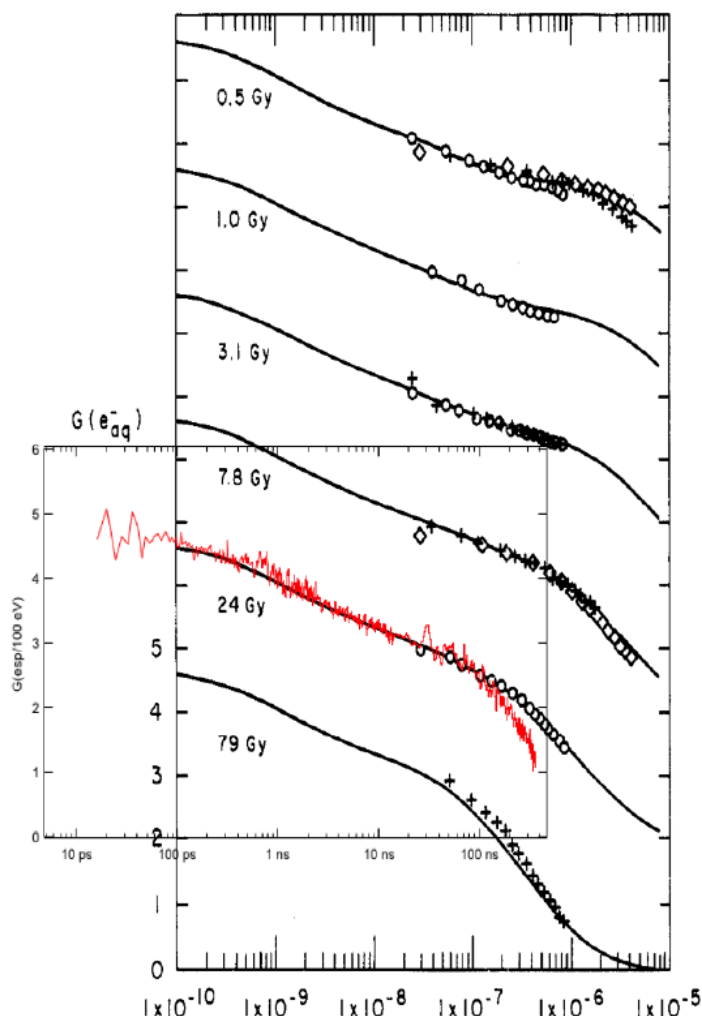


**Figure 3.18** Dosimetry effect on the time dependent decay of  $e_s^-$  in  $H_2O$ . Points are experimental results of Fanning.<sup>33</sup> Solid line in black compared to calculated result by Trumbore *et al.*<sup>34</sup> Solid line in red reports the work of Torche *et al.*<sup>36</sup>

To study the dose effect on the decay of solvated electron in  $D_2O$ , the experiments were performed up to 5  $\mu s$  in neat  $D_2O$  saturated with Ar gas under 3.2 and 55 Gy, respectively. As shown in the **Figure 3.19**, the variation in the yield of the electron is independent of the dose rate and the density of the solvated electron. However, the effect of the dose rate became more obvious after 10 ns. The decay of  $e_s^-$  in  $D_2O$  under 55 Gy was faster than that under 3.2 Gy beyond 10 ns. In this work, the time dependent yield of  $e_s^-$  in  $D_2O$  is measured up to 10 ns, where it is not affected by the change of dose per pulse. As shown above, the dose effect can be observed at large time scale than 10 ns.

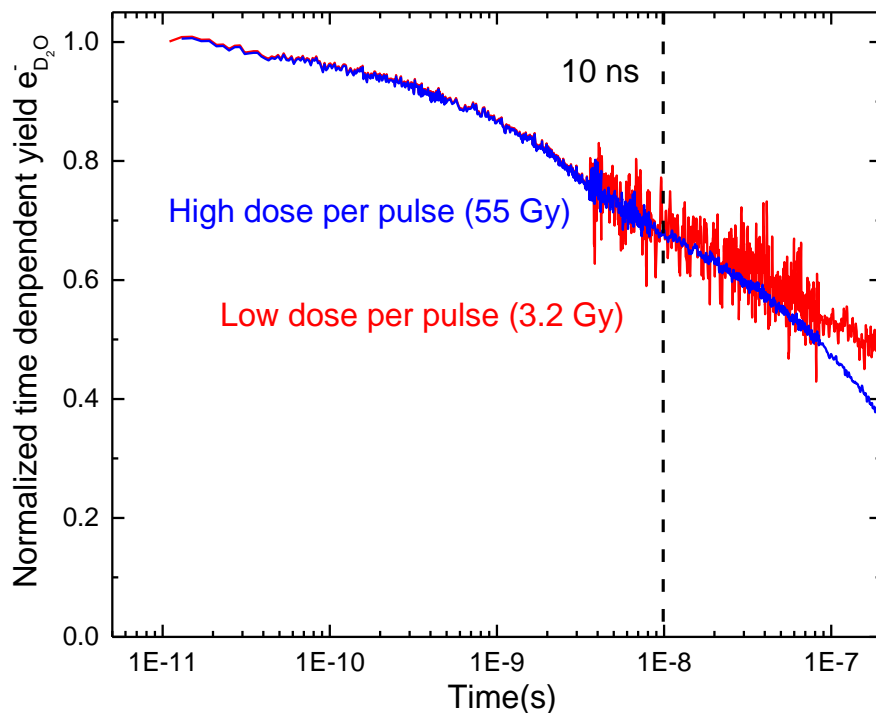


**Figure 3.19** Dosimetry effect on the time dependent decay of  $e_s^-$  in  $D_2O$ .

### 3.4 Time-dependent yield of OD<sup>•</sup> radical

As described in **Figure 3.5**, the region where OD<sup>•</sup> radical absorbs is in UV. The extinction coefficient spectrum has already been reported by S. O. Nielson (210 ~ 260 nm) and G. V. Buxton (220 ~ 320 nm), respectively. Moreover, the results of both of their works are consistent. To obtain the time dependent yield of OD<sup>•</sup> radical, first of all it is essential to find the condition to measure the time dependent decay of OD<sup>•</sup> radical. For this purpose, the measurements were performed at 260 nm by picosecond pump-probe.

The absorption measured at 260 nm in neat  $D_2O$  by picosecond pulse radiolysis is due to three absorption components: the solvated electron, the transient produced in the solid state — the windows of fused silica optical flow cell (marked as FSOFC), and the OD<sup>•</sup> radical. Therefore, the measured absorption can be written as:

$$A_{\lambda=260}^{measured}(t) = A_{\lambda=260}^{e_s^-}(t) + A_{\lambda=260}^{FSOFC}(t) + A_{\lambda=260}^{OD^\bullet}(t) \quad \text{EQ. 3-9}$$

For the contribution of the hydrated electron  $A_{\lambda=260}^{e_{D_2O}^-}(t)$ , it is possible to use the kinetics in the visible part of spectra, for example at 600 nm (**Figure 3.16**). And taking the ratio of the extinction coefficients at 260 and 600 nm into account, the kinetics of the hydrated electron at 260 nm can be determined. Therefore,

$$A_{\lambda=260}^{e_{D_2O}^-}(t) = \frac{A_{\lambda=600}^{e_{D_2O}^-}(t) \times \epsilon_{\lambda=260}^{e_{D_2O}^-}}{\epsilon_{\lambda=600}^{e_{D_2O}^-}} \quad \text{EQ. 3-10}$$

For the purpose of deducing the transient absorption of OD<sup>•</sup> at 260 nm, the absorption due to FSOFC also needs to be confirmed and then subtracted in first approximation from EQ. 3-9.

### 3.4.1 Transient absorption induced in FSOFC

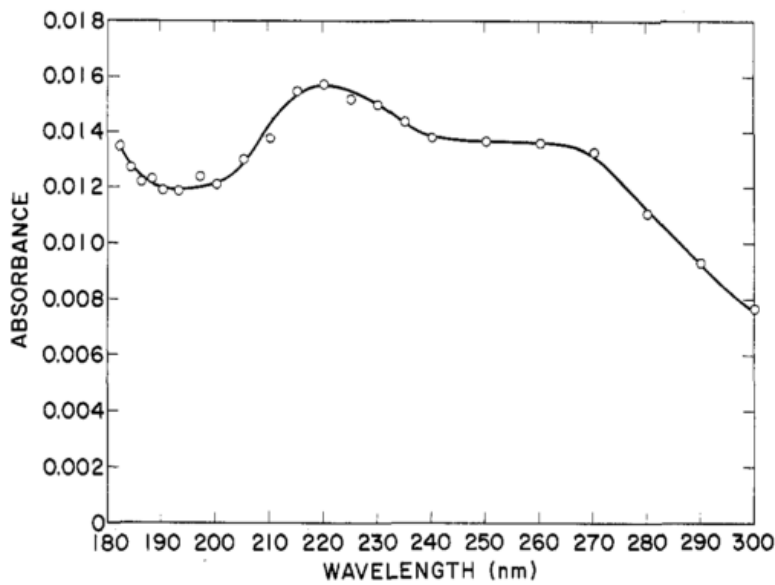


**Figure 3.20** Transient absorption spectra in irradiated Suprasil sample of 1 mm thickness. Measured immediately after 3  $\mu$ s electron pulse by Nielson *et al.*<sup>20</sup> Dose per pulse is 240 Gy per pulse.

In 1950s, the coloration of the fused silica after irradiation was reported by several works. The nature of the corresponding absorption bands is studied from then on.<sup>37-40</sup> On 1976, the transient absorbed spectrum in fused silica from 180 to 300 nm was measured by Nielsen *et al.*<sup>20</sup> (**Figure 3.20**). The spectrum was found to be scaled in proportion to the dose and Suprasil path length. In order to determine correctly the ultraviolet absorption spectra of  $e_s^-$ , OH<sup>•</sup>, H<sup>•</sup>, OD<sup>•</sup> and D<sup>•</sup>, the

contribution induced by the fused silica cell is necessary to be subtracted.

In 2006, Janata reported the transient absorption in fused silica induced by 3.8 MeV electron pulses using a 2 ns electron accelerator. He observed the main absorption was in the UV more than the visible.<sup>41</sup> The absorption bands with varying decay kinetics indicated that different color centers or lattice defects were formed (**Figure 3.21**).

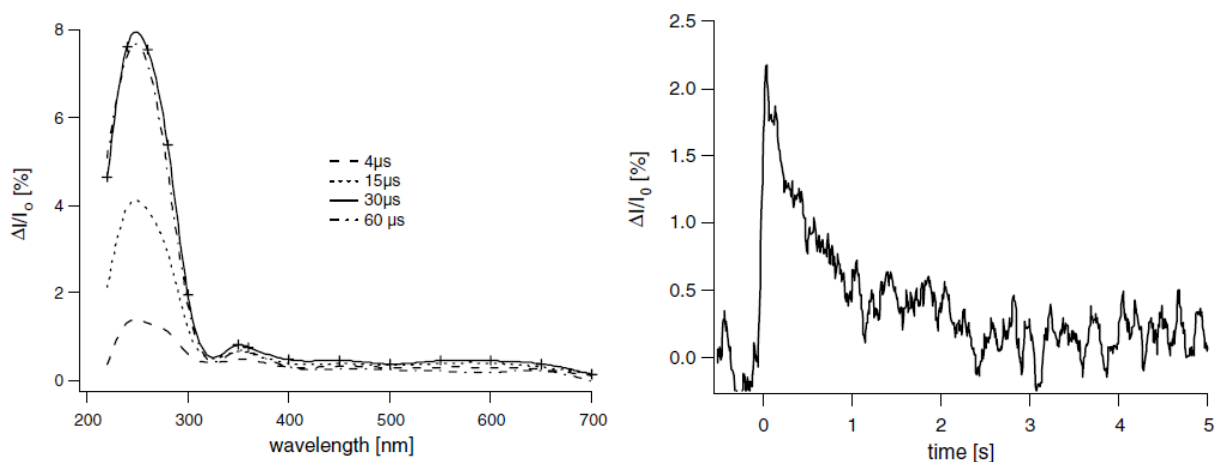


**Figure 3.21** Transient absorbed spectra at various time after the beginning of irradiation (Left) and long-time decay of absorption at 260 nm (Right) in fused silica by E. Janata.<sup>41</sup>

In ELYSE, a FSOFC with two fused silica windows, each 1 mm thick, plane-parallel to each other and at a distance of 5 mm corresponding to the cell was used in experiment in the early time. Schmidhammer *et al.* performed the measurements in the empty FSOFC carefully and presented the transient absorbed spectrum of FSOFC recorded at 50 ps after irradiated by picosecond electron pulse in ELYSE.<sup>42</sup> As demonstrated in **Figure 3.22**, at least two absorbed bands (around 260 nm and around 590 nm) can be concluded. The ratio of the transient absorption measured directly in the empty FSOFC between 260 and 590 nm (the ratio is 4) is very close to that presented by Janata at 4  $\mu$ s.

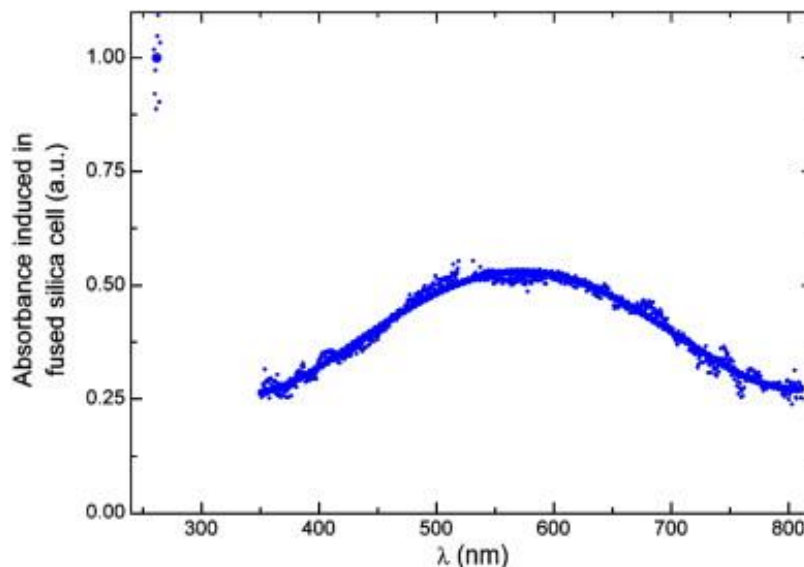


**Figure 3.22** Transient absorbed spectra normalized at 260 nm in fused silica recorded at 50 ps after excited by electron pulse.<sup>42</sup>

To eliminate the effect of the contribution due to FSOFC, two thinner windows were made in the windows of FSOFC (As shown in **Figure 3.23 bottom**), and the thickness of the window of FSOFC was shortened 5 times to 200  $\mu\text{m}$ . However, the contribution of the new FSOFC is still comparable with the total absorbance in  $\text{D}_2\text{O}$  at 260 nm. The absorption induced by FSOFC should be removed from the measured absorbance at 260 nm. Besides, this procedure that measures the transient absorption of FSOFC could not be strictly valid and could depend on the experimental conditions, as the electron beam is scattered not only by the thin aluminum mirror and the first optical window of FSOFC but also by the solution (**Figure 3.23**). Consequently, the electron beam scattering reduces the dose received by the second window. Therefore, the contribution of the transient produced in the solid state (marked as  $A_{\lambda=260}^{\text{FSOFC}}(t)$ ), is higher for an empty cell than for a cell full of water. The difference between the absorbance depends on the optical path length.

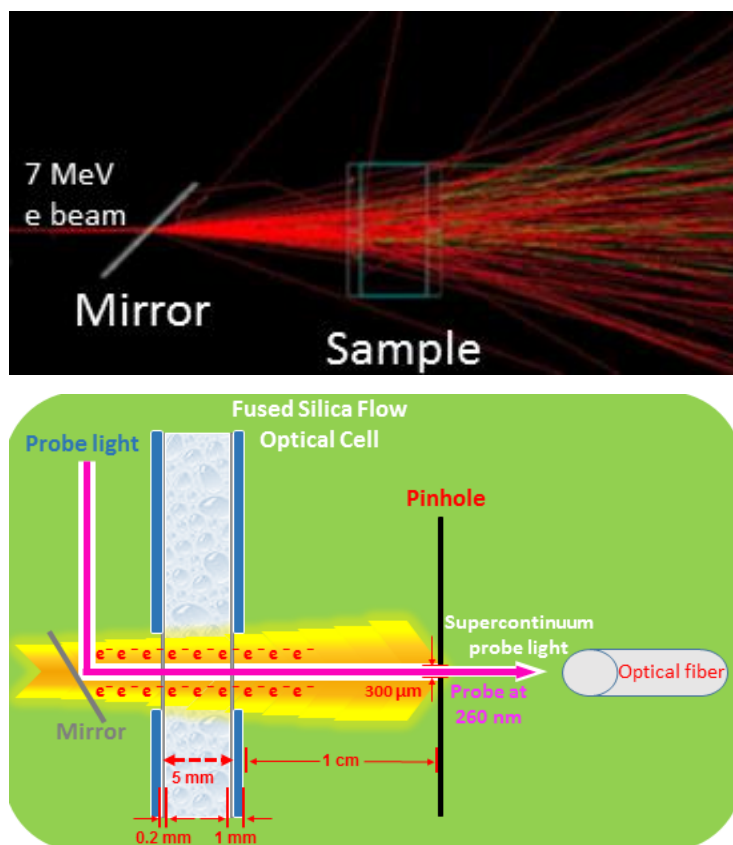


**Figure 3.23** Top: Simulations of electron beam propagation and its scattering by the mirror, air, cell windows and the sample. Bottom: Scheme of the setup for measuring the yield of  $OD^\bullet$  at 260 nm by insuring that the supercontinuum probe light and 260 nm probe the same irradiated volume. For that purpose, a pinhole with 300  $\mu\text{m}$  diameter is placed 1 cm after the sample.

**Figure 3.23** shows the experimental configuration of pump and probe beams (bottom) and in particular the electron beam propagation (top). The latter was simulated by EGSnrc (electron gamma shower by national research council Canada) code and considers the electron scattering by the mirror located just after the exit of the accelerator line, by air, by the windows of optical cell and also by the sample. For the precise quantitative determination of the different transient contributions, the probe beams have to measure the same irradiated volume in the optical cell. If the probe beam at 260 nm and the supercontinuum (for example at 600 nm, the wavelength used for measuring the dose per pulse/ the solvated electron concentration) are not probing the same volume of the sample, a dose difference could occur and the value of the yield of the radical  $OD^\bullet$  could be affected. As the diameter and the position of the probe beams at 260 nm and 600 nm are not necessarily exactly the same, a pinhole is positioned with a diameter of 300  $\mu\text{m}$  located just

after the sample and before the detection system (**Figure 3.23** Bottom). The pinhole ensured that the same irradiated volume of the sample would be probed and in consequence that there would be the identical dose per pulse for probing at 600 and 260 nm. Due to the attenuation of probe beam intensities by the pinhole, the acquisition time had to be increased in order to maintain a low noise level, which is necessary to detect the transient signals on the low mOD level.

To gain better understanding of the effect of the scattering of the electron, we performed experiments in the empty optical cell and a fused silica plate with a thickness of 200  $\mu\text{m}$ . For the same dose per pulse, the kinetics were recorded in empty optical cell ( $A_{\lambda=260}^{FSOFC}(t)$ ) and also in a fused silica plate of 200  $\mu\text{m}$  (marked as  $A_{\lambda=260}^{200\mu\text{m}/\text{Fused silica}}(t)$ ) placed at the same position with the entrance window of FSOFC (as demonstrated in **Figure 3.24**).

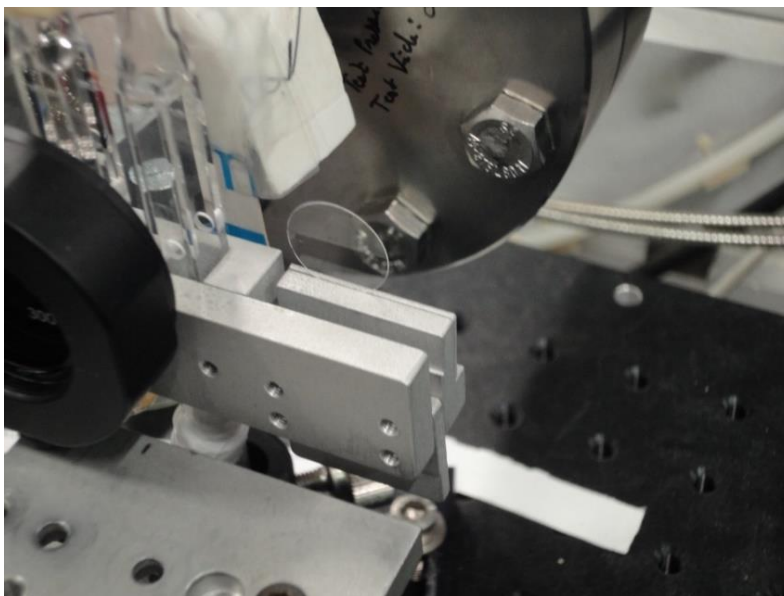


**Figure 3.24** Measurement with an empty FSOFC and a plate of 200  $\mu\text{m}$  under the same condition.

In the same dose condition, the transient absorbance induced in the windows of the empty optical cell is not two times higher than that induced in the single fused silica plate of 200  $\mu\text{m}$ . The absorbance induced in the empty optical cell,  $A_{\lambda=260}^{FSOFC}(t)$ , is 1.5 time larger than that in single fused silica plate ( $1.5 \times 10^{-3}$  OD). As the fused silica state was placed in the same position with the entrance of FSOFC, the dose received by the exit window (the second window) is almost two times less than that received by the entrance one (the first window) when the optical cell is empty. When



the FSOFC is full of water, an additional electron beam scattering is present and the dose absorbed by the exit window should be lower than two times.

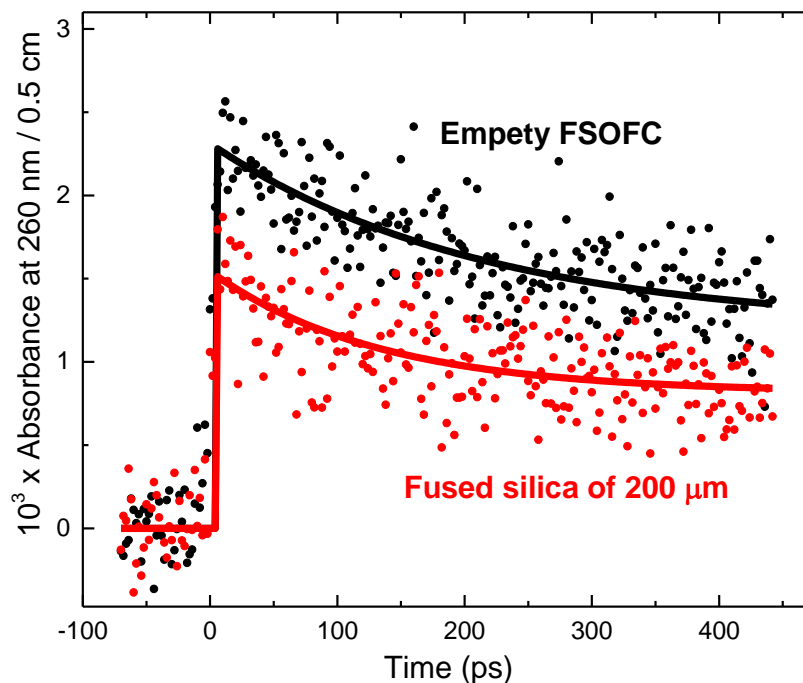


**Figure 3.25** Decays obtained at 260 nm for the same dose (45 Gy per pulse) in the empty fused silica optical flow cell (containing two plate of 200  $\mu\text{m}$  thickness) and in a fused silica plate with 200  $\mu\text{m}$  thickness. The lines serve as guides to the eyes.

In collaboration with Z. Zong at the Institut de Physique Nucléaire d'Orsay, the electron beam scattering by water in the optical cell was estimated by Monte Carlo (MC) simulation with EGSnrc code,<sup>43</sup> which is a general purpose program to simulate the coupled transport of electrons and photons in an arbitrary geometry. Particles with energies above several keV up to hundreds of GeV can be processed in EGSnrc. For easily modeling the geometry, the EGSnrc C++ class library<sup>44</sup> is used to follow the corresponding geometric layout of the experiments. In the simulations, the electron beam exiting from the accelerator is set as a circle shape, and the electron density distribution follows a Gaussian function centered at  $z = 0$ , with a sigma value of 0.1 mm for the radius of the circle. Inside the sample FSOFC, air-filled and water-filled cases were simulated, respectively.

As the dose deposited in the windows of FSOFC is sensitive to the offset from the beam axis (z-axis), the dose scoring regions are set as cylinders centering on the beam axis, with different

radius in the first and the second FSOFC windows. The integral dose as a function of the radius can be obtained as  $D_1(r)$  and  $D_2(r)$  for the entrance and exit windows, respectively. Thus, the ratio of  $\eta(r) = D_1(r)/D_2(r)$  can be directly used to compare with the results measured in the experiments.

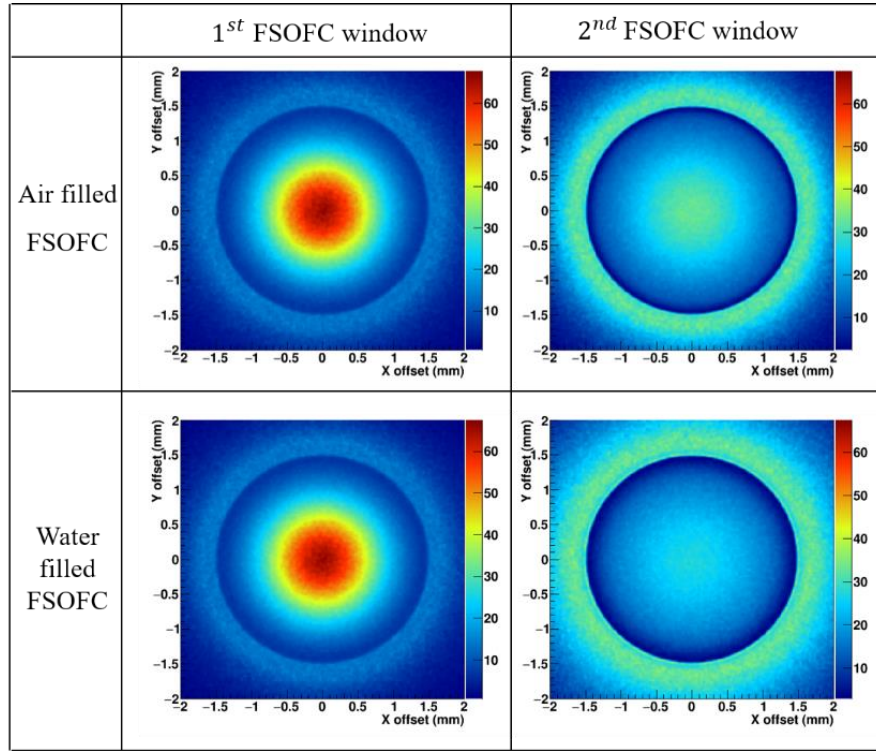


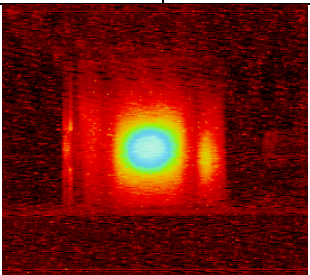
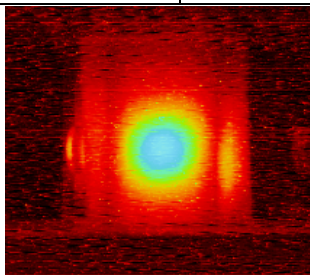
**Figure 3.26** Simulation of the radial dose distribution in 1<sup>st</sup> and 2<sup>nd</sup> window of FSOFC obtained by EGSnrc code for FSOFC filled with air or water. The color presents the dose intensity scale.

**Figure 3.26** shows a dosimetry distribution in both windows of the sample cell filled with air and water, respectively. The palette displays the relative dose. Due to the scattering in the cell, electrons are more spread outward from the beam axis in the second window than in the first window. As the diameter of the laser probe used in our experiment is around 200 $\mu$ m, the concerned area of  $\eta(r)$  is around  $r = 150 \mu$ m. With air-filled sample cell, the simulation shows a dose ratio  $\eta(r \sim 150\mu\text{m}) \sim 2.0$ , which is in good agreement with the experimental result (**Figure 3.25**). The simulations show that in the presence of water in FSOFC, the dose received by the second window is almost 3 times lower than that received by the first window. It means that the effect of water on the electron beam scattering is not negligible (**Figure 3.26**). Consequently, in EQ.3-8 the value of

the  $A_{\lambda=260}^{FSOFC}(t)$  can be estimated by using the experimental value at 260 nm obtained in plate of 200  $\mu\text{m}$   $A_{\lambda=260}^{200\mu\text{m}/\text{Quartz}}(t)$ , and by using the following equation:

$$A_{\lambda=260}^{FSOFC}(t) \leq \frac{4}{3} A_{\lambda=260}^{200\mu\text{m fused silica}}(t) \quad \text{EQ. 3-11}$$

In addition, the image of electron beam on the surface of the windows was obtained by placing a lanex film (a chromatic film made by KODAK) on the same positions as that of the first and second window. It shows that the size of the beam at the exit windows is  $\sim 1.7$  times larger than that at entrance window (**Figure 3.27**).

	Air filled FSOFC		Water filled FSOFC		The ratio of the electron beam surface on 2 <sup>nd</sup> FSOFC window
	1 <sup>st</sup> FSOFC window	2 <sup>nd</sup> FSOFC window	1 <sup>st</sup> FSOFC window	2 <sup>nd</sup> FSOFC window	
FWHM in the horizon / mm	4.4	4.4	4.4	5.5	1.62
FWHM in the vertical / mm	3.7	4.2	3.7	4.8	
The image of electron beam obtained on the lanex film					

**Figure 3.27** Full width at half maximum in the horizon and vertical of the image of electron beam on the surface of the windows obtained by placing lanex film (Chromatic film made by KODAK) on the same positions on the first and second FSOFC window.

As the absorbed dose is proportional to the irradiated surface, it means that the dose is around 4 time smaller at the exit window than at the entrance one. Therefore, the absorbed dose at the exit window should be between 3 ~ 4 times less according to EGSnrc calculations and beam imaging, respectively. As the signal of the transient induced in the entrance window is already low ( $1.5 \times 10^{-3}$  OD), the contribution of the second one is within the precision ( $\sim 0.001$ ). Therefore, in water filled FSOFC, the value of the dose received by the windows is almost equal to that received by the first window. According to the above consideration, in our condition the absorbance due to the radicals produced in liquid can be found by using the equation:

$$A_{\lambda=260}^{OD^{\bullet}}(t) \approx A_{\lambda=260}^{measured}(t) - A_{\lambda=260}^{200\mu m/Fused\ silica}(t) - \frac{A_{\lambda=600}^{e_{D_2O}^-}(t) \times \epsilon_{\lambda=260}^{e_{D_2O}^-}}{\epsilon_{\lambda=600}^{e_{D_2O}^-}} \quad \text{EQ. 3-12}$$

By taking into account these points — the consideration of the electron beam scattering in the cuvette and a precise positioning and sizing of the two probe beams with a pinhole, it becomes possible to measure precisely the time dependent yield of OD<sup>•</sup> radical.

### 3.4.2 Determination of the time-dependent yield of OD<sup>•</sup> radical

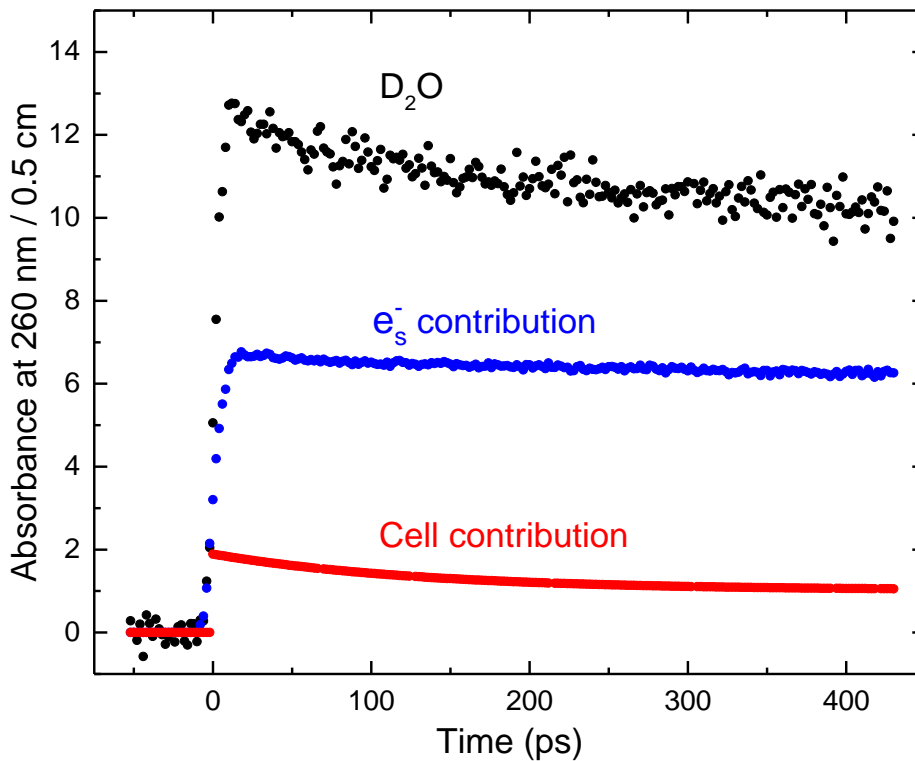


**Figure 3.28** Absorption measured at 260 nm in the FSOFC (with a thickness of 200  $\mu\text{m}$  for each window) containing neat D<sub>2</sub>O. Absorbance due to the species formed in solid state in the windows of the optical cell at 260 nm (according to EQ. 3-10 and the contribution of the solvated electron at 260 nm (according to EQ. 3-9). The dose per pulse is 42.5 Gy.

Concluding all the results above, the contribution due to of  $e_{D_2O}^-$  and the one due to the transient absorption induced in FSOFC were determined and normalized to the same dose condition with the absorbance measured at 260 nm in D<sub>2</sub>O (**Figure 3.28**). After reducing the contribution of

$e_{D_2O}^-$  and FSOFC, and time dependent decay of OD<sup>•</sup> radical is deduced with the extinction coefficient  $\varepsilon_{\lambda=260nm}^{OD^{\bullet}} = 425 M^{-1} cm^{-1}$  from the work of Nielsen and Buxton (**Figure 3.29**) and the dosimetry according to the electron absorption at 600 nm. The yield of OD<sup>•</sup> at 10 ps is almost identical with the value of OH<sup>•</sup>  $(5.0 \pm 0.2) \times 10^{-7} \text{ mol J}^{-1}$ .

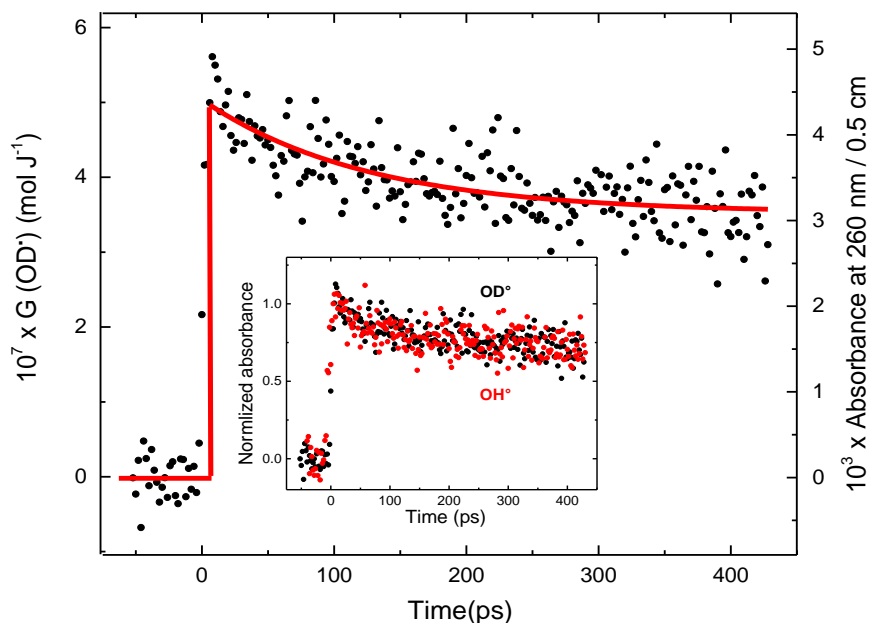


**Figure 3.29** Time dependent absorption and yield of OD<sup>•</sup> at ps range. Inset: the normalized kinetics compared with OH<sup>•</sup> kinetics (Dose per pulse 42.5 Gy).

To study the isotopic effect on OD<sup>•</sup> and OH<sup>•</sup> decay, the comparison was performed on short and long time. As shown in **Figure 3.30 Inset**, there is no obvious difference in the decay of OD<sup>•</sup> and OH<sup>•</sup> in short time (500 ps) or longer time (9.5 ns). This behavior is different from that present in the decay of the solvated electron in H<sub>2</sub>O and D<sub>2</sub>O in **Figure 3.17**.

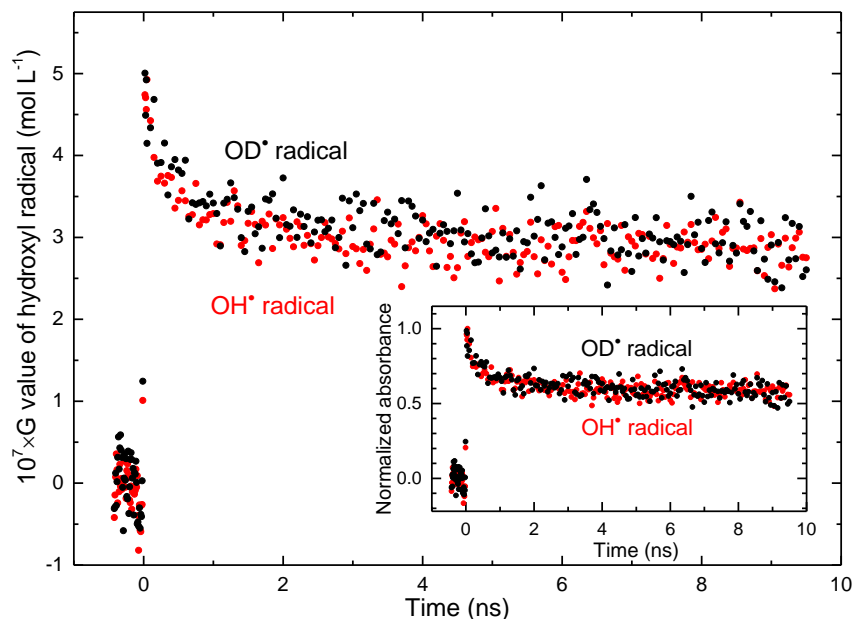


**Figure 3.30** Comparison of time dependent yield of OH<sup>•</sup> and OD<sup>•</sup> radicals up to 9.5 ns. The inset is the normalized time dependent decay of OH<sup>•</sup> and OD<sup>•</sup> radicals, respectively.

We improved investigations in the impact of the transient absorption induces in the fused silica and the solution inside in this work. As discussed, the absorbance due to the fused silica is particularly important in the UV region, even when the thickness of the windows of FSOFC is reduced to 200  $\mu\text{m}$ . Moreover, consideration of the scattering effects not only by the fused silica but also by the solution in the treatment make the determination of the absorbance of the species absorbing in UV e.g. OD<sup>•</sup> radical correctly. If the scattering effects are not taken into consideration in the subtraction, important effort on the analysis can be the consequence. A flow jet without undesirable contribution and the necessary post-acquisition data treatment could be more applicative in the critical case.

### 3.5 Conclusions

The solvated electron is a unique species that can be produced in most polar and low polar solvents. The study of its properties is an important key factor to understand the dynamics and kinetics reactions in solutions. Moreover, the hydrated electron in neat D<sub>2</sub>O is used for the measurements at high temperatures to study the temperature effect on the radical yield and the spur kinetics.<sup>15, 45</sup> Then the knowledge of its properties and its reactions in various solvents is a key

issue in physical chemistry. In radiation chemistry, the measurements of the absolute value of the radical yields at shortest time is obviously necessary to obtain two important information: the energy deposition in the spurs of ionization and the yield of secondary radical which can be produced when the solutes are present in the solutions. For this objective, it is necessary to obtain two independent parameters of the hydrated electron in neat D<sub>2</sub>O: the initial yield and the absorption spectra with molar absorption coefficient. Here, careful and systematic measurements, by taking into account the absorption induced in the windows of the optical cell and the radical hydroxyl, allowed us to determine precisely the absolute absorption spectra of the hydrated electron in D<sub>2</sub>O from 250 to 1500 nm. The shape and its amplitude are different from those reported previously in the literature. The amplitude of the absorption band as found here is different by 10% from that reported in the literature.<sup>11</sup> Additionally, the shape of the absorption spectra of the solvated electron reported by Freeman often used is not accurate. For example, the ratio of  $G\epsilon_{\max}(e_s^-)$  between D<sub>2</sub>O and H<sub>2</sub>O in Freeman's work is 1.25, but in this work it is 1.15, and the extinction coefficient value of the hydrated electron in D<sub>2</sub>O at 300 nm is almost 20% higher than that reported by Freeman(**Table 3.4**).<sup>15, 22</sup>

**Table 3.4** The radiolytic yield of solvated electron and hydroxyl radical in the spur reaction of H<sub>2</sub>O and D<sub>2</sub>O.

	$e_{H_2O}^-$	$e_{D_2O}^-$	OH* radical	OD* radical
$\lambda_{\max}$ (nm)	713	704	—	—
$\epsilon_{\max}$ (M <sup>-1</sup> cm <sup>-1</sup> )	19700	22900	—	—
$G_{t=7ps}$ (10 <sup>-7</sup> mol J <sup>-1</sup> )	4.5	4.5	5.0	5.0
$G_{t=1ns}$ (10 <sup>-7</sup> mol J <sup>-1</sup> )	3.83	3.96	3.17	3.41
$G_{t=3ns}$ (10 <sup>-7</sup> mol J <sup>-1</sup> )	3.46	3.65	2.91	3.04
$G_{t=9ns}$ (10 <sup>-7</sup> mol J <sup>-1</sup> )	3.00	3.17	2.91	3.02

The use of the isosbestic point for the determination of the extinction coefficient with a specific scavenger is more appropriate because it is based only on the knowledge of the molar absorption coefficient of the reaction product. We found that the value of the initial yield of the hydrated electron and the hydroxyl radical, observed at 7 ps, are equal (within the experimental errors) to

those found in H<sub>2</sub>O, but the kinetics of the solvated electron are slower in D<sub>2</sub>O than in H<sub>2</sub>O. Meanwhile, the kinetics of the hydroxyl radical presented no difference in D<sub>2</sub>O and H<sub>2</sub>O. The isotopic effect was explained initially by the fact that the initial spatial distribution between electron and hole in D<sub>2</sub>O is 1.18-1.41 times larger in D<sub>2</sub>O than in H<sub>2</sub>O.<sup>13</sup> However, laser photolysis measurements<sup>16</sup> showed that the main reason of slower decay of the solvated electron in D<sub>2</sub>O is due to the lower rate constant of the two main reactions responsible for the decay of the solvated electron in water at short time:



But the yields are not comparable when the solvated electrons are produced by laser photolysis or by ionizing radiation. In our work, thanks to the determination of the initial yields (7 ps) of the hydrated electron and of the hydroxyl radical that are found to be same in neat water and in neat deuterated water, it can be concluded that the geminate recombination reactions are not affected significantly in D<sub>2</sub>O. Therefore, the slower decay can be explained well by the change of reaction rate of EQ. 3-13 and 3-14. The reaction EQ. 3-14 is diffusion controlled and as the diffusion coefficient is lower in D<sub>2</sub>O than H<sub>2</sub>O, the slower decay of solvated electron in D<sub>2</sub>O is to be expected. The reaction EQ. 3-13 is not fully limited by diffusion. In D<sub>2</sub>O, however, it needs higher reorganization energy and it can be considered slower in D<sub>2</sub>O than in H<sub>2</sub>O. Another point should be considered: due to the isotopic effect and the change of the vibration frequency which is responsible of hydroxyl radical formation through proton transfer, the formation of OD<sup>•</sup> through deuterated of D<sub>2</sub>O<sup>•+</sup> should be slower than that of OH<sup>•</sup> and we had expected a lower yield of OD<sup>•</sup> and  $e_{D_2O}^-$  at picosecond range.<sup>10</sup> Because the geminate recombination between electron and the radical water hole (D<sub>2</sub>O<sup>•+</sup>) should be favored when the proton transfer is slowed down by isotopic effect. However, the initial yields are found to be the same within the measurements precision. Therefore, our conclusion is that the change of water hole lifetime does not affect significantly the geminate reaction.

Finally, the present experimental work giving the time dependent yield of the hydrated electron and hydroxyl radical in neat deuterated water can also contribute to improve the simulation codes usually used in radiation chemistry by treating the energy deposition in the spurs and the kinetics



in the spurs. The simulation codes are very important for the chemistry of the nuclear reactors such as CANDU in which D<sub>2</sub>O is used.

## Reference

- (1) LaVerne, J. A.; Pimblott, S. M. Scavenger and Time Dependences of Radicals and Molecular Products in the Electron Radiolysis of Water: Examination of Experiments and Models. *J. Phys. Chem.* **1991**, 95, 3196–3206.
- (2) Bartels, D. M.; Cook, A. R.; Mudaliar, M.; Jonah, C. D. Spur Decay of the Solvated Electron in Picosecond Radiolysis Measured with Time-Correlated Absorption Spectroscopy. *J. Phys. Chem. A* **2000**, 104, 1686–1691.
- (3) Muroya, Y.; Lin, M.; Wu, G.; Iijima, H.; Yoshii, K.; Ueda, T.; Kudo, H.; Katsumura, Y. A Re-Evaluation of the Initial Yield of the Hydrated Electron in the Picosecond Time Range. *Radiat. Phys. Chem.* **2005**, 72, 169–172.
- (4) El Omar, A. K.; Schmidhammer, U.; Jeunesse, P.; Larbre, J.-P.; Lin, M.; Muroya, Y.; Katsumura, Y.; Pernot, P.; Mostafavi, M. Time-Dependent Radiolytic Yield of  $OH^{\bullet}$  Radical Studied by Picosecond Pulse Radiolysis. *J. Phys. Chem. A* **2011**, 115, 12212–12216.
- (5) Muroya, Y.; Sanguanmith, S.; Meesungnoen, J.; Lin, M.; Yan, Y.; Katsumura, Y.; Jay-Gerin, J.-P. Time-Dependent Yield of the Hydrated Electron in Subcritical and Supercritical Water Studied by Ultrafast Pulse Radiolysis and Monte-Carlo Simulation. *Phys. Chem. Chem. Phys.* **2012**, 14, 14325.
- (6) Meesungnoen, J.; Jay-Gerin, J.-P. Radiation Chemistry of Liquid Water with Heavy Ions. In *Charged Particle and Photon Interactions with Matter*; CRC Press, 2010; pp 355–400.
- (7) De Waele, V.; Lampre, I.; Mostafavi, M. Time-Resolved Study on Nonhomogeneous Chemistry Induced by Ionizing Radiation with Low Linear Energy Transfer in Water and Polar Solvents at Room Temperature. In *Charged Particle and Photon Interactions with Matter*; CRC Press, 2010; pp 289–324.
- (8) Elliot, A.; Ouellette, D. C.; Stuart, C. R. The Temperature Dependence of the Rate Constants and Yields for the Simulation of the Radiolysis of Heavy Water. **1996**, No. December.
- (9) Swiatla-Wojcik, D. .; Buxton, G. V. . V. Isotopic Effect in the Radiolysis of Water. Diffusion-Kinetic Modelling up to 300°C. *Res. Chem. Intermed.* **2001**, 27, 875–889.
- (10) Chernovitz, A.; Jonah, C. Isotopic Dependence of Recombination Kinetics in Water. *J. Phys.*

*Chem.* **1988**, 92, 5946–5950.

- (11) Fielden, E. M.; Hart, E. J. Radical Yields and Some Rate Constants in Primary Heavy Water  $\text{D}_2\text{O}$ . *Radiat. Res.* **1968**, 33, 426–436.
- (12) Jha, K. H.; Ryan, T. G.; Freeman, G. R. Radiolysis of  $\text{H}_2\text{O}$  and  $\text{D}_2\text{O}$  between 0 and 300°. *J. Phys. Chem.* **1975**, 79, 868–870.
- (13) Schmidt, K. H.; Han, P.; Bartels, D. M. Radiolytic Yields of the Hydrated Electron from Transient Conductivity: Improved Calculation of the Hydrated Electron Diffusion Coefficient and Analysis of Some Diffusion-Limited ( $\text{e}^-$ ) Reaction Rates. *J. Phys. Chem.* **1995**, 99, 10530–10539.
- (14) Singh, A.; Chase, W. J.; Hunt, J. W. Reactions in Spurs : Mechanisms of Hydrated Electron Formation in Radiolysis of Water. *Faraday Discuss. Chem. Soc.* **1976**, 28–36.
- (15) Jou, F.; Freeman, G. R. Temperature and Isotope Effects on the Shape of the Optical Absorption Spectrum of Solvated Electrons in Water. *J. Phys. Chem.* **1979**, 83, 2383.
- (16) Jonah, C. D.; Chernovitz, A. C. The Mechanism of Electron Thermalization in  $\text{H}_2\text{O}$ ,  $\text{D}_2\text{O}$ , and HDO. *Can. J. Phys.* **1990**, 68, 935–939.
- (17) Swiatla-Wojcik, D. .; Buxton, G. V. . Isotopic Effect in the Radiolysis of Water. Diffusion-Kinetic Modelling up to 300°C. *Res. Chem. Intermed.* **2001**, 27, 875–889.
- (18) Asmus, K. D.; Fendler, J. H. Use of Sulfur Hexafluoride to Determine  $G(\text{e}^-_{\text{D}_2\text{O}})$  and Relative Reaction Rate Constants in Deuterium Oxide. *J. Phys. Chem.* **1969**, 73, 1583–1584.
- (19) Chase, W. J.; Hunt, J. W. Solvation Time of the Electron in Polar Liquids. Water and Alcohols. *J. Phys. Chem.* **1975**, 79, 2835–2845.
- (20) Nielsen, S. O.; Michael, B. D.; Hart, E. J. Ultraviolet Absorption Spectra of Hydrated Electrons, Hydrogen, Hydroxyl, Deuterium, and Hydroxyl-d Radicals from Pulse Radiolysis of Aqueous Solutions. *J. Phys. Chem.* **1976**, 80, 2482–2488.
- (21) Buxton, G. V.; Lynch, D. A.; Stuart, C. R. Radiation Chemistry of  $\text{D}_2\text{O}$  - Time Dependence of the Yields of the Radicals at Ambient Temperature and Rate Constants for the Reactions  $\text{OD} + \cdot\text{OD}$  and  $\text{D} + \cdot\text{OD}$  up to 200 °C. *J. Chem. Soc. Trans.* **1998**, 94, 2379–2383.
- (22) Bartels, D. M.; Takahashi, K.; Cline, J. A.; Marin, T. W.; Jonah, C. D. Pulse Radiolysis of

- Supercritical Water. 3. Spectrum and Thermodynamics of the Hydrated Electron. *J. Phys. Chem. A* **2005**, *109*, 1299–1307.
- (23) Delaire, J.; Cordier, P.; Belloni, J.; Billiau, F.; Delcourt, M. O. Nanosecond Pulse Radiolysis of Hydrazine. *J. Phys. Chem.* **1976**, *80*, 1687–1690.
- (24) Krasna, A. I. ACRIDINES, DEAZAFLAVINS, AND TRIS(2,2'-BIPYRIDINE)RUTHENIUM AS CATALYSTS FOR PHOTOPRODUCTION OF HYDROGEN FROM ORGANIC COMPOUNDS. *Photochem. Photobiol.* **1980**, *31*, 75–82.
- (25) Solar, S.; Solar, W.; Getoff, N.; Holcman, J.; Sehested, K. Hydrogen-Atom Attack on Methyl Viologen in Aqueous Solution Studied by Pulse Radiolysis. *J. Chem. Soc. Faraday Trans. I* **1984**, *80*, 2929–2934.
- (26) Tadashi Watanabe and Kenichi Honda; Watanabe, T.; Honda, K. Measurement of the Extinction Coefficient of the Methyl Viologen Cation Radical and the Efficiency of Its Formation by Semiconductor Photocatalysis. *J. Phys. Chem.* **1982**, *86*, 2617–2619.
- (27) Torche, F.; Marignier, J. L. Direct Evaluation of the Molar Absorption Coefficient of Hydrated Electron by the Isosbestic Point Method. *J. Phys. Chem. B* **2016**, *120*, 7201–7206.
- (28) Buxton, G. V.; Greenstock, C. L.; Helman, W. P.; Ross, A. B. Critical Review of Rate Constants for Reactions of Hydrated Electrons, Hydrogen Atoms and Hydroxyl Radicals ( $^{\bullet}OH/^{\bullet}O^-$ ) in Aqueous Solution. *J. Phys. Chem. Ref. Data* **1988**, *17*, 513–886.
- (29) Solar, S.; Solar, W.; Getoff, N.; Holcman, J.; Sehested, K. Pulse Radiolysis of Methyl Viologen in Aqueous Solutions. *J. Chem. Soc. Faraday Trans. I Phys. Chem. Condens. Phases* **1982**, *78*, 2467–2477.
- (30) Stuart, C. R.; Ouellette, D. C.; Elliot, A. J. Pulse Radiolysis Studies of Liquid Heavy Water At Temperature up to 250 °C. *AECL-12107* **2002**.
- (31) Hare, P. M.; Price, E. A.; Stanisky, C. M.; Janik, I.; Bartels, D. M. Solvated Electron Extinction Coefficient and Oscillator Strength in High Temperature Water †. *J. Phys. Chem. A* **2010**, *114*, 1766–1775.
- (32) Muroya, Y.; Lin, M.; Wu, G.; Iijima, H.; Yoshii, K.; Ueda, T.; Kudo, H.; Katsumura, Y. A Re-Evaluation of the Initial Yield of the Hydrated Electron in the Picosecond Time Range.

- Radiat. Phys. Chem.* **2005**, 72, 169–172.
- (33) J. E. Fanning. Ph. D Thesis, University of Delaware, Newark, Del., 1975.
- (34) Trumbore, C. N.; Short, D. R.; Fanning, J. E.; Olson, J. H. Effects of Pulse Dose on Hydrated Electron Decay Kinetics in the Pulse Radiolysis of Water. A Computer Modeling Study. *J. Phys. Chem.* **1978**, 82, 2762–2767.
- (35) Trumbore, C. N.; Youngblade, W.; Short, D. R. Computer Modeling of Data from Pulse Radiolysis Studies of Aqueous Solutions Containing Scavengers of Spur Intermediates. *J. Phys. Chem.* **1984**, 88, 5057–5061.
- (36) Torche, F. Contribution à l'étude Des Électrons Solvatés Dans l'eau et Les Alcools et Des Processus Radiolytiques Dans Les Carbonates Organiques Par Radiolyse Impulsionnelle Picoseconde, Université Paris-Sud, 2012.
- (37) Ryosuke YOKOTA. Color Centers in Fused Quartz. *J. Phys. Soc. Japan* **1952**, 7, 1952.
- (38) Alvin J. Cohen. Neutron Specific Color Center in Fused Silica and an Impurity Band of Identical Wavelength\*. *Phys. Rev.* **1957**, 105, 1151–1155.
- (39) R.R. Gulamova; N.A. Kasimov; M.I. Muminov. Fused Silica in Ionizing-Radiation Dosimetry. *At. Energiya* **1984**, 56, 40–43.
- (40) Griscom, D. L. Trapped-Electron Centers in Pure and Doped Glassy Silica: A Review and Synthesis. *J. Non. Cryst. Solids* **2011**, 357, 1945–1962.
- (41) Janata, E. Transient Absorption in Fused Silica Induced by Trains of High-Energy Electron Pulses. *Chem. Phys. Lett.* **2006**, 417, 170–172.
- (42) Schmidhammer, U.; El Omar, A. K.; Balcerzyk, A.; Mostafavi, M. Transient Absorption Induced by A Picosecond Electron Pulse in the Pused Silica Windows of An Optical Cell. *Radiat. Phys. Chem.* **2012**, 81, 1715–1719.
- (43) Kawrakow, I.; Rogers, D. W. O.; Tessier, F.; Walters, B. R. B. R. B.; Mainegra-Hing, E.; Rogers, D. W. O.; Tessier, F.; Walters, B. R. B. R. B. *The EGSnrc Code System: Monte Carlo Simulation of Electron and Photon Transport*; Ottawa, Canada, 2000.
- (44) Kawrakow, I. *Egspp: The EGSnrc C++ Class Library*; NRCC Report PIRS-899: Canada, 2005.

- (45) Elliot, A.; Bartels, D. The Reaction Set, Rate Constants and g-Values for the Simulation of the Radiolysis of Light Water Over the Range 20 to 350 °C Based on Information Available in 2008. *At. Energy Canada Ltd. Rep.* **2009**, 153–127160.

**Appendix:** Molar absorption coefficient of  $e_s^-$  in D<sub>2</sub>O (250 to 1500 nm) obtained in the present work.

$\lambda/\text{nm}$	$\varepsilon/\text{M}^{-1}\text{cm}^{-1}$	$\lambda/\text{nm}$	$\varepsilon/\text{M}^{-1}\text{cm}^{-1}$	$\lambda/\text{nm}$	$\varepsilon/\text{M}^{-1}\text{cm}^{-1}$	$\lambda/\text{nm}$	$\varepsilon/\text{M}^{-1}\text{cm}^{-1}$
250.1	646.1	306.5	1093.0	363.0	1848.7	419.4	3127.0
251.0	652.0	307.5	1102.9	363.9	1865.5	420.4	3155.3
252.0	657.9	308.5	1113.0	364.9	1882.5	421.4	3183.8
253.0	663.9	309.4	1123.1	365.9	1899.6	422.4	3212.7
253.9	670.0	310.4	1133.3	366.9	1916.9	423.3	3241.7
254.9	676.1	311.4	1143.6	367.8	1934.4	424.3	3271.1
255.9	682.2	312.4	1154.0	368.8	1952.0	425.3	3300.7
256.9	688.4	313.3	1164.5	369.8	1969.7	426.2	3330.6
257.8	694.7	314.3	1175.1	370.8	1987.7	427.2	3360.7
258.8	701.0	315.3	1185.8	371.7	2005.7	428.2	3391.1
259.8	707.4	316.2	1196.6	372.7	2024.0	429.1	3421.8
260.8	713.8	317.2	1207.5	373.7	2042.4	430.1	3452.8
261.7	720.3	318.2	1218.5	374.6	2061.0	431.1	3484.0
262.7	726.9	319.2	1229.6	375.6	2079.8	432.0	3515.6
263.7	733.5	320.1	1240.8	376.6	2098.7	433.0	3547.4
264.7	740.2	321.1	1252.1	377.6	2117.8	434.0	3579.5
265.6	746.9	322.1	1263.5	378.5	2137.1	434.9	3611.9
266.6	753.7	323.1	1275.0	379.5	2156.5	435.9	3644.6
267.6	760.6	324.0	1286.6	380.5	2176.1	436.9	3677.5
268.5	767.5	325.0	1298.3	381.5	2195.9	437.8	3710.8
269.5	774.5	326.0	1310.1	382.4	2215.9	438.8	3744.4
270.5	781.6	327.0	1322.1	383.4	2236.1	439.8	3778.3
271.5	788.7	327.9	1334.1	384.4	2256.5	440.8	3812.5
272.4	795.9	328.9	1346.3	385.4	2277.0	441.7	3847.0
273.4	803.1	329.9	1358.5	386.3	2297.7	442.7	3881.8
274.4	810.4	330.8	1370.9	387.3	2318.6	443.7	3916.9
275.4	817.8	331.8	1383.4	388.3	2339.7	444.6	3952.4
276.3	825.2	332.8	1395.9	389.2	2361.0	445.6	3988.1
277.3	832.8	333.8	1408.7	390.2	2382.5	446.6	4024.2
278.3	840.3	334.7	1421.5	391.4	2407.8	447.5	4060.6
279.3	848.0	335.7	1434.4	392.3	2429.6	448.5	4097.4
280.2	855.7	336.7	1447.5	393.3	2451.6	449.5	4134.4
281.2	863.5	337.7	1460.7	394.3	2473.8	450.4	4171.9
282.2	871.4	338.6	1474.0	395.2	2496.2	451.4	4209.6
283.1	879.3	339.6	1487.4	396.2	2518.8	452.4	4247.7
284.1	887.3	340.6	1500.9	397.2	2541.6	453.3	4286.1
285.1	895.4	341.6	1514.6	398.1	2564.6	454.3	4324.9
286.1	903.5	342.5	1528.4	399.1	2587.9	455.3	4364.0
287.0	911.8	343.5	1542.3	400.1	2611.3	456.2	4403.5
288.0	920.1	344.5	1556.3	401.0	2634.9	457.2	4443.4
289.0	928.4	345.4	1570.5	402.0	2658.8	458.2	4483.6
290.0	936.9	346.4	1584.8	403.0	2682.8	459.2	4524.1
290.9	945.4	347.4	1599.2	403.9	2707.1	460.1	4565.1
291.9	954.0	348.4	1613.7	404.9	2731.6	461.1	4606.4
292.9	962.7	349.3	1628.4	405.9	2756.4	462.1	4648.0
293.9	971.5	350.3	1643.3	406.9	2781.3	463.0	4690.1
294.8	980.3	351.3	1658.2	407.8	2806.5	464.0	4732.5
295.8	989.3	352.3	1673.3	408.8	2831.9	465.0	4775.3
296.8	998.3	353.2	1688.5	409.8	2857.5	465.9	4818.5
297.8	1007.4	354.2	1703.9	410.7	2883.4	466.9	4862.1
298.7	1016.5	355.2	1719.4	411.7	2909.5	467.9	4906.1
299.7	1025.8	356.2	1735.1	412.7	2935.9	468.8	4950.5
300.7	1035.1	357.1	1750.9	413.6	2962.4	469.8	4995.3
301.6	1044.5	358.1	1766.8	414.6	2989.2	470.8	5040.4
302.6	1054.0	359.1	1782.9	415.6	3016.3	471.7	5086.0
303.6	1063.6	360.0	1799.1	416.5	3043.6	472.7	5132.0
304.6	1073.3	361.0	1815.5	417.5	3071.1	473.7	5178.4
305.5	1083.1	362.0	1832.0	418.5	3098.9	474.6	5225.3

*Chapter III: Time Dependent Yield of the Solvated Electron and the OD<sup>•</sup> Radical in Deuterated Water at Low LET Studied by Picosecond Pulse Radiolysis*

$\lambda/\text{nm}$	$\varepsilon/\text{M}^{-1}\text{cm}^{-1}$	$\lambda/\text{nm}$	$\varepsilon/\text{M}^{-1}\text{cm}^{-1}$	$\lambda/\text{nm}$	$\varepsilon/\text{M}^{-1}\text{cm}^{-1}$	$\lambda/\text{nm}$	$\varepsilon/\text{M}^{-1}\text{cm}^{-1}$
475.6	5272.6	531.5	9168.6	587.3	14909.5	643.5	20439.2
476.6	5320.2	532.3	9239.6	588.3	15014.9	644.5	20515.1
477.6	5368.3	533.1	9311.5	589.3	15120.2	645.4	20589.9
478.5	5416.9	534.1	9400.8	590.2	15225.4	646.4	20663.9
479.5	5465.9	535.0	9490.6	591.2	15330.6	647.4	20736.8
480.5	5515.3	536.0	9580.9	592.2	15435.7	648.3	20808.7
481.4	5565.2	537.0	9671.9	593.1	15540.6	649.3	20879.5
482.4	5615.6	537.9	9763.2	594.1	15645.4	650.3	20949.4
483.4	5666.3	538.9	9855.1	595.1	15750.1	651.2	21018.2
484.3	5717.6	539.9	9947.5	596.0	15854.5	652.2	21085.9
485.3	5769.3	540.8	10040.5	597.0	15958.8	653.2	21152.5
486.3	5821.5	541.8	10133.9	598.0	16062.9	654.1	21218.1
487.2	5874.1	542.8	10227.7	598.9	16166.9	655.1	21282.5
488.2	5927.2	543.7	10322.2	599.9	16270.5	656.1	21345.8
489.2	5980.8	544.7	10417.0	600.9	16373.9	657.0	21408.1
490.1	6034.9	545.7	10512.3	601.8	16477.1	658.0	21469.1
491.1	6089.5	546.6	10608.0	602.8	16580.0	659.1	21536.7
492.1	6144.5	547.6	10704.3	603.8	16682.6	660.1	21595.3
493.0	6200.1	548.6	10800.9	604.7	16784.8	661.0	21652.7
494.0	6256.2	549.5	10897.9	605.7	16886.9	662.0	21708.9
495.0	6312.7	550.5	10995.5	606.7	16988.5	663.0	21764.0
496.0	6369.8	551.5	11093.4	607.7	17089.7	663.9	21817.8
496.9	6427.4	552.5	11191.6	608.6	17190.7	664.9	21870.4
497.9	6485.5	553.4	11290.3	609.6	17291.2	665.9	21921.8
498.9	6544.1	554.4	11389.5	610.6	17391.3	666.9	21971.9
499.6	6585.1	555.4	11488.9	611.5	17490.9	667.8	22020.8
500.5	6653.4	556.3	11588.7	612.5	17590.3	668.8	22068.4
501.5	6722.3	557.3	11689.0	613.5	17689.0	669.8	22114.8
502.5	6791.9	558.3	11789.5	614.4	17787.4	670.7	22159.9
503.4	6862.1	559.2	11890.3	615.4	17885.2	671.7	22203.7
504.4	6932.9	560.2	11991.5	616.4	17982.6	672.7	22246.2
505.4	7004.4	561.2	12093.0	617.3	18079.4	673.6	22287.4
506.3	7076.6	562.1	12194.8	618.3	18175.7	674.6	22327.2
507.3	7149.3	563.1	12296.9	619.3	18271.5	675.6	22365.8
508.3	7222.7	564.1	12399.3	620.2	18366.6	676.5	22403.0
509.2	7296.8	565.0	12502.0	621.2	18461.2	677.5	22438.9
510.2	7371.4	566.0	12604.9	622.2	18555.2	678.5	22473.5
511.2	7446.7	567.0	12708.0	623.1	18648.6	679.4	22506.7
512.2	7522.6	567.9	12811.5	624.1	18741.3	680.4	22538.5
513.1	7599.1	568.9	12915.1	625.1	18833.4	681.4	22569.0
514.1	7676.3	569.9	13018.9	626.1	18924.9	682.3	22598.1
515.1	7754.1	570.9	13123.0	627.0	19015.6	683.3	22625.8
516.0	7832.5	571.8	13227.2	628.0	19105.7	684.3	22652.2
517.0	7911.5	572.8	13331.5	629.0	19195.0	685.3	22677.1
518.0	7991.2	573.8	13436.1	629.9	19283.7	686.2	22700.7
518.9	8071.4	574.7	13540.8	630.9	19371.5	687.2	22722.9
519.9	8152.3	575.7	13645.7	631.9	19458.6	688.2	22743.6
520.9	8233.8	576.7	13750.6	632.8	19545.0	689.1	22763.0
521.8	8315.8	577.6	13855.6	633.8	19630.5	690.1	22781.0
522.8	8398.4	578.6	13960.9	634.8	19715.3	691.1	22797.5
523.8	8481.7	579.6	14066.1	635.7	19799.2	692.0	22812.7
524.7	8565.6	580.5	14171.4	636.7	19882.3	693.0	22826.4
525.7	8650.0	581.5	14276.9	637.7	19964.5	694.0	22838.7
526.7	8734.9	582.5	14382.3	638.6	20045.9	694.9	22849.5
527.6	8820.6	583.4	14487.7	639.6	20126.4	695.6	22856.2
528.6	8906.7	584.4	14593.1	640.6	20206.0	696.6	22869.3
529.6	8993.4	585.4	14698.7	641.5	20284.6	697.6	22880.2
530.6	9080.8	586.3	14804.1	642.5	20362.4	698.5	22888.9



$\lambda/\text{nm}$	$\varepsilon/\text{M}^{-1}\text{cm}^{-1}$	$\lambda/\text{nm}$	$\varepsilon/\text{M}^{-1}\text{cm}^{-1}$	$\lambda/\text{nm}$	$\varepsilon/\text{M}^{-1}\text{cm}^{-1}$	$\lambda/\text{nm}$	$\varepsilon/\text{M}^{-1}\text{cm}^{-1}$
699.5	22895.8	755.4	21028.5	811.6	16972.9	871.0	12025.4
700.5	22901.0	756.4	20970.6	812.6	16895.3	872.0	11942.3
701.5	22904.7	757.4	20912.2	813.5	16817.5	873.0	11859.1
702.4	22907.2	758.3	20853.2	814.5	16739.6	874.1	11776.0
703.4	22908.6	759.3	20793.7	815.5	16661.6	875.1	11692.9
704.4	22909.0	760.3	20733.5	816.4	16583.6	876.1	11609.8
705.3	22908.6	761.2	20672.8	817.4	16505.5	877.2	11526.7
706.3	22907.1	762.2	20611.6	818.4	16427.2	878.2	11443.7
707.3	22904.6	763.2	20549.8	819.3	16349.0	879.2	11360.7
708.2	22900.9	764.1	20487.5	820.3	16270.6	880.3	11277.8
709.2	22895.7	765.1	20424.8	821.3	16192.2	881.3	11194.9
710.2	22888.8	766.1	20361.5	822.2	16113.8	882.4	11112.1
711.1	22880.0	767.0	20297.6	823.2	16035.3	883.4	11029.4
712.1	22869.2	768.0	20233.3	824.2	15956.8	884.5	10946.8
712.8	22856.5	769.0	20168.6	825.1	15878.2	885.5	10864.3
713.8	22833.2	769.9	20103.3	826.1	15799.7	886.6	10781.9
714.7	22809.0	770.9	20037.6	827.1	15721.1	887.6	10699.6
715.7	22783.7	771.9	19971.4	828.1	15642.5	888.7	10617.4
716.7	22757.6	772.9	19904.8	829.0	15563.9	889.8	10535.4
717.7	22730.5	773.8	19837.7	830.0	15485.3	890.8	10453.5
718.6	22702.4	774.8	19770.3	831.0	15406.7	891.9	10371.8
719.6	22673.5	775.8	19702.4	831.9	15328.1	893.0	10290.2
720.6	22643.6	776.7	19634.1	832.9	15249.6	894.1	10208.8
721.5	22612.8	777.7	19565.4	833.9	15171.1	895.1	10127.5
722.5	22581.1	778.7	19496.3	834.8	15092.6	896.2	10046.4
723.5	22548.6	779.6	19426.8	835.8	15014.1	897.3	9965.5
724.4	22515.1	780.6	19356.9	836.8	14935.7	898.4	9884.9
725.4	22480.8	781.6	19286.7	837.7	14857.3	899.5	9804.4
726.4	22445.6	782.5	19216.2	838.7	14778.9	900.6	9724.1
727.3	22409.6	783.5	19145.2	839.7	14700.7	901.7	9644.0
728.3	22372.7	784.5	19073.9	840.8	14519.2	902.8	9564.2
729.3	22334.9	785.4	19002.3	842.2	14404.4	903.9	9484.6
730.2	22296.3	786.4	18930.4	843.6	14289.2	905.0	9405.2
731.2	22256.9	787.4	18858.1	845.0	14173.4	906.1	9326.1
732.2	22216.7	788.3	18785.6	846.4	14057.2	907.2	9247.3
733.2	22175.6	789.3	18712.8	847.8	13940.6	908.3	9168.7
734.1	22133.8	790.3	18639.7	849.2	13823.5	909.4	9090.3
735.1	22091.2	791.3	18566.2	850.6	13706.0	910.5	9012.3
736.1	22047.8	792.2	18492.5	851.0	13674.3	911.6	8934.5
737.0	22003.6	793.2	18418.6	852.0	13593.0	912.8	8857.0
738.0	21958.6	794.2	18344.3	853.0	13511.5	913.9	8779.8
739.0	21912.9	795.1	18269.8	854.0	13429.9	915.0	8702.9
739.9	21866.5	796.1	18195.1	854.9	13348.1	916.1	8626.4
740.9	21819.3	797.1	18120.2	855.9	13266.2	917.3	8550.1
741.9	21771.4	798.0	18045.0	856.9	13184.1	918.4	8474.1
742.8	21722.7	799.0	17969.6	857.9	13102.0	919.5	8398.5
743.8	21673.3	800.0	17894.0	858.9	13019.6	920.7	8323.2
744.8	21623.3	800.9	17818.1	859.9	12937.2	921.8	8248.2
745.7	21572.5	801.9	17742.1	860.9	12854.7	923.0	8173.6
746.7	21521.0	802.9	17666.0	861.9	12772.1	924.1	8099.3
747.7	21468.9	803.8	17589.6	862.9	12689.3	925.3	8025.4
748.6	21416.1	804.8	17513.0	863.9	12606.5	926.4	7951.8
749.6	21362.6	805.8	17436.3	864.9	12523.7	927.6	7878.6
750.6	21308.5	806.7	17359.5	865.9	12440.7	928.7	7805.8
751.5	21253.8	807.7	17282.4	866.9	12357.7	929.9	7733.3
752.5	21198.4	808.7	17205.2	867.9	12274.7	931.1	7661.2
753.5	21142.3	809.7	17128.0	868.9	12191.6	932.2	7589.5
754.5	21085.7	810.6	17050.5	870.0	12108.5	933.4	7518.2

*Chapter III: Time Dependent Yield of the Solvated Electron and the OD<sup>•</sup> Radical in Deuterated Water at Low LET Studied by Picosecond Pulse Radiolysis*

$\lambda/\text{nm}$	$\varepsilon/\text{M}^{-1}\text{cm}^{-1}$	$\lambda/\text{nm}$	$\varepsilon/\text{M}^{-1}\text{cm}^{-1}$	$\lambda/\text{nm}$	$\varepsilon/\text{M}^{-1}\text{cm}^{-1}$	$\lambda/\text{nm}$	$\varepsilon/\text{M}^{-1}\text{cm}^{-1}$
934.6	7447.2	1008.2	4080.0	1094.4	2134.0	1196.8	1162.3
935.8	7376.7	1009.6	4035.3	1096.0	2110.5	1198.7	1151.1
936.9	7306.5	1011.0	3991.0	1097.7	2087.3	1200.6	1140.2
938.1	7236.8	1012.3	3947.1	1099.3	2064.3	1202.6	1129.3
939.3	7167.4	1013.7	3903.7	1100.9	2041.7	1204.5	1118.6
940.5	7098.5	1015.1	3860.6	1102.6	2019.3	1206.5	1108.1
941.7	7030.0	1016.5	3818.1	1104.2	1997.2	1208.5	1097.6
942.9	6961.9	1017.9	3775.9	1105.8	1975.4	1210.4	1087.4
944.1	6894.2	1019.3	3734.2	1107.5	1953.9	1212.4	1077.2
945.3	6826.9	1020.7	3692.9	1109.1	1932.6	1214.4	1067.2
946.5	6760.1	1022.1	3652.0	1110.8	1911.6	1216.4	1057.4
947.7	6693.6	1023.5	3611.5	1112.5	1890.8	1218.4	1047.6
948.9	6627.7	1024.9	3571.4	1114.1	1870.3	1220.4	1038.0
950.1	6562.1	1026.3	3531.8	1115.8	1850.1	1222.4	1028.6
951.4	6497.0	1027.8	3492.6	1117.5	1830.1	1224.4	1019.2
952.6	6432.3	1029.2	3453.8	1119.2	1810.3	1226.4	1010.0
953.8	6368.1	1030.6	3415.3	1120.9	1790.8	1228.5	1000.9
955.0	6304.3	1032.0	3377.3	1122.6	1771.5	1230.5	991.9
956.3	6240.9	1033.5	3339.7	1124.3	1752.5	1232.5	983.1
957.5	6178.0	1034.9	3302.5	1126.0	1733.8	1234.6	974.3
958.7	6115.5	1036.4	3265.7	1127.7	1715.2	1236.6	965.7
960.0	6053.5	1037.8	3229.3	1129.4	1696.9	1238.7	957.2
961.2	5992.0	1039.3	3193.3	1131.1	1678.8	1240.8	948.8
962.5	5930.8	1040.7	3157.6	1132.8	1661.0	1242.9	940.6
963.7	5870.2	1042.2	3122.4	1134.6	1643.4	1244.9	932.4
965.0	5810.0	1043.6	3087.5	1136.3	1626.0	1247.0	924.4
966.2	5750.2	1045.1	3053.0	1138.1	1608.8	1249.1	916.4
967.5	5690.9	1046.6	3018.9	1139.8	1591.8	1251.2	908.6
968.7	5632.1	1048.1	2985.2	1141.6	1575.1	1253.3	900.9
970.0	5573.7	1049.6	2951.8	1143.3	1558.6	1255.5	893.3
971.3	5515.8	1051.0	2918.8	1145.1	1542.3	1257.6	885.8
972.5	5458.4	1052.5	2886.2	1146.8	1526.2	1259.7	878.4
973.8	5401.4	1054.0	2853.9	1148.6	1510.3	1261.9	871.0
975.1	5344.8	1055.5	2822.1	1150.4	1494.6	1264.0	863.8
976.4	5288.8	1057.0	2790.5	1152.2	1479.1	1266.2	856.7
977.7	5233.1	1058.5	2759.3	1154.0	1463.8	1268.3	849.7
979.0	5178.0	1060.0	2728.5	1155.8	1448.7	1270.5	842.8
980.3	5123.3	1061.6	2698.0	1157.6	1433.8	1272.7	836.0
981.5	5069.0	1063.1	2667.9	1159.4	1419.1	1274.9	829.2
982.8	5015.3	1064.6	2638.1	1161.2	1404.6	1277.1	822.6
984.2	4962.0	1066.1	2608.7	1163.0	1390.3	1279.3	816.1
985.5	4909.1	1067.7	2579.6	1164.8	1376.1	1281.5	809.6
986.8	4856.7	1069.2	2550.8	1166.7	1362.2	1283.7	803.2
988.1	4804.8	1070.7	2522.4	1168.5	1348.4	1285.9	796.9
989.4	4753.3	1072.3	2494.3	1170.3	1334.8	1288.1	790.8
990.7	4702.3	1073.8	2466.5	1172.2	1321.4	1290.4	784.6
992.0	4651.7	1075.4	2439.1	1174.1	1308.2	1292.6	778.6
993.4	4601.6	1077.0	2411.9	1175.9	1295.1	1294.9	772.7
994.7	4551.9	1078.5	2385.1	1177.8	1282.2	1297.1	766.8
996.0	4502.7	1080.1	2358.6	1179.6	1269.5	1299.4	761.0
997.4	4454.0	1081.7	2332.5	1181.5	1256.9	1301.7	755.3
998.7	4405.7	1083.2	2306.6	1183.4	1244.5	1304.0	749.7
1000.1	4357.8	1084.8	2281.0	1185.3	1232.3	1306.3	744.2
1001.4	4310.4	1086.4	2255.8	1187.2	1220.2	1308.6	738.7
1002.8	4263.4	1088.0	2230.8	1189.1	1208.3	1310.9	733.3
1004.1	4216.9	1089.6	2206.2	1191.0	1196.6	1313.2	728.0
1005.5	4170.9	1091.2	2181.8	1192.9	1185.0	1315.5	722.8
1006.8	4125.2	1092.8	2157.7	1194.8	1173.6	1317.9	717.6

$\lambda/\text{nm}$	$\varepsilon/\text{M}^{-1}\text{cm}^{-1}$	$\lambda/\text{nm}$	$\varepsilon/\text{M}^{-1}\text{cm}^{-1}$
1320.2	712.5	1472.1	511.6
1322.6	707.5	1475.0	509.4
1324.9	702.5	1477.9	507.2
1327.3	697.6	1480.9	505.0
1329.7	692.8	1483.8	502.9
1332.1	688.0	1486.8	500.8
1334.5	683.3	1489.8	498.7
1336.9	678.7	1492.8	496.7
1339.3	674.2	1495.8	494.7
1341.7	669.7	1498.8	492.7
1344.1	665.2	1501.9	490.8
346.6	660.9	1504.9	488.8
1349.0	656.6		
1351.5	652.3		
1353.9	648.1		
1356.4	644.0		
1358.9	639.9		
1361.4	635.9		
1363.9	631.9		
1366.4	628.0		
1368.9	624.2		
1371.4	620.4		
1374.0	616.6		
1376.5	612.9		
1379.1	609.3		
1381.7	605.7		
1384.2	602.1		
1386.8	598.6		
1389.4	595.2		
1392.0	591.8		
1394.6	588.5		
1397.3	585.2		
1399.9	581.9		
1402.5	578.7		
1405.2	575.5		
1407.9	572.4		
1410.5	569.3		
1413.2	566.3		
1415.9	563.3		
1418.6	560.4		
1421.3	557.5		
1424.1	554.6		
1426.8	551.8		
1429.5	549.0		
1432.3	546.2		
1435.1	543.5		
1437.9	540.9		
1440.6	538.2		
1443.4	535.6		
1446.3	533.1		
1449.1	530.5		
1451.9	528.1		
1454.8	525.6		
1457.6	523.2		
1460.5	520.8		
1463.4	518.5		
1466.3	516.1		
1469.2	513.9		

# Chapter IV: Ultra-fast Charge Migration Competes with Proton Transfer in the Early Chemistry of $\text{H}_2\text{O}^{\bullet+}$

## **Table of content**

### 4.1 State of the art

#### 4.1.1 General introduction

#### 4.1.2 Oxidation reactions by radicals

#### 4.1.3 Reactivity of $\text{H}_2\text{O}^{\bullet+}$ in halide solutions

#### 4.1.4 Reactivity of $\text{H}_2\text{O}^{\bullet+}$ in concentrated acidic solutions

### 4.2 Results — Reactivity of radical cation of water in $\text{D}_2\text{SO}_4$ / $\text{D}_2\text{O}$ system

#### 4.2.1 Transient absorption spectra

#### 4.2.2 Analysis of the kinetics

#### 4.2.2 Yield of scavenging $\text{H}_2\text{O}^{\bullet+}$

### 4.3 Results — Reactivity of radical cation of water in $\text{D}_2\text{SO}_4$ / $\text{D}_2\text{O}$ system

#### 4.3.1 Experiment on isotopic effect

#### 4.3.2 Discussion and analysis

### 4.4 Conclusion

### Reference

## Chapter IV: Ultra-fast Charge Migration Competes with Proton Transfer in the Early Chemistry of $H_2O^{\bullet+}$

### 4.1 State of the art

#### 4.1.1 General introduction

Liquid water is the key compound for our existence on this planet and it is involved in nearly all biological and chemical processes. The role of contemporary physics and chemistry of liquid water exposed to ionizing radiation (photon, fast electron, X-rays, heavy ions, etc.) is significant in such diverse fields as photon science, radiotherapy, nuclear reactors, radiation chemistry and nuclear waste management *etc.*<sup>1-3</sup> Since the discovery of X-rays and natural radioactive phenomena, the chemistry derived from water radiolysis has been studied intensively over the last one hundred years. The interaction of highly energetic photons or charged particles with water initially results in the ejection of a quasi-free electron from the valence shell in general, leaving behind a positively charged radical cation ( $H_2O^{\bullet+}$ ). The earliest time of  $H_2O^{\bullet+}$  formation is estimated to be on the timescale of attoseconds ( $10^{-18}$  s) or *subfemtosecond* based on the uncertainty relationship ( $\Delta E \Delta t \approx \hbar$ ).<sup>4</sup> In addition to their recombination, both of these two charged species ( $e^-$  and  $H_2O^{\bullet+}$ ) subsequently follow their own pathway of chemical reactivity. The hot electron relaxes into solvent molecules and gets trapped as a hydrated electron ( $e_s^-$ ) whilst  $H_2O^{\bullet+}$  rapidly forms the oxidizing  $OH^\bullet$  radical via proton transfer.



The chemical framework in which water radiolysis involving  $OH^\bullet$  and  $e_s^-$  occur is now well understood experimentally as well as theoretically. The  $OH^\bullet$  radical is thought to be mainly responsible for an important number of the radiation-induced oxidation that occurs in dilute aqueous solutions and biological system. Even if this statement is still consistent for an important number of situation, the ultrafast chemistry of its precursor, water hole ( $H_2O^{\bullet+}$ ) immediately following ionization of liquid water, is a puzzling and very challenging subject in radical chemistry induced by ionizing radiation. The situations where  $H_2O^{\bullet+}$  undergoes ultrafast one-electron

oxidation in competition with proton transfer have important practical influences upon nuclear waste storage, nuclear fuel processing and radiotherapy, and remain to be clarified in order to better assess the safety concerns such as the component corrosion and hydrogen emission.

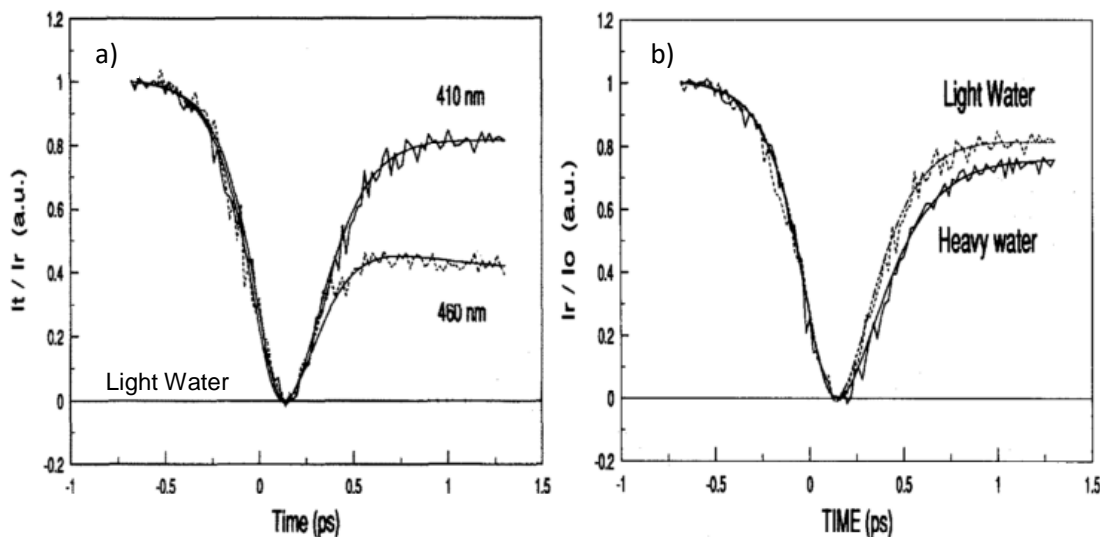


**Figure 4.1.** a) Time dependence of the induced absorbance at 460 and 410 nm following the femtosecond photoionization of pure liquid  $\text{H}_2\text{O}$  by ultraviolet pulse (310 nm). b) Influence of an H/D isotope substitution on the time resolved induced absorbance (410 nm) following the femtosecond photoionization of water molecules ( $\text{X}_2\text{O}$  with  $\text{X}=\text{H}$  or  $\text{D}$ ) by ultraviolet pulses (310 nm). The computed fits of the experimental curves yield a relaxation time of 100 fs in  $\text{H}_2\text{O}$  against 170 fs in  $\text{D}_2\text{O}$ . By Gauduel *et al.*<sup>5</sup>

Until now, real-time observation of this species  $\text{H}_2\text{O}^{+\bullet}$  is still lacking because of the limitation of the time resolution in currently available high energy pulse techniques to typical picosecond time scales. The proton transfer rate constant in the gas phase is about  $8 \times 10^{12} \text{ L mol}^{-1} \text{ s}^{-1}$ .<sup>6</sup> The extrapolation of this constant by simply taking into account the concentration of water gives an extremely short lifetime which is estimated at approximately twenty femtoseconds, i.e.  $18 \times 10^{-15} \text{ s}$ . Indeed, *ab initio* molecular dynamic simulations suggested the lifetime of this radical cation in liquid phase is actually less than 40 fs.<sup>7</sup> Alternatively, the chemical reactivity of  $\text{H}_2\text{O}^{+\bullet}$  was arisen not long after the discovery of hydrated electron in 1962. Hamill *et al.*<sup>8,9</sup> suggested that holes in water could be trapped prior to hydration using sufficiently high concentrations of solutes such as  $\text{NaX}$  ( $\text{X} = \text{Cl}, \text{Br}, \text{F}, \text{I}$ ) or sulfate salts. The high values for the yields of secondary radicals  $\text{NO}_3^\bullet$ ,  $\text{Cl}_2^{\bullet-}$  or  $\text{SO}_4^{\bullet-}$  from steady-state scavenger or time-resolved nanosecond pulse radiolysis measurements were attributed partially to electron transfer from  $\text{H}_2\text{O}^{+\bullet}$  radical to anions.<sup>8-10</sup> In bulk liquid water, Gauduel *et al.* reported that the water radical cation could present a transient

absorbance around 410 nm. The half-time of the ion-molecule reaction (EQ. 4-1) was estimated as 100 fs in light water, vs. 170 fs in heavy water (**Figure 4.1**). However, the charge localization step of  $\text{H}_2\text{O}^{*+}$  towards water molecules was suggested to require less than 40 fs by theoretical simulations.<sup>5</sup> Nevertheless, very recently, a polarization anisotropy measurement estimated that the lifetime of this transient species in  $\text{H}_2\text{O}$  is as long as  $196 \pm 5$  fs (**Figure 4.2**).<sup>11</sup> It was suggested that after an ultrafast X-ray core ionization of water, a doubly charged species, with two positive charges located on different water units,  $[\text{H}_2\text{O}^{*+} \dots \text{H}_2\text{O}^{*+}]_{\text{aq}}$  can be formed.<sup>12</sup> This pioneering experimental and theoretical works brought insights into the electronic signature of this radical cation and prompted further investigations using more sophisticated dynamic technology with a time resolution of several femtoseconds or even better. In addition, the water cation radical produced in an inner hydration layer of DNA was considered as a direct-type damage based on the ESR (electron spin resonance) measurements at low temperature.<sup>13</sup> These early studies suggested that the  $\text{H}_2\text{O}^{*+}$  radical could initiate oxidation processes both in the homogeneous solutions and in interfacial biological systems prior to the generation of  $\text{OH}^{\bullet}$  radical, but the results are very speculative because the time scales for these reactions are very fast ( $\sim 100$  fs). Moreover, as the direct effect of radiation on the solute produces similar chemical species with those produced by the oxidation of the solute by  $\text{H}_2\text{O}^{*+}$ , difference between these two reactions was not obvious, and the role of  $\text{H}_2\text{O}^{*+}$  in electron transfer reaction remained controversial. In general, the direct measurement of the  $\text{H}_2\text{O}^{*+}$  decay has not been performed in pure water.



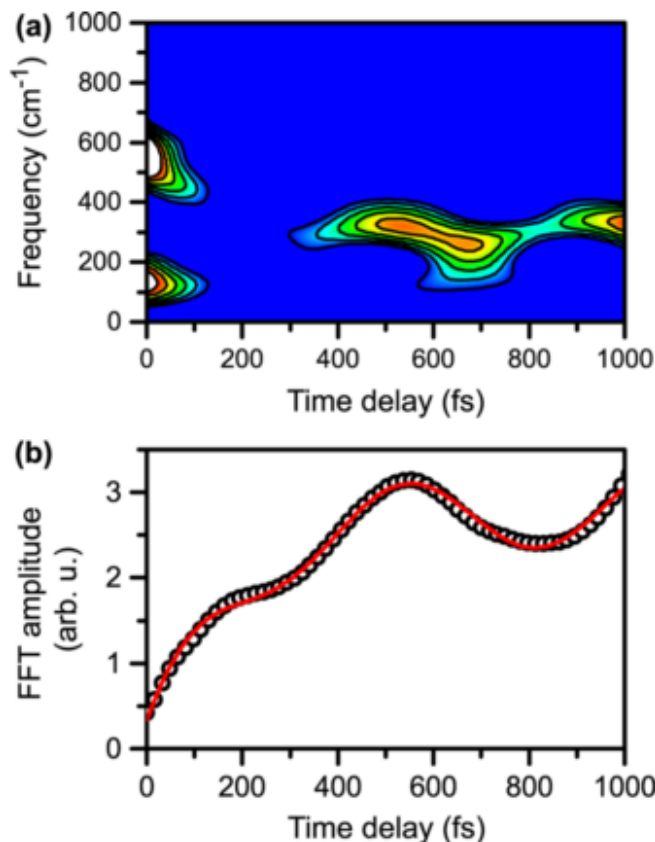


**Figure 4.2** (a) The time-frequency spectrogram for the anisotropic signal shows the disappearance of the 150 and 500  $\text{cm}^{-1}$  frequency components at early times and the concomitant rise of the frequency component at 310  $\text{cm}^{-1}$ . (b) The FFT amplitude at 310  $\text{cm}^{-1}$  reveals an oscillatory rise (symbol), from which a fit to first-order kinetics (solid line) yields a lifetime of  $196 \pm 5$  fs for the aqueous  $\text{H}_2\text{O}$  radical cation. This work was presented by J. Li *et al.*<sup>11</sup>

Despite the difficulties of observing this short-lived species directly, the possibility of using the reactivity of  $\text{H}_2\text{O}^{\bullet+}$  with other ions or molecules has been proposed as an indirect probe. An oxidizing free radical, for instance,  $\text{M}^{\bullet+}$  is often involved in the stepwise oxidization of an electron donor via one-electron transfer mechanism. Therefore, the reduction potentials of the couples  $\text{M}^{\bullet+} / \text{M}$  is of particular value for predicting the direction of the free-radical redox reactions and in some case the rate constant on the basis of Marcus electron transfer theory. Conventional electrochemical techniques are not applicable to determine this thermodynamic property of the individual step because the intermediates are short lived and they are not easy to observe. The pulse radiolysis setup consists of an accelerator which delivers a high energy electron pulse to create reactive radicals, or charged species via ionizing or exciting the medium. When coupled with detecting

methods such as transient absorption spectroscopy, it allows the production of the transients in a controlled manner and to directly study the redox reactions and relevant physical properties of those intermediates in liquids at various time scales. Therefore, it should be very useful to determinate the redox potential of each individual step. As an example, the DNA nucleotides oxidative reactions or others involving  $\text{OH}^\bullet$  radical can be investigated by saturating the irradiated solutions with the  $\text{N}_2\text{O}$  gas to remove the reducing hydrated electrons ( $\text{e}_s^- + \text{N}_2\text{O} \rightarrow \text{N}_2 + \text{O}^-$ ).<sup>14</sup> Additionally, pulse radiolysis techniques can also produce the strong oxidizing  $\text{SO}_4^{\bullet-}$  radicals to study the one-electron oxidation reactions when the solution contains appreciate amount of  $\text{NaS}_2\text{O}_8$  salts ( $\text{e}_s^- + \text{S}_2\text{O}_8^{2-} \rightarrow \text{SO}_4^{2-} + \text{SO}_4^{\bullet-}$ ).<sup>15,16</sup> In this case, the redox potential of DNA bases (T, G, A, C) radical cation was subsequently measured, indicating the sites of hole transfer along the DNA duplex and how easily the DNA can be oxidized by free radicals.<sup>17,18</sup>

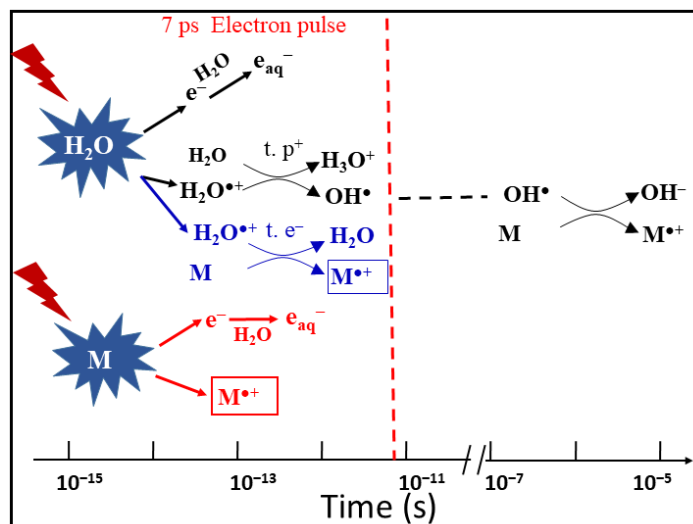


**Figure 4.3** Schematic description of the reactions occurring in solutions containing a solute M at high concentration. At *subpicosecond* time scales involving proton transfer (t. p<sup>+</sup>, black), direct ionizing of solutes M (red), ultrafast electron transfer (t.e<sup>-</sup>, blue) and electron relaxation. Picosecond electron pulse radiolysis is ready to observe the formation of  $\text{M}^{\bullet+}$  within the pulse. The oxidation of M by  $\text{OH}^\bullet$  radical takes place at longer time, which does not affect our observation.<sup>19</sup>

In radiation chemistry, the majority of fast radicals or electrons-induced reactions occur at a diffusion or nearly-diffusion controlled process with a second-order rate constant ranging from  $10^9$ - $10^{10} \text{ L}^{-1} \text{ mol s}^{-1}$  under ambient conditions.<sup>20,21</sup> For this reason, over past decades, pulse radiolysis based on a nanosecond electron pulse has been shown to be sufficient to fully resolve

numerous radicals' reactions on their own reaction time. However, as mentioned above, the water radical cation  $\text{H}_2\text{O}^{\bullet+}$  proceeds the chemical events much faster than 1 picosecond and hence a deep understanding of this radical's chemistry called for a shorter electron pulse. The femtosecond laser-driven accelerator has been established as our ELYSE facility, which achieves a high energy (7-8 MeV) electron beam with a pulse width of 7 ps.<sup>22</sup> The detecting system is based on the transient absorption spectroscopy with a probe light ranging from 380 nm to 1500 nm.<sup>23</sup> Similar picosecond pulse radiolysis facilities have been established over the world, such as the LEAF facility at Brookhaven National Laboratory and LINAC facility at Tokyo University *etc*, and many of them have reached their full capacity.<sup>24, 25, 26</sup> Therefore, this unique time resolved technique based on high energy electron pulse enables us, although not ideally, to explore the ultrafast chemical reactivity of  $\text{H}_2\text{O}^{\bullet+}$  through the scavenging method in a variety of highly concentrated aqueous solutions.

Accordingly, a short review of the key findings is presented to show the occurrence of ultrafast electron transfer of  $\text{H}_2\text{O}^{\bullet+}$  by using highly concentrated solutions. By observing the formation of secondary radicals such as  $\text{NO}_3^\bullet$ ,  $\text{SO}_4^{\bullet-}$ ,  $\text{X}_2^{\bullet-}$  ( $\text{X} = \text{Cl}, \text{Br}$ ) or  $\text{H}_2\text{PO}_4^\bullet$  at picosecond scale, the radiolytic yield of  $\text{H}_2\text{O}^{\bullet+}$  participating in the reaction as a function of concentration is obtained and isotopic effects have been comparatively studied. Our results imply the chemical situations where the reactivity of  $\text{H}_2\text{O}^{\bullet+}$  or  $\text{D}_2\text{O}^{\bullet+}$  plays a more important role in competition with proton transfer to generate  $\text{OH}^\bullet$  or  $\text{OD}^\bullet$  radicals. By further using the diffusion-kinetic simulations of the spur reactions induced by the incident electrons, we established the first semi-quantitative estimation of the  $\text{H}_2\text{O}^{\bullet+}$  radicals scavenging fractions for a wide range of solutes. In addition, it is suggested that  $\text{H}_2\text{O}^{\bullet+}$  is the strongest oxidative radical comparing with other oxidants in aqueous solutions based on an estimation of its redox potential value. Finally, it is rationalized that the oxidation of  $\text{H}_2\text{O}^{\bullet+}$  might be extended to the interface chemistry or biological system which constitutes as a similar water closely trapped environment with that in concentrated solutions.

#### 4.1.2 Oxidation reactions by radicals

Oxidation reaction is a very important class of chemical reactions in solution. One example is corrosion, that is to say, the alteration of a material by an oxidant, or oxidative stress which is a type of aggression of the constituents of the cell, involved in many diseases.<sup>27,28,29</sup> Some oxidizing species such as  $\text{O}_2$  are stable, but there are also many other reactive oxidizing species, which are

not stable in solution. The very oxidizing free radicals commonly known in aqueous solutions include  $\text{OH}^{\bullet}$ ,  $\text{O}_2^{\bullet-}$ ,  $\text{HO}_2^{\bullet}$ ,  $\text{CO}_3^{\bullet-}$ ,  $\text{NO}_3^{\bullet}$ ,  $\text{SO}_4^{\bullet-}$  and  $\text{HPO}_4^{\bullet-}$  *etc.* and can be generated in a radiation-chemical procedure.<sup>30</sup> These reactive radical species play a very important role because they act as intermediates in many mechanisms. Free radicals instinctually associated with unpaired electrons in their outer orbitals react with organic or inorganic compounds in various ways. They may abstract a hydrogen atom or add to an unsaturated bond, and they may also reduce or oxidize a substrate via one-electron transfer mechanism. Therefore, the chemistry of free radicals is very rich. In particular, their reactivity is very much studied in the metabolic system of the human being where they can trigger serious diseases.<sup>31</sup> But some of these radicals can also be used to treat certain diseases, such as cancer using radiation therapy. Because of their very high reactivity, the lifetime of these species is often very short, ranging from milliseconds to picoseconds. Their lifetime depends very much upon their environment. To observe the reactivity of these species, it is necessary to resort to sophisticated experimental setups that allow the monitoring of their reactions, sometimes ultrafast, as a function of time. Thus, to create these radical species, lasers or pulsed electron accelerators are often used, and coupled with a time-resolved detection method, thus exploiting the optical properties of transient species.

In past decades, numerous studies have been performed in relation with their properties using pulse radiolysis or photolysis methods.<sup>32</sup> The term of oxidizing a molecule means capturing an electron from another molecule. The oxidation force of a species is defined by its redox potential. The redox potential is an empirical quantity expressed in volts and denoted by  $E^\circ$  for the standard potential under conditions of normal concentration.<sup>33</sup> The values of the redox potential are expressed with respect to the reference potential of the standard or normal hydrogen electrode (NHE) taken equal to zero.<sup>2,34</sup> The higher the value of the redox potential is, the more oxidizing the species is. For example, molecule oxygen is an oxidative species and forms  $\text{O}_2^{\bullet-}$  by capturing an electron of a molecule and the redox potential of the  $\text{O}_2/\text{O}_2^{\bullet-}$  couple is -0.33 vs NHE.<sup>35</sup>

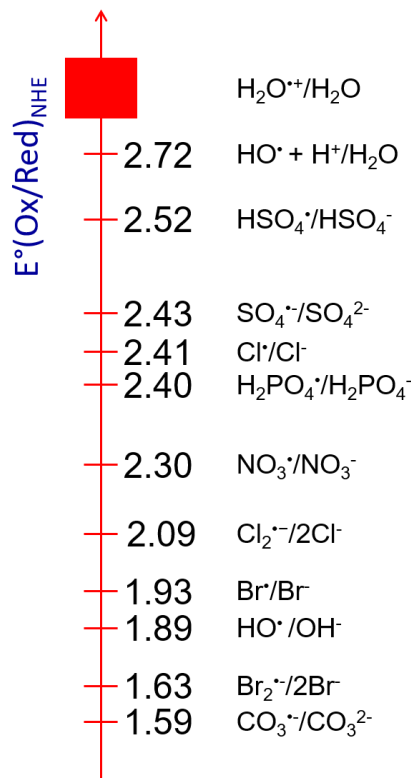


**Figure 4.4** Scale of the values of the redox potential of certain transient radicals with respect to the standard hydrogen electrode (V/NHE).<sup>19</sup>

The values of the redox potential of some transient radical species are reported in **Figure 4.4**. It is determined kinetically by pulse techniques according to their ability to oxidize molecules of known potential. In this series, the  $\text{OH}^\bullet$  radical in acid medium is a very strong oxidizing radical in aqueous solutions, comparing with others, such as  $\text{SO}_4^{\bullet-}$  (2.43 eV) or  $\text{H}_2\text{PO}_4^\bullet$  (2.40 eV).<sup>36</sup> It is reasonable because  $\text{OH}^\bullet$  radical is able to oxidize solutes such as  $\text{SO}_4^{2-}$  leading to the formation of the secondary radical  $\text{SO}_4^{\bullet-}$ . In water radiolysis, however, the oxidizing ability of its precursor ( $\text{H}_2\text{O}^{*+}$ ) due to its ultrafast proton transfer has not yet been considered. We use a simple thermodynamically cycle for a rough estimation of the redox potential of these radicals. The ionizing potential of a liquid water molecule is measured to be 11.16 eV by liquid-jet photoelectron spectroscopy, which is in accordance with the value (11.7 eV) from theoretical predictions by Mozumber.<sup>37</sup> The solvation energy of  $\text{H}_2\text{O}^{*+}$  is unknown but it is assumed that this energy value is similar with that of  $\text{H}_3\text{O}^+$ . In light of this, the standard redox potential of  $\text{H}_2\text{O}^{*+}/\text{H}_2\text{O}$  couple is higher than 3 eV vs NHE, showing it is indeed the strongest oxidizing species in liquid water (**Figure 4.4**).

Comparing with the high mobility of electrons produced in water radiolysis, the mobility of  $\text{H}_2\text{O}^{*+}$  is considered to be relatively low as the infrared spectroscopy study of water cluster radical cations  $(\text{H}_2\text{O})_n^{*+}$  ( $n = 3-11$ ) showed that it is localized and weakly hydrogen bound with its neighbouring water molecules.<sup>38</sup> The role of  $\text{H}_2\text{O}^{*+}$  in previous radiation chemical studies of dilute solutions was completely ignored. In fact, its chemistry strongly depends on the environment and much differ from that of  $\text{OH}^{\bullet}$  radicals, which often reacts with a substance via H abstraction or addition instead of one-electron transfer.<sup>39</sup> One may wonder how a radical cation that has such a short life can oxidize another species. Indeed, before reacting, the radical and the species that will be oxidized should diffuse to get closer to each other. But even if the electron transfer reaction is ultrafast, the diffusion of the reactants through the solvent molecules would require a minimum time (a diffusion limit of the rate constant). For example, the radical  $\text{OH}^{\bullet}$ , which has a very large diffusion coefficient ( $D = 2 \times 10^{-9} \text{ m}^2 \text{ s}^{-1}$ ),<sup>21</sup> must nevertheless diffuse during about 1  $\mu\text{s}$  to reach a molecule in solution at a concentration of the order of  $10^{-4} \text{ M}$ . If the solute is in 1 molar concentration, this diffusion time is reduced to 60 ps. Under these conditions, the reaction is not likely to take place for the radical cation  $\text{H}_2\text{O}^{*+}$  because of its immediate proximity with  $\text{H}_2\text{O}$  and its proton transfer reaction has a lifetime much shorter than the time required for diffusion. Therefore, the only possibility of reaction for this radical is the in situ reaction. That is to say, this radical must be in contact with a target molecule in a concentration of similar magnitude to that of water. Thus the diffusion is no longer necessary and it can possibly oxidize the molecule which is in its immediate vicinity. The verification of the occurrence of the ultrafast electron transfer of  $\text{H}_2\text{O}^{*+}$  has initially been made in aqueous NaX ( $X = \text{Cl}, \text{Br}$ ) solutions by picosecond pulse radiolysis.<sup>40-43</sup> In these systems, the energy in proportion to the electrons fraction, is also deposited on the solutes, so the direct ionizing of the solute itself cannot be avoided, resulting in the additional yield of secondary radicals ( $\text{X}^{\bullet}$  or  $\text{X}_2^{\bullet-}$ ). To make it easier to be understood, it is worth to note that in radiation-induced chemical reactions, the amount or concentration of radicals generated is associated with the radiation dose. The radiolytic yield or a more specific name G value is defined as the number of mole produced per joule of absorbed dose. Halide and concentrated acidic aqueous solutions are proper system to probe the reactivity of  $\text{H}_2\text{O}^{*+}$ .

As noted above, there is additivity between direct and indirect effects of ionizing radiation in the sample. The energy deposited in the solute is related its electron fraction. Consequently, for a given concentrated aqueous solution the observed radiolytic yield can be expressed as follow:

$$G_{obs} = \frac{A_{obs}}{\varepsilon \times l \times Dose \times F} \quad \text{EQ.4-2}$$

$$G_{obs} = f_s G_{dir} + (1-f_s) G_{indir} \quad \text{EQ.4-3}$$

Here,  $G_{obs}$  is the observed radiolytic yield,  $G_{dir}$  is the yield of the direct effect expressed in the molecules formed per Joule absorbed by the solute. It is assumed to be independent of the concentration of the solute S.  $G_{indir}$  is the maximum yield of the indirect effect. It depends essentially on the yields of the primary species formed by water radiolysis which react with S give the considered transformation.  $f_s$  is the electron fraction of the solute, and  $(1-f_s)$  is the electron fraction of water. F is the dose corrected factor which is related to the density and the electron concentration of the solution.<sup>44</sup> It could be determined as follows:

$$F = \frac{d(solution)}{d(H_2O)} \times \frac{N_{e^-}(Solute) \times \frac{p}{M(solute)} + N_{e^-}(D_2O) \times \frac{100-p}{M(D_2O)}}{N_{e^-}(H_2O) \times \frac{100}{M(H_2O)}} \quad \text{EQ.4-4}$$

Where  $d$  is the density,  $N_{e^-}$  is the electron number,  $p$  is the weight of the solute in 100 g of solution,  $(100-p)$  is the weight of the solvent, i.e.  $D_2O$  in 100 g of the solution, and  $M$  is the molecular weight. Accordingly, the indirect effect of water cation radical could be deduced.

### 4.1.3 Reactivity of $H_2O^{*+}$ in halide solution

Several studies in the highly concentrated  $Br^-$  and  $Cl^-$  solutions have been performed on the purpose of capturing  $H_2O^{*+}$ .<sup>40-43</sup> As an example in  $Cl^-$  aqueous solution, the products of radiation-induced oxidation of  $Cl^-$  ions are observed at 370 nm as shown in **Figure 4.5**. The following reactions are considered:

**Table 4.1** The primary radiation induced reactions involved in  $\text{Cl}^-/\text{H}_2\text{O}$  solution

<i>Primary radiation induced reaction</i>	<i>Rate coefficient (<math>\text{L mol}^{-1} \text{s}^{-1}</math>)</i>	
$\text{H}_2\text{O} \rightarrow \text{H}_2\text{O}^{\bullet+} + \text{e}^-$		R1
$\text{e}^- + \text{H}_2\text{O}^{\bullet+} \rightarrow \text{H}_2\text{O}^*$		R2
$\text{H}_2\text{O}^{\bullet+} + \text{H}_2\text{O} \rightarrow \text{H}_3\text{O}^+ + \text{OH}^\bullet$	$8.0 \times 10^{12}$	R3
$\text{e}_s^- + \text{H}_3\text{O}^+ \rightarrow \text{H}^\bullet + \text{H}_2\text{O}$	$2.3 \times 10^{10}$	R4
<i>Reactions <math>\text{Cl}^-/\text{H}_2\text{O}</math></i>		
$\text{Cl}^- \rightarrow \text{Cl}^\bullet + \text{e}^-$		R5
$\text{OH}^\bullet + \text{Cl}^- \rightarrow \text{ClOH}^{\bullet-}$	$4.3 \times 10^9$	R6
$\text{ClOH}^{\bullet-} \rightarrow \text{Cl}^- + \text{OH}^\bullet$	$6.1 \times 10^9$	R7
$\text{Cl}^\bullet + \text{Cl}^- \rightarrow \text{Cl}_2^{\bullet-}$	$8.5 \times 10^9$	R8
$\text{Cl}^- + \text{H}_2\text{O}^{\bullet+} \rightarrow \text{Cl}^\bullet + \text{H}_2\text{O}$		R9
<i>Reactions <math>\text{Cl}^-/\text{H}_3\text{O}^+</math></i>		
$\text{ClOH}^{\bullet-} + \text{H}^+ \rightarrow \text{Cl}^\bullet + \text{H}_2\text{O}$		R10

The reaction R5 is due to the direct effect that means one-electron oxidation of  $\text{Cl}^-$  by ionizing radiation. It occurs when the number of electron of the solute in the solution is not negligible compared to that of water (**Figure 4.5**). It happens when the concentration is higher than around 0.5 M. The reaction R6 is issued from the water radiolysis. That reaction is not complete because the reaction R7 takes place. The reaction R8 is controlled by diffusion and finally, the electron transfer reaction R9 is ultrafast and can occur if the radical cation of water is formed in contact of  $\text{Cl}^-$ .



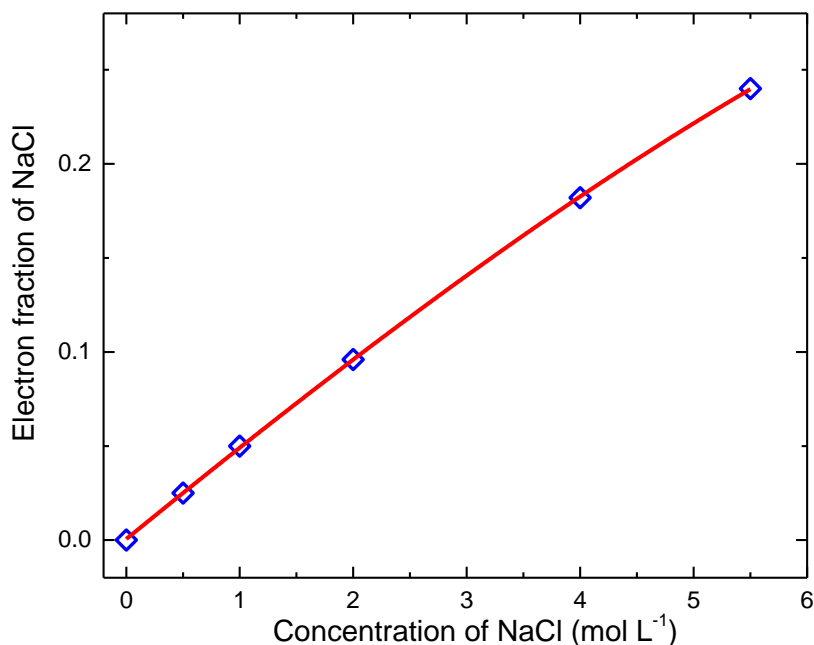


**Figure 4.5** The electron fraction of NaCl in aqueous solution as function of concentration. The red solid line is a guide for eyes. Data adapted from ref <sup>41</sup>.

The initial absorbance reported in **Figure 4.6** corresponds to the formation of  $\text{ClOH}^{\bullet-}$  and  $\text{Cl}_2^{\bullet-}$  radicals both absorbing around 370 nm, but with different extinction coefficient.  $\text{ClOH}^{\bullet-}$  radicals are produced by an equilibrium with  $\text{OH}^{\bullet}$  scavenging reaction and  $\text{Cl}_2^{\bullet-}$  is generated from direct ionizing of  $\text{Cl}^-$  and probably from  $\text{H}_2\text{O}^{*+}$  oxidation followed by a fast reaction of  $\text{Cl}^{\bullet}$  with  $\text{Cl}^-$ . As the extinction coefficient of each species at 370 nm is well-known, the yield of the radicals can be analyzed from the kinetics. The kinetics simulations show the amount of  $\text{Cl}_2^{\bullet-}$  formation within the electron pulse increases notably at an increased  $\text{Cl}^-$  concentration. It also reveals that the direct ionization of  $\text{Cl}^-$  cannot solely explain the significant amount of fast  $\text{Cl}_2^{\bullet-}$  formation at short timescale. When the acid is used  $\text{ClOH}^{\bullet-}$  is converted into  $\text{Cl}^{\bullet}$  (R10), one can readily see in **Figure 4.6** that the total absorption in 0.5 M acid solutions very nearly matches that for 8 M  $\text{Cl}^-$  neutral solutions where the  $\text{OH}^{\bullet}$  radical scavenging capacity is much higher.<sup>41</sup>

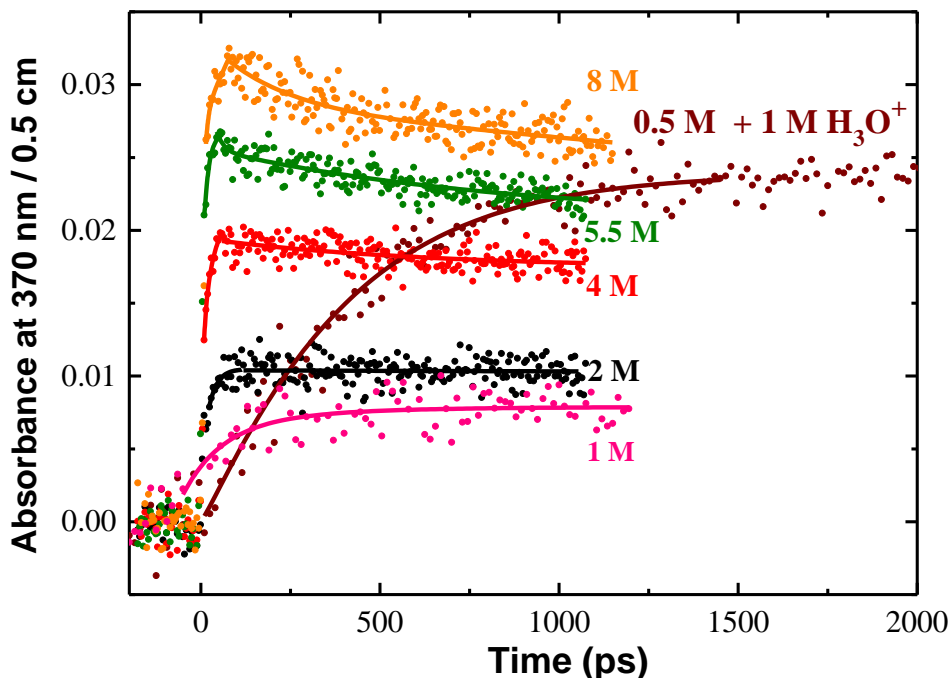


**Figure 4.6** Transient kinetics observed at 370 nm in a wide range of NaCl aqueous solutions to show the products of oxidation of  $\text{Cl}^-$ . The absorbance of hydrated electron and transient signal from irradiated fused silica were subtracted from the raw data. The solid lines are drawn to guide the eye. The absorbed dose (22.5 Gy per pulse) was the same for all kinetics. The acid used to adjust the pH of solution was  $\text{HClO}_4$ . Adapted from REF <sup>41</sup>

This difference between acid and neutral solutions is shown in **Figure 4.6** for 0.5 M  $\text{Cl}^-$  solutions. Conversion of the  $\text{ClOH}^{\bullet-}$  is relatively slow in acid solutions, but it is total and continues to a much greater extent than in neutral solutions.

The predictions of the diffusion kinetic modeling of the spur for solutions containing 5.5 M  $\text{Cl}^-$  are shown in **Figure 4.7**. Also shown in **Figure 4.7** are the predicted yields for just the  $\text{Cl}_2^{\bullet-}$  radical alone. The standard water radiolysis model gives a much slower products' formation and predicts a maximum that is considerably lower than the observed absorbance. The direct ionization of  $\text{Cl}^-$  to give  $\text{Cl}^{\bullet}$  and  $\text{e}_s^-$  in 5.5 M  $\text{Cl}^-$  solutions can be included by assuming 0.24 percent of the energy is deposited directly into the  $\text{Cl}^-$ . Again the model predictions are too slow and the maximum is lower than the observed absorbance. Clearly, the only method to the increase production of  $\text{ClOH}^{\bullet-}$  and  $\text{Cl}_2^{\bullet-}$  radicals on the short time scale is to have a scavenging process for  $\text{Cl}^-$  reaction with a water transient species. Inclusion of the reaction of  $\text{Cl}^-$  with  $\text{H}_2\text{O}^{\bullet+}$  increases the

predicted absorbance with faster rise times. For 5.5 M  $\text{Cl}^-$  solution almost 30% of the  $\text{H}_2\text{O}^{\bullet+}$  must be scavenged by  $\text{Cl}^-$  to match the observed absorbance measurements.

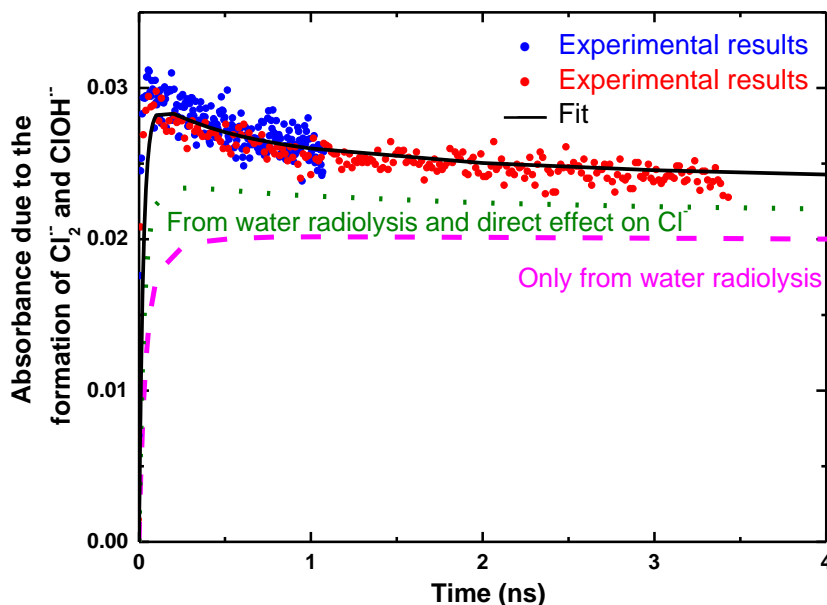


**Figure 4.7** Observed absorbance decay (blue and red data for short and long time scale) in solution containing 5.5 M NaCl. with model simulations of spur reactions: (dashed line) simple water model alone without any direct effect; (dotted line) with direct ionization of  $\text{Cl}^-$ ; (solid line) with direct ionization of  $\text{Cl}^-$  and 30% scavenging of  $\text{H}_2\text{O}^{\bullet+}$  by  $\text{Cl}^-$ . The dose was 22.5 Gy per pulse. Adapted from reference<sup>41</sup>.

Therefore, it is concluded that the precursor of the  $\text{OH}^\bullet$  radical, i.e.,  $\text{H}_2\text{O}^{\bullet+}$  radical, forms  $\text{Cl}^\bullet$  atom within the electron pulse and the  $\text{Cl}^\bullet$  atom reacts subsequently with  $\text{Cl}^-$  to form  $\text{Cl}_2^{\bullet-}$  on very short time scales. It is important to note that the reduction potential of  $\text{Cl}^-$  is very high and only a powerful oxidizing species can transform  $\text{Cl}^-$  into  $\text{Cl}^\bullet$  ( $E^\circ \text{Cl}^\bullet/\text{Cl}^- = 2.41 \text{ V}$ ,  $E^\circ \text{OH}^\bullet/\text{OH}^- = 1.9 \text{ V}$  in neutral solution)<sup>45</sup>.

#### 4.1.4 Reactivity of $\text{H}_2\text{O}^{\bullet+}$ in concentrated acidic solution

As presented in **Figure 4.4**,  $\text{H}_2\text{PO}_4^-$ ,  $\text{NO}_3^-$  and  $\text{SO}_4^{2-}$  can be oxidized by  $\text{H}_2\text{O}^{\bullet+}$  according to their redox potential. Unfortunately, as the yield of the secondary radicals from direct ionizing is not quantitatively known, the exact radiolytic yield and reactivity of  $\text{H}_2\text{O}^{\bullet+}$  in various concentrations still remain to be elucidated. Recently, several studies have performed experiments

by picosecond pulse radiolysis to probe the chemistry of  $\text{H}_2\text{O}^{\bullet+}$  in the aqueous solutions containing various concentration of  $\text{SO}_4^{2-}$ ,  $\text{H}_2\text{PO}_4^-$  and  $\text{NO}_3^-$ .<sup>46</sup>

#### I. $\text{H}_3\text{PO}_4/\text{H}_2\text{O}$

In analogy to  $\text{H}_2\text{SO}_4$  system,  $\text{H}_3\text{PO}_4$  solutions also have the above-mentioned advantages. Firstly, the oxidation of phosphoric acid by  $\text{OH}^\bullet$  is more difficult than that of sulfuric acid. The rate constant of the reaction between  $\text{OH}^\bullet$  and the phosphoric acid is low ( $10^4 \text{ L mol}^{-1} \text{ s}^{-1}$ , as shown in the **Table 4.3**). Second, the acidic form of phosphate radicals ( $\text{H}_2\text{PO}_4^\bullet$ ) exhibiting an absorption peak at 520 nm with a molar extinction coefficient of  $1850 \text{ Lmol}^{-1}\text{cm}^{-1}$  is the indicator of direct and  $\text{H}_2\text{O}^{\bullet+}$  oxidation. Last and worthy to be noted, the phosphate group ubiquitously occurs in bio systems.

For example, if a biomolecule such as DNA is under the exposure of ionizing radiation, the sugar – phosphate backbone can be damaged either by direct detachment or by indirect oxidation from the water radicals and the phosphate centered radicals are expected to be formed with appreciable yields, leading to subsequent biological effects.<sup>47,48</sup> The Phosphate radical reacts with numerous organic or inorganic compounds by abstraction or addition and also by electron transfer. It is therefore important to estimate the yield of damage through the direct radiation effect and through oxidation by  $\text{H}_2\text{O}^{\bullet+}$ . Consequently, the picosecond pulse radiolysis measurements were further performed in the phosphate system.<sup>49</sup>

**Table 4.3** The primary radiation induced reactions involved in  $\text{H}_3\text{PO}_4/\text{H}_2\text{O}$  solution

<i>Primary radiation induced reaction</i>	<i>Rate coefficient (<math>\text{L mol}^{-1} \text{s}^{-1}</math>)</i>	
$\text{H}_2\text{O} \rightarrow \text{H}_2\text{O}^{\bullet+} + \text{e}^-$		R1
$\text{e}^- + \text{H}_2\text{O}^{\bullet+} \rightarrow \text{H}_2\text{O}^*$		R2
$\text{H}_2\text{O}^{\bullet+} + \text{H}_2\text{O} \rightarrow \text{H}_3\text{O}^+ + \text{OH}^\bullet$	$8.0 \times 10^{12}$	R3
$\text{e}_s^- + \text{H}_3\text{O}^+ \rightarrow \text{H}^\bullet + \text{H}_2\text{O}$	$2.3 \times 10^{10}$	R4
<i>Reactions <math>\text{H}_3\text{PO}_4/\text{H}_2\text{O}</math></i>		
$\text{PO}_4^{3-} \rightarrow \text{PO}_4^{\bullet 2-} + \text{e}^-$		R11
$\text{H}_3\text{PO}_4 + \text{H}_2\text{O}^{\bullet+} \rightarrow \text{H}_2\text{PO}_4^\bullet + \text{H}_3\text{O}^+$		R12
$\text{H}_3\text{PO}_4 + \text{OH}^\bullet \rightarrow \text{H}_2\text{PO}_4^\bullet + \text{H}_2\text{O}$	$4.2 \times 10^4$	R13
$\text{H}_2\text{PO}_4^- + \text{OH}^\bullet \rightarrow \text{HPO}_4^{\bullet -} + \text{H}_2\text{O}$	$2.0 \times 10^4$	R14
$\text{H}_2\text{PO}_4^\bullet + \text{H}^\bullet \rightarrow \text{H}_3\text{PO}_4$	$1.3 \times 10^{10}$	R15
$\text{H}_2\text{PO}_4^\bullet + \text{H}_2\text{PO}_4^\bullet \rightarrow \text{H}_4\text{P}_2\text{O}_8$	$2.5 \times 10^9$	R16
$\text{H}_2\text{PO}_4^\bullet + \text{OH}^\bullet \rightarrow \text{H}_3\text{PO}_5$	$4.0 \times 10^9$	R17
$\text{H}_2\text{PO}_4^\bullet + \text{HO}_2^\bullet \rightarrow \text{H}_3\text{PO}_4 + \text{O}_2$	$3.0 \times 10^9$	R18
$\text{H}_2\text{PO}_4^\bullet + \text{H}_2\text{O}_2 \rightarrow \text{H}_3\text{PO}_4 + \text{HO}_2^\bullet$	$3.5 \times 10^9$	R19

As shown in Figure 4.8, the overall trend is found to increase with the electron fraction of solute and reaches the maximum in the neat phosphoric acid. As the oxidation of  $\text{H}_3\text{PO}_4$  by  $\text{OH}^\bullet$  radical is too slow to occur on the picosecond time scale, the supplementary yield that could be deduced by EQ. 4-2 and 4.3,  $G_{\text{indir}}$ , observed for each concentration is considered solely due to the scavenging of  $\text{H}_2\text{O}^{\bullet+}$  by rapid electron transfer reaction.

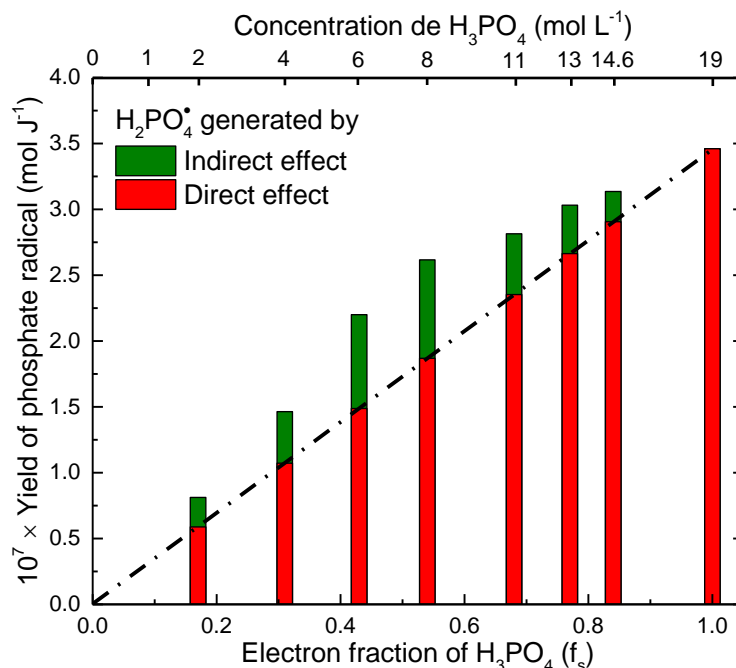


**Figure 4.8** Radiolytic yield of phosphoric acid radical versus the electron fraction of the solute. The obtained yield at 19 M is considered as the direct effect yield that is linearly extrapolated to the zero (dash line). The superliner contribution (green bars) is due to the charge transfer reaction involving water radical cation (revised)  $\text{H}_2\text{O}^{*+}$ .

## II. $\text{HNO}_3/\text{H}_2\text{O}$

$\text{HNO}_3$  is also a suitable acid to study the chemistry of  $\text{H}_2\text{O}^{*+}$  as it could generate nitrite radical,  $\text{NO}_2^{\bullet}$  that exhibits a broad absorption band in the visible range. As shown in **Table 4.4**, it is worth noting that the rate coefficient of the reaction  $\text{OH}^{\bullet}$  and  $\text{HNO}_3$  is 4 times higher than that with  $\text{H}_2\text{SO}_4$ . For  $\text{H}_3\text{PO}_4$ , this reaction cannot be taken in account in picosecond radiolysis measurements because the reaction occurs in millisecond range. Furthermore, concentrated  $\text{HNO}_3$  is able to decompose to  $\text{NO}_2$ ,  $\text{O}_2$  and  $\text{H}_2\text{O}$  at room temperature so it is necessary to pay particular attention to the concentration of  $\text{HNO}_3$ . To date, several investigations have been performed to study the formation pathways of  $\text{NO}_2^{\bullet}$  with different time scale pulse radiolysis and simulations.<sup>10,40,50,51</sup> Balcerzyk et al. succeeded in separating the direct and indirect effect of radiation on  $\text{HNO}_3$ , and found that the direct effect on the formation of  $\text{NO}_2^{\bullet}$  is not negligible when the concentration of  $\text{HNO}_3$  is higher than 1 M. Very recently, Musat *et al.* presented a systematic investigation of the radiolysis of  $\text{HNO}_3$  acid from picosecond to nanosecond both under room temperature and 80°C conditions.

**Table 4.4** The primary radiation induced reactions involved in  $\text{H}_3\text{NO}_3/\text{H}_2\text{O}$  solution

<i>Primary radiation induced reaction</i>	<i>Rate coefficient (<math>\text{L mol}^{-1} \text{s}^{-1}</math>)</i>	
$\text{H}_2\text{O} \rightarrow \text{H}_2\text{O}^{\bullet+} + \text{e}^-$		R1
$\text{e}^- + \text{H}_2\text{O}^{\bullet+} \rightarrow \text{H}_2\text{O}^*$		R2
$\text{H}_2\text{O}^{\bullet+} + \text{H}_2\text{O} \rightarrow \text{H}_3\text{O}^+ + \text{OH}^\bullet$	$8.0 \times 10^{12}$	R3
$\text{e}_s^- + \text{H}_3\text{O}^+ \rightarrow \text{H}^\bullet + \text{H}_2\text{O}$	$2.3 \times 10^{10}$	R4
<i>Reactions <math>\text{H}_2\text{SO}_4/\text{H}_2\text{O}</math></i>		
$\text{NO}_3^- \rightarrow \text{NO}_3^\bullet + \text{e}^-$		R20
$\text{NO}_3^- + \text{e}^- \rightarrow \text{NO}_3^{\bullet 2-}$	$4.5 \times 10^{12}$	R21
$\text{NO}_3^- + \text{H}_2\text{O}^{\bullet+} \rightarrow \text{NO}_3^\bullet + \text{H}_2\text{O}$		R22
$\text{HNO}_3 + \text{OH}^\bullet \rightarrow \text{NO}_3^\bullet + \text{H}_2\text{O}$	$5.3 \times 10^7$	R23
$\text{NO}_3^- + \text{H}^\bullet \rightarrow \text{HNO}_3^{\bullet-}$	$1.0 \times 10^7$	R24
$\text{NO}_3^- + \text{e}_s^- \rightarrow \text{NO}_3^{\bullet 2-}$	$9.7 \times 10^9$	R25

The absorbance of  $\text{NO}_3^\bullet$  recorded just after the electron pulse with increasing concentration keeps the same trend with the one observed in  $\text{H}_3\text{PO}_4$  (**Figure 4.9**). **Figure 4.10** presents the recorded kinetics at 640 nm on picosecond and nanosecond range in the solutions containing different concentrations of  $\text{HNO}_3$ . The time evolution absorption of the  $\text{NO}_3^\bullet$  at 640 nm for solutions at different concentration shows no decay up to 400 ps after subtracting the contribution of the solvated electron. At longer time, the yield of  $\text{NO}_3^\bullet$  increases due to the reaction of  $\text{OH}^\bullet$  and  $\text{HNO}_3$ .

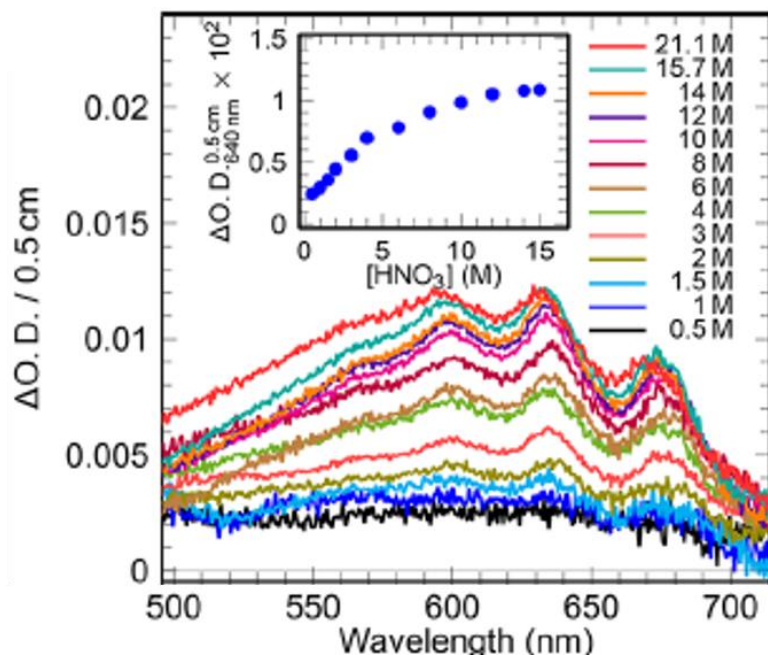


**Figure 4.9** Transient absorption spectra at 22.5 °C of  $\text{NO}_3^\bullet$  recorded just after the passage of the 7 ps electron pulse for  $\text{HNO}_3$  solutions >2 M. The transient spectra for 0.5, 1, 1.5, and 2 M are recorded after the decay of the solvated electron signal (300, 200, 200, and 100 ps, respectively, after the electron pulse). The spectra are shifted by 1.5 mOD for clarity. The inset presents the variation of the measured absorbance at 640 nm as a function of the solution concentration. By Musat *et al.*<sup>10</sup>

**Figure 4.11** shows that the observed yield of  $\text{NO}_3^\bullet$  just after the 7 ps electron pulse increases with the concentration of  $\text{HNO}_3$ . When considering the initial radiolytic yields of  $\text{NO}_3^\bullet$  radicals, we also need to consider the scavenging of the  $\text{H}_2\text{O}^{*+}$  by  $\text{NO}_3^-$  (**R22**). In the case of concentrated  $\text{HNO}_3$  solutions, this reaction becomes non-negligible. This mechanism is known to play a role in the formation of the radicals of  $\text{HNO}_3$  and has also been observed in concentrated sulfuric acid and phosphoric acid solutions. In this work, Musat *et al.* assumed that the yield of the  $\text{H}_2\text{O}^{*+}$  is the same as that of hydrated electrons measured in the picosecond range, i.e.,  $4.5 \times 10^{-7} \text{ mol J}^{-1}$ , then calculated the value of the coefficient of  $\text{H}_2\text{O}^{*+}$  that reacts with  $\text{NO}_3^-$ . They estimated the value of  $\alpha$  is of 60% for the 15.7 M solution of  $\text{HNO}_3$ , and of 20% for the 2 M solution **Figure 4.14 (b)**.



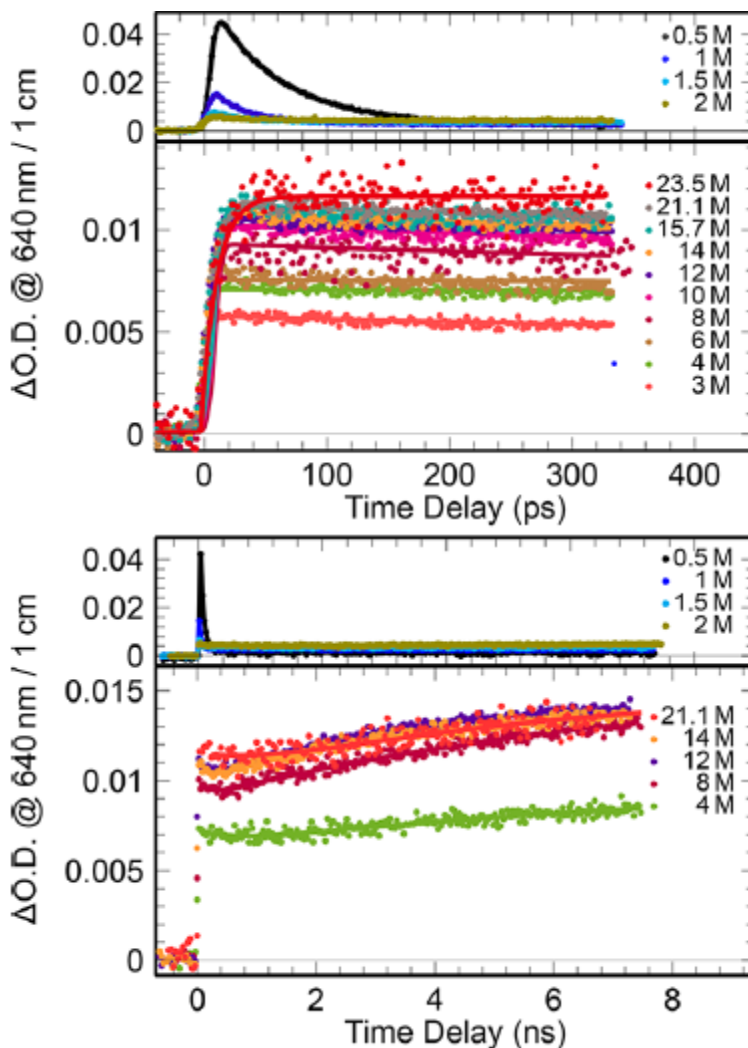


**Figure 4.10** Recorded kinetics at 640 nm in solutions containing different concentrations of  $\text{HNO}_3$  at 22.5 °C. By Musat et al.<sup>10</sup>

The total scavenging yield of oxidizing radicals ( $\text{OH}^\bullet$  and its precursor  $\text{H}_2\text{O}^{*+}$ ) could be determined by subtraction the direct effect yield of  $\text{NO}_3^\bullet$  from its maximum yield,  $G(\text{NO}_3^\bullet)_{\text{max}}$  and by taking into account the dose absorbed by water. To find total scavenging yield as mentioned above, we excluded the two solutions with the highest concentrations for which the value of  $f_w$  is very low, inducing large errors in the calculations (**Table 4.4**). The maximum value of  $(4.7 \pm 0.4) \times 10^{-7} \text{ mol J}^{-1}$  indicates that almost all  $\text{H}_2\text{O}^{*+}$  and  $\text{OH}^\bullet$  are scavenged by  $\text{HNO}_3$ , forming  $\text{NO}_3^\bullet$ . This value is close to the yield of  $\text{OH}^\bullet$  radical measured recently at 7 ps in neat water,  $(5.0 \pm 0.2) \times 10^{-7} \text{ mol} \cdot \text{J}^{-1}$  and the maximum scavenged yield of  $\text{H}_2\text{O}^{*+}$  in sulfuric acid,  $(4.75 \pm 0.2) \times 10^{-7} \text{ mol} \cdot \text{J}^{-1}$ , a value

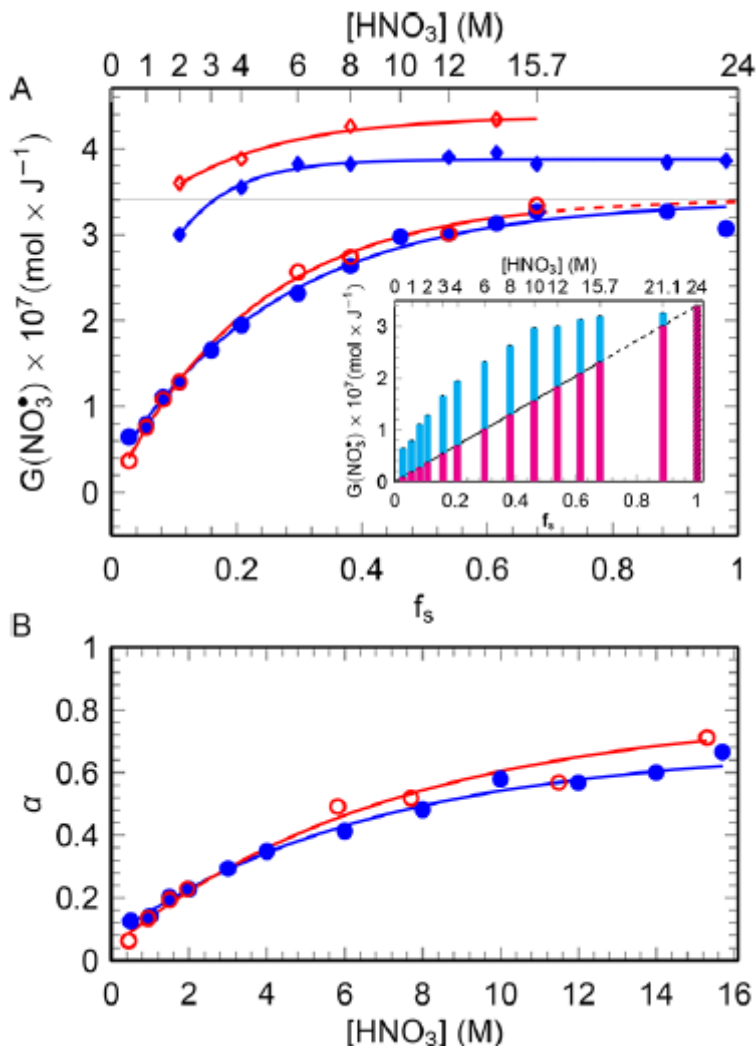
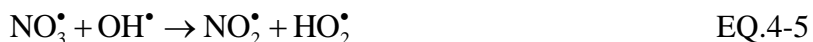


**Figure 4.11** (A) Observed radiolytic yields of  $\text{NO}_3^\bullet$  after the 7 ps electron pulse as a function of the solvent electron fraction in the investigated solutions at 22.5 °C (blue) and 80 °C (red), and the maximum yield of  $\text{NO}_3^\bullet$  measured at different concentrations. For the lowest concentrations the presented yields are measured after the decay of the solvated electron. Inset: Observed radiolytic yields of  $\text{NO}_3^\bullet$  after the 7ps electron pulse as a function of the solvent fraction in the investigated solutions at 22.5 °C, displaying the contribution of direct effects (red) and indirect effects (blue) to the observed yield. (B) Contribution of the ultrafast indirect effect (value of  $\alpha$ ) to the observed  $\text{NO}_3^\bullet$  radiolytic yields as a function of the investigated solutions concentration at 22.5 °C (blue) and 80 °C (red). The work was performed by Musat *et al.*<sup>10</sup>

higher than the corresponding one in homogeneous step,  $(2.8 \pm 0.2) \times 10^{-7} \text{ mol} \cdot \text{J}^{-1}$ . The high yield of  $\text{NO}_3^\bullet$  formed from the reactions with  $\text{OH}^\bullet$  and its precursor  $\text{H}_2\text{O}^{*+}$  in concentrated  $\text{HNO}_3$  solutions (8–15.7 M) indicates that the decay of  $\text{NO}_3^\bullet$  in the nonhomogeneous step (spur reactions)

is negligible, contrary to the case of  $\text{OH}^\bullet$  radical and solvated electron in water. In fact, the only efficient reaction of  $\text{NO}_3^\bullet$  decay, during the first nanosecond, is



This reaction is in competition with the reaction R23, which is dominant at the high concentration of undissociated  $\text{HNO}_3$ . Other decay reactions are rather slow to occur on a nanosecond time-scale.

### III. $\text{H}_2\text{SO}_4/\text{H}_2\text{O}$

Sulfuric acid solution constitutes an ideal system to verify the hypothesis and to investigate the reactivity of  $\text{H}_2\text{O}^{\bullet+}$  due to several reasons. First, it is a homogenous phase without molecules clustering, which guarantees the sufficient close encounters ( $\text{H}_2\text{O}^{\bullet+} \dots \text{SO}_4^{2-}$ ).<sup>52</sup> Second, the yield of  $\text{SO}_4^{\bullet-}$  from the direct effect can be measured from the almost neat sulfuric acid (18 M) and it is possible to correlate this contribution to various concentrations by using the factor of the electron fraction. Third, as shown in **Table 4.2**, the rate constant of the reaction of  $\text{OH}^\bullet$  radicals with  $\text{HSO}_4^-$  (or  $\text{H}_2\text{SO}_4$ ) is relatively low ( $10^8 \text{ L}^{-1} \text{ mol cm}^{-1}$ ) and the reaction time is several nanoseconds at even the highest concentration.<sup>53</sup> Fourth, the counter ion of acid is  $\text{H}^+$  without valence electron. Thus, unlike the salt ions such as  $\text{Na}^+$  or  $\text{Mg}^{2+}$ , the direct ionizing of  $\text{H}^+$  itself does not yield to any oxidizing species. The last reason is that the spectrum and the molar extinction efficiency  $1600 \text{ M}^{-1} \text{ cm}^{-1}$  on the maximum of secondary radicals  $\text{SO}_4^{\bullet-}$  are well-known, so the yield is ready to be deduced.<sup>10,49,54</sup>

**Figure 4.3** presents the schematic description of the possible reactions occurring in sulfuric acid solutions at *subpicosecond* time scales involving proton transfer (t.  $\text{p}^+$ , black), direct ionizing of solutes  $\text{SO}_4^{2-}$  (red), ultrafast electron transfer (t.  $\text{e}^-$ , blue) and electron relaxation. In order to clarify all of these processes, we performed a picosecond pulse radiolysis investigation of solutions containing a wide range of sulfuric acid concentration.<sup>46</sup> **Figure 4.12** displays the absorption spectrum of  $\text{SO}_4^{\bullet-}$  in a variety of sulfuric acid solutions ranging from 1 M up to 18 M observed on the ps timescale (immediately after the 7 ps electron pulse). It has a typical absorption band at 450 nm. The shape of this band does not depend to the concentration and no significant change in extinction coefficient was found in the concentrated sulfuric acid as previous reported.<sup>52</sup> It only slightly shifts to higher wavelength in response to higher concentration owing to the acid equilibrium of  $\text{SO}_4^{\bullet-}$  to  $\text{HSO}_4^\bullet$ . As it is known the  $\text{SO}_4^{\bullet-}$  formation does not correspond to  $\text{OH}^\bullet$

radical at this observed timescale, only two possible pathways accounts for producing  $\text{SO}_4^{\bullet-}$  radicals, that is direct ionizing and ultrafast electron transfer from  $\text{H}_2\text{O}^{\bullet+}$ .

**Table 4.2** The primary radiation induced reactions involved in  $\text{H}_2\text{SO}_4/\text{H}_2\text{O}$  solution

<i>Primary radiation induced reaction</i>	<i>Rate coefficient (<math>\text{L mol}^{-1} \text{s}^{-1}</math>)</i>	
$\text{H}_2\text{O} \rightarrow \text{H}_2\text{O}^{\bullet+} + \text{e}^-$		R1
$\text{e}^- + \text{H}_2\text{O}^{\bullet+} \rightarrow \text{H}_2\text{O}^*$		R2
$\text{H}_2\text{O}^{\bullet+} + \text{H}_2\text{O} \rightarrow \text{H}_3\text{O}^+ + \text{OH}^\bullet$	$8.0 \times 10^{12}$	R3
$\text{e}_s^- + \text{H}_3\text{O}^+ \rightarrow \text{H}^\bullet + \text{H}_2\text{O}$	$2.3 \times 10^{10}$	R4
<i>Reactions <math>\text{H}_2\text{SO}_4/\text{H}_2\text{O}</math></i>		
$\text{SO}_4^{2-} \rightarrow \text{SO}_4^{\bullet-} + \text{e}^-$		R20
$\text{H}_2\text{SO}_4 + \text{H}_2\text{O}^{\bullet+} \rightarrow \text{HSO}_4^\bullet + \text{H}_3\text{O}^+$		R21
$\text{H}_2\text{SO}_4 + \text{OH}^\bullet \rightarrow \text{HSO}_4^{\bullet-} + \text{H}_2\text{O}$	$1.4 \times 10^7$	R22
$\text{HSO}_4^- + \text{OH}^\bullet \rightarrow \text{SO}_4^{\bullet-} + \text{H}_2\text{O}$	$4.7 \times 10^5$	R8
$\text{SO}_4^{\bullet-} + \text{H}^\bullet \rightarrow \text{HSO}_4^-$	$1.0 \times 10^{10}$	R9
$\text{SO}_4^{\bullet-} + \text{SO}_4^{\bullet-} \rightarrow \text{S}_2\text{O}_8^{2-}$	$7.6 \times 10^8$	R10
$\text{SO}_4^{\bullet-} + \text{OH}^\bullet \rightarrow \text{HSO}_5^-$	$1.0 \times 10^9$	R11
$\text{SO}_4^{\bullet-} + \text{S}_2\text{O}_8^{2-} \rightarrow \text{S}_2\text{O}_8^{\bullet-} + \text{SO}_4^{2-}$	$6.6 \times 10^5$	R12
$\text{SO}_4^{\bullet-} + \text{HO}_2^\bullet \rightarrow \text{HSO}_4^- + \text{O}_2$	$3.5 \times 10^9$	R13
$\text{S}_2\text{O}_8^{2-} + \text{H}^\bullet \rightarrow \text{SO}_4^{\bullet-} + \text{HSO}_4^-$	$2.5 \times 10^7$	R14
$\text{HSO}_5^- + \text{H}^\bullet \rightarrow \text{SO}_4^{\bullet-} + \text{H}_2\text{O}$	$2.2 \times 10^8$	R15

From **Figure 4.12**, it can be seen that after dose correction, the absorbance of  $\text{SO}_4^{\bullet-}$  in relation with its radiolytic yield is increasing with the sulfuric concentration from 1 M to 12 M. This can be understood because the direct ionizing becomes more important as more solutes are present. Interestingly, from 12 M to 18 M as water molecules are not abundant, the absorbance continuously drops. These observations clearly present an evidence that direct ionizing alone cannot be the only

effect, interpreting the formation of  $\text{SO}_4^{\bullet-}$  is due to at least two pathways, otherwise the absorption would keep increasing. There must exist an ultrafast process of  $\text{H}_2\text{O}^{*+}$  that occurs on the timescale of femtosecond, accounting for the supplementary yield of  $\text{SO}_4^{\bullet-}$ .

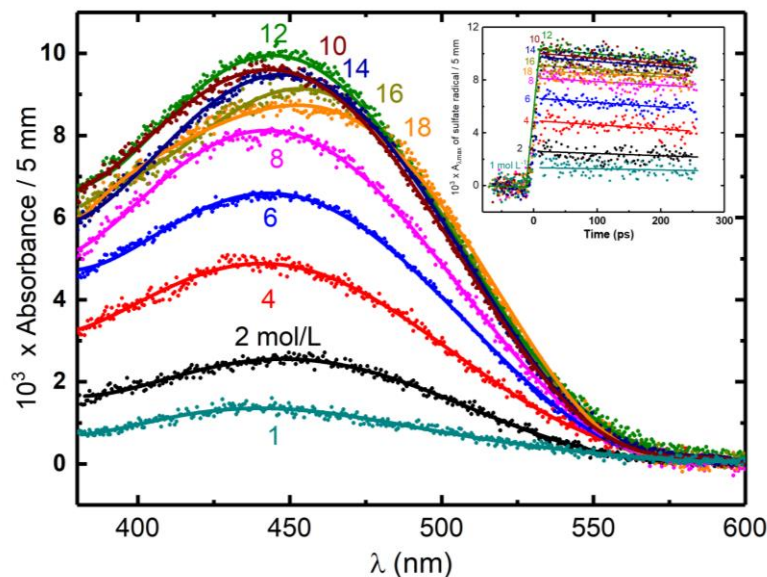


**Figure 4.12** Transient absorption spectrum of  $\text{SO}_4^{\bullet-}$  or  $\text{HSO}_4^{\bullet-}$  at maximum of absorption versus concentration of acid observed immediately after 7 ps electron pulse. Insert figure shows the corresponding transient kinetics of  $\text{SO}_4^{\bullet-}$  or  $\text{HSO}_4^{\bullet-}$ . The contribution of solvated electron in 1 to 6 M  $\text{H}_2\text{SO}_4$  is subtracted from the signal on the basis of the known extinction coefficient at various wavelengths. The dose deposited in the solutions has been corrected with  $F$  value. The dose was 31.3 Gy per pulse. Adapted from <sup>46</sup>.

The radiolytic yield of  $\text{SO}_4^{\bullet-}$  is directly deduced to be  $(3.75 \pm 0.2) \times 10^{-7} \text{ mol J}^{-1}$  from the 18 M sulfuric acid. Based on the electron fraction of solutes in solutions, the yield contribution of direct and indirect effect can be obtained according to EQ. 4-2 and 4-3.

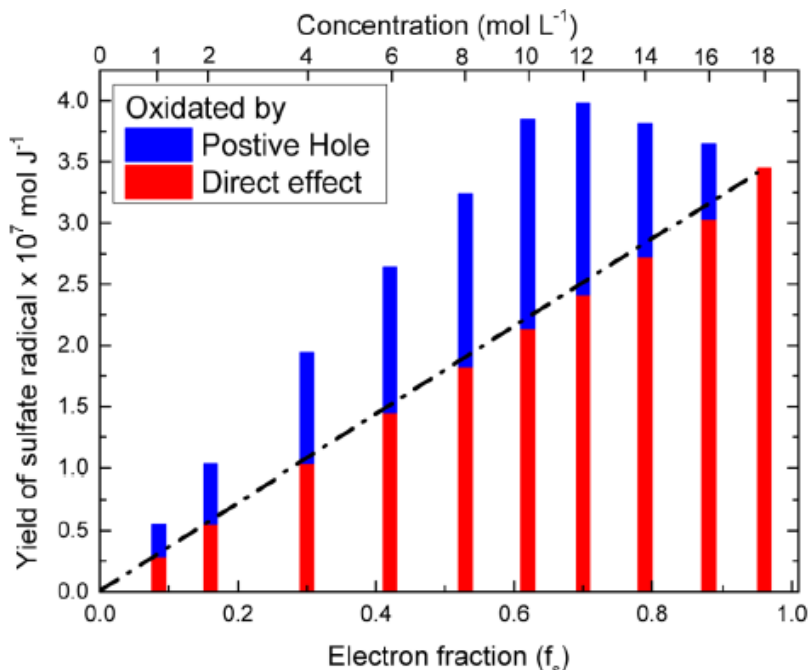


**Figure 4.13** Yield of sulfuric acid radical formation versus electron fraction of the solute. The value at 18 M is considered to be the direct effect yield and is linearly extrapolated to the zero concentration. The supplementary yield is considered to be due to the electron-transfer reaction with radical cation  $\text{H}_2\text{O}^{*+}$ . Performed by Ma *et al.*<sup>46</sup>

From the above analysis, the yield of  $\text{H}_2\text{O}^{*+}$ , which participates in ultrafast oxidation is deduced and their values are plotted as a function of the concentration correlated with the electron fraction. The analyzed results in **Figure 4.13** show four striking characteristics. First, at very low concentration or in dilute medium, neither direct effect nor  $\text{H}_2\text{O}^{*+}$  oxidation is important as the formation of  $\text{SO}_4^{\cdot-}$  is not observed. Second, the yield of  $\text{H}_2\text{O}^{*+}$  is highly dependent on the concentration, particularly below 12 M, where we observed a continuously increasing trend with the rising of the solute concentration. This is in agreement with our predications and it suggests that the probability of electron transfer of  $\text{H}_2\text{O}^{*+}$  is greater at higher concentration. Third, after 12 M, the yield is saturated to  $(4.75 \pm 0.5) \times 10^{-7} \text{ mol J}^{-1}$ , which is found to be similar with the value of  $\text{OH}^{\cdot}$  radical yield reported at picosecond timescale in neat water.<sup>55</sup> In these cases, it can be concluded that after certain concentration, all of the precursors of  $\text{OH}^{\cdot}$  react with sulfuric solutes.

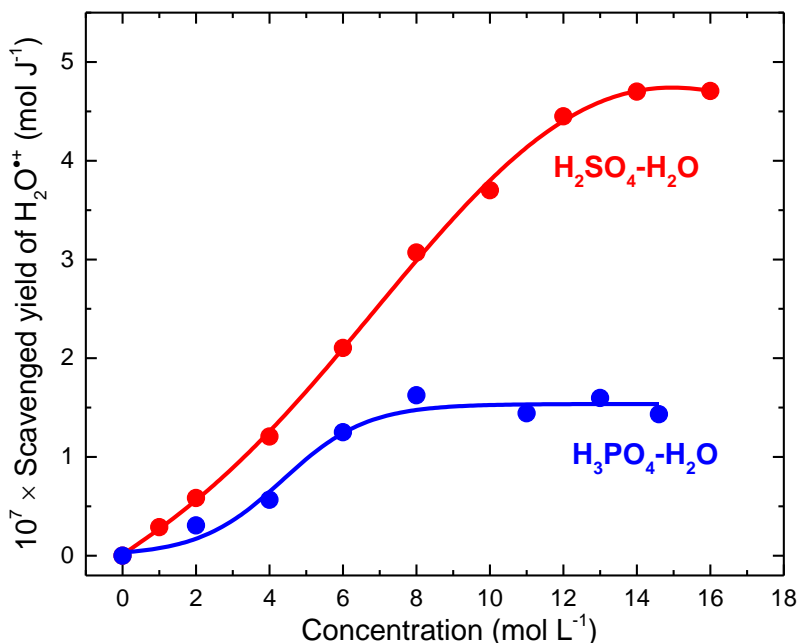


**Figure 4.14** End of pulse radiolytic yield of scavenged radical cation  $\text{H}_2\text{O}^{*+}$  in aqueous sulfuric and phosphoric acid solutions(Revised). Performed by Ma. *et al*<sup>49</sup>.

The scavenged yield of  $\text{H}_2\text{O}^{*+}$  in sulfuric acid solutions is compared with that in phosphate acid (**Figure 4.14**). It clearly shows that the saturated yield of  $\text{H}_2\text{O}^{*+}$  is significantly lower compared with that in sulfuric acid solutions. The reasons why the water hole trapping in phosphoric acid is not efficient are not clear. However, on the basis of microscopic structure of phosphate solutions from X-rays diffraction measurements,<sup>56,57</sup> we may propose that the existence of aggregations of phosphates should be taken into account for this. Because of the formation of dimer or trimer at higher concentrations, the amount of close encounters between water and phosphate is relatively less than those in sulfuric acid under identical molar concentration, and thus the efficiency of *in situ*  $\text{H}_2\text{O}^{*+}$  capturing reaction is lower.

In spite of studies of  $\text{H}_2\text{O}^{*+}$  reactivity towards  $\text{HNO}_3$ ,  $\text{H}_2\text{SO}_4$  and  $\text{H}_3\text{PO}_4$ , as yet there are two additional acids (perchlorate acid and hydrofluoric acid) remaining to be of interest in aqueous systems. Unfortunately, direct ionizing of perchlorate acid gives rise to two components of radicals ( $\text{ClO}_4^{\bullet}$  and  $\text{ClO}_3^{\bullet}$ ) with very low value of extinction coefficient, so it might not be easy to correctly deduce the secondary radical yield from  $\text{H}_2\text{O}^{*+}$ . The fact that the element fluorine has a high electron affinity may result in a high value of redox potential of one electron couple  $\text{F}^{\bullet}/\text{F}^-$ , which has not been known yet. It is of great interests to testify on the oxidizing ability of  $\text{H}_2\text{O}^{*+}$  by

observing the formation of  $\text{F}^\bullet$  or  $\text{F}_2^{\bullet-}$  in pulse radiolysis of highly concentrated HF solution. This measurement has not been performed so far because it requires a very specific fused cell and solution cycling system to avoid the corrosions from HF samples and safety issues when handling with HF.

One may assume that  $\text{H}_2\text{O}^{\bullet+}$  is, in fact, the acidic form of  $\text{OH}^\bullet$  in aqueous solutions but the  $pK_a$  value is not clear. It is known that  $\text{OH}^\bullet$  radical will attack guanine molecules, the most easily oxidized DNA bases, through a series of complex processes. It involves H-abstraction, adducting and one-electron oxidation reaction at similar rates, leading to the formation of a variety of guanine based radicals. Interestingly, our recent study of radiation-induced guanine oxidation in highly concentrated phosphoric acid (6 M) shows all of  $\text{OH}^\bullet$  radicals in strong acid condition solely oxidize guanine molecule to guanine cation ( $\text{G}^{\bullet+}$   $\text{G}^{++}$ ) (**Figure 4.15**). It is therefore inferred that  $\text{H}_2\text{O}^{\bullet+}$  radical cation in some cases indeed displays a distinguished reactivity from  $\text{OH}^\bullet$  radicals. Besides, we are carrying out pulse radiolysis measurements of highly concentrated DNA subunits solutions in order to extend our findings obtained in inorganic solutions to a situation that is biologically relevant.

Moreover, the absence of information on the yield of a direct effect of radiation on the solute was also another barrier in making definitive conclusions about the reactivity of  $\text{H}_2\text{O}^{\bullet+}$ . Meanwhile, in biological systems, it was shown by electron spin resonance at low temperatures that hole transfer occurs from the inner hydration layer to DNA after  $\gamma$  rays irradiation.<sup>13</sup> However, there has been no direct observation of electron transfer involving the radical cation of water.



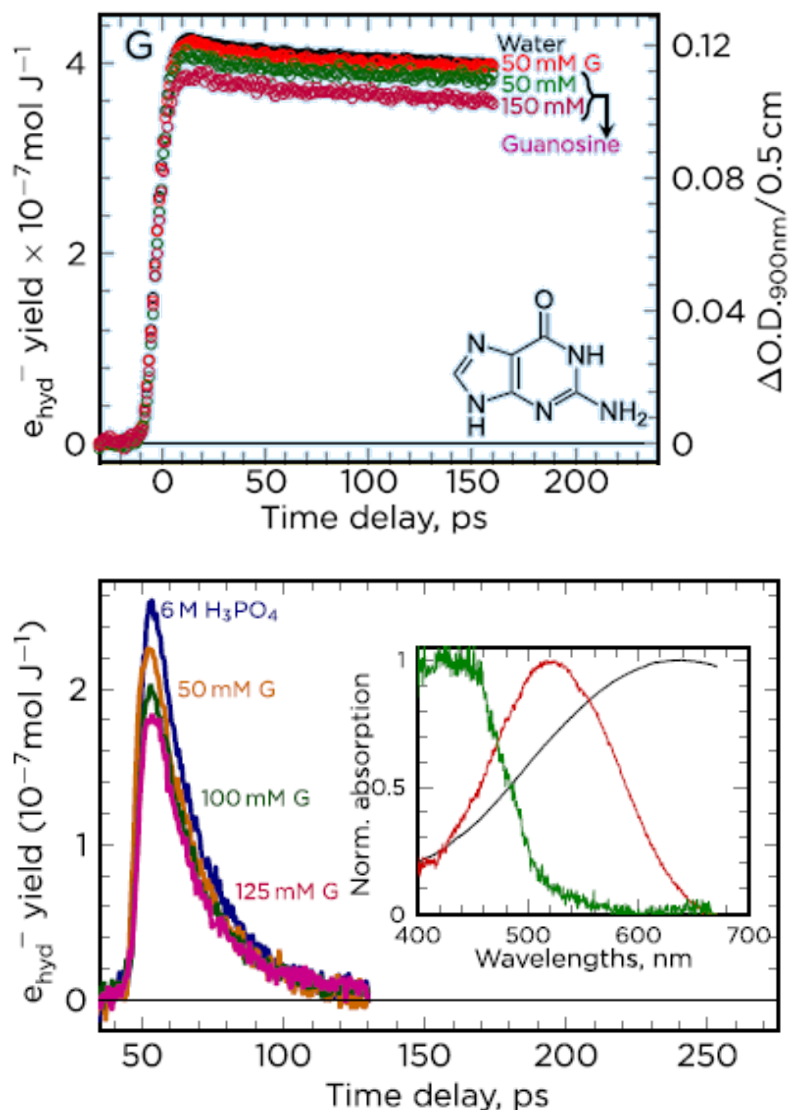


**Figure 4.15** Transient absorption kinetic traces of  $e_s^-$  in liquid water containing Guanine, Adenine, Cytosine, and Thymine compounds with different concentrations (10 to 150 mM). To increase the solubility of purine nucleobases, the solutions were prepared in 90 mM NaOH followed by the work of Wang *et al.*<sup>58</sup>. Radiolytic yields of  $e_s^-$  are shown in the left axes, and these correspond to the absorbance in the right axes. The dose per electron pulse was 55.3 grays (Gy). The radiolytic yield of  $e_s^-$  is not affected even in 50 mM G solution within 1% uncertainty. The solid line is the theoretical fit; we have obtained it using time-dependent rate constants. DO.D.900nm, optical density at 900 nm. By Ma *et al.*<sup>59</sup>

Despite these achievements, conclusions could not be made about the actual mechanism of  $\text{H}_2\text{O}^{+\bullet}$  reactivity. The purpose of this study is to elucidate the detailed mechanism of electron transfer from the combination of new experiments in hydrogenated and deuterated solutions along

with theoretical simulations. Towards this end, our strategy is to investigate the change of the yield of the oxidative pathway upon isotopic substitution (H by D). We expect to bring new insights into the competition between the two parallel reactions, proton transfer toward another water molecule and electron transfer from the solute, both involving the radical cation of water.

## **4.2 Results — Reactivity of radical cation of water in $\text{D}_2\text{SO}_4$ / $\text{D}_2\text{O}$ system**

Deuterium oxide ( $\text{D}_2\text{O}$ ) is a form of water that contains two hydrogen isotope deuterium (D) that replace hydrogen in water.  $\text{D}_2\text{O}$  has larger density, viscosity and molecule weight than  $\text{H}_2\text{O}$  (see Chapter III **Table 3.1**), meanwhile the same electron number as  $\text{H}_2\text{O}$ .

Deuterium sulfuric acid ( $\text{D}_2\text{SO}_4$ ), which also contains two hydrogen isotopes deuterium, has larger molecular weight and density than  $\text{H}_2\text{SO}_4$ . As  $\text{D}_2\text{SO}_4/\text{D}_2\text{O}$  solution is a homogenous system like  $\text{H}_2\text{SO}_4/\text{H}_2\text{O}$ , it is a highly appreciated system to study the isotopic effect on water radical cation by H/D. Moreover, the parameters of the solvated electron and hydroxyl radical in  $\text{D}_2\text{O}$  in the spur reaction have been studied in Chapter III, thus it will help to learn about the radiation reaction in  $\text{D}_2\text{SO}_4/\text{D}_2\text{O}$  system

The primary reactions occurring in  $\text{D}_2\text{SO}_4/\text{D}_2\text{O}$  system are presented in detail in **Table 4.5**.<sup>60</sup> Compared with  $\text{H}_2\text{SO}_4/\text{H}_2\text{O}$ , there is less information about the ionizing reaction in the  $\text{D}_2\text{SO}_4/\text{D}_2\text{O}$  system. Most rate constants of the reactions involved in  $\text{D}_2\text{SO}_4$  /  $\text{D}_2\text{O}$  system have not been established.

**Table 4.5** The primary radiation induced reactions involved in  $\text{D}_2\text{SO}_4/\text{D}_2\text{O}$  solution

<i>Primary radiation induced reaction</i>	<i>Rate coefficient (<math>\text{L mol}^{-1} \text{s}^{-1}</math>)</i>	
$\text{D}_2\text{O} \rightarrow \text{D}_2\text{O}^{\bullet+} + \text{e}^-$		R1
$\text{e}^- + \text{D}_2\text{O}^{\bullet+} \rightarrow \text{D}_2\text{O}^*$		R2
$\text{D}_2\text{O}^{\bullet+} + \text{D}_2\text{O} \rightarrow \text{D}_3\text{O}^+ + \text{OD}^\bullet$	—	R3
$\text{e}_s^- + \text{D}_3\text{O}^+ \rightarrow \text{D}^\bullet + \text{D}_2\text{O}$	$9.5 \times 10^{9\ 60}$	R4
<i>Reactions <math>\text{D}_2\text{SO}_4/\text{D}_2\text{O}</math></i>		
$\text{SO}_4^{2-} \rightarrow \text{SO}_4^{\bullet-} + \text{e}^-$		R26
$\text{SO}_4^{2-} + \text{D}_2\text{O}^{\bullet+} \rightarrow \text{SO}_4^{\bullet-} + \text{D}_2\text{O}$		R27
$\text{D}_2\text{SO}_4 + \text{OD}^\bullet \rightarrow \text{DSO}_4^{\bullet-} + \text{D}_2\text{O}$	—	R28
$\text{DSO}_4^- + \text{OD}^\bullet \rightarrow \text{SO}_4^{\bullet-} + \text{D}_2\text{O}$	—	R29
$\text{SO}_4^{\bullet-} + \text{D}^\bullet \rightarrow \text{DSO}_4^-$	—	R30
$\text{SO}_4^{\bullet-} + \text{SO}_4^{\bullet-} \rightarrow \text{S}_2\text{O}_8^{2-}$	$7.6 \times 10^8$	R31
$\text{SO}_4^{\bullet-} + \text{OD}^\bullet \rightarrow \text{DSO}_5^-$	—	R32
$\text{SO}_4^{\bullet-} + \text{S}_2\text{O}_8^{2-} \rightarrow \text{S}_2\text{O}_8^{\bullet-} + \text{SO}_4^{2-}$	$6.6 \times 10^5$	R33
$\text{SO}_4^{\bullet-} + \text{DO}_2^\bullet \rightarrow \text{DSO}_4^- + \text{O}_2$	—	R34
$\text{S}_2\text{O}_8^{2-} + \text{D}^\bullet \rightarrow \text{SO}_4^{\bullet-} + \text{DSO}_4^-$	—	R35
$\text{DSO}_5^- + \text{D}^\bullet \rightarrow \text{SO}_4^{\bullet-} + \text{D}_2\text{O}$	—	R36

#### 4.2.1 Transient absorption spectra

A series of experiments in  $\text{D}_2\text{SO}_4/\text{D}_2\text{O}$  from 0 to 18 M were performed. The transient absorption spectra at 15 ps after electron pulse are presented in **Figure 4.16a**. The large absorption band located in the red regions are mainly due to the solvated electron pair ( $\text{e}_s^-$ ,  $\text{D}_3\text{O}^+$ ), and it decreases with increasing the sulfuric acid concentration from 0 ~ 6 M and produce  $\text{D}^\bullet$  atom (R4)

which is known to absorb far in UV. The blue shift with increasing sulfuric acid concentration is as the result of the formation of  $(\text{e}_s^-, \text{D}_3\text{O}^+)$ , as reported by Ma et al.<sup>61</sup>

**Table 4.6** The wavelength where solvated electron absorbs maximum in 0 to 6 M  $\text{D}_2\text{SO}_4$

Concentration of $\text{D}_2\text{SO}_4$ (mol $\text{L}^{-1}$ )	$\lambda_{\text{max}}$ of $A_{t=15\text{ ps}}^{e_s^-}$ (nm)
0	704
1	680
2	660
4	620
6	600

As shown in **Figure 4.16b**, the absorption maximum of  $\text{e}_s^-$  moves to lower wavelength with increasing the concentration of  $\text{D}_2\text{SO}_4$ .  $\text{e}_s^-$  has been totally scavenged within the pulse when the concentration of  $\text{D}_2\text{SO}_4$  is over 8 M. **Table 4.6** presents the wavelength where the  $\text{e}_s^-$  appears to have the maximum absorbance in the concentration range of 0 to 6 M  $\text{D}_2\text{SO}_4$ .

As more and more presolvated electron is scavenged by  $\text{D}_3\text{O}^+$  with the concentration increasing, another absorption band became more significant in concentrated solutions with a maximum around 370 to 520 nm. The absorbing signal of solvated electron in the visible completely vanishes for concentrations higher than 8 M.

The absorption measured by pump-probe in our experiments from 370 nm to 720 nm contains not only the contribution of  $\text{SO}_4^{\bullet-}$  (or  $\text{HSO}_4^{\bullet}$ ), but also that of non-scavenged solvated electron in less concentrated sulfuric solutions as well as the transient species induced in the fused silica optical flowing cell (FSOFC) (as shown in **Figure 3.21** Chapter III). **Figure 4.17** is the transient absorbed spectra from 2 to 18 M obtained after subtracting the contribution due to the solvated electron and the transients in FSOFC carefully.

As an example, at 15 ps in 4 M  $\text{D}_2\text{SO}_4$ , the transient absorbance could be expressed as

$$A_{\lambda}^{\text{measured}}(t=15\text{ ps}) = A_{\lambda}^{\text{SO}_4^{\bullet-}}(t=15\text{ ps}) + A_{\lambda}^{e_s^-}(t=15\text{ ps}) + A_{\lambda}^{\text{FSOFC}}(t=15\text{ ps}) \quad \text{EQ.4-6}$$

Here,  $A_{\lambda}^{\text{measured}}(t=15\text{ ps})$  is the observed absorbance at 15 ps in the experiments,  $A_{\lambda}^{\text{SO}_4^{\bullet-}}(t=15\text{ ps})$  is the transient absorbance arising from  $\text{SO}_4^{\bullet-}$  (or  $\text{HSO}_4^{\bullet}$ ), and  $A_{\lambda}^{e_s^-}(t=15\text{ ps})$  is arising from the

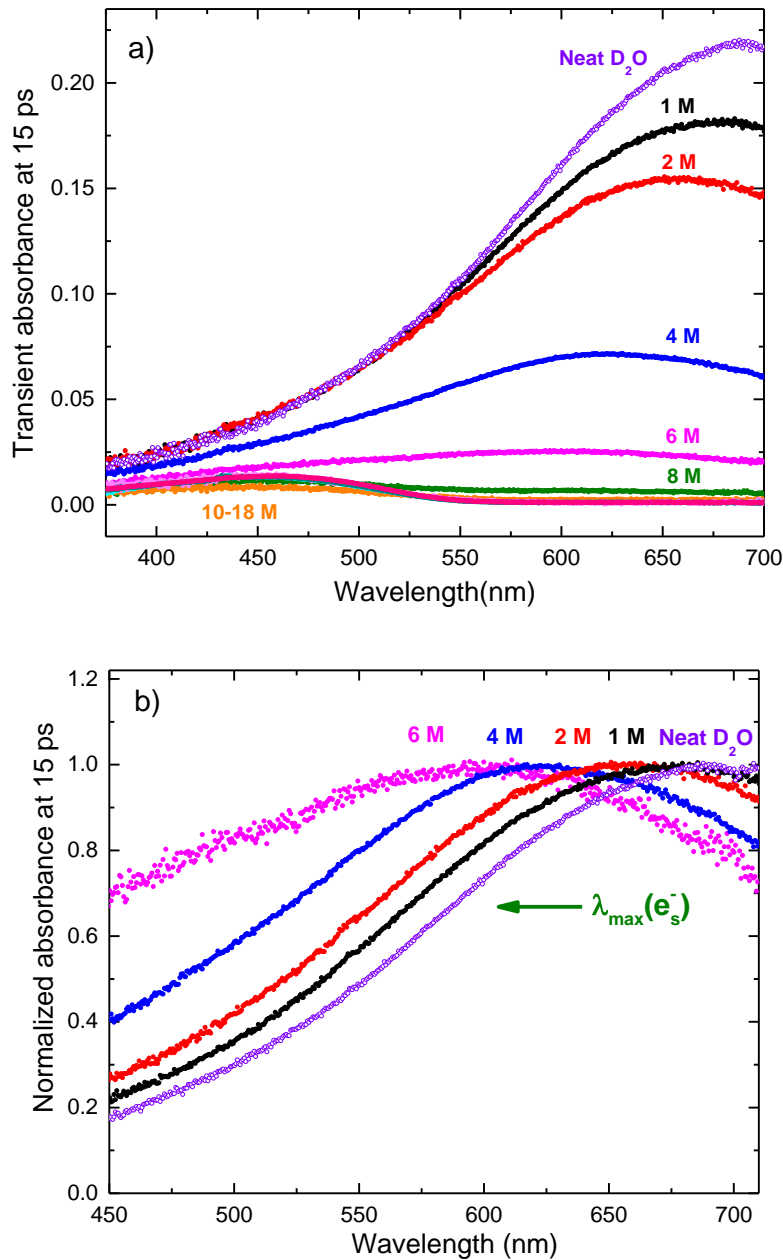


**Figure 4.16** a) Transient spectra recorded at 15 ps after electron pulse in 0 to 18 M  $\text{D}_2\text{SO}_4/\text{D}_2\text{O}$  solutions. The dose per pulse was 42.5 Gy. b) Normalized absorbance at 15 ps after electron pulse in 0 to 6 M  $\text{D}_2\text{SO}_4/\text{D}_2\text{O}$  solutions.

solvated electron.  $A_{\lambda}^{FSOFC}(t=15ps)$  is the contribution of the transient formed in the fused silica cell after irradiation, which is negligible compared with the absorbance due to  $SO_4^{\bullet-}$  and solvated electron. The absorbed spectrum of the solvated electron has been determined in Chapter III.

According to the blue shift of the solvated electron in 4 M (**Figure 4.16 b** and **Table 6**) and the transient absorbance at 15 ps,  $A_{\lambda}^{e_s^-}(t=15ps)$  could be deduced:

$$A_{\lambda}^{SO_4^{\bullet-}}(t=15ps) \approx A_{\lambda}^{measured}(t=15ps) - A_{\lambda}^{e_s^-}(t=15ps) \quad \text{EQ. 4-7}$$

The same procedure was performed for the concentrations from 2 to 6 M. As the presolvated electron has reacted with  $D_3O^+$  fully when the concentration is higher than 8 M, the observed absorbance at 15 ps solely arises from  $SO_4^{\bullet-}$ . The results are shown in **Figure 4.17**.

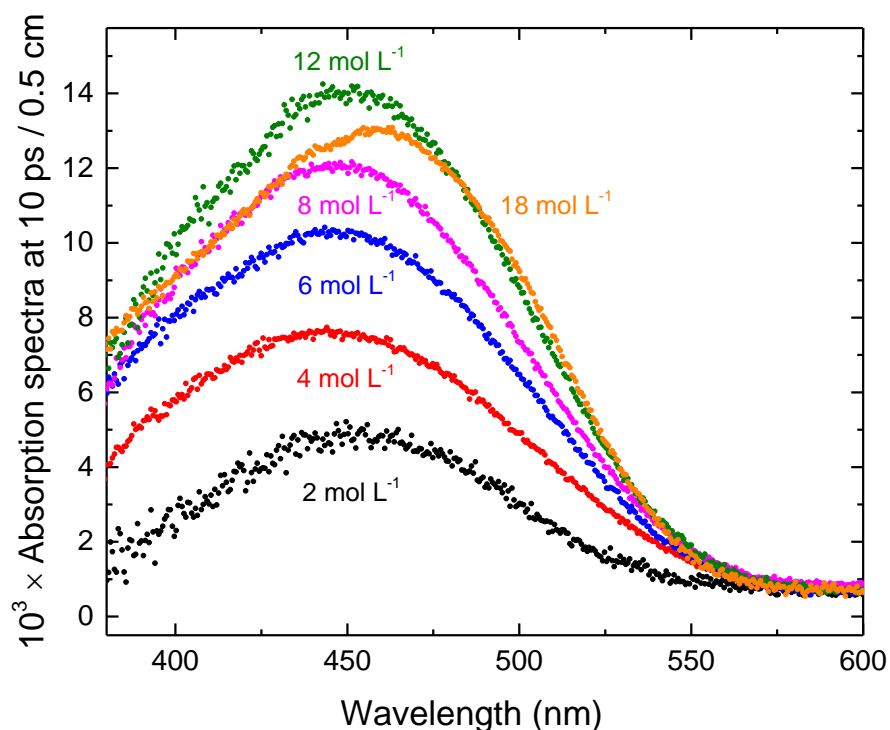


**Figure 4.17** Example of the transient absorption spectra of the sulfate radical ( $HSO_4^{\bullet}$  and  $SO_4^{\bullet-}$ ) recorded at 10 ps in  $D_2SO_4$  at different concentration. The contribution of solvated electron and the transient induced in the optical cell are subtracted from the observed signal. The dose was 42.5 Gy per pulse.

An absorption band with a maximum at 450 nm is clearly observed in solutions from 2 to 12 M, which is identical with the spectrum of  $SO_4^{\bullet-}$  reported in the literatures by radiolysis and

photolysis measurements<sup>53</sup> both in diluted and concentrated solutions up to 10 M. It is remarkable that the peak of the absorption band in 18 M shifts to 460 nm. This is in account of the protonation of  $SO_4^{\bullet-}$  as the non-dissociation  $D_2SO_4$  molecules are the predominate species in extremely high concentration. The reaction is as:



To determine the radiolysis, the molar extinction coefficient of  $SO_4^{\bullet-}$  is necessary. In this study, the value of the molar extinction coefficient of  $SO_4^{\bullet-}$  at 450 nm is also taken as most reliable one as  $1600 \text{ M}^{-1} \text{ cm}^{-1}$  reported in the literatures.<sup>10,49,54</sup> Moreover, it is assumed that this value remains constant and is not dependent on the concentration of the sulfuric acid solution.

#### 4.2.2 Analysis of the kinetics

**Figure 4.18(a)** describes the time dependent decay measured at 450 nm in the sulfuric solutions from 2 to 18 M. As noted above, the absorption measured at 450 nm consisted not only the contribution of  $SO_4^{\bullet-}$ , but also the contribution of the pair ( $e_s^-$ ,  $D_3O^+$ ) and the transient induced in fused silica optical flow cell (FSOFC). To understand the formation process of  $SO_4^{\bullet-}$ , the contribution of the pair ( $e_s^-$ ,  $D_3O^+$ ) and the transient induced in FSOFC should be subtracted from the kinetics measured at 450 nm. The time dependent absorbance at 450 nm can be elucidated as:

$$A_{\lambda=450}^{measured}(t) = A_{\lambda=450}^{SO_4^{\bullet-}}(t) + A_{\lambda=450}^{e_s^-}(t) + A_{\lambda=450}^{FSOFC}(t) \quad \text{EQ.4-9}$$

The time dependent absorbance of FSOFC has been achieved carefully in Chapter III. As the transient absorbed spectra of the fused silica is already known (**Figure 3.21** in Chapter III), so the signal contributed from FSOFC can be obtained as:

$$A_{\lambda=450}^{FSOFC}(t) = A_{\lambda=260}^{FSOFC}(t) \times \frac{I_{\lambda=450}^{FSOFC}}{I_{\lambda=260}^{FSOFC}} \quad \text{EQ.4-10}$$

The fast decay just after electron pulse results from the reaction between  $e_s^-$  and  $D_3O^+$  in the concentration of 2 to 8 M. Additionally,  $D_3O^+$  could also scavenge the presolvated electron with a higher rate constant. When the concentration is larger than 8 M, the decay remains stable and shows

almost zero absorbance, it is on account of that the whole presolvated electron has been captured by  $\text{D}_3\text{O}^+$ .

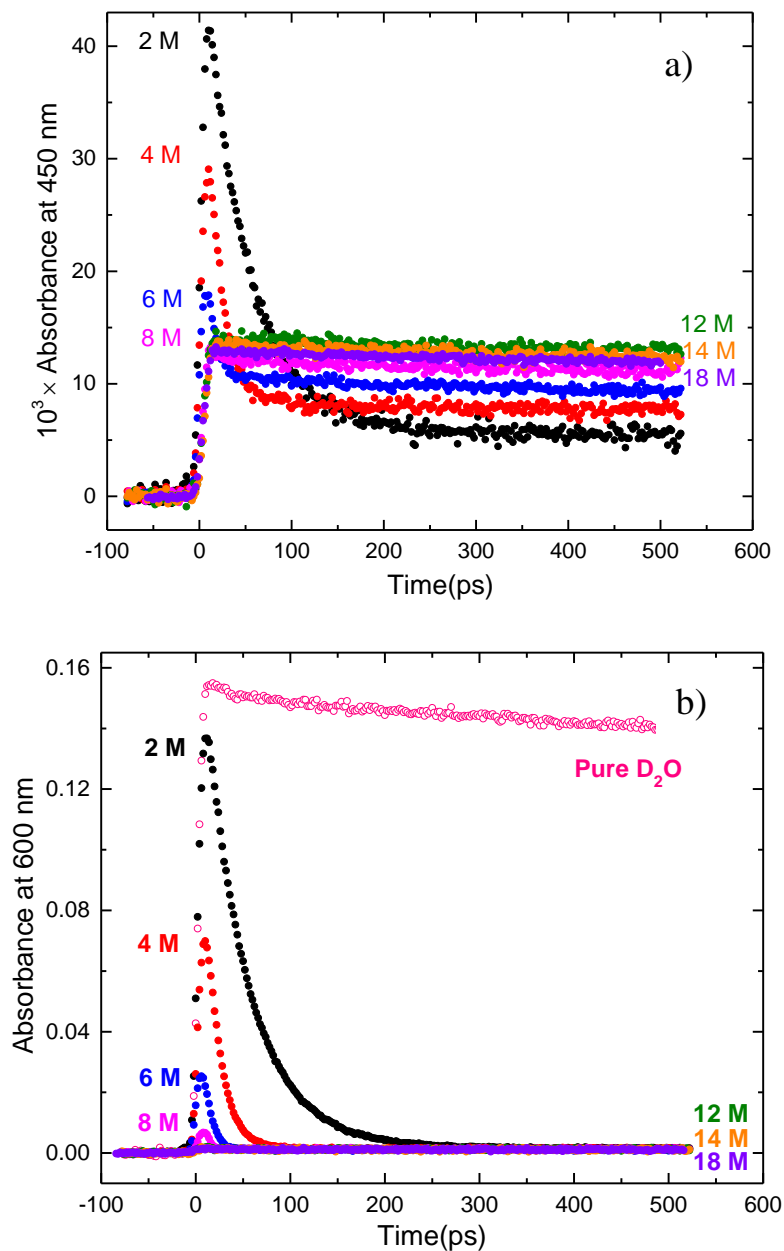


**Figure 4.18** Kinetics at 450 nm (a) and 600 nm (b) on picosecond scale for  $\text{D}_2\text{SO}_4/\text{D}_2\text{O}$  solution in neat  $\text{D}_2\text{O}$  and 2 to 18 M<sup>1</sup> sulfuric acid solutions. The dose per pulse was 42.5 Gy.



For the contribution of the pair ( $e_s^-$ ,  $D_3O^+$ ), it can be deduced from the absorbance at 600 nm by the ratio of the molar extinction coefficient (**Figure 3.14** in Chapter III) as the absorbance of  $SO_4^\bullet$  is negligible in the wavelength range larger than 570 nm. The time dependent decay measured at 600 nm in different concentration of sulfuric acid is shown in **Figure 4.18 (b)**. In a consequence, the contribution of the pair ( $e_s^-$ ,  $D_3O^+$ ) can be written as:

$$A_{\lambda=450}^{(e_s^-, D_3O^+)}(t) = A_{\lambda=600}^{(e_s^-, D_3O^+)}(t) \times \frac{\epsilon_{\lambda=450}^{e_{D_2O}^-}}{\epsilon_{\lambda=600}^{e_{D_2O}^-}} \quad \text{EQ.4-11}$$

The formation process of  $SO_4^\bullet$  is presented in **Figure 4.19** after subtracting the signal of the pair ( $e_s^-$ ,  $D_3O^+$ ) and the transient in FSOFC. The results show that there is no significant decay at 450 nm up to 500 ps with increasing concentration. It is worth noting that the initial absorbance at 7 ps increases in the first series of the concentrations as expected, then it reaches the maximum at 12 M and drops down slightly. It indicates that a second parallel mechanism is involved in the formation of  $SO_4^\bullet$  radical.

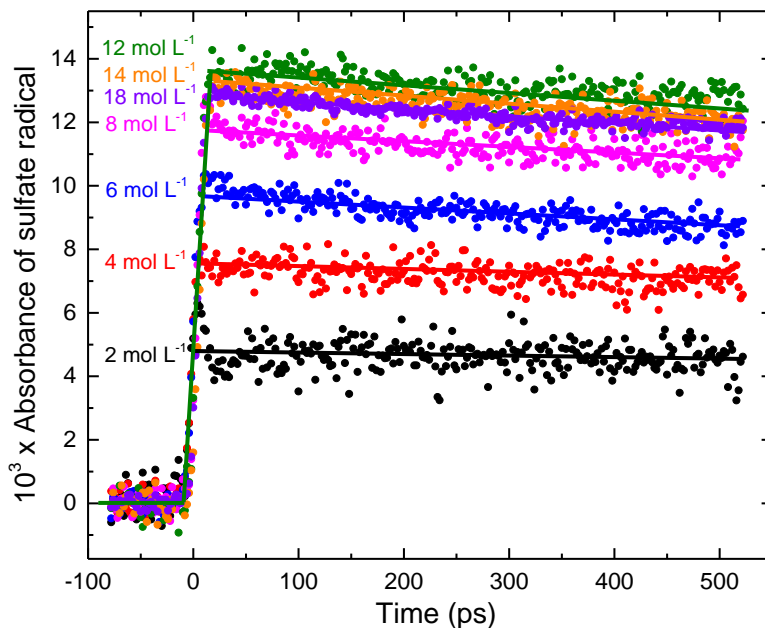


**Figure 4.19** Kinetics of sulfate radical ( $SO_4^{\bullet-}$  or  $HSO_4^\bullet$ ) on absorption maximum wavelength. The contribution of solvated electron has been subtracted from the signal. The dose per pulse was 42.5 Gy.

#### 4.2.2 Yield of scavenging $D_2O^{*+}$ in $D_2SO_4/D_2O$ solution

Since the time dependent absorbance of  $SO_4^{\bullet-}$  corresponding to different concentration at 450 nm is known, the time dependent radiolytic yield of  $SO_4^{\bullet-}$  can be deduced by:

$$A_{\lambda=450}^{SO_4^{\bullet-}}(t) = \varepsilon_{\lambda=450}^{SO_4^{\bullet-}} \times G^{SO_4^{\bullet-}}(t) \times D_{sol} \times l \quad \text{EQ.4-12}$$

Where  $\varepsilon_{\lambda=450}^{SO_4^{\bullet-}}$  is  $1600 \text{ M}^{-1} \text{ cm}^{-1}$  as mentioned,  $D_{sol}$  is the dose deposited in the solution and  $l$  is the length of the optical path. Additionally,

$$D_{sol} = D_{H_2O} \times F \quad \text{EQ.4-13}$$

**Table 4.7** Concentration of sulfuric acid solutions and their corresponding parameters:

$[D_2SO_4]$	$[D_2O]$	$\frac{[D_2O]}{[D_2SO_4]}$	$f_s^a$	$f_{D_2O}^b$	Density (g ml <sup>-1</sup> )	$F^c$ (g cm <sup>-3</sup> )	$G_{7ps}^{SO_4^{\bullet-} d}$ ( $\times 10^7 \text{ mol J}^{-1}$ )
1	53.4	53.4	0.09	0.91	1.17	1.06	0.84
2	51.4	25.7	0.16	0.84	1.23	1.11	1.44
4	46.8	11.7	0.30	0.70	1.34	1.21	2.24
6	42.4	7.07	0.41	0.59	1.45	1.31	2.92
8	37.9	4.74	0.51	0.49	1.56	1.41	3.50
10	33.0	3.30	0.60	0.40	1.66	1.50	3.87
12	27.0	2.25	0.69	0.31	1.74	1.57	3.96
14	20.4	1.46	0.77	0.23	1.81	1.64	3.95
16	12.5	0.78	0.87	0.13	1.85	1.67	3.86
18	2.7	0.15	0.97	0.03	1.88	1.70	3.75

<sup>a</sup> The electron density fraction of solute  $f_s$ . <sup>b</sup> The electron density fraction of  $D_2O$   $f_{D_2O}$ . <sup>c</sup> The absorbed dose factor  $F$ . <sup>d</sup> The Yield of  $SO_4^{\bullet-}$  observed after 7 ps electron pulse which is deduced from the kinetics according to the data from **Figure 4.19**:  $A_{\lambda=450}^{SO_4^{\bullet-}}(t) = A_{\lambda=450}^{measured}(t) - A_{\lambda=450}^{e_s^-}(t) - A_{\lambda=450}^{FSOFC}(t)$ .

Where  $D_{H_2O}$  is the dose deposited in  $H_2O$  under the same experimental condition, and  $F$  is the correction factor to estimate the dose deposited in the solution.  $F$  is related to the density and the electron concentration of the solution.<sup>44</sup> It could be determined according to EQ. 4-4.

The experimental yields of  $\text{SO}_4^{\bullet-}$  just after electron pulse ( at 7 ps) on the function of the concentration was calculated and listed in **Table 4.7** and shown in **Figure 4.20**. Additionally, the amount of water molecule is exceedingly low and unlikely to generate  $\text{D}_2\text{O}^{*+}$  when the concentration of sulfuric acid increases to 18 M. In this case, the radiolytic yield of  $\text{SO}_4^{\bullet-}$  at 7 ps can be considered solely due to ionizing radiation. Then the contribution of the direct effect on the oxidation is dependent on the function of electron fraction. As clearly shown in **Figure 4.20**, the dash-dot linear slope demonstrates the proceeds of  $\text{SO}_4^{\bullet-}$  formed by the direct effect. This line makes it clear that the direct effect alone cannot be responsible for the whole ultrafast build-up of the oxidation product of sulfuric acid.

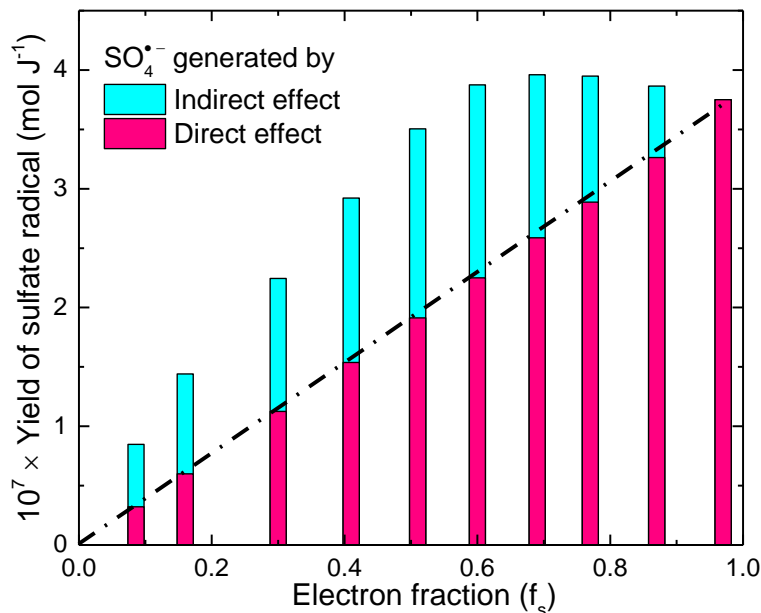


**Figure 4.20** Yield of  $\text{SO}_4^{\bullet-}$  versus the electron fraction of the solute  $\text{D}_2\text{SO}_4$  in  $\text{D}_2\text{O}$ . The value at 18 M is considered as the direct effect yield and is linearly extrapolated to zero concentration. The supplementary yield is due to the electron transfer reaction to  $\text{D}_2\text{O}^{*+}$ .

The rate coefficient of  $\text{OD}^{\bullet}$  radical with sulfuric ion and molecule (R28 and R29) is slow and unlikely to occur in picosecond timescale. Hence, the additional formation of sulfate radical can be attributed to the ultrafast electron transfer reaction between  $\text{D}_2\text{O}^{*+}$  and  $\text{SO}_4^{\bullet-}$  (R27). This contribution is not proportional to the electron fraction of  $\text{D}_2\text{O}$  in the solution. It reaches the maximum while  $f_s = 0.6 \sim 0.7$ . It can be explained rationally that  $\text{D}_2\text{O}$  plays a principal role and still majority of  $\text{D}_2\text{O}^{*+}$  reacts with the water molecule to generate  $\text{OD}^{\bullet}$  radical. With increasing the

centration of sulfuric acid, the electron transfer reaction plays a favorable role in the competition and the amount of  $\text{D}_2\text{O}^{\bullet+}$  oxidizing  $\text{SO}_4^{\bullet-}$  becomes larger. Whereas the concentration of sulfuric acid reaches maximum, the amount of water is negligible and the proton transfer reaction (R27) is insignificant.

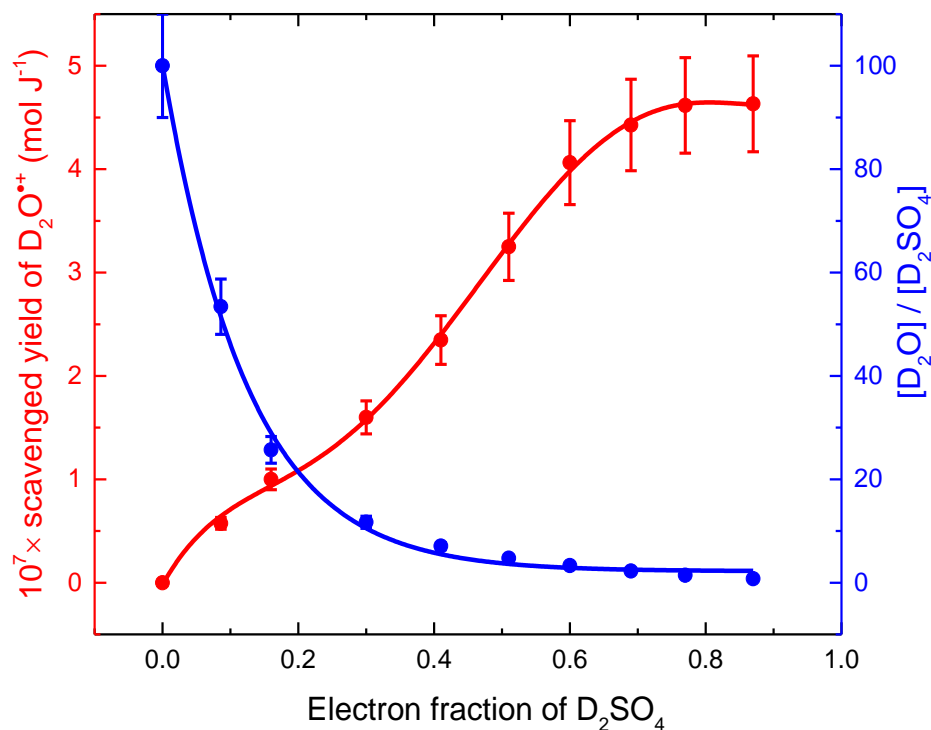


**Figure 4.21** The scavenged yield of  $\text{D}_2\text{O}^{\bullet+}$  (Left axis) and the ratio of the concentration between  $\text{D}_2\text{O}$  and  $\text{D}_2\text{SO}_4$  (Right axis) on the function of the electron fraction of  $\text{D}_2\text{SO}_4$ .

**Figure 4.21** presents the yield of  $\text{D}_2\text{O}^{\bullet+}$  scavenged by sulfate anion. It is notable that the scavenged yield of  $\text{D}_2\text{O}^{\bullet+}$  increases with the electron fraction of sulfuric acid and reaches a plateau with a value around  $(4.75 \times 10^{-7}) \text{ mol J}^{-1}$ . Particularly, this behavior is observed on the concentration of 14 and 16 M, where the amount of water is so low that the reaction R2 is almost suppressed and total  $\text{D}_2\text{O}^{\bullet+}$  is scavenged by sulfuric ion in few tens femtosecond. For these solutions, the yield of  $\text{D}_2\text{O}^{\bullet+}$  is in close proximity to that generated just after ionizing radiation. Moreover, the value obtained is larger than the yield of hydrated electron in  $\text{D}_2\text{O}$  (confirmed in Chapter III). That meant that the proton transfer (R2) and electron transfer (R27) reactions are in competition with the germinate recombination:



Therefore, it can be considered that the amount of ionized water by irradiation at  $10^{-15}$  s is no less than the value of  $(4.75 \times 10^{-7}) \text{ mol J}^{-1}$  within the experimental uncertainty.

### 4.3 Results — Isotopic effect on the chemistry of $\text{H}_2\text{O}^{\bullet+}$

#### 4.3.1 Experiment on isotopic effect

Measurements in  $\text{D}_2\text{O}$  using  $\text{D}_2\text{SO}_4$  as the solute, and new measurements with  $\text{H}_2\text{SO}_4$  solutions in exactly the same conditions, were performed. Solutions of  $\text{D}_2\text{SO}_4$  (and  $\text{H}_2\text{SO}_4$ ) in concentrations ranging from 1 to 18 M have been studied by picosecond pulse radiolysis (**Table 4.7**).

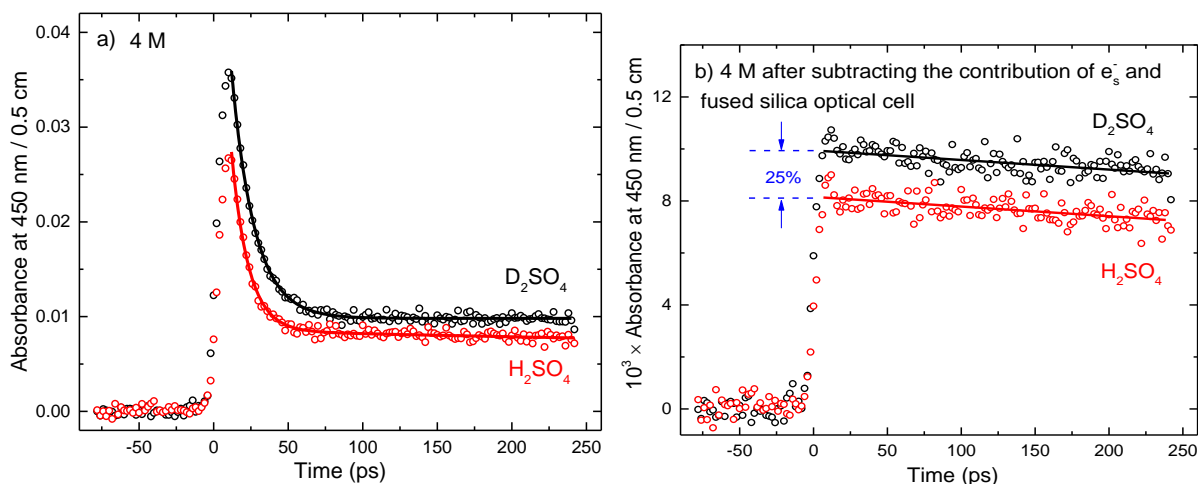


**Figure 4.22** a) Ultrafast absorbance kinetics after the electron pulse in neat deuterated and hydrogenated sulfuric acid solutions in 4 M solutions in  $\text{H}_2\text{O}$  and  $\text{D}_2\text{O}$ . b) The kinetics at 450 nm after subtraction of the absorbance of solvated electron and the transient induced in fused silica cell for 4 M solutions.

The radical  $\text{SO}_4^{\bullet-}$  (or its protonated form  $\text{HSO}_4^{\bullet}$ ) is observed at 450 nm, 7 ps after the electron pulse. Observing on this timescale guarantees that the sulfate radicals have not been formed upon oxidation by the hydroxyl radical since it reacts very slowly.

The formation yield of the sulfuric acid radical is obtained in hydrogenated and deuterated solutions, respectively. Isotopic effects on the competitive reactions will be discussed later.

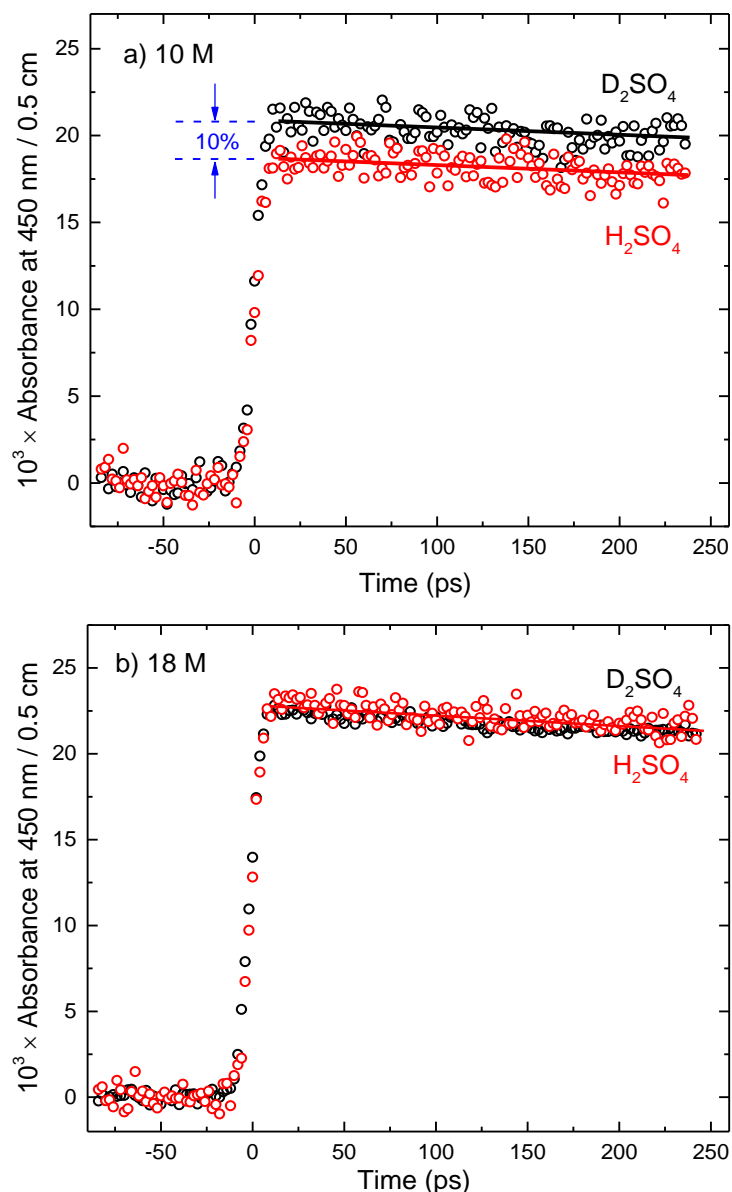


**Figure 4.23** Ultrafast absorbance kinetics observed at 450 nm after the electron pulse in deuterated and hydrogenated sulfuric acid solutions in 10 M (a) and 18 M (b) solutions in  $\text{H}_2\text{O}$  and  $\text{D}_2\text{O}$ .

Examples of the kinetics are shown for three conditions in hydrogenated and deuterated solutions (**Figure 4.22** and **4.23**). At low concentration (4 M) the fast decay observed at 450 nm just after the 7 ps electron pulse is mostly due to the reaction of the solvated electron with the acid. The decay is slightly faster in hydrogenated solution. The residual absorbance is due to the  $\text{HSO}_4^\bullet$  radical. By subtracting the absorbance of the solvated electron, only the contribution of the radical  $\text{HSO}_4^\bullet$  is obtained (**Figure 4.22b**).

The yield of the radical  $\text{HSO}_4^\bullet$  is 25% higher in the deuterated solution than in hydrogenated one. For 10 M solutions, the signature of the solvated electron is absent because at this concentration the pre-solvated electron is totally scavenged by  $\text{H}_3\text{O}^+$  ( $\text{D}_3\text{O}^+$ ). Therefore, only the  $\text{HSO}_4^\bullet$  radical is observed at 450 nm and again the absorbance is higher in  $\text{D}_2\text{O}$  than in  $\text{H}_2\text{O}$  solution but only by 10% (**Figure 4.23a**).

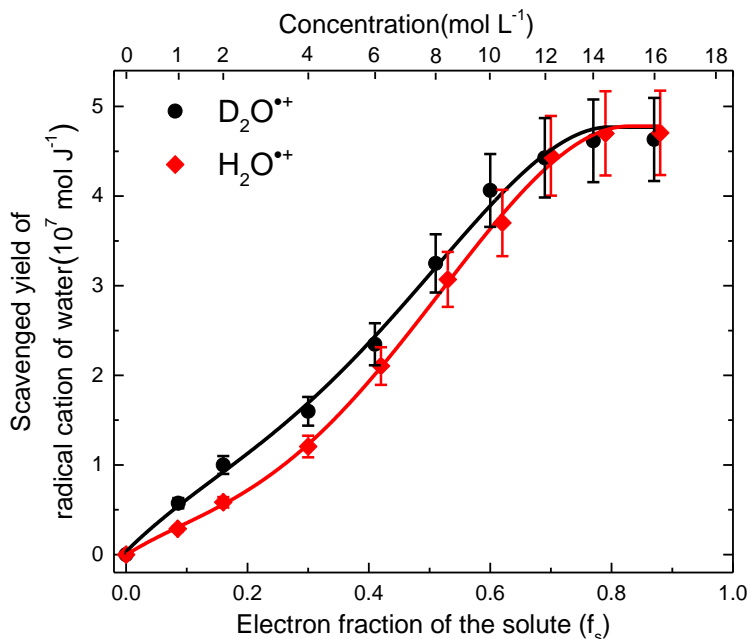


**Figure 4.24** Yields of  $\text{H}_2\text{O}^{*+}$  scavenging versus concentration case of  $\text{H}_2\text{SO}_4$  and  $\text{D}_2\text{SO}_4$ . The difference between  $\text{H}_2\text{SO}_4$  and  $\text{D}_2\text{SO}_4$  are zoomed in insert figure to better present the isotope effect in proton transfer.

At a concentration higher than 10 M, the difference between the amplitude of the radical absorbance in the two solutions almost vanishes. Finally, the yield of  $\text{HSO}_4^\bullet$  radical in pure sulfuric acid is the same for deuterated and hydrogenated solutions (**Figure 4.23b**).

In both deuterated and hydrogenated solutions, the yield of the sulfate radical increases with the acid concentration up to a plateau; then at higher concentration and in neat sulfuric acid it decreases slightly. The maximum yield of the sulfate radical is found for a concentration around 12 M (**Figure 4.24**). In the case of neat sulfuric acid, the mechanism of sulfate radical formation is by the direct effect of energy absorption by  $\text{SO}_4^{2-}$  (or acidic forms  $\text{HSO}_4^-$  and  $\text{H}_2\text{SO}_4$ , and  $\text{DSO}_4^-$  and  $\text{D}_2\text{SO}_4$ , respectively) presented as the following reaction R26:<sup>54</sup>



The yield of reaction R26 is the same in deuterated and hydrogenated neat sulfuric acid and is equal to  $G_{\text{dir}} = (3.75 \pm 0.05) \times 10^{-7} \text{ mol J}^{-1}$ . In sulfuric acid solutions, the sulfate radical can also be formed by the electron transfer from solute to the primary radical cation  $\text{D}_2\text{O}^{+\bullet}$  in aqueous systems. Knowing the value of  $G_{\text{dir}}$  (**Figure 4.20**), it is possible to deduce the yield of the scavenged radical cation ( $\text{H}_2\text{O}^{+\bullet}$  and  $\text{D}_2\text{O}^{+\bullet}$ ) according to EEQ. 4-2 and 4-3. The scavenging yield of the radical cation in two solutions, deuterated and hydrogenated, versus concentration of acid is shown on **Figure 4.24**. It is important to note that at these relatively low concentrations of the solute, a significant part of the energy is deposited in water following the electron density of water. A difference between the yield of sulfate radical in deuterated and hydrogenated solutions is observed.

#### 4.3.2 Analysis and discussion

For example, the scavenged yield of the radical cation in deuterated water is 2.0, 1.5 and 1.3 times higher for  $f_s$  equal to 0.08, 0.16 and 0.3, respectively (**Figure 4.25**). As the concentration increases, the difference of the yield between the two solutions decreases and both reach almost the same plateau where all radical cations are scavenged. Obviously, there is an isotopic effect on the competitive reactions.

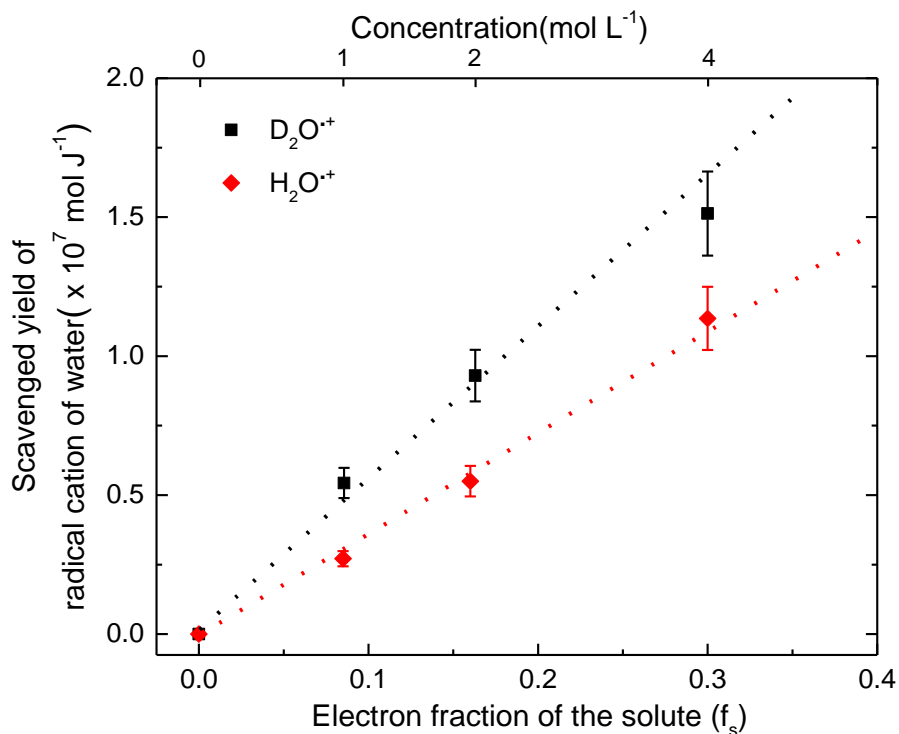


**Figure 4.25** Yield of scavenged radical cation ( $\text{H}_2\text{O}^{+\bullet}$  and  $\text{D}_2\text{O}^{+\bullet}$ ).



To explain these experimental results, we carried out theoretical simulations of electron transfer from  $\text{DSO}_4^-$  ( $\text{HSO}_4^-$ ) to  $\text{D}_2\text{O}^{*+}$  ( $\text{H}_2\text{O}^{*+}$ ). Different mechanisms can govern the electron transfer (ET) reaction depending on the amplitude of the quantum-mechanical coupling between the  $\text{H}_2\text{O}^{*+}/\text{HSO}_4^-$  and  $\text{H}_2\text{O}/\text{HSO}_4^\bullet$  electronic states. We evaluated the non-adiabatic ET rate constants arising from the hypothesis of weak coupling (electronic perturbative case) by the Jortner-Bixon formulation of ET theory.<sup>62</sup> This theory combines a quantized treatment of the inner-sphere vibrations with a classical electrostatic treatment of the outer-sphere response to ET. It turns out that an ET mechanism governed by nuclear motions cannot be competitive with a femtosecond proton transfer reaction because of the associated free energy barriers. Actually, traditional electron transfer theories are not likely to apply in the present case. In fact, the sudden ionization of a water molecule caused by the interaction with the accelerated electron beam, leaves the electron density in an out-of-equilibrium state. The excess of electronic energy may propel charge migration with surrounding molecules. To assess this possibility, we carried out real-time electron dynamics simulations at fixed nuclear positions. The almost +1 charge on water that results from ionization oscillates back-and-forth on the femtosecond time scale between the water and the  $\text{HSO}_4^-$  ion (**Figure 4.25a**, simulations 2 and 3). Ionization does not systematically lead to charge migration. It is dependent on the identity of the water molecular orbital that is initially depopulated. Subsequent charge migration is possible if the relative orientation and distance between the partners permit strong electronic coupling. Interestingly, since charge migration takes place at fixed position of atom nuclei, the process is not sensitive to isotopic substitution. This contrasts with proton transfer that *de facto* is dependent on nuclear vibrations and leads to kinetic isotopic effects.<sup>6</sup>

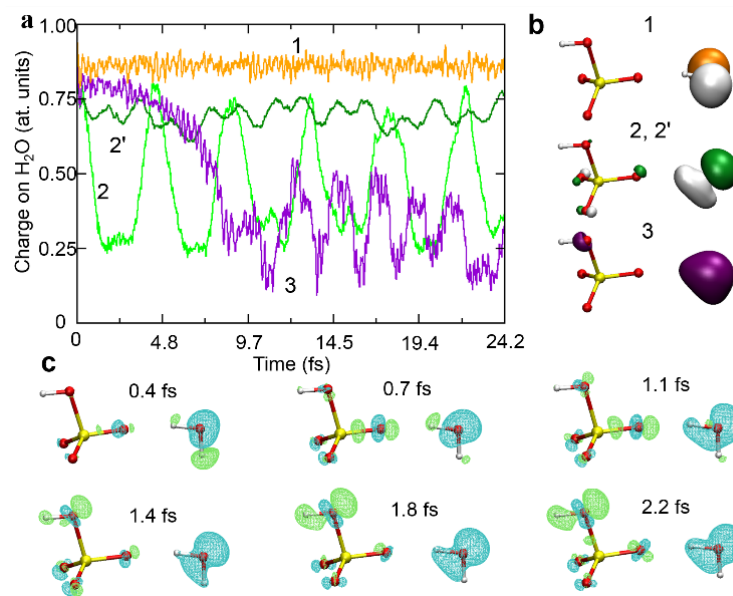


**Figure 4.25** Electronic Dynamics Simulations. a: evolution of the charge of the water molecule hydrogen bonded to  $\text{HSO}_4^-$ . Ionization takes place at  $t = 0$ . Each plot corresponds to a different electronic dynamics generated by depopulating different valence MOs, the representations of which are shown in panel b (for isosurfaces of  $\pm 0.08 \text{ bohr}^{-3/2}$ ). The two green curves (2 and 2') correspond to ionization from the same MO but with different values of the hydrogen bond length between  $\text{H}_2\text{O}$  and  $\text{HSO}_4^-$ , namely 1.8 and 2.4 Å, respectively. c: isosurfaces of the difference charge density with respect to the initial time for dynamics 2 and for different times spanning the first half period of charge migration. Blue and green isosurfaces indicate accumulation and depletion of electron density, respectively. Performed by A. De La Lande.

The succession of isosurfaces depicted on **Figure 4.25** reveals the mechanism of charge migration in the case of simulation 2. It first involves an internal polarization of the water molecule (0-0.4 fs) followed by charge migration along the hydrogen bond (0.7-1.1 fs), and finally localization of the hole mainly on the SOH group (1.8-2.2 fs) of  $\text{HSO}_4^\bullet$ . The excess energy thus appears to be sufficient to lead charge transfer to  $\text{HSO}_4^-$  ion. Our computational approach does not take into account energy dissipation caused by the response of atomic nuclei with electronic migration. Energy dissipation would have the effect of damping the oscillations, likely on the femtosecond time scale.

## 4.4 Conclusions

In this study, the radiolytic yield of  $\text{D}_2\text{O}^{\bullet+}$  in  $\text{D}_2\text{SO}_4/\text{D}_2\text{O}$  system is found to be  $(4.75 \pm 0.2) \times 10^{-7} \text{ mol J}^{-1}$ . Accordingly, the geminate recombination between presolvated electron and  $\text{D}_2\text{O}^{\bullet+}$  occurs within 1 ps and reduces the yield of hydrated electron. Besides, with the observed kinetics, our results show clearly that in deuterated solutions, the electron transfer is favored over proton transfer in competition reactions of the radical cation of water. In addition, numerical simulations show that electron transfer can take place within a few fs via a mechanism that is not governed by nuclear dynamics. Therefore, it is not sensitive to the isotopic substitution. Hence, we can conclude that the observed isotopic effects are solely due to the modulation of the proton transfer rates. Taken together, our experimental and theoretical data permit to elucidate the mechanism of direct oxidation triggered by  $\text{H}_2\text{O}^{\bullet+}$  ( $\text{D}_2\text{O}^{\bullet+}$ ) in competition with proton transfer in the condensed phase. According to the simulation, charge migration is propelled by the excess energy present in the electronic cloud just after ionization and not by nuclear motions as in standard chemical theories of electron transfer. The present study is a rare example of a competition between two chemical reactions whose branching ratio is driven by a faster electronic dynamic (**Figure 4.26**).

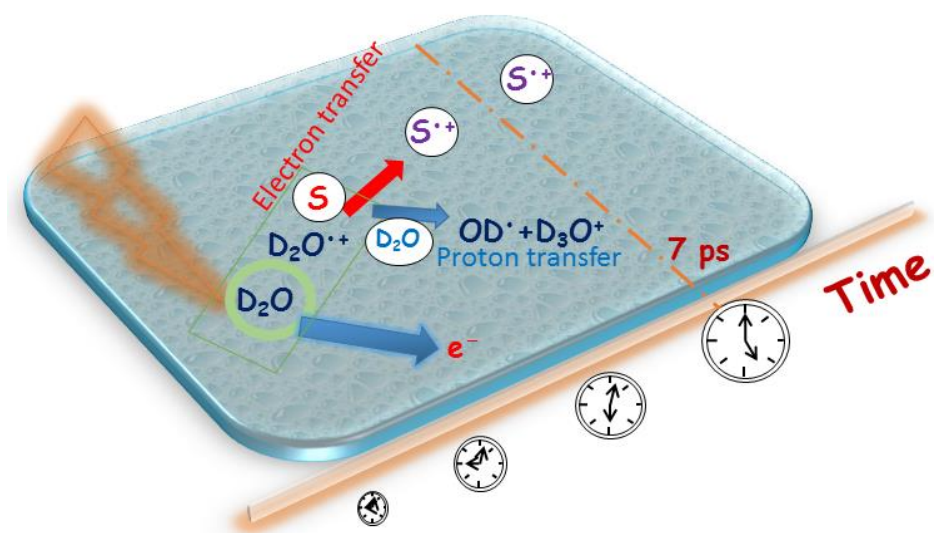


**Figure 4.26** Schematic of probing the competition reactions of the radical cation  $\text{D}_2\text{O}^{\bullet+}$ . 7 ps is the time resolution of the setup for probing the sulfate radical in this work.

Our study demonstrates that the radical cation of water is engaged not only in proton transfer reactions but also in redox reactions when  $\text{H}_2\text{O}^{\bullet+}$  ( $\text{D}_2\text{O}^{\bullet+}$ ) is formed in the vicinity of molecules different from water. Future studies will have to unravel if alternative reactions such as  $\text{H}_2\text{O}^{\bullet+}$  additions or  $\text{H}^{\bullet}$  abstraction may also be competitive with proton transfers. Finally, we remark that due to lack of information, the simulation codes, used by important communities working in the nuclear energy domain or in the radiobiology domain, do not take into account the oxidation reactivity of the radical cation of water. This makes little sense and should be reconsidered.

## References

- (1) Hatano, Y.; Mozumder, A. Introduction. In *Charged Particle and Photon Interactions with Matter*; CRC Press, 2003; pp 1–8.
- (2) Garrett, B. C.; Dixon, D. A.; Camaioni, D. M.; Chipman, D. M.; Johnson, M. A.; Jonah, C. D.; Kimmel, G. A.; Miller, J. H.; Rescigno, T. N.; Rossky, P. J.; et al. Role of Water in Electron-Initiated Processes and Radical Chemistry: Issues and Scientific Advances. *Chem. Rev.* **2005**, *105*, 355–390.
- (3) Buxton G.V. An Overview of the Radiation Chemistry of Liquids. In *Radiation Chemistry- From basics to applications in material and life sciences*; Spothem-Maurizot, M., Mostafavi, M., Douki, T., Belloni, J., Eds.; EDP SCIENCES: Les Ulis Cedex A, France, 2008; pp 35–52.
- (4) Mozumder, A. Events in Radiation Chemistry: An Introduction. **1989**, *34*, 1–3.
- (5) Gauduel, Y.; Pommeret, S.; Migus, A.; Antonetti, A. Some Evidence of Ultrafast  $\text{H}_2\text{O}^{*+}$ -Water Molecule Reaction in Femtosecond Photoionization of Pure Liquid Water: Influence on Geminate Pair Recombination Dynamics. *Chem. Phys.* **1990**, *149*, 1–10.
- (6) Anicich, V. G. Evaluated Bimolecular Ion-Molecule Gas Phase Kinetics of Positive Ions for Use in Modeling Planetary Atmospheres, Cometary Comae, and Interstellar Clouds. *J. Phys. Chem. Ref. Data* **1993**, *22*, 1469–1569.
- (7) Marsalek, O.; Elles, C. G.; Pieniazek, P. A.; Pluhařová, E.; VandeVondele, J.; Bradforth, S. E.; Jungwirth, P. Chasing Charge Localization and Chemical Reactivity Following Photoionization in Liquid Water. *J. Chem. Phys.* **2011**, *135*, 224510.
- (8) Khorana, S.; Hamill, W. H. Electronic Processes in The Pulse Radiolysis of Aqueous Solutions of Halide Ions. *J. Phys. Chem.* **1971**, *75*, 3081–3088.
- (9) Kim, K.-J.; Hamill, W. H. Direct and Indirect Effects in Pulse Irradiated Concentrated Aqueous Solutions of Chloride and Sulfate Ions. **1976**, *80*, 2320–2325.
- (10) Musat, R.; Denisov, S.; Marignier, J.-L.; Mostafavi, M. Decoding the Three-Pronged Mechanism of  $\text{NO}_3^\bullet$  Radical Formation in  $\text{HNO}_3$  Solutions at 22°C and 80°C Using

- Picosecond Pulse Radiolysis. *J. Phys. Chem. B* **2018**.
- (11) Li, J.; Nie, Z.; Zheng, Y. Y.; Dong, S.; Loh, Z.-H. Elementary Electron and Ion Dynamics in Ionized Liquid Water. *J. Phys. Chem. Lett.* **2013**, *4*, 3698–3703.
- (12) Thürmer, S.; Ončák, M.; Ottosson, N.; Seidel, R.; Hergenhausen, U.; Bradforth, S. E.; Slavíček, P.; Winter, B. On the Nature and Origin of Dicationic, Charge-Separated Species Formed in Liquid Water on X-Ray Irradiation. *Nat. Chem.* **2013**, *5*, 590–596.
- (13) La Vere, T.; Becker, D.; Sevilla, M. D. Yields of  $\cdot\text{OH}$  in Gamma-Irradiated DNA as A Function of DNA Hydration: Hole Transfer in Competition with  $\cdot\text{OH}$  Formation. *Radiat. Res.* **1996**, *145*, 673–680.
- (14) Janata, E.; Schuler, R. H. Rate Constant for Scavenging  $e_{\text{Aq}}^-$  in Nitrous Oxide-Saturated Solutions. *J. Phys. Chem.* **1982**, *86*, 2078–2084.
- (15) Roebke, W.; Renz, M.; Henglein, A. Pulsradiolyse Der Anionen  $\text{S}_2\text{O}_8^{2-}$  Und  $\text{HSO}_5^-$  in Wässriger Lösung. *Int. J. Radiat. Phys. Chem.* **1969**, *1*, 39–44.
- (16) Hentz, R. R.; Farhataziz; Hansen, E. M. Pulse Radiolysis of Liquids at High Pressures. II. Diffusion-Controlled Reactions of the Hydrated Electron. *J. Chem. Phys.* **1972**, *56*, 4485–4488.
- (17) Steenken, S.; Jovanovic, S. V. How Easily Oxidizable Is DNA? One-Electron Reduction Potentials of Adenosine and Guanosine Radicals in Aqueous Solution. *J. Am. Chem. Soc.* **1997**, *119*, 617–618.
- (18) Kobayashi, K.; Tagawa, S. Direct Observation of Guanine Radical Cation Deprotonation in Duplex DNA Using Pulse Radiolysis. *J. Am. Chem. Soc.* **2003**, *125*, 10213–10218.
- (19) Ma, J.; Wang, F.; Mostafavi, M. Ultrafast Chemistry of Water Radical Cation,  $\text{H}_2\text{O}^{\bullet+}$ , in Aqueous Solutions. *Molecules* **2018**, *23*, 244.
- (20) Neta, P.; Huie, R. E.; Ross, A. B. Rate Constants for Reactions of Inorganic Radicals in Aqueous Solution. *J. Phys. Chem. Ref. Data* **1988**, *17*, 1027–1284.
- (21) Buxton, G. V.; Greenstock, C. L.; Helman, W. P.; Ross, A. B. Critical Review of Rate Constants for Reactions of Hydrated Electrons, Hydrogen Atoms and Hydroxyl Radicals ( $\cdot\text{OH}/\cdot\text{O}^-$ ) in Aqueous Solution. *J. Phys. Chem. Ref. Data* **1988**, *17*, 513–886.

- (22) Belloni, J.; Monard, H.; Gobert, F.; Larbre, J.-P. P.; Demarque, A.; De Waele, V.; Lampre, I.; Marignier, J.-L. L.; Mostafavi, M.; Bourdon, J. C. C.; et al. ELYSE—A Picosecond Electron Accelerator for Pulse Radiolysis Research. *Nucl. Instruments Methods Phys. Res. Sect. A Accel. Spectrometers, Detect. Assoc. Equip.* **2005**, 539, 527–539.
- (23) Schmidhammer, U.; Jeunesse, P.; Stresing, G.; Mostafavi, M. A Broadband Ultrafast Transient Absorption Spectrometer Covering the Range from Near-Infrared (NIR) down to Green. *Appl. Spectrosc.* **2014**, 68, 1137–1147.
- (24) Wishart, J. F.; Cook, A. R.; Miller, J. R. The LEAF Picosecond Pulse Radiolysis Facility at Brookhaven National Laboratory. *Rev. Sci. Instrum.* **2004**, 75, 4359–4366.
- (25) Muroya, Y.; Lin, M.; Han, Z.; Kumagai, Y.; Sakumi, A.; Ueda, T.; Katsumura, Y. Ultra-Fast Pulse Radiolysis: A Review of The Recent System Progress and Its Application to Study on Initial Yields and Solvation Processes of Solvated Electrons in Various Kinds of Alcohols. *Radiat. Phys. Chem.* **2008**, 77, 1176–1182.
- (26) Saeki, A.; Kozawa, T.; Tagawa, S. Picosecond Pulse Radiolysis Using Femtosecond White Light with A High S/N Spectrum Acquisition System in One Beam Shot. *Nucl. Instruments Methods Phys. Res. Sect. A Accel. Spectrometers, Detect. Assoc. Equip.* **2006**, 556, 391–396.
- (27) Finkel, T.; Serrano, M.; Blasco, M. A. The Common Biology of Cancer and Ageing. *Nature* **2007**, 448, 767–774.
- (28) Stadtman, E. R. Protein Oxidation and Aging. *Free Radic. Res.* **2006**, 40, 1250–1258.
- (29) Imlay, J.; Linn, S. Damage and Oxygen Radical. *Science (80-. )*. **1988**, 240, 1302–1309.
- (30) Mallard, W. G.; Ross, A. B.; Helman, W. P. NDRL/NIST Solution Kinetics. Notre Dame Radiation Laboratory and National Institute of Standards and Technology: Gaithersburg, MD 1998.
- (31) Davidkova, M.; Spothem-maurizot, M. Predicting Radiation Damage Distribution in Biomolecules. In *Radiation Chemistry-From basics to applications in material and life sciences* *From Basics to Applications in Material and Life Science*; Spothem-Maurizot, M., Mostafavi, M., Douki, T., Belloni, J., Eds.; EDP SCIENCES: Les Ulis Cedex A, France, 2008; pp 265–276.

- (32) Wishart, J. F.; Nocera, D. G. *Photochemistry and Radiation Chemistry*; Wishart, J. F., Nocera, D. G., Eds.; Advances in Chemistry; American Chemical Society: Washington, DC, 1998; Vol. 254.
- (33) Trasatti, S. The Absolute Electrode Potential: An Explanatory Note (Recommendations 1986). *Pure Appl. Chem.* **1986**, 58, 417–428.
- (34) Reiss, H.; Heller, A. The Absolute Potential of The Standard Hydrogen Electrode: A New Estimate. *J. Phys. Chem.* **1985**, 89, 4207–4213.
- (35) Wardman, P. Reduction Potentials of One-Electron Couples Involving Free Radicals in Aqueous Solution. *J. Phys. Chem. Ref. Data* **1989**, 18, 1637–1755.
- (36) Neta, P. Redox Properties of Free Radicals. *J. Chem. Educ.* **1981**, 58, 110–113.
- (37) Mozumder, A. Ionization and Excitation Yields in Liquid Water Due to The Primary Irradiation: Relationship of Radiolysis with Far UV-Photolysis Presented at The Symposium on Recent Trends in Photochemical Sciences, Trivandrum, January 8-10, 2000. *Phys. Chem. Chem. Phys.* **2002**, 4, 1451–1456.
- (38) Mizuse, K.; Kuo, J.-L.; Fujii, A. Structural Trends of Ionized Water Networks: Infrared Spectroscopy of Watercluster Radical Cations  $(\text{H}_2\text{O})_n^+$  ( $n = 3-11$ ). *Chem. Sci.* **2011**, 2, 868–876.
- (39) Dorfman, L. M.; Adams, G. E. *Reactivity of the Hydroxyl Radical in Aqueous Solutions.*; National bureau of standards: U.S., 1973.
- (40) Balcerzyk, A.; LaVerne, J.; Mostafavi, M. Direct and Indirect Radiolytic Effects in Highly Concentrated Aqueous Solutions of Bromide. *J. Phys. Chem. A* **2011**, 115, 4326–4333.
- (41) El Omar, A. K.; Schmidhammer, U.; Rousseau, B.; LaVerne, J.; Mostafavi, M. Competition Reactions of  $\text{H}_2\text{O}^{\bullet+}$  Radical in Concentrated  $\text{Cl}^-$  Aqueous Solutions: Picosecond Pulse Radiolysis Study. *J. Phys. Chem. A* **2012**, 116, 11509–11518.
- (42) Balcerzyk, A.; Schmidhammer, U.; El Omar, A. K.; Jeunesse, P.; Larbre, J.-P.; Mostafavi, M. Picosecond Pulse Radiolysis of Direct and Indirect Radiolytic Effects in Highly Concentrated Halide Aqueous Solutions. *J. Phys. Chem. A* **2011**, 115, 9151–9159.
- (43) El Omar, A. K.; Schmidhammer, U.; Balcerzyk, A.; LaVerne, J.; Mostafavi, M. Spur



- Reactions Observed by Picosecond Pulse Radiolysis in Highly Concentrated Bromide Aqueous Solutions. *J. Phys. Chem. A* **2013**, *117*, 2287–2293.
- (44) Pucheault, J.; Ferradini, C.; Julien, R.; Deysine, A.; Gilles, L.; Moreau, M. Radiolysis of Concentrated Solutions. 1. Pulse and .Gamma. Radiolysis Studies of Direct and Indirect Effects in Lithium Chloride Solutions. *J. Phys. Chem.* **1979**, *83*, 330–336.
- (45) Stanbury, D. M. Reduction Potentials Involving Inorganic Free Radicals in Aqueous Solution. *Adv. Inorg. Chem* **1989**, *33*, 69–138 pp.
- (46) Ma, J.; Schmidhammer, U.; Mostafavi, M. Picosecond Pulse Radiolysis of Highly Concentrated Sulfuric Acid Solutions: Evidence for the Oxidation Reactivity of Radical Cation  $\text{H}_2\text{O}^{*+}$ . *J. Phys. Chem. A* **2014**, *118*, 4030–4037.
- (47) Sevilla, M. D.; Bernhard, W. A. Mechanism of Direct Radiation Damage to DNA. In *Radiation Chemistry from Basics to Applications in Material and Life Science*; M., S.-M., Mostafavi, M., Douki, T., Belloni, J., Eds.; EDP SCIENCES: Les Ulis, France, 2008; pp 191–201.
- (48) Steenken, S.; Goldbergerova, L. Photoionization of Organic Phosphates by 193 Nm Laser Light in Aqueous Solution: Rapid Intramolecular H-Transfer to the Primarily Formed Phosphate Radical. A Model for Ionization-Induced Chain-Breakage in DNA? *J. Am. Chem. Soc.* **1998**, *120*, 3928–3934.
- (49) Ma, J.; Schmidhammer, U.; Mostafavi, M. Picosecond Pulse Radiolysis of Highly Concentrated Phosphoric Acid Solutions: Mechanism of Phosphate Radical Formation. *J. Phys. Chem. B* **2014**, *119*, 7180–7185.
- (50) Balcerzyk, A.; El Omar, A. K.; Schmidhammer, U.; Pernot, P.; Mostafavi, M. Picosecond Pulse Radiolysis Study of Highly Concentrated Nitric Acid Solutions: Formation Mechanism of  $\text{NO}_3\bullet$  Radical. *J. Phys. Chem. A* **2012**, *116*, 7302–7307.
- (51) Garaix, G.; Horne, G. P.; Venault, L.; Moisy, P.; Pimblott, S. M.; Marignier, J. L.; Mostafavi, M. Decay Mechanism of  $\text{NO}_3\bullet$  Radical in Highly Concentrated Nitrate and Nitric Acidic Solutions in the Absence and Presence of Hydrazine. *J. Phys. Chem. B* **2016**, *120*, 5008–5014.
- (52) Kameda, Y.; Hosoya, K.; Sakamoto, S.; Suzuki, H.; Usuki, T.; Uemura, O. Hydrogen-

- Bonded Structure in Aqueous Sulfuric Acid Solutions. *J. Mol. Liq.* **1995**, 65–66, 305–308.
- (53) Tang, Y.; Thorn, R. P.; Mauldin, R. L.; Wine, P. H. Kinetics and Spectroscopy of The  $\text{SO}_4^-$  Radical in Aqueous Solution. *J. Photochem. Photobiol. A Chem.* **1988**, 44, 243–258.
- (54) Jiang, P.-Y.; Katsumura, Y.; Nagaishi, R.; Domae, M.; Ishikawa, K.; Ishigure, K.; Mechanism, F. Pulse Radiolysis Study of Concentrated Sulfuric Acid Solutions. *J. Chem. Soc. Faraday Trans.* **1992**, 88, 1653–1658.
- (55) El Omar, A. K.; Schmidhammer, U.; Jeunesse, P.; Larbre, J.-P.; Lin, M.; Muroya, Y.; Katsumura, Y.; Pernot, P.; Mostafavi, M. Time-Dependent Radiolytic Yield of  $\text{OH}^\bullet$  Radical Studied by Picosecond Pulse Radiolysis. *J. Phys. Chem. A* **2011**, 115, 12212–12216.
- (56) Elmore, K. L.; Hatfield, J. D.; Dunn, R. L.; Jones, A. D. Dissociation of Phosphoric Acid Solutions at 25° <sup>1</sup>. *J. Phys. Chem.* **1965**, 69, 3520–3525.
- (57) Caminiti, R.; Cucca, P.; Atzei, D. Phosphate-Water Interactions in Concentrated Aqueous Phosphoric Acid Solutions. *J. Phys. Chem.* **1985**, 89, 1457–1460.
- (58) Wang, C.-R.; Nguyen, J.; Lu, Q.-B. Bond Breaks of Nucleotides by Dissociative Electron Transfer of Nonequilibrium Prehydrated Electrons: A New Molecular Mechanism for Reductive DNA Damage. *J. Am. Chem. Soc.* **2009**, 131, 11320–11322.
- (59) Ma, J.; Wang, F.; Denisov, S. A.; Adhikary, A.; Mostafavi, M. Reactivity of Prehydrated Electrons toward Nucleobases and Nucleotides in Aqueous Solution. *Sci. Adv.* **2017**, 3, e1701669.
- (60) Stuart, C. R.; Ouellette, D. C.; Elliot, A. J. Pulse Radiolysis Studies of Liquid Heavy Water At Temperature up to 250 °C. *AECL-12107* **2002**.
- (61) Ma, J.; Schmidhammer, U.; Mostafavi, M. Direct Evidence for Transient Pair Formation between a Solvated Electron and  $\text{H}_3\text{O}^{+}$  Observed by Picosecond Pulse Radiolysis. *J. Phys. Chem. Lett.* **2014**, 5, 2219–2223.
- (62) Kestner, N. R.; Logan, J.; Jortner, J. Thermal Electron Transfer Reactions in Polar Solvents. *J. Phys. Chem.* **1974**, 78, 2148.

## Chapter V: Summary

## **Table of content**

5.1 General conclusion

5.2 Perspective

References

## Chapter V: Conclusions and perspectives

### 5.1 Conclusions

From the first measurement by Hart *et al.*<sup>1</sup> during the 1960's, the progress in the knowledge of radiation chemistry throughout is accelerated by the deep-going studies by pulse radiolysis. The importance of the pulse radiolysis technology is undoubtedly underlined. The picosecond pulse-probe facility ELYSE allows us to explore the ultrafast radiolysis process in solutions induced by high energy radiation (6-9 MeV). In ELYSE, short-lived species is generated with a pulse of electrons much shorter than the time constants of the subsequent reactions, and detected by time-resolved optical techniques. Time-resolved absorbance measurements of the short-lived species at picosecond range are achieved by two complementary fast detection systems. One is a pump-probe set-up, which synchronize the laser beam and the electron beam to measure the absorbance. The pump is the electron pulse meanwhile the probe is a part of the laser beam delayed by a variable optical delay (7 ps–12 ns). The probe light originated from the laser source could cover the wavelength range from 360 nm to 1500 nm to detect the intermediates that absorb in these region. Another system is based on a high dynamic range streak camera (250–800nm) and pulsed laser diodes (absorbance kinetics at given wavelengths) or a Xenon flash lamp. Streak camera could be used to observe from ps to 1 ms sweep time. Both systems display high signal-to-noise ratios suitable for fast transient absorption kinetics studies. The pump-probe and streak camera systems permit to trace the ultrafast reactions or chemical processes induced by the fast electron taking place from the timescale of picosecond to millisecond.

The focus of my thesis is on the solvated electron, hydroxyl radical and water cation radical in deuterated water. Firstly, we studied the radiolytic properties of the solvated electron in D<sub>2</sub>O. The solvated electron is a unique species that can be produced in most polar and low polar solvents. The study of its properties is an important key factor to understand the dynamics and kinetics reactions in solutions. Moreover, the hydrated electron in neat D<sub>2</sub>O is used for the measurements at high temperatures to study the temperature effect on the radical yield and the spur kinetics.<sup>2, 3</sup> Then the knowledge of its properties and its reactions in various solvents is a key issue in physical chemistry. In radiation chemistry, the measurements of the absolute value of the radical yields at shortest time is obviously necessary to obtain two important information: the energy deposition in

the spurs of ionization and the yield of secondary radical which can be produced when the solutes are present in the solutions. For this objective, it is necessary to obtain two independent parameters of the hydrated electron in neat D<sub>2</sub>O: the initial yield and the absorption spectra with molar absorption coefficient. In Chapter III careful and systematic measurements, by taking into account the absorption induced in the windows of the optical cell and the radical hydroxyl, allowed us to determine precisely the absolute absorption spectra of the hydrated electron in D<sub>2</sub>O from 250 to 1500 nm. The shape and its amplitude are different from those reported previously in the literature. The amplitude of the absorption band as found here is different by 10% from that reported in the literature.<sup>4</sup> Additionally, the shape of the absorption spectra of the solvated electron reported by Freeman often used is not correct. For example, the ratio of  $G\varepsilon_{\max}(e_s^-)$  between D<sub>2</sub>O and H<sub>2</sub>O in Freeman's work is 1.25, but in this work it is 1.15, and the extinction coefficient value of the hydrated electron in D<sub>2</sub>O at 300 nm is almost 20% higher than that reported by Freeman.<sup>2, 5</sup>

The use of the isosbestic method for the determination of the extinction coefficient with a specific scavenger is more appropriate because it is based only on the knowledge of the molar absorption coefficient of the reaction product. We found that the value of the initial yield of the hydrated electron and the hydroxyl radical, observed at 7 ps, are equal (within the experimental errors) to those found in H<sub>2</sub>O, but the kinetics of the solvated electron are slower in D<sub>2</sub>O than in H<sub>2</sub>O meanwhile that of hydroxyl radical presented no obvious different in D<sub>2</sub>O and H<sub>2</sub>O. The isotopic effect was explained initially by the fact that the initial spatial distribution between electron and hole in D<sub>2</sub>O is 1.2-1.4 times larger in D<sub>2</sub>O than in H<sub>2</sub>O.<sup>6</sup> Then laser photolysis measurements<sup>7</sup> showed that the main reason of slower decay of the solvated electron in D<sub>2</sub>O is due to the lower rate constant of the two main reactions responsible for the decay of the solvated electron in water at short time:



But the yields are not comparable when the solvated electrons are produced by laser photolysis or by ionizing radiation. In our work, thanks to the determination of the initial yields (7 ps) of the hydrated electron and of the hydroxyl radical that are found to be same in neat water and in neat

deuterated water, it can be concluded that the geminate recombination reactions are not affected significantly in D<sub>2</sub>O. Therefore, the slower decay can be explained well by the change of reaction rate of EQ.5-1 and 5-2. The reaction EQ.5-2 is diffusion controlled and as the diffusion coefficient is lower in D<sub>2</sub>O than H<sub>2</sub>O, the slower decay of solvated electron in D<sub>2</sub>O is understandable. The reaction EQ.5-1 is not fully limited by diffusion. In D<sub>2</sub>O, however, it needs higher reorganization energy and it can be considered slower in D<sub>2</sub>O than in H<sub>2</sub>O. Another point should be considered: due to the isotopic effect and the change of the vibration frequency which is responsible of hydroxyl radical formation through proton transfer, the formation of OD• through deuterated of D<sub>2</sub>O<sup>•+</sup> should be slower than that of OH• and we had expected a lower yield of OD• and  $e_{D_2O}^-$  at picosecond range.<sup>8</sup> Because, the geminate recombination between electron and the radical water hole (D<sub>2</sub>O<sup>•+</sup>) should be favored when the proton transfer is slowed down by isotopic effect. However, the initial yields are found to be the same within the measurements precision. Therefore, our conclusion is that the change of water hole lifetime does not affect significantly the geminate reaction.

In Chapter VI, the reactivity of water cation radical in D<sub>2</sub>O has been investigated by picosecond pulse radiolysis. In this study, by using the scavenging method at picosecond range the radiolytic yield of D<sub>2</sub>O<sup>•+</sup> in D<sub>2</sub>SO<sub>4</sub>/D<sub>2</sub>O system is found to be  $(4.75 \pm 0.2) \times 10^{-7}$  mol J<sup>-1</sup>. Accordingly, the geminate recombination between presolvated electron and D<sub>2</sub>O<sup>•+</sup> occurs within 1 ps and reduce the yield of hydrated electron. Besides, with the observed kinetics, our results show clearly that in deuterated solutions, electron transfer is favored over proton transfer in competition reactions of the radical cation of water. In addition, numerical simulations show that electron transfer can take place within a few fs by a mechanism that is not governed by nuclear dynamics. Therefore, it is not sensitive to the isotopic substitution. Hence, we can conclude that the observed isotopic effects are solely due to the modulation of the proton transfer rates. Taken together, our experimental and theoretical data permit to elucidate the mechanism of direct oxidation triggered by H<sub>2</sub>O<sup>•+</sup> (D<sub>2</sub>O<sup>•+</sup>) in competition with proton transfer in the condensed phase. According to the simulation, charge migration is propelled by the excess energy present in the electronic cloud just after ionization and not by nuclear motions as in standard chemical theories of electron transfer. The present study is a rare example of a competition between two chemical reactions whose branching ratio is driven by a faster electronic dynamic.

## 5.2 Perspectives

Water plays an indispensable role in radiation chemistry. Better understanding of reaction mechanism in water after irradiation is essential for further application. However, the initial excitation and ionization process in water just after radiation is not confirmed due to the limitation of the resolution of time resolved spectroscopy. In my thesis, the reactivity of the solvated electron, hydroxyl radical and water cation radical in D<sub>2</sub>O have been studied and compared with those in H<sub>2</sub>O. The time dependent radiolytic yields of solvated electron and hydroxyl radical in D<sub>2</sub>O have been determined by direct measurements after 7 ps. And the scavenged yield of water cation radical in D<sub>2</sub>O also has been estimated by indirect measurements.

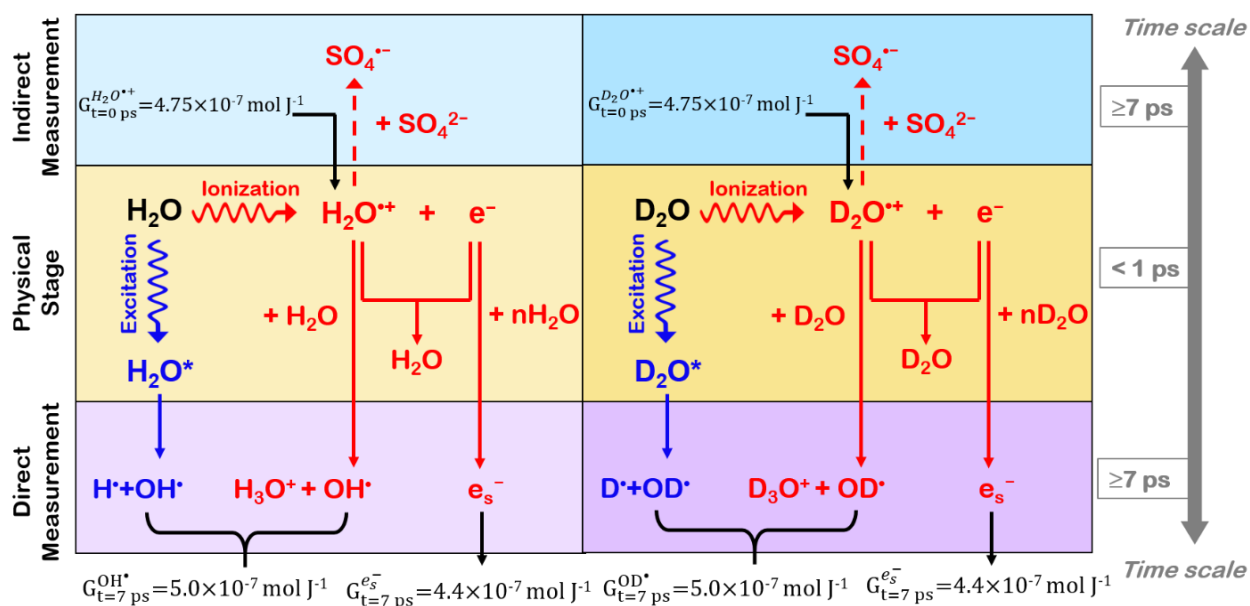


**Figure 5.1** Diagram of the radiolytic yield of hydrated electron, hydroxyl radical and water cation radical at 7 ps by direct or indirect measurements.

As present in **Figure 5.1**, these value could help us roughly deduce the initial reaction mechanism in water and point a direction for further researching. Considering the radiolytic yields of solvated electron at 7 ps and the scavenged yield of water cation radical in H<sub>2</sub>O and D<sub>2</sub>O are same, we could conclude that the geminate recombination in water is not influenced by isotopic effect. However, there is uncertainty for that the scavenged yield of water cation radical was determined indirectly in concentrated acidic solution. The direct measurement of the yield of the water cation radical



would be supportable. Up to now, the direct observation of water cation radical is still lack of certain information. It is a challenging subject to investigate the property (absorption, kinetics, *etc.*) of water cation radical. For example, to observe the water cation radical that is expected to absorb in the UV region with low extinction coefficient, the time resolution of the time-resolved spectroscopy should be lower than 100 fs when the water cation radical has not yet totally been transformed into hydroxyl radical.

In addition, our study demonstrates that the radical cation of water is engaged not only in proton transfer reactions but also in redox reactions when  $\text{H}_2\text{O}^{\bullet+}$  ( $\text{D}_2\text{O}^{\bullet+}$ ) is formed in the vicinity of molecules different from water. The proton transfer reaction is slowed down by isotopic effect. Future studies will have to unravel if alternative reactions such as  $\text{H}_2\text{O}^{\bullet+}$  additions or  $\text{H}^{\bullet}$  abstraction may also be competitive with proton transfers.

## References

- (1) Hart, E. J.; Boag, J. W. Absorption Spectrum of the Hydrated Electron in Water and in Aqueous Solutions. *J. Am. Chem. Soc.* **1962**, *84*, 4090–4095.
- (2) Jou, F.; Freeman, G. R. Temperature and Isotope Effects on the Shape of the Optical Absorption Spectrum of Solvated Electrons in Water. *J. Phys. Chem.* **1979**, *83*, 2383.
- (3) Elliot, A.; Bartels, D. The Reaction Set, Rate Constants and g-Values for the Simulation of the Radiolysis of Light Water Over the Range 20 to 350 °C Based on Information Available in 2008. *At. Energy Canada Ltd. Rep.* **2009**, 153–127160.
- (4) Fielden, E. M.; Hart, E. J. Radical Yields and Some Rate Constants in Primary Heavy Water <sup>3</sup>. *Radiat. Res.* **1968**, *33*, 426–436.
- (5) Bartels, D. M.; Takahashi, K.; Cline, J. A.; Marin, T. W.; Jonah, C. D. Pulse Radiolysis of Supercritical Water. 3. Spectrum and Thermodynamics of the Hydrated Electron. *J. Phys. Chem. A* **2005**, *109*, 1299–1307.
- (6) Schmidt, K. H.; Han, P.; Bartels, D. M. Radiolytic Yields of the Hydrated Electron from Transient Conductivity: Improved Calculation of the Hydrated Electron Diffusion Coefficient and Analysis of Some Diffusion-Limited (e<sup>-</sup>) Reaction Rates. *J. Phys. Chem.* **1995**, *99*, 10530–10539.
- (7) Jonah, C. D.; Chernovitz, A. C. The Mechanism of Electron Thermalization in H<sub>2</sub>O, D<sub>2</sub>O, and HDO. *Can. J. Phys.* **1990**, *68*, 935–939.
- (8) Chernovitz, A.; Jonah, C. Isotopic Dependence of Recombination Kinetics in Water. *J. Phys. Chem.* **1988**, *92*, 5946–5950.

## Publications During Thesis

1. **Furong Wang**, Gregory P. Horne, Pascal Pernot, Pierre Archirel, and Mehran Mostafavi. “Picosecond Pulse Radiolysis Study on the Radiation-Induced Reactions in Neat Tributyl Phosphate.” *The Journal of Physical Chemistry B* 122, no. 28 (July 19, 2018): 7134–42. <https://doi.org/10.1021/acs.jpcb.8b03715>.
2. **Furong Wang**, Uli Schmidhammer, Jean-Philippe Larbre, Zizhao Zong, Jean-Louis Marignier, and Mehran Mostafavi. “Time-Dependent Yield of the Hydrated Electron and the Hydroxyl Radical in D<sub>2</sub>O: A Picosecond Pulse Radiolysis Study.” *Physical Chemistry Chemical Physics* 20, no. 23 (2018): 15671–79. <https://doi.org/10.1039/C8CP02276C>.
3. **Furong Wang**, Fanny Varenne, Daniel Ortiz, Valentin Pinzio, Mehran Mostafavi, and Sophie Le Caër. “Degradation of an Ethylene Carbonate/Diethyl Carbonate Mixture by Using Ionizing Radiation.” *ChemPhysChem* 18, no. 19 (October 6, 2017): 2799–2806. <https://doi.org/10.1002/cphc.201700320>.
4. **Furong Wang**, Pascal Pernot, Pierre Archirel, Uli Schmidhammer, Daniel Ortiz, Sophie Le Caër, and Mehran Mostafavi. “Observation and Simulation of Transient Anion Oligomers (LiClO<sub>4</sub>)<sub>n</sub><sup>−</sup> (n = 1–4) in Diethyl Carbonate LiClO<sub>4</sub> Solutions.” *The Journal of Physical Chemistry B* 121, no. 31 (August 10, 2017): 7464–72. <https://doi.org/10.1021/acs.jpcb.7b04982>.
5. **Furong Wang**, Pierre Archirel, Yusa Muroya, Shinichi Yamashita, Pascal Pernot, Chengying Yin, Abdel Karim El Omar, Uli Schmidhammer, Jean-Marie Teuler, and Mehran Mostafavi. “Effect of the Solvation State of Electron in Dissociative Electron Attachment Reaction in Aqueous Solutions.” *Physical Chemistry Chemical Physics* 19, no. 34 (2017): 23068–77. <https://doi.org/10.1039/C7CP03997B>.
6. **Furong Wang**, Uli Schmidhammer, Aurélien de La Lande, and Mehran Mostafavi. “Ultra-Fast Charge Migration Competes with Proton Transfer in The Early Chemistry of H<sub>2</sub>O<sup>•+</sup>.” *Physical Chemistry Chemical Physics* 19, no. 4 (2017): 2894–99. <https://doi.org/10.1039/C6CP07013B>.
7. Khashayar Ghandi, **Furong Wang**, Cody Landry, and Mehran Mostafavi. “Naked Gold Nanoparticles and Hot Electrons in Water.” *Scientific Reports* 8, no. 1 (May 8, 2018): 7258.

- <https://doi.org/10.1038/s41598-018-25711-2>.
8. Jun Ma, **Furong Wang**, and Mehran Mostafavi. “ $\text{H}_2\text{O}^+$ , L’espèce La Plus Fugace et Oxydante.” *L’actualité Chimique* 429 (2018): 32.
  9. Jun Ma, **Furong Wang**, and Mehran Mostafavi. “Ultrafast Chemistry of Water Radical Cation,  $\text{H}_2\text{O}^+$ , in Aqueous Solutions.” *Molecules* 23, no. 2 (January 26, 2018): 244. <https://doi.org/10.3390/molecules23020244>.
  10. Jun Ma, **Furong Wang**, Sergey A Denisov, Amitava Adhikary, and Mehran Mostafavi. “Reactivity of Prehydrated Electrons toward Nucleobases and Nucleotides in Aqueous Solution.” *Science Advances* 3, no. 12 (December 15, 2017): e1701669. <https://doi.org/10.1126/sciadv.1701669>.
  11. Balcerzyk, Anna, Uli Schmidhammer, **Furong Wang**, Aurélien de la Lande, and Mehran Mostafavi. “Ultrafast Scavenging of the Precursor of  $\text{H}\cdot$  Atom, ( $\text{e}^-$ ,  $\text{H}_3\text{O}^+$ ), in Aqueous Solutions.” *The Journal of Physical Chemistry B* 120, no. 34 (September 1, 2016): 9060–66. <https://doi.org/10.1021/acs.jpcb.6b04944>.
  12. Balcerzyk, Anna, Uli Schmidhammer, Gregory Horne, **Furong Wang**, Jun Ma, Simon M Pimblott, Aurélien de la Lande, and Mehran Mostafavi. “Unexpected Ultrafast Silver Ion Reduction: Dynamics Driven by the Solvent Structure.” *The Journal of Physical Chemistry B* 119, no. 31 (August 6, 2015): 10096–101. <https://doi.org/10.1021/acs.jpcb.5b04907>.

## Résumé

Le travail de thèse présenté se situe dans le prolongement des études fondamentales menées depuis de nombreuses décennies dans le but de mieux comprendre les mécanismes de formation et de réaction ultrarapides des espèces chimiques radicalaires formées dans les premiers instants de la radiolyse de l'eau. Parmi ces espèces, l'électron, le radical hydroxyle et son précurseur, le radical cation  $\text{H}_2\text{O}^{+\bullet}$ , sont des plus intéressantes à étudier. En particulier, l'oxydation compétitive ultrarapide de  $\text{H}_2\text{O}^{+\bullet}$ , qui nécessite des conditions expérimentales d'observation spécifiques, n'a pas été explorée jusqu'ici.

L'étude présentée se fonde sur des données cinétiques originales, obtenues auprès de la plateforme expérimentale ELYSE d'Orsay, permettant d'étudier les effets isotopiques sur les réactivités de ces espèces.

Le premier chapitre du manuscrit, introductif, traite de l'intérêt de la radiolyse dans de nombreux domaines scientifiques et industriels. Les concepts de transfert d'énergie linéaire et de rendement radiolytique qui seront importants par la suite sont définis clairement. En outre, trois étapes principales, physiques, physico-chimiques et chimiques, des transformations induites par le rayonnement dans la phase aqueuse sont rappelées brièvement.

Le deuxième chapitre du manuscrit, consacré aux matériels et méthodes, pose le cadre général de l'étude expérimentale et de son analyse future. Il est construit sur une description complète des moyens d'excitation et de détection, de même que des produits utilisés pour la réalisation des échantillons et des milieux d'expérience. La source d'excitation est constituée de l'accélérateur d'électrons ELYSE, du Laboratoire de Chimie-Physique d'Orsay. Une ligne expérimentale, essentiellement constituée d'un canon HF, d'un booster et d'éléments quadrupolaires permet d'amener le faisceau d'électrons à l'échantillon. L'observable expérimentale est, par exemple, le déclin de la densité optique de l'espèce étudiée, à l'échelle de quelques picosecondes à quelques centaines de nanosecondes. La mesure s'effectue par l'utilisation d'un laser sonde et d'une caméra à balayage de fente.

Le troisième chapitre est consacré à l'étude temporelle, à faible TEL, du rendement radiolytique de l'électron solvaté et du radical  $\text{OD}^\bullet$  dans l'eau deutérée. Il débute par un état des connaissances scientifiques dans ce domaine. Une première sous-partie, consacrée à l'électron

solvaté, présente les résultats expérimentaux obtenus (spectres d'absorption dans  $\text{H}_2\text{O}$  et  $\text{D}_2\text{O}$ , spectres d'absorption transitoires, cinétiques de déclin, effets de doses). Une seconde sous-partie, consacrée à  $\text{OD}^\bullet$ , reprend la même méthodologie, mais dans le cadre de conditions expérimentales plus difficiles nécessitant de prendre en compte, par exemple, les absorbances des fenêtres ou la propagation du faisceau d'électrons. Une dernière partie conclut l'ensemble du chapitre. On note plusieurs résultats originaux. En particulier, l'obtention du spectre d'absorption de l'électron, sur une large gamme de longueurs d'ondes, entre 250 et 1500 nm, apportant des informations plus précises que celles décrites dans la littérature. La détermination, dans ce travail, du rendement de l'électron et du radical hydroxyle à 7 ps a permis d'expliquer de façon complète et particulièrement convaincante l'absence d'effet isotopique sur la recombinaison géminée.

Le quatrième chapitre est consacré à la chimie à temps court de  $\text{H}_2\text{O}^{+\bullet}$ , notamment à la compétition entre la migration de charge ultra rapide et le transfert de proton. Une première partie, relativement importante et très exhaustive, fait le point sur l'état de l'art en la matière. Une seconde partie détaille les résultats originaux obtenus sur la réactivité du radical cation de l'eau dans  $\text{D}_2\text{SO}_4/\text{D}_2\text{O}$ . Une troisième partie est consacrée aux effets isotopiques sur la chimie de  $\text{H}_2\text{O}^{+\bullet}$ . Le chapitre se conclut par un résultat particulièrement original et important dans le domaine, mettant en évidence une oxydation directe déclenchée par  $\text{H}_2\text{O}^{+\bullet}$  ( $\text{D}_2\text{O}^{+\bullet}$ ) en compétition avec le transfert de proton. Les simulations numériques permettent d'attribuer le phénomène à une migration rapide de l'électron activée par un excès d'énergie du nuage électronique excité par les électrons du faisceau incident, échappant donc à la substitution isotopique. Ce résultat révèle une nouvelle voie de relaxation de l'énergie primaire qui, jusqu'à présent, était attribuée à un couplage avec le transfert de proton.

Un cinquième et dernier chapitre conclut ce travail de thèse par une synthèse des résultats obtenus et dresse les perspectives de nouvelles études à temps court en présentant un nouveau diagramme complet de l'ensemble des mécanismes radiolytiques et de leurs rendements.

**Titre :** Réactivité de l'électron solvaté, du radical hydroxyle et de son précurseur dans l'eau lourde, étudiée par la radiolyse pulsée picoseconde

**Mots clés :** électron solvaté, radical hydroxyle, radical cationique de l'eau, eau lourde, radiolyse pulsée

**Résumé :** Des mesures de radiolyse impulsionnelle avec des paquets d'électron de 7 picosecondes ont été effectuées dans des systèmes D<sub>2</sub>O et D<sub>2</sub>SO<sub>4</sub> / D<sub>2</sub>O purs afin d'étudier l'effet isotopique sur la réactivité de l'électron solvaté ( $e_s^-$ ), du radical hydroxyle (OH<sup>•</sup>) et de son radical cation cationique (H<sub>2</sub>O<sup>•+</sup>). Dans le système D<sub>2</sub>O, le spectre d'absorption molaire de l'électron solvaté dans D<sub>2</sub>O a été déterminé entre 250 et 1500 nm en utilisant la méthode du point isosbestique. Sur la base de ce coefficient d'extinction, le rendement radiolytique de  $e_s^-$  dans D<sub>2</sub>O juste après l'impulsion d'électrons de 7 ps a été déterminé à  $(4,4 \pm 0,2) \times 10^{-7} \text{ mol J}^{-1}$ , ce qui coïncide avec celui dans H<sub>2</sub>O. Le rendement du radical OD<sup>•</sup> juste après l'impulsion d'électrons s'est révélée être  $(5,0 \pm 0,2) \times 10^{-7} \text{ mol J}^{-1}$ . Dans le cas de l'électron solvaté la vitesse de déclin

dans D<sub>2</sub>O est plus lent que dans H<sub>2</sub>O, tandis que la vitesse de déclin de OD<sup>•</sup> est similaire à celui de OH<sup>•</sup>.

Dans le système D<sub>2</sub>SO<sub>4</sub> / D<sub>2</sub>O, la réactivité de D<sub>2</sub>O<sup>•+</sup> a été sondée dans des solutions d'acide sulfurique deutérées de diverses concentrations et comparée à celle de H<sub>2</sub>O<sup>•+</sup>. Le soluté oxydé, le radical sulfate a été observé à 7 ps et des rendements plus élevés ont été trouvés dans les solutions deutérées. Les effets isotopiques révèlent la compétition entre deux réactions ultra-rapides : le transfert de protons vers H<sub>2</sub>O (D<sub>2</sub>O) et le transfert d'électrons de H<sub>2</sub>O<sup>•+</sup> (D<sub>2</sub>O<sup>•+</sup>). Les simulations par la théorie de la densité fonctionnelle décryptent le mécanisme du transfert d'électrons : elles se font par migration de charge sub-femtoseconde et ne sont pas affectées par la substitution isotopique.

**Title:** Reactivity of the Solvated Electron, the Hydroxyl Radical and its Precursor in Deuterated Water Studied by Picosecond Pulse Radiolysis

**Keywords:** solvated electron, hydroxyl radical, water cation radical, heavy water, pulse radiolysis

**Abstract:** Picosecond pulse radiolysis measurements were performed in neat D<sub>2</sub>O and D<sub>2</sub>SO<sub>4</sub>/D<sub>2</sub>O system in order to study the isotopic effect on the reactivity of the solvated electron ( $e_s^-$ ), the hydroxyl radical (OH<sup>•</sup>) and its precursor—water cation radical (H<sub>2</sub>O<sup>•+</sup>). In D<sub>2</sub>O system, the molar absorption coefficient spectra of spectrum in D<sub>2</sub>O was determined between 250 to 1500 nm using the isosbestic point method. Based on this extinction coefficient, the radiolytic yield of  $e_s^-$  in D<sub>2</sub>O just after the 7 ps electron pulse was determined to be  $(4.4 \pm 0.2) \times 10^{-7} \text{ mol J}^{-1}$ , which coincides with the one for in H<sub>2</sub>O. The yield of the radical OD<sup>•</sup> just after the 7 ps electron pulse was found to be  $(5.0 \pm 0.2) \times 10^{-7} \text{ mol J}^{-1}$ . In the spurs of ionization, the

decay rate of  $e_s^-$  is slower in D<sub>2</sub>O than that in H<sub>2</sub>O, whereas the decay rate of OD<sup>•</sup> is similar to the one of OH<sup>•</sup>. In D<sub>2</sub>SO<sub>4</sub>/D<sub>2</sub>O system, the reactivity of and D<sub>2</sub>O<sup>•+</sup> was probed in deuterated sulfuric acid solutions of various concentrations and compared with that of H<sub>2</sub>O<sup>•+</sup>. The oxidized solute sulfate radical was observed at 7 ps and remarkably higher yields are found in deuterated solutions. The isotopic effects reveal the competition between two ultrafast reactions: proton transfer toward H<sub>2</sub>O (D<sub>2</sub>O) and electron transfer from HSO<sub>4</sub><sup>-</sup> to H<sub>2</sub>O<sup>•+</sup> (D<sub>2</sub>O<sup>•+</sup>). Density functional theory simulations decipher the electron transfer mechanism: it proceeds via sub-femtosecond charge migration and is not affected by isotopic substitution.

